POLITECNICO DI MILANO
DEPARTMENT OF AEROSPACE SCIENCE AND TECHNOLOGY
DOCTORAL PROGRAMME IN AEROSPACE ENGINEERING

MULTIPLE SATELLITES FORMATION FLYING FOR EARTH OBSERVATION APPLICATIONS IN LOW EARTH ORBIT

Doctoral Dissertation of:
Francesca Scala

Supervisors:
Prof. Camilla Colombo
Dr. Gabriella Gaias

Accademic Year 2022 – Cycle XXXV

Doctoral Dissertation of:	Francesca Scala
Supervisors:	Prof. Camilla Colombo Dr. Gabriella Gaias
Tutor:	Prof. Franco Auteri
Coordinator of the Doctoral Program:	Prof. Pierangelo Masarati
External reviewers:	Prof. Roberto Opromolla Dr. Sofya Spiridonova

Scala Francesca (2023), *Multiple satellites formation flying for Earth Observation applications in Low Earth Orbit*, PhD thesis, Politecnico di Milano, Supervisors: Colombo, Camilla, and Gaias, Gabriella.

To Mirko, for the constant love and support,
and to my parents, Teresa e Giordano

Abstract

EARTH observation has gained importance in the last decades to support daily life and better understand natural processes, driven by the need to study global climate changes. Most space agencies around the globe have developed sophisticated systems to collect data about planet Earth based on microwave, optical or magnetometer sensors. Currently, several missions carry synthetic aperture radars (SAR) or interferometers to measure key parameters in the microwave range. However, most of these missions, such as Cloudsat, MetOp, SMOS, SMAP and many others, are based on a monolithic satellite architecture. This approach limits the potentiality to improve data quality and spatial resolution to monitor natural events: with a monolithic approach, this can only be obtained by employing rather large antennas. The introduction of constellations and distributed systems promises a significant improvement in data quality and coverage. In the context of active SAR, few mission concepts have been developed based on distributed systems improving scientific data quality by observing the same terrain area from different platforms. One example is the TanDEM-X - TerraSAR-X mission launched in 2010 by the German Aerospace Center. On the other hand, no distributed missions carrying passive radiometers have been designed and launched, and few studies are currently available to design such missions. There are several research and technological challenges connected to these mission concepts. First, vehicles should be separated by a few tens of meters to perform passive interferometry with a swarm/formation, which indeed triggers many difficulties in operating such space systems. Second, precise navigation and control techniques are required, even for the real-time relative guidance, navigation, and control sub-system. In this thesis, we start from these challenges and assess to what extent distributed missions can be realistically implemented to improve the spatial resolution of passive interferometers. Consequently, the research questions regard how we can design guidance, navigations and control techniques to support distributed systems compliant with the need for on-board autonomy and robust control techniques to fill the current gap in the literature. This work proposes a preliminary mission design technique to enable future distributed multi-satellite systems for high-resolution interferometry and to understand how operational and payload constraints can be included in the design from the early phases of the process. To this end, first, the needs for future mission concepts for microwave observations are identified, and different cluster geometries are analysed in terms of performances achievable by the combined scientific instrument. Then, the generation of guidance profiles for the maintenance and reconfiguration of a formation is addressed. The latter is designed based on a convex description of the fuel optimal problem employing a continuous control law. Such a computation of the relative trajectory is then embedded into a relative guidance, navigation and control framework to simulate in a reliable, robust, and fast way the overall achievable performances of the distributed system, including operational requirements. Finally, the methodology is applied to test case studies involving active and passive microwave-distributed systems. As a result, this research provides a possible baseline for mission analysis design and preliminary outcomes of passive microwave applications, including typical control and navigation errors. This dissertation shows that indeed distributed systems can be designed to support future missions carrying microwave antennas and future cluster studies. In addition to the results associated with the specifically investigated microwave architectures, the significance of this study relies on the flexibility of the developed methodology, which can be applied to several multiple-spacecraft formation concepts, not only in the Earth observation field. Furthermore, the proposed approach can be extended to other orbital regions and space applications, opening the path for new passive microwave remote sensing applications.

Sommario

NEGLI ultimi decenni, l'osservazione della terra è diventata fondamentale in supporto alla vita quotidiana e allo studio dei processi naturali, guidati dalla necessità di comprendere i cambiamenti climatici. La maggior parte delle agenzie spaziali ha sviluppato dei sistemi complessi per raccogliere dati con su sensori a microonde, ottici o magnetici. Attualmente, svariate missioni sono dotate di sistemi radar ad apertura sintetica (SAR) o di interferometri per misurare diversi parametri scientifici. La maggior parte di queste missioni, come Cloudsat, MetOp, SMOS, SMAP e molte altre, sono basate su un'architettura monolitica, che può limitare la qualità dei dati e la risoluzione spaziale per monitorare eventi naturali che non si potrebbero osservare altrimenti. Con un'architettura monolitica, una qualità migliore si può ottenere solo sviluppando antenne più grandi. L'introduzione delle costellazioni e dei sistemi distribuiti ha dimostrato un miglioramento significativo nella qualità dei dati e nella copertura. Nel contesto di SAR attivi, alcune missioni distribuite hanno dimostrato questa capacità osservando la Terra da diverse piattaforme combinate. Un esempio è la missione TanDEM-X - TerraSAR-X lanciata nel 2010 dall'agenzia spaziale tedesca (DLR). D'altro canto, nessun sistema distribuito con interferometri passivi è stato disegnato e lanciato; e fino ad ora, pochi studi sono disponibili per progettare questo tipo di missioni. Ci sono diverse sfide connesse a questo tipo di missione: i satelliti devono volare a distanza di poche decine di metri per permettere l'interferometria combinata, e questo richiede lo sviluppo di tecniche per controllo e navigazione accurata e precisa. In questa tesi, vogliamo investigare in quale modo le missioni distribuite possano essere progettate per migliorare la risoluzione spaziale dell'interferometria passiva. La domanda alla base di questa ricerca vuole comprendere come si possano sviluppare tecniche di guida, navigazione e controllo in supporto a sistemi distribuiti, considerando autonomia a bordo e tecniche di controllo robuste per migliorare lo stato dell'arte attuale. Questo lavoro propone un approccio per il disegno preliminare di missione per rendere possibili sistemi basati su satelliti distribuiti per interferometria ad alta risoluzione e per comprendere come i requisiti operativi e dello strumento possano essere inclusi nel progetto. Per questo motivo, come prima cosa sono stati identificati i requisiti dei sistemi a microonde, e diverse geometrie di formazione di satelliti sono state analizzate in base alle prestazioni dell'interferometria combinata. Successivamente, a partire dalle tecniche disponibili, il mantenimento della formazione e le manovre sono state sviluppate con un sistema di controllo ottimo convesso basato su spinta continua. Infine, questa metodologia è stata integrata in un framework di guida, navigazione e controllo per simulare in modo robusto e efficiente i sistemi distribuiti, includendo i requisiti operativi. La precedente metodologia è stata applicata a diversi casi studio considerando voli in formazione con sistemi a microonde attivi e passivi. Questa ricerca fornisce un punto di partenza per il

disegno di missione e lo studio preliminare delle prestazioni di strumenti a microonde, includendo le incertezze del controllo e navigazione di bordo. Questa tesi mostra come sistemi distribuiti possano essere sviluppati in supporto a mission future, con strumenti a microonde attivi e passivi, ed a studi futuri di voli in formazione. L'importanza di questo studio si basa sulla flessibilità del modello sviluppato, che può essere applicato a diversi studi, non solo nel campo dell'osservazione della terra. Per concludere, questa ricerca può adattarsi allo studio in altre regioni orbitali e a differenti applicazioni spaziali, aprendo nel contempo la strada per approcci innovativi per il telerilevamento con sistemi passivi a microonde.

Acknowledgements

> *Lo spazio in cui siamo immersi è talmente grande, talmente immenso che c'è quasi da spaventarsi a guardarlo dentro un telescopio.*
>
> — Piero Angela

First, I would like to acknowledge and express my gratitude to my supervisor, Prof Camilla Colombo, for the scientific guidance and support and for allowing me to work on such stimulating topics. I am also grateful to my supervisor, Dr Gabriella Gaias, for her precious advice. I want to acknowledge Manuel Martin-Neira and Berthyl Duesmann for guiding me during my research stay at ESTEC and for their invaluable support. Thank you for sharing your experience on Earth Observation missions and guiding me through my doctoral research.

I want to thank my colleagues in the COMPASS team, who accompanied me for these three years. Mirko, Giacomo, Lorenzo, Andrea, Martina, Marco, Alessandro, Xiaodong and Juan, thank you for the unforgettable moment we shared, from the conferences in Dubai and Paris to mountain trekking and climbing. Also, a special thanks to my colleagues from EOP-PES, Sergio, Marcos and Montse, for their kindness and guidance during my visit. Laura, Ricardo, and Diogo, thank you for sharing invaluable experiences and making me feel at home with your kindness, joy and happiness. I hope our paths will cross again in the future. Thanks to my friends from Milano, who supported me from the start, especially Erica, Marzia, Francy and Fede, for the many moments we shared. I also thank the friends I found in Leiden, Valentina, Arianna, Chiara and Benedetta, for the moments and experiences spent together.

Finally, thank to my mum and dad, who make this path possible and for supporting me no matter what. Thank you Mirko for every day we shared, for every single laugh, your endless love, and your unlimited support and patience.

The doctoral research presented in this thesis has received funding from the European Research Council (ERC) under the European Union's Horizon 2020 research and innovation programme as part of project COMPASS (Grant agreement No 679086), and from the European Space Agency (ESA) through an ESA contract (Contract No. 4000128576/19). The view expressed in this thesis can in no way be taken to reflect the official opinion of the European Space Agency.

Contents

List of Figures

List of Tables

Acronyms

ASI	Italian Space Agency
AF	Array Factor
CNES	Centre National d’Études Spatiales
COCP	Convex Optimal Control Problem
CSA	Canadian Space Agency
CSPM	Cold Sky Pointing Mode
DLR	German Aerospace Center
EME2000	Earth Mean Equator and Equinox of J2000
EKF	Extended Kalman Filter
EO	Earth Observation
ESA	European Space Agency
ESTEC	European Space Research and Technology Centre
EPM	Earth Pointing Mode
FFLAS	Formation Flying L-band Aperture Synthesis
GCO	General Circular Orbit
GEO	Geostationary Earth Orbit
GNC	Guidance, Navigation, and Control
GNSS	Global Navigation Satellite System
GPS	Global Positioning System
GPS-Time	Global Positioning System Time
HEO	Highly Elliptical Orbit
HCW	Hill-Clohessy-Wiltshire
INPE	National Institute for Space Research, Brazil

ITRF	International Terrestrial Reference Frame
ISL	Inter-Satellite Link
JAXA	Japan Aerospace eXploration Agency
LEO	Low Earth Orbit
LQR	Linear Quadratic Regulator
LTAN	Local Time of the Ascending Node
MC	Monte Carlo
MEO	Medium Earth Orbit
MPC	Model Predictive Control
MJD	Modified Julian Date
NASA	National Aeronautics and Space Administration
OCP	Optimal Control Problem
PCO	Projected Circular Orbit
RAAN	Right Ascension of the Ascending Node
ROEs	Relative Orbital Elements
RTN	Radial-Transversal-Normal
SAR	Synthetic Aperture Radar
SKiLLeD	Simulation Kit for Logic Layout Design of Formation Flying
SRP	Solar Radiation Pressure
SSO	Sun-Synchronous Orbit
STM	State Transition Matrix
TDX	TanDEM-X
TAI	International Atomic Time
ToD	True of Date
TSX	TerraSAR-X
TT	Terrestrial Time
TriHex	Three Hexagonal
UCS	Union of Concerned Scientists
UTC	Coordinated Universal Time
UT	Universal Time

CHAPTER 1

Introduction

> *Space is for everybody. It's not just for a few people in science or math, or for a select group of astronauts. That's our new frontier out there, and it's everybody's business to know about space.*
>
> — Christa McAuliffe

RELATIVE motion has become of interest for space missions in several fields, from active debris removal to in-orbit servicing and from interplanetary to remote sensing missions. The latter plays a significant role in studying the Earth's environment and global climate changes. Currently, single spacecraft architectures are primarily used in Earth Observation (EO) for data collection and relay. Nowadays, the requirement of high resolution for environmental studies has become more stringent. In single satellite architecture, one possibility is the design of large sensors and antennas to improve the quality of observation data. On the other hand, going toward the idea of miniaturisation and distributed systems, relative motion within a formation flying framework can significantly improve the performances of the missions, with spacecraft acting as distributed nodes of a network of sensors. Understanding the advantages of distributed spacecraft for performing remote sensing requires modelling and design of the formation flying, as well as the guidance, navigation and control algorithms. Such research allows an understanding of the feasibility and performance of future multiple spacecraft mission studies in the EO field. Section 1.1 introduces the space missions for EO and the current context. The scope of the thesis is outlined in Section 1.2, where the hypotheses and the motivations of the work are discussed. The current state of the art of previous work that dealt with the thesis scope is presented in Section 1.3. Finally, the contributions and novelties of this work are presented in Section 1.4, and Section 1.5 drafts the structure of the thesis.

1.1 Background

The history of observing planet Earth began in the late 1850s, after the invention of photography. Tethered balloons were first employed to take pictures from an altitude of 80 m [1]. Some decades after, with the introduction of aeroplanes and military missiles, aerial photography captured the distribution of clouds from an altitude slightly above 100 km. In 1947, the United States Air force launched the first V-2 missile, and the Soviet Union launched the first Long Range Ballistic Rockets [1]. They were equipped with sensors to capture the upper atmosphere and demonstrated the potential of observing Earth from space. Nevertheless, the space era only began ten years later, with the launch of the first satellite, Sputnik-1. It provided the first measurements of the upper atmosphere density [1]. However, only in the 1960s dedicated spacecraft for observing the Earth were designed. The National Aeronautics and Space Administration (NASA) Tiros-1 spacecraft officially began the Earth observation era from space in 1960 [2]. It was the first satellite dedicated to weather forecast data acquisition. It acquired the first photo of Earth from space, as reported in Figure 1.1a.

Since the 1960s, the number of spacecraft dedicated to EO has increased and enabled essential applications from weather forecasting, agriculture and resource management to wildlife conservation, natural disaster and climate monitoring. To give some example, many space agencies, such as NASA, the European Space Agency (ESA), the Canadian Space Agency (CSA) and the Japan Aerospace eXploration Agency (JAXA), have developed many sophisticated space systems for collecting essential data about the planet Earth. Moreover, more recently, after the introduction of global indicators and targets for environmental, social and economic sustainability, the United Nations Office for Outer Space Affairs remarked on the crucial role of EO in providing data for monitoring and understanding natural processes across various sectors [3]:

"*The role of Earth observation (EO) and geolocation (provided by Global Navigation Satellite System (GNSS)) is recognized by the United Nations in supporting the achievement of the 17 Sustainable Development Goals (SDGs).*"

Indeed, space technologies can enhance the quality of data acquisition for geospatial information [4, 5]. For example, thanks to EO data, new policies are conceived for environmental protection and sustainable management of natural resources [6].

1.1.1 Current state of Earth observation missions

As of 1st May 2022, the satellite database by the Union of Concerned Scientists (UCS) indicated that there are more than 1000 active spacecraft for EO or Earth Science [7]. Specifically, we can identify three main macro-areas of application for space missions around Earth: Communication, Earth Observation, and Technology Demonstrator. Figure 1.1b shows the number of satellites currently in orbit divided into macro-areas. For each of them, the spacecraft are classified by orbit region: Highly Elliptical Orbit (HEO), Geostationary Earth Orbit (GEO), Medium Earth Orbit (MEO), and Low Earth Orbit (LEO). Focusing on the EO field, the primary outcome of the analysis shows the predominance of missions in the LEO region (more than 1000 spacecraft). Overall, it is the most crowded area around Earth, where also communication satellites are highly present. Initially, most space missions in LEO dedicated to observing Earth consisted of a single satellite architecture with a large platform equipped with the payload instrument. Subsequently, the constellations demonstrated the benefit of different platforms working for the same scope. Indeed, they allow better coverage and improvement in data acquisition performances. In the last decades, the need to reduce the dimension and, consequently, the cost of a mission has brought toward employing distributed systems to fulfil the scope previously carried out by monolithic missions. For this reason, in addition to constellations,

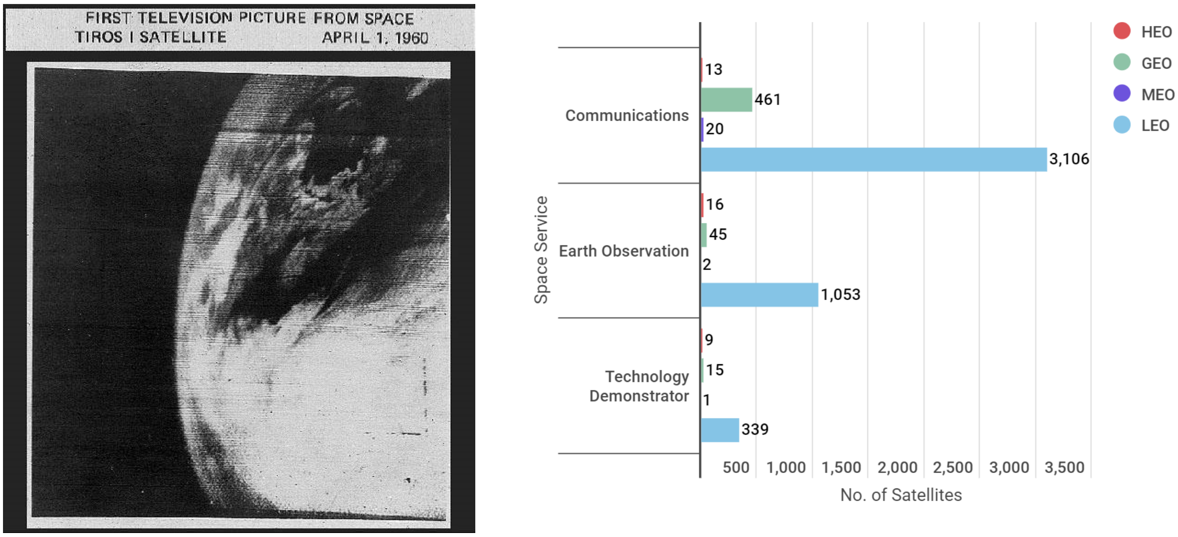

(a) *The first photo of Earth taken by the TIROS-1 satellite on April 1, 1960. Courtesy of NASA/NASA Content Administrator [2].*

(b) *Number of satellites per macro-area of space services around the Earth, divided into orbit types. Data catalogue courtesy of the UCS [7].*

Figure 1.1: *First Earth picture from space (a) and satellites classification per service (b).*

the concept of relative motion, specifically formation flying, has been introduced in the field. This concept relies on combining the instrument data to improve the performances so that the distributed payloads work as a single instrument. Among others, some EO missions are reported in Table 1.1, where the name, operator, launch date, payload instrument and orbit type are reported [7]. Most are in the Sun-Synchronous Orbit (SSO) or Polar orbit for better coverage of the Earth's surface and constant illumination conditions. The following paragraph reports the consideration of some of those missions to understand the role of constellation and formation flying for EO. We divide the discussion depending on the equipped sensors. In general, we can divide electro-optical instruments into two families: active and passive sensors. Moreover, we also considered the magnetometer sensors in Table 1.1 since they provide some important considerations for using formation flying in EO (e.g. *Cluster* mission [8] and *SWARM* mission [9]).

Active sensors. This family comprises instruments that actively produces a pulse in the electromagnetic spectrum and measures the backscattered signal. Active sensors include different instruments operating mainly in the infrared and microwave band of the electromagnetic spectrum. The Lidar is a light detection and ranging instrument that produces high-energy pulses and measures the reflected light in the infrared and ultraviolet range. It is typically used to measure information on the Earth's shape and surface characteristics, as for the *Cloudsat* mission [13]. Passing to the microwave spectrum, active sensors are called Synthetic Aperture Radar (SAR) and Scatterometers, which measures different parameters of the Earth's surface by emitting microwaves. Focusing on missions carrying active radar instruments, NASA's missions *Aqua*, *Aura*, and *Cloudsat* are part of the so-called A-train, composed of five satellites flying in sequence on the same orbit [11–13]. This configuration allows *Cloudsat* to follow the ground track of *Aqua*, to perform simultaneous measurements. Such a mission was an example of satellites operating for the same scope, with the introduction of the formation

Table 1.1: *Partial list of Earth's observation missions in the LEO, of major space agencies. Data catalogue courtesy of the UCS [7].*

Name	Agency	Year	Payload	Orbit	Reference
Terra	NASA	1999	five multi-spectral radiometers	SSO	[10]
Cluster	ESA, NASA	2000	magnetometer, ion spectrometry	HEO	[8]
Aqua	NASA, INPE, JAXA	2002	four multi-spectral radiometer	SSO	[11]
Aura	NASA	2004	four mid-infrared spectroradiometer	SSO	[12]
Cloudsat	NASA, CSA	2006	lidar and radar	SSO	[13]
MetOP	ESA, CNES	2006	radiometer, sounder, interferometer	SSO	[14]
SMOS	ESA, CNES	2009	passive multi-spectral radiometer	SSO	[15]
TDX/TSX	ESA,DLR	2010	X-band radar	SSO	[16]
Swarm	ESA	2013	magnetometer and accelerometer	Polar	[9]
SMAP	NASA, CSA	2015	passive multi-spectral radiometer	SSO	[17]
Icesat-2	NASA	2018	laser high-accuracy altimeter	Polar	[18]
Aeolus	ESA	2018	laser Doppler instrument	SSO	[19]
GRACE Follow-On	NASA, DLR	2018	microwave and laser interferometer	Polar	[20]
PRISMA	ASI	2019	hyperspectral camera	SSO	[21]

flying concept. Nevertheless, they carry different onboard instruments, which operate independently from each other [13]. An example of a mission involving formation flying and carrying SAR instrument is the *TanDEM-X (TDX)/TerraSAR-X (TSX)* mission [16]. It consists of two satellites flying in formation carrying an X-band radar to simultaneously image Earth's terrain from different angles for better accuracy. It was one of the first missions to deal with the Helix-formation concept, ensuring safe operations and minimising the collision risk [16]. A similar mission is the *GRACE* follow-on mission, where two spacecraft carrying microwave and laser interferometers measure changes in gravitational pull [20].

Passive sensors. Differently from the previous family, these instruments detect the energy in the electromagnetic spectrum emitted or reflected by an object. This family comprises a wide range of radiometers and spectrometers. Starting from sensors operating in the visible to near-infrared spectrum, the Hyperspectral Imaging and the imaging radiometer instruments are widely used to measure the characteristics of Earth's surface. The *PRISMA* mission is an example of spacecraft using a hyperspectral camera for measurement acquisition [21]. Passing to the microwave range of the spectrum, the passive microwave radiometers receive and measure the thermal radio emission of natural objects without emitting any signal, differently from SAR instruments. In the passive radiometer framework, two crucial missions are the *SMOS* and *SMAP* satellites [15, 17]. They both provide multi-spectral measurements in the L-band to monitor global soil moisture, vital for numerical weather prediction and seasonal climate models. Currently, no mission in the passive radiometer framework involving formation flying has been designed and launched.

1.1.2 Importance of formation flying for microwave missions

As described in Section 1.1.1, constellations, specifically formation flying, were employed to improve the performances of active SAR sensor missions. Several research studies highlighted the importance of designing a cluster of SAR satellites flying in close formation [22, 23]. One possibility for the interferometry technique foresees that each sensor in the cluster is considered an isolated instrument that provides bistatic images. Thus, the interferometry solution is given by the combination of multiple

SAR receivers [23, 24]. A second solution relies on the possibility of separating the transmission and reception functions of the SAR among the cluster. For example, only one satellite transmits the signal, and the other platforms work as many receivers [24]. The main advantage of these two configurations is the possibility of improving the quality of the resulting image by combining the interferometry products of each platform [24, 25]. Moreover, the system is more flexible than a monolithic approach for different imaging requirements. A cluster also goes toward miniaturisation with nanosatellites, reducing the mass of the single platform at launch time.

A different concept can be introduced for passive microwave radiometers. In this case, the instrument is made only by the receiver. One possibility to improve the measurement accuracy is to increase the sensor size with a monolithic platform design [26]. A different solution relies on the possibility of having a cluster of satellites flying in formation. The interferometric technique for this scenario considers the whole cluster as a unique "virtual" single instrument, where each spacecraft is a node of this virtual sensor, as proposed in [27, 28]. The terminology "virtual" is introduced to specify how the radiometer is not a physical instrument part of one single satellite, but it is a result of the combination of several physical passive microwave radiometers onboard each platform. This solution's flexibility envisions the possibility of reconfiguring the formation geometry in orbit by adding or removing a node during the mission lifetime to improve the performance of the combined radiometry products.

Currently, no missions studies have been developed to realise high-resolution passive interferometry with distributed systems. Given this gap in the literature on formation flying for passive microwave applications, this thesis proposes a methodology for the preliminary design of a mission concept involving a cluster of spacecraft. As a result, this work provides a tool for the preliminary design of formation flying missions, including operational constraints, payload architecture requirements and performances.

1.2 Research question

To address the need to improve EO data quality, the work presented in this thesis envisions the possibility of designing formation flying missions to improve interferometer performances and fill the lack of studies of distributed missions for passive microwave applications, as mentioned above. The research addresses the need to improve satellite data in the direction of miniaturising the platform for a reduced mission cost. The goal of this research can be summarised as

> *"the definition of a preliminary design strategy for future distributed multi-satellites missions for high-resolution interferometry, including main operational and payload constraints".*

Three main research questions have been identified to explore such an objective.

The FIRST research question deals with understanding the current scenario for EO missions, and identifying the needs of future mission concepts for microwave observation. The thesis discusses and defines possible improvements in payload performances exploiting distributed systems. The problem is approached by defining preliminary equations to model the radiometer and its performances, to relate them to the platform cluster geometry and the subsequent mission analysis study. A fundamental challenge from the technology and design point of view has been identified for the passive microwave distributed systems: close-distance formations with a separation among the platforms of 5 to $10\,\mathrm{m}$ are required. This thesis address the need to develop specific algorithms to demonstrate the feasibility and safety of such close-distance formations.

SECOND, the central part of the study explores the current techniques available in the literature to design optimal formation maintenance and reconfiguration, depending on the operational phases of the mission. Specifically, algorithms that could be implemented onboard are analysed, to deal with the challenges of metre-level distance among spacecraft. This work develops a fast and reliable tool for the design of delta-v optimal manoeuvres, considering a continuous control approach, starting from the literature findings.

THIRD, this dissertation integrates such core tools within the relative Guidance, Navigation, and Control (GNC) framework. For this purpose, the research objective translates into the need to design fast, robust and autonomous GNC algorithms for distributed systems. These algorithms are applied to active and passive microwave-distributed systems with different operational requirements. The overall framework developed in the research provides a quick but accurate profile of the mission performance from the control, delta-v budget, and navigation points of view. It should be flexible to be applied to several different formation flying scenarios and the most common operational phases of a space mission, from nominal operations to safe mode in case of a system failure. Aside from the mission analysis and the GNC study, this research also provides a preliminary outcome of the passive microwave payload during the nominal phase of the mission. Combining the control accuracy and the radiometry product is fundamental, as the payload is affected by errors and uncertainties of the GNC behaviour.

Overall, the primary goal of this research is the definition of a strategy for preliminary mission analysis and design for passive radiometry missions, GNC algorithm definition, and preliminary payload performance characterisation. This work could serve as a framework for the feasibility assessment of future cluster studies in view of phase 0 and phase A activities typical of space mission design and development.

1.3 State of the art

After defining the research questions, key literature contributions have been identified in the research field. Finally, three main macro-areas have been outlined in the background and research question paragraphs (See Sections 1.1 and 1.2): radiometry algorithms for microwave payloads, formation flying design in LEO, and techniques for relative Guidance, Navigation, and Control (GNC). The latter two are the most relevant for this dissertation, providing the backbone of the analysis, while the former serves as a starting point for the formation requirements and payload definition.

1.3.1 Microwave remote sensing

This section describes the techniques developed for microwave remote sensing applications. As described in [29], microwave measurements enhance the capability to penetrate clouds, vegetation and the ground itself, differently from other radio frequencies. Specifically, longer wavelengths, such as microwaves, ensure a deeper penetration in the vegetation, depending on the moisture content and density, than other frequencies, such as optical waves. Furthermore, differently from the visible and infrared optical sensors, microwave techniques extend the measurements for dry or wet soil to more than a few centimetres of penetration and provide measurements independent of the illumination condition of the Sun. Overall, microwave, optical, visible and infrared complement each other measurements for a better understanding of natural processes. At this point, we consider active SAR and passive radiometers for the the microwave techniques. The former is based on the sole measurement of the emitted electromagnetic signal from the origin. The latter, instead, provides the emission of the electromagnetic signal and the reception of the reflected one by the object itself [29].

Active microwave techniques Since the introduction of monostatic configurations of radar systems in the late 1880s [30], it has become of great interest for civil and military applications. In 1951, the concept of Synthetic Aperture Radar (SAR) was introduced by Carl Wiley [31]. Due to the DOppler effect, its working principle is based on the capability to produce an image by measuring the reflected signal as a function of the time delay, due to the Doppler effect [31, 32]. As described in [32], SAR application for satellites typically consists of a synthetic aperture with a length of 3 to 7 km long. In monostatic radar, the receiver and the transmitter are in the same position. The synthetic aperture is represented by the locations of the antennas during the illumination of a target [33]. Differently, a bi-/multistatic radar can be represented in space by exploiting different locations or platforms, and the synthetic aperture is provided by the synchronised antennas [33]. The latter case introduces the concept of distributed systems for SAR applications (e.g. TDX-TSX). Figure 1.2 shows the working principle of these two different modes. In Figure 1.2 (top), the two spacecraft work separately, each acting as both a transmitter and a receiver. The footprint of the second spacecraft (in blue) follows in time the exact area covered by the first spacecraft (in green), resulting in better data coverage from the combination of the knowledge of the formation. In Figure 1.2 (bottom), the bistatic mode is represented. The two spacecraft cover the same footprint simultaneously; only one spacecraft works as a transmitter (the green one). The second spacecraft, instead, functions as a receiver. Different techniques have been developed for reconstructing the synthetic image when two platforms are involved in a multistatic system. Two main combinations can be identified: coherent and incoherent. The coherent combination was applied to both along-track and cross-track interferometry for different

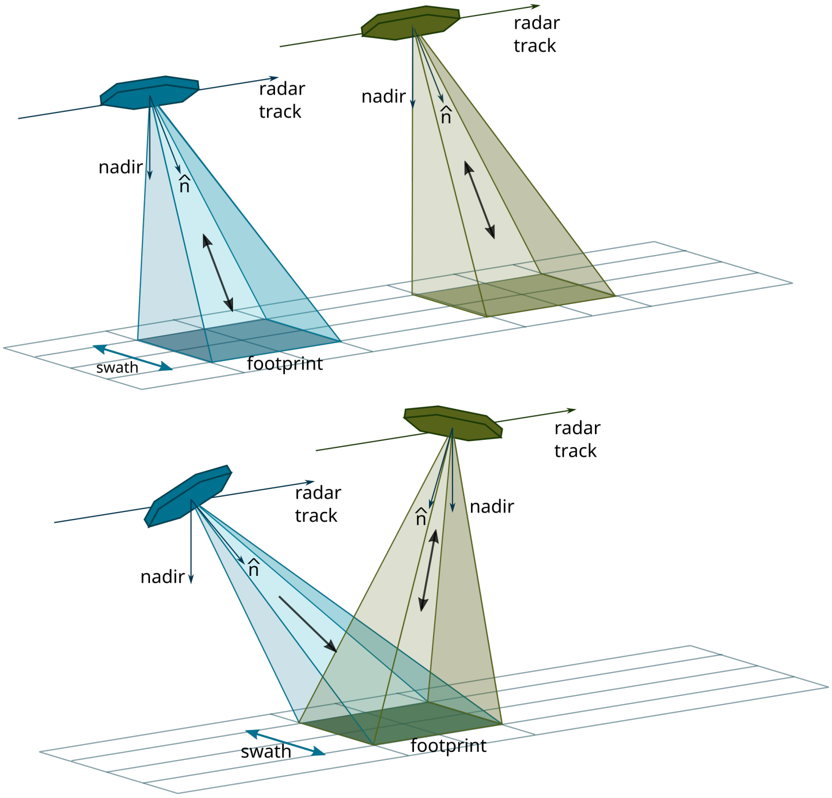

Figure 1.2: *Monostatic (top) and bistatic (bottom) acquisition mode for a two-spacecraft SAR formation.*

applications. In the along-track, the image is acquired by two platforms with identical configurations, shortly separated in time [34–36], where one antenna is used for the transmission. Cross-track interferometry, instead, combines the measurements from two separated antennas, exploiting the phase difference [37–39]. On the other hand, an incoherent combination is based on the difference in the image observed by different platforms (i.e. the distributed receivers). This methodology is mainly applied to the measurements of terrain slope or surface roughness, as in [40, 41]. An example of an application of multi-platform SAR in space is given by the TDX-TSX mission, launched in 2010 [24, 37]. It consisted of two spacecraft flying in close formation in LEO to achieve SAR interferometry.

Passive microwave techniques Starting from the concept of incident energy absorption and/or reflection by a medium, different studies proposed the possibility of exploiting a sensor to measure electromagnetic radiation [41]. Specifically, a microwave radiometer can be adopted to measure the radiation received by the surroundings. Since the 1950s, these sensors have been employed for astronomical and atmospheric measurements [42]. In 1972, the meteorological satellite Nimbus 5 introduced a new technique, called electrically scanning microwave radiometer, which allows reaching an image resolution of 50 km. It measured both rainfall and sea ice properties. A few years later, the work in [43] identified how soil's moisture content influences the radiometric measurements, giving the radiometer an important role in assessing this parameter. In this scenario, the main interferometric technology developed for image reconstruction is aperture synthesis [44]. It is based on the combination of the products of small antenna pairs located at a predefined spacing to create a large aperture [44, 45]. Figure 1.3 shows the working principle of passive microwave: the sensors measure the reflected radiation by different means. The left part of Figure 1.3 represents the acquisition mode for a single satellite configuration, while on the right, the combination of small spacecraft to create large aperture is represented.

The nature of the aperture synthesis techniques allows some preliminary studies for having multiple sensors deployed in space [45], where a preliminary concept of two antennas, one spiralling around the other, was briefly presented. However, the concept of locating these two sensors on different platforms was still missing, and one large spacecraft, carrying the antenna array was proposed. Furthermore, most mission concepts developed in early 2000 were based on a single platform. Ex-

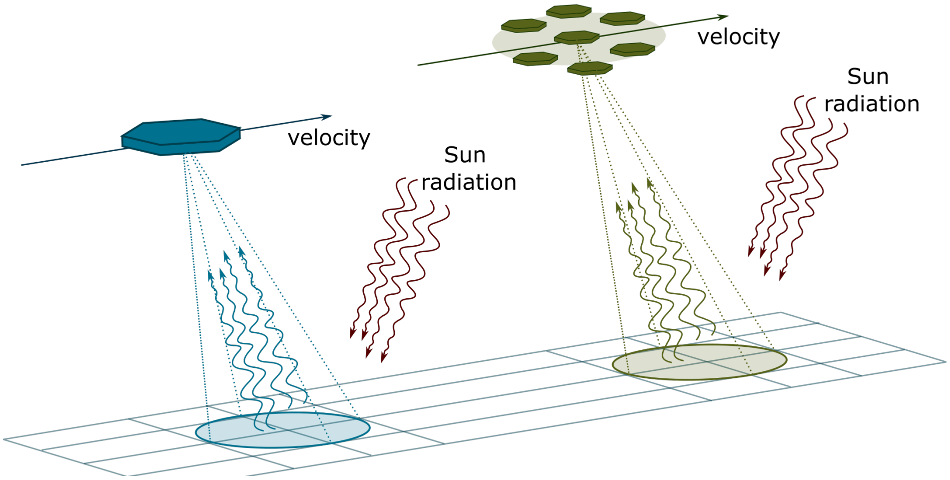

Figure 1.3: *Acquisition mode for passive microwave: single satellite (left) and formation of satellites (right).*

amples are the *SMOS* and *SMAP* satellites, as mentioned in Section 1.1. For these two missions, different algorithms for the retrieval of the data were implemented depending on the application (i.e. soil moisture or vegetation monitoring) [46].

Differently from SAR applications, few studies to exploit distributed systems exist in the literature for passive microwave measurements. More recently, one solution was identified in the work by [47], where the concept of formation flying was implemented to design possible space missions in the GEO region for passive microwave radiometers. This work proposed several techniques and requirements for defining the formation geometry and its control in orbit. Moreover, a different concept was proposed by [48], where a 3-D array configuration is identified and studied for a synthesized array based on satellite formation flying. The advantage of employing a distributed system for passive interferometry relies on the possibility of separating the antenna arrays on smaller platforms. Then the synthetic aperture is realised considering the distributed antenna arrays as part of a single unique instrument, improving the aperture dimensions and spatial resolution [27]. The lack of studies in this field is mainly caused by the need to maintain a rigid and fixed formation among the platform to realise synthetic aperture, and keep the spacecraft at a distance of metre level. These aspects pose several challenges to GNC design and development. Compared to the studies for active techniques (e.g. SAR), the gap for passive microwave requires further study and development of formation flying techniques for future mission study in the LEO region.

1.3.2 Formation flying for Earth observation

This section presents the current context of formation flying techniques and the main contribution in the Earth observation field in LEO. Most of the research in the literature is applied to active microwaves, specifically SAR interferometry. In the latter case, the formation requirements are more relaxed in comparison to the passive antenna case: the platforms can stay at a kilometre level distance, and a variable baseline of the formation is exploited for SAR interferometry. On the other hand, as aforementioned, this is not the case for passive microwave distributed antennas: the distance among the platform shall be in ta few tens of metres range, and the formation shall be kept rigid and fixed by the onboard control system, resulting in a much more challenging design and requiring onboard autonomy. The relatively short distance requirements can apply (not only to passive interferometry) also to the distributed SAR (also known as Formation Flying SAR) concept, in which the inter-satellite distances can be of the order of few tens of meters.

Starting from SAR technology, the work by Gill et al. [25] exploits the concept of along-track interferometry with two SAR spacecraft. The payload requirements and the consequent constraints on the geometry were presented for deriving and selecting of the formation flying strategy. This work provides some preliminary requirements for safe operations of spacecraft in formation, identifying a need for control accuracy of $x/10$ and a sensor accuracy of $x/100$, with x the separation distance among the spacecraft. The selection of active L-band or X-band SAR poses a requirement on the along-track separation of hundreds and tens of metres, respectively. The need for a fully-autonomous formation keeping was identified in this work.

Following this study, more developments for SAR interferometry were identified based on a two-spacecraft formation. Based on the acquired know-how of GRACE program [49], the research in [37,50] proposes the study for developing the TDX/TSX mission. It consists of two SAR satellites, operating in X-band, with a separation baseline in an along-track of 2 km and a cross-track of 300 to 500 metres. This mission applies the concept of eccentricity /inclination (e/i) vector separation - originally developed to handle the co-location of geostationary satellites in the same longitude window [51] - to carry out safe proximity operations in LEO. Similarly to previous work, an autonomous control

Table 1.2: *State of the art of missions§ and studies* considering formation flying for remote sensing application around the Earth.*

Name	Type	No. of s/c	Separation distance	References
GRACE§	Gravity and climate measurements	2	220 ± 50 km	[49]
ATI-SAR in X-Band*	Active along-track interferometry	2	30 ± 10 m	[25]
ATI-SAR in L-Band*	Active along-track interferometry	2	225 ± 75 m	[25]
TDX/TSX in X-band§	Active interferometry	2	300 to 500 m	[37, 50]
INSAR*	Active interferometry	2	600 to 900 m	[53, 58]
BISSAT*	Active interferometry	2	0.07 to 3 km	[54]

routine was foreseen and controlled by the ground-based flight dynamics team [52]. The TSX mission, launched in 2007, was followed by the TDX spacecraft in 2010 to perform formation flying activities. It represents a breakthrough in the study of SAR formation flying. More concepts were developed in literature considering both "close" and "large" formations, with a few kilometres to hundreds of kilometres separation, respectively. An example is the work developed in [53], where a two-spacecraft SAR mission was characterised, starting from the know-how of the in-orbit results of GRACE and TDX/TSX missions. It presents an analytical model to design J_2-invariant relative orbits to realise an effective baseline of 500 to 700 metres. Similarly, the work in [54] proposes a tandem configuration for the COSMO-SkyMed Italian constellation adding a fifth satellite named BISSAT. Both cross-track and along-track interferometry with two spacecraft in formation were proposed with coplanar formation configurations. More recently, the works in [55–57] propose new design approaches for bounded relative trajectories for active remote sensing and close proximity operations. New applications to clusters of more than two spacecraft are described for formation flying, on-orbit servicing, and active debris removal. Important remarks are provided in terms of collision risks and safety procedures. Moreover, an innovative path planning algorithm for SAR formation was proposed in [57], with both centralised and decentralised approaches.

In this context, the need to extend the methodologies already available in the literature to passive remote sensing is identified, leading to the definition of the main requirements from the payload point of view. Specifically, passive remote sensing can exploit the formation of satellites flying with a separation distance of tens of metres. Most formation concepts and missions described in the literature are characterised by a separation distance of hundreds to thousands of metres, as in Table 1.2.

This thesis addresses the need to develop specific algorithms and approaches to deal with the challenges of close-distance formations, with separation among the satellite of 5 to 20 metres.

1.3.3 Relative dynamical models

This section presents the state of the art of dynamical models for relative motion. First, we can identify two main approaches: numerical and analytical models. With numerical models, we identify the techniques that require numerical integration of the equations of motions, while the analytical techniques are based on closed-form linear models of the relative motion. In this context, closed-form solutions develop the State Transition Matrix (STM) of the relative motion. Several literature surveys present the existing methodologies and their accuracy level, as in [59, 60], which offers a concise survey on the relative motion, and in [61–64] which instead present an extensive survey of the state-of-the-art techniques. For this study, we mainly focus on existing analytical techniques which can be applied to an efficient design of guidance and control methodologies, giving an immediate description of the relative motion. The models used are compared against the Keplerian truth to evaluate the accuracy and the modelling error. Specifically, for the close distances required by the passive interferometry, at metres level, linear models of the dynamic can accurately describe the relative motion and can support autonomous onboard algorithms, requiring less computational effort than a non-linear model.

At this point, we identify three different coordinate systems for the dynamical description: the Cartesian state, the orbital element differences and the Relative Orbital Elements (ROEs) representations. The former is the most used and studied in the literature, starting from the Hill-Clohessy-Wiltshire (HCW) equations [65, 66]. The latter two are based on the difference among the absolute orbital elements of the spacecraft in the formation. The ROEs are functions of the absolute orbital elements, derived from the relative eccentricity and inclination vectors [67]. Furthermore, they can be written as integration constants of the HCW equations, combining the Cartesian and the orbital elements representation [50]. In this perspective, this dissertation focuses mainly on relative models for quasi-circular reference orbit in the LEO region and adopts the ROEs representation, as a means to express the integration constants of the HCW equations. The quasi-circular nature of the reference orbit derives from the interferometry application of the study. Specifically, the circular orbit is selected to guarantee similar and consistent observation data during the operations, with no or little variations in the orbit altitude. The selection of the ROEs to develop linear control theory derives from the possibility of adding an astrodynamics perspective to the results.

Cartesian state representation Most of the research developed in the last decades on relative motion is based on the HCW equations, which describe the relative equations of motion in the Cartesian coordinates [65, 66]. The work by Clohessy and Wiltshire provides an initial description of terminal guidance for relative motion [66]. This formulation neglects external perturbations other than the first-order differential gravity among the spacecraft. The coordinate frame used to describe the variation of Cartesian coordinates is the Hill frame [65], which is commonly used to express the relative motion of two objects in a rectilinear relative state. Subsequent works introduced the idea of a curvilinear relative state to improve the model description and accuracy [68]. The inclusion of the external orbital perturbation was considered in several works to incorporate and predict the effect of the environmental forces. Starting from the LEO region, the two main perturbing effects are the Earth's oblateness, J_2, and differential atmospheric drag. The former effect was included in the models developed in [69, 70]. Similarly, the combined effect of the drag model and J_2 differential effect was developed in an analytical STM by [71]. This work demonstrated that the error on the relative position of the linear model with respect to the non-linear propagator could go down to $2\,\mathrm{cm}$ after 15 orbital periods for a leader-follower formation with an initial along-track separation of $1\,\mathrm{km}$. These results have been obtained for a non-drifting initial condition with a rectilinear relative Cartesian state. In the same work, if the same but drifting initial conditions are considered, the model error goes up to $5\,\mathrm{km}$ after 15 orbital periods [71]. The development of more and more reliable models is fundamental for properly assessing the relative dynamical behaviour with respect to the full non-linear real world. By employing the element differences and/or ROEs, the inclusion of external perturbation is more straightforward, enhancing precise relative motion description, with generally simpler functional expressions.

Orbital elements differences In [72], a description in Delunay orbital elements are used to derive element differences. This model includes the effect of the mean Earth's oblateness J_2 effect. A similar model developed in [73] is based on the analytical description and derivation of an STM including the first-order J_2 effect, in terms of non-singular difference of orbital elements. The main advantage of working with orbital elements difference is the reduction of the linearisation error in the initial conditions, and a more straightforward inclusion of the initial conditions. The STM expressions in elements differences are derived for the mean elements and require a transformation from and to osculating elements. For this reason, they provide relatively compact expressions, thanks to the use of the mean argument of latitude.

Relative Orbital Elements representation The ROEs state is introduced as a function of absolute orbital elements and can be written as integration constants of the HCW equation, as described in [50]. The advantage of this representation is based on the connection with the absolute orbital elements of each satellite. As for the orbital element differences, the ROEs enhance the possibility of including external perturbation via Lagrange planetary or Gauss variational equations. In addition, the ROEs provide a better physical insight into the analytical representation than the HCW, thanks to the immediate identification of the effect of each acceleration term on the relative orbit elements. Finally, the ROEs have been used to develop efficient collision avoidance strategies for the relative motion, based on the relative eccentricity/inclination vector separation, as described in [74]. The possibility of designing a passive safety methodology based on a simple representation of the minimum distance between the spacecraft in the radial and normal direction is essential for safe operations. The inclusion of relevant perturbations for the LEO region has been proposed in several models. The work in [75, 76] derived an STM including the J_2 and differential drag effects. More recently, [77, 78] developed a semi-analytical and analytical model for a precise description of the relative motion, capable of including the effect up to a generic order of the gravitational harmonics. Similar considerations apply to the orbital elements' differences. The different methodologies for deriving the STM in ROEs are mainly based on the mean effect of the geo-potential and require a transformation between mean and osculating elements. This aspect is essential for improving the model accuracy for far-range relative motion, with an inter-satellite distance larger than $1\,\mathrm{km}$. As aforementioned, for distributed systems carrying passive microwave instruments, the formation consists of spacecraft flying in close proximity, with a distance of a few tens of metres. In this case, the linearisation and the difference between mean/osculating have a smaller influence on the relative dynamics, since the oscillations almost cancel out due to the close proximity, resulting in a smaller error between mean and osculating relative elements.

1.3.4 GNC techniques for relative motion

This section presents the current Guidance, Navigation, and Control techniques and research dealing with relative motion, specifically formation flying and swarms of satellites. The techniques and methodologies used for the relative GNC depend on different factors.

First, different considerations are required, depending on the operational range of the formation. In this dissertation, the main application for passive interferometry requires methodologies for close-range spacecraft with an operational range of a few tens of metres. Furthermore, a rigid and fixed formation is required to realised of a virtual synthetic aperture. Consequently, continuous corrections are required for different phases of the mission, specifically the formation keeping. The continuous control approach is based on low-thrust technology, such as ion or cold gas thrusters. Since these engines are operated continuously, and the spacecraft are close to each other, the effect of plume impingement shall be considered for the geometry selection of the formation. In fact, it could cause degradation on solar panels and interfere with the payload itself. Differently, for the secondary application of this work, with SAR instruments, the operational range of the formation is at kilometre level. In this case, the control approach is more relaxed and both impulsive or continuous corrections can be implemented. The impulsive control scheme has already been implemented successfully on-board

SAR missions, such as the TDX/TSX mission [37]. In this dissertation, the possibility of implementing continuous control for formation maintenance of SAR distributed mission is analysed to assess the performance compared to the impulsive approach.

Second, different control strategies are required, depending on the mission phase. The initialisation of the formation and the transitions to safe mode or a different nominal configuration (as for the calibration of the microwave antenna) requires the implementation of formation reconfiguration manoeuvres. This thesis focuses on the design of the manoeuvre with a continuous control scheme. Similarly, a low thrust control is developed to perform trajectory tracking for formation maintenance.

For a more efficient realisation of the control, guidance for different operative phases is developed, and subsequently, a tracking control law is implemented. Due to the dynamical coupling among the satellites, the desired relative state profile is associated with a tracking control law, and similarly, the reconfiguration among the agents in the formation depends on control techniques to realise the guidance strategy [59]. Precisely, the approach followed for the relative GNC is based on the following procedure:

1. Development of a guidance and control, depending on the phase of the mission, in an open loop scheme.
2. Development of a tracking control law to follow the guidance trajectory and control of point (1), in a closed-loop scheme.
3. Development of an absolute and relative navigation algorithm based on GNSS sensors.
4. Inclusion of the closed-loop control techniques (2) in a GNC framework, including the modelling of the navigation subsystem (3), to assess the performance and feasibility of different mission geometries.

The accuracy required from the GNC framework depends on the application. For the passive interferometry scenario, a centimetre and millilitre level navigation accuracy is envisioned for on-board and ground reconstruction, respectively. Consequently, a control accuracy of the relative position in the centimetre level is envisioned to guarantee a correct virtual synthetic aperture and a safe formation. Differently, the requirements for SAR applications are more relaxed, and 10 to $20\,\mathrm{m}$ is required for the relative control accuracy from the lesson learnt with TDX/TSX mission. Similarly, a GNSS-based navigation accuracy in the order of tens of centimetres is envisioned [79].

The state of the art of the relative GNC is presented following the aforementioned approach, focusing on continuous control methodologies and GNSS navigation for missions and studies around the Earth.

Open-loop control guidance

The open-loop approach is based on control guidance with no feedback from the current state error in the control matrix. The optimal control could be energy or fuel optimal. The former refers to the guidance with minimum energy connected to the norm-2 of the delta velocity. The latter, instead, is connected to the fuel optimal for the tridimensional manoeuvrability using the norm-1 of the delta velocity. An approach for fuel-optimal control for formation reconfiguration manoeuvres is presented in [80, 81]. The procedure is based on an analytical representation of the control law, involving the variational Hamiltonian function to set up a minimum fuel problem. This control problem formulation exploits the natural dynamics already present in the relative motion for the control design procedure, including the main disturbance effects of the Earth's oblateness J_2 [81]. The idea of exploiting natural motion for control design procedures was implemented in several works [82–86]. In [82], an impulsive control technique was derived based on Gauss' variational equations, to include the natural drifts due to the main LEO perturbations. Similarly, the control technique developed in [83] implements formation maintenance by balancing the fuel consumption rate among identical satellites. This aspect is essential in this dissertation, as fuel balancing results in a similar design of the different platforms and similar wet mass. The latter aspect is important to have similar effects of the orbital perturbations, particularly the atmospheric drag, on the spacecraft trajectories. In this work, the feed-forward control is added to a closed-loop control logic, to augment the feedback control matrix (LQR). A similar open-loop logic is implemented in [84], where the methodology is applied to continuous control of the Sun vector tracking problem and forced relative motion. Passing to numerical techniques, the work in [85] presents a linear control system to minimise the relative deviation for the tracking problem. Numerical optimisation techniques, such as genetic algorithms, are implemented to solve the linear control system.

A different feed-forward approach is based on convex optimisation techniques, as in [57, 87–89]. The main idea is to use linear programming techniques to write the control problem, the relative dynamics, and the dynamical constraints in a discrete convex formulation. The nature of convex formulation allows for a global optimum of the control problem useful for trajectory and manoeuvre planning under continuous thrust. Subsequently, [87] complements the results of the convex formulation with a feedback control logic to correct for uncertainties in the final relative state. More recently, the work in [57, 89] extends the convex optimisation approach with the genetic algorithm for path planning of autonomous management of spacecraft reconfiguration. These approaches are promising for the implementation onboard, due to their relatively small computational effort required to solve the optimisation problem. A similar approach has been developed in [90], when an impulsive relative guidance and control unit was demonstrated within the AVANTI experiment. Thanks to the use of ROEs, it was possible to solve a convex energy-optimal problem in a fully analytical way, including the mean J_2 and differential drag effects.

Several studies propose to implement sequential convex programming as a starting point for a Model Predictive Control (MPC) logic. Differently from the classic convex optimisation, the MPC updates the optimal trajectory during the formation maintenance or the reconfiguration, and simultaneously reduces the algorithm's computational effort [91, 92]. Consequently, this approach could be applied to a swarm of many spacecraft without significantly increasing the computational time. The MPC logic has been applied in the PRISMA mission to design fuel-efficient relative trajectories for the autonomous formation flying GNC module [93]. Moreover, also for the AVANTI experiment, an MPC control scheme based on ROEs has been developed with a receding finite-time horizon [90], including the mean J_2 and differential drag effect with an impulsive manoeuvre scheme.

Closed-loop control techniques

The closed-loop approach has the advantage of providing a feedback gain matrix to the control law, based on the error for the relative state of the formation. An example of a classic feedback control technique is the Linear Quadratic Regulator (LQR) controller, applied in the literature to different formation-keeping problems [94–97]. In [95], both a continuous and a discrete-time formulation of the LQR control is applied to a centralised control system. More recently, the LQR technique was augmented with artificial potential functions, to implement evasive manoeuvres during proximity operations [97]. This work demonstrated the potentiality of LQR techniques for collision avoidance procedures. Similarly, the work in [98] proposes a continuous feedback control strategy based on Lyapunov candidate functions for guidance tracking problems. In [99], a linear feedback control based on the solution of the LQR Riccati's equation is proposed to realise an L_1 norm controller in the presence of non-linear dynamics. Moreover, the closed-loop dynamics is implemented in [100], where the algorithm includes the limitations to the thrust magnitude. The approach is applied to the design of safe trajectory planning. Finally, the feedback system is called Linear Quadratic Gaussian controller when the LQR is coupled with an optimal observer for the state vector estimation [101]. This approach was implemented to realise autonomous navigation for spacecraft formation in [96], where a decentralised logic is implemented. In this work, the LQR has been adopted in the closed-loop GNC tool developed to simulate different operational phases of a mission study. Specifically, the idea to provide trajectory tracking control has been adopted, using as reference trajectory and reference control the ones computed with open loop techniques.

In addition, in the context of multi-satellite formations and spacecraft swarms, several researchers propose robust and safe feedback control law, as in [102–104]. The work in [102] proposes an innovative approach based on the feedback error on ROEs framework, for the definition of the commanded acceleration. Such an approach is used to derivate switching lines for thrust in in-/anti-flight directions, which are subsequently modulated for each specific reconfiguration logic. The advantage of this approach is the capability to provide a safe and robust initialisation procedure for swarm studies. For this reason, the LQR model developed in this work has been tested against uncertainties in the initial conditions. Such uncertainties are typically connected to an error in the formation initialisation in orbit with respect to the nominal case, or an error in the control profile of the onboard thrusters.

Navigation techniques for relative motion

Different navigation techniques are available for relative motion reconstruction and, specifically, formation flying missions. This dissertation considers spacecraft flying in close formation with a baseline in the metre-to-kilometre range. Consequently, accurate navigation techniques are needed to provide millimetre to centimetre level accuracy. Several studies, as the work in [64], identify that such accuracy level in the LEO region can be provided by three main navigation techniques: GNSS-based systems, vision-based systems, and laser-based systems. The former technique can provide measurements for the spacecraft's absolute and relative state, exploiting the measurements from GNSS and Global Positioning System (GPS) constellations. Due to the nature of the measurement, this technique can be applied only to cooperative spacecraft, capable of sharing and processing GNSS signals. The latter two provide information on the relative range, line-of-sight, and relative attitude. The vision-based techniques could reach an accuracy in the order of millimetres, and it is typically used in relative motion involving both cooperative and uncooperative targets. On the other hand, the laser-based system suffers from the high mass and power required to operate correctly. Therefore, it is used for specific close-range applications, such as LiDAR (Light Detection and Ranging) systems for on-orbit servicing and docking applications. This work focuses on the GNSS-based navigation techniques, starting from systems and considerations that have been widely implemented in literature and real mission scenarios. Furthermore, due to the close proximity of the vehicles, it is important to address the need for autonomous navigation solutions and accuracy of the absolute and relative state reconstruction onboard. Different levels of navigation accuracies are typically required depending on the separations among vehicles. For example, as described in [33], the navigation accuracy is ten times better than the control accuracy, which should be ten times better than the formation size. Thus, longer separations typically require less accurate relative navigation. Furthermore, achieving accurate relative navigation for spacecraft operating tens of kilometres apart is more complex than for spacecraft in close proximity. The accuracy level of the GNSS-based relative navigation depends on several factors:

- Single or dual frequency GNSS receiver. The former is mostly used to achieve medium navigation precision and for small satellite missions; instead, the latter can provide precise orbit determination and navigation, eliminating the error due to the ionospheric effect. Note that for short separation ($< 10\,\mathrm{km}$), the ionospheric error may be negligible, and the single frequency GNSS receivers provide precise navigation.

- GNSS observation measurements: pseudo-range and/or carrier phase measurements. The former is the code observation of the signal travelling in time and provides the range of the antenna phase centre. The latter provides the phase difference plus an integer number of carrier cycles by tracking the carrier into the code with a replica and typically can provide more precise measurements of about two orders of magnitude.

- Single or double difference models for orbit determination. The former exploits the difference of two GNSS observations with the same frequency taken by two spacecraft (A, B) from the same GPS satellite. The latter performs the difference of two single difference observations of satellites (A, B) taken from two different GPS satellites simultaneously. The double difference directly estimates carrier phase ambiguities, providing high-precision differential positions.

- Broadcast of raw GNSS measurements or navigation solution. The transmission of raw measurements among the formation allows the satellites to determine their relative states accurately. On the other hand, the transmission of navigation solutions brings the uncertainty of the absolute state vector reconstruction of each spacecraft.

Moreover, pseudo-range and carrier phase measurements are affected by the clock offset error due to the non-perfect synchronisation of the internal clock of GPS satellites and receiver antenna and by the ionospheric path delays and course thermal measurement noises. The ionospheric path delays are significative with longer separations, while short separation ($<10\,\mathrm{km}$) could translate into mm/cm noise levels [105]. The idea of exploiting navigation measurements to derive position differences is presented in the work by Guinn et al. [106], who extended the analysis done for single spacecraft to autonomous orbit determination with GPS measurements for formation flying around the Earth. It proposes a methodology to compute navigation solutions by deriving total position differences between on-board navigation measurements. This approach requires the transmission of the navigation solution of each satellite to the remaining components of the formation. A few years later, the research in [107] proposes a real-time navigation system based on a decentralised architecture. This concept is preferable to centralised systems, thanks to the flexibility and robustness of single-point failure, which could compromise the mission status if the navigation solution is computed only by the master spacecraft, as in a centralised system. The work in [107] proposes a methodology for on-board computation of the navigation solution, where the spacecraft is equipped with GPS sensors and can compute the current state in terms of absolute position and velocity via a Kalman filter. The raw measurements are also transmitted to the other components of the formation, and the relative state is reconstructed via differential processing. It demonstrated precise relative position is achievable for spacecraft with a separation of a few kilometres. The concept of decentralised architecture is adopted in this dissertation. It is important to understand the current state of the art in the relative navigation performances for formation flying missions. A distinction must be made between on-ground and on-board navigation accuracy of the orbit determination. The former is based on the post-processing of orbit product for precise baseline determination a posteriori; the latter provides the real-time relative orbit estimation on-board of the navigation solution and is used for autonomous procedures in orbit. Table 1.3 shows the current relative navigation performance for different formation flying missions, considering the

Table 1.3: *State of the art in spacecraft relative navigation for formation flying.*

Name	Separation	Real-time Position	On-ground Position
GRACE	220 ± 50 km	/	sub-millimetre
PRISMA	200-800 km	sub-decimetre	sub-centimetre
TDX/TSX	300 km	sub-decimetre	sub-millimetre

on-board orbit estimation. The first relevant mission in this context is the GRACE formation [49], equipped with dual-frequency GPS receivers, which can correct the relative ionospheric path delay. Then, as described in [108], single-difference GPS observations are used to reconstruct the navigation solution, processing both pseudo-range and carrier phase measurements via an Extended Kalman Filter. This work demonstrated the possibility of obtaining accuracy on the post-facto relative position of about $1\,\mathrm{mm}$ in the along-track direction when the ambiguities of the carrier phase are fixed [108]. This was developed by collecting GPS flight data of GRACE mission and defining the baseline for the navigation techniques based on the carrier phase [52]. Based on these results, the PRISMA mission introduced new methodologies for precisely estimating the relative state with GPS data [105, 109]. First, the raw measurements of pseudo-range and carrier-phase are combined in the GRAPHIC data type, and then a single difference model is implemented [105]. Finally, the real-time relative position is reconstructed with sub-decimetre level accuracy, as discussed in [109]. Similarly, for TDX/TSX the navigation is mainly based on the ground-in-the-loop solution reconstruction. To correctly process the SAR data, the baseline has to be known within $1\,\mathrm{mm}$ accuracy, and this level of accuracy is connected to an a posteriori processing of navigation data [108, 110]. The TDX spacecraft was also equipped with an Autonomous Formation Flying (TAFF) system, intended to demonstrate the capability to perform some autonomous control activities. Specifically, the experiment the autonomy of the navigation and control algorithm to perform in-plane impulsive formation keeping, resulting in an accuracy of sub-decimetre level for the relative position [79]. Going toward more autonomous navigation and control is fundamental to facilitating and implementing future operations of close proximity relative motion. However, the main limitation of the ground-in-the-loop orbit control is connected to the limited number of ground stations and limited visibility windows. Moreover, with the recent increase in space traffic, ground stations will be more and more stressed from the control and flight dynamics point of view.

Starting from the outcome in the literature, this thesis mainly implements a GNSS-based system for navigation solutions, with an eye on the possibility of extending the system with a vision-based sensor to improve the results in a future study.

1.4 Thesis contribution

1.4.1 Novel contributions

This doctoral thesis contributes to the Earth observation field in several disciplines. The main outcomes can be grouped into three parts.

The first part of the thesis in Chapter 2 contributes to the geometry selection and formation flying design for future distributed missions carrying microwave sensors. It evaluates the main requirements and operational constraints for the design of distributed missions with microwave interferometry payload and develops a preliminary model of passive microwave sensors. The advantages of implementing passive interferometry on multiple platforms are identified, and different formation geometries are analysed. Outcomes have been disseminated in an interactive presentation at the 2022 International Astronautical Congress in Paris, France [111], where the work has been awarded the "Best Interactive Presentation Award" for the IAF Earth observation symposium. In addition to the formation geometry design, I supervised the development of algorithms to model passive L-band sensors. The outcome is under consideration for publication in the Advances in Space Research journal [112].

The second part of the thesis - see Chapters 3 and 4 - focuses on the development of the Guidance, Navigation, and Control algorithms. The proposed method for open-loop guidance presents a novel strategy for optimal relative trajectory design in the ROEs coordinate system. Specifically, an original algorithm for convex optimisation is derived in both classical relative Cartesian state and ROEs coordinate system. Thanks to the properties of convex optimisation, a unique solution for the guidance and control problem is derived, which includes the effect of the Earth’s oblateness perturbation and operational and collision avoidance constraints. Furthermore, the methodology proposes a continuous control approach, providing a valuable contribution to the ROE-based techniques, which mainly limit their use to impulsive control schemes. The derivation and application to different distributed systems have been published in two articles in the Advances in Space Research Journal. The first one implements the convex algorithm, including the effect of Earth’s oblateness in the relative dynamics and provides an insight into the computation performances with an increasing number of spacecraft in the system [113]. It was applied to different operational scenarios of the Formation Flying L-band Aperture Synthesis (FFLAS) study and presented at the 2020 AAS/AIAA Astrodynamics Specialist Conference [114]. The second has been developed as part of the co-supervision of an MSc thesis and extends the convex algorithm by employing a STM that includes higher order terms of the zonal harmonics [115]. Moreover, the extended core algorithm is embedded into the GNC system to provide a robust framework for distributed system simulations - see Chapter 5. The developed control technique employs a LQR and includes an accurate propulsion system model for the reliable inclusion of uncertainties and noises in the final control. In addition to the classical Cartesian coordinates, the methodology is derived in the ROEs coordinate system. The navigation is based on GNSS measurements and implements noises and uncertainties typical of currently available GNSS receivers. Both algorithms and GNC structure are presented, describing the main building blocks and the interfaces to guarantee flexibility for its applicability on different distributed systems. Most of this work has been presented in two conferences proceeding at the 16th Space Operations Conference (SpaceOps 2021) [116] and at the 2022 AIAA SciTech Forum [117]. This part of the work is an important contribution to the preliminary design and GNC performance assessment of future formation flying missions, considering the main operational and in-orbit constraints of an EO mission.

The third and final part of the thesis - see Chapters 6 and 7 - proposes and analyses formation geometries, carrying both active and passive interferometry instruments. The distributed systems with SAR payload are inspired by the TSX/TDX mission. The novelty and contribution of active interferometry is the extension of the control methodologies to continuous thrust control to compare and evaluate possible advantages in this applicative scenario. On the other hand, novel geometries and formation architecture have been proposed for passive microwaves. Specifically, the FFLAS study introduces an innovative formation concept to perform combined interferometry with continuous control. The main mission phases, from launch to disposal, have been analysed in the thesis, as part of the FFLAS study in collaboration with Airbus Defence and Space, under an ESA project. This part of the thesis has been presented in three conference proceedings at the 2020 International Astronautical Congress [111], the 2021 International Astronautical Congress [118], and the 2022 ESA Living Planet Symposium [119]. Moreover, other innovative scenarios with three to twelve spacecraft have been analysed regarding the performance of GNC and payload. In addition to these solutions that require continuously forced motion, analytical solutions of the relative motion have been applied for the first time to multiple spacecraft scenarios with passive L-band interferometry. The potentiality and the advantages of such an approach are discussed and highlighted in view of future mission studies. This final part of the thesis has been presented in an interactive presentation at the 2022 International Astronautical Congress [111].

1.4.2 Publications and outreach

The research presented in this thesis is part of my original work carried out during my PhD. Moreover, I performed some collaborations during my PhD. The PhD was co-funded by the European Research Council (ERC) under the European Unions Horizon 2020 research and innovation program (grant agreement No. 679086 COMPASS), and by the FFLAS study, in collaboration with Airbus Defence and Space Madrid and founded by the European Space Agency (Contract No. 4000128576/19). Moreover, some test cases in Chapter 6, instead, are part of the work carried out during a 6-month period at the ESA-European Space Research and Technology Centre (ESTEC) in the Mission Analysis Support section of the Earth Observation Program department (EOP-PES) under the supervision of Berthyl Duesmann.

Finally, part of the content published in this thesis has been presented at several international conferences and workshops and has been published or submitted for review in scientific journal articles.

Journal Publications

1. Scala, F., Gaias, G., Colombo, C., Martín-Neira, M.. Design of optimal low-thrust manoeuvres for remote sensing multi-satellite formation flying in low Earth orbit. *Advances in Space Research*, 68(11), 4359-4378, 2021 doi:10.1016/j.asr.2021.09.030

2. Scala, F., Colombo, C., Duesmann, B., Martín-Neira, M.. Enabling distributed passive interferometry through natural relative trajectories. Unpublished manuscript in preparation for Aerospace Science and Technology.

3. Monteiro-Miñan, A., Scala, F., Colombo, C.. Manoeuvre planning algorithm for satellite formations using mean relative orbital elements. *Advances in Space Research*,71(1), 585-603, 2022, doi:10.1016/j.asr.2022.09.043

4. Martín-Neira, M., Scala, F., Zurita, A., Suess, M., Piera, M., Duesmann, B., Drusch, M., Colombo, C., De Wilde, D., Closa, J., Gandini, E., Diez Garcia, R., Oliva, R., Corbella, I.. TriHex: combining formation flying, general circular orbits and alias-free imaging, for high resolution L-band aperture synthesis. Accepted for publication in *IEEE Transactions on Geoscience and Remote Sensing (TGRS)* on Apr 2023, doi: 10.1109/TGRS.2023.3268560.

5. Piera Martinez, M., Scala, F., Colombo, C., Zurita, A., Duesmann, B., Martín-Neira, M.. Formation Flying L-band Aperture Synthesis mission concept. Unpublished manuscript submitted for review to *IEEE Transactions on Geoscience and Remote Sensing* on Nov 2022.

6. Erbeia, C., Scala, F., Colombo, C.. Robustness analysis and station-keeping control of an interferometer formation flying mission in low Earth orbit. Unpublished manuscript submitted for review to *Advances in Space Research* on Jan 2023.

Conference Proceedings

1. Scala, F., Gaias, G., Colombo, C., Martín-Neira, M.. Formation flying l-band aperture synthesis: Design challenges and innovative formation architecture concept. In *Proceedings of the International Astronautical Congress, IAC20*, 2020.
2. Scala, F., Gaias, G., Colombo, C., Martín-Neira, M.. Three satellites formation flying: deployment and acquisition using relative orbital elements. In *Advances in the Astronautical Sciences*, 2021, 175, pp. 3981-3997.
3. Scala, F., Colombo, C., Martín-Neira, M..Design of natural collision-free trajectories for the mission extension phase of a remote sensing formation flying mission. In *Proceedings of the International Astronautical Congress, IAC21*, 2021.
4. Scala, F., Colombo, C., Martín-Neira, M.. A decentralised approach for formation flying reconfiguration and maintenance using GNSS-based navigation. In *Proceedings of the AIAA Science and Technology Forum and Exposition, AIAA SciTech Forum 2022*, AIAA 2022-2463, 2022.
5. Scala, F., Colombo, C., Duesmann, B., Martín-Neira, M.. Analysis and design of future multiple satellite formation flying L-band missions in low Earth orbit. In *Proceedings of the International Astronautical Congress, IAC22*, 2022.

Conference/Workshop Presentations

1. Scala, F., Gaias, G., Colombo, C., Martín-Neira, M.. GNSS-based navigation for a remote sensing three-satellite formation flying. In *SpaceOps 2021 Virtual Edition*, p. 1-18, virtual edition, 3-5 May 2021.
2. Scala, F., Colombo, C., Piera, M., Zurita, A., Duesmann, B., Martín-Neira, M.. Performance Assessment of the Formation Flying L-Band Aperture Synthesis Mission Concept. In *ESA Living Planet Symposium 2022*, Bonn (Germany), 23-27 May 2022.
3. Scala, F., Colombo, C., Zurita, A., Martín-Neira, M.. Formation flying design for the TriHex mission concept. In *SMOS-HR workshop*, Paris (France), 28-29 Nov 2022.
4. Liu, X., Colombo, C., Scala, F., Chen D.. Model Predictive Control for Rigid Satellites Formation with Underactuated Propulsive System Based on Relative Orbital Elements. In *Aerospace Europe Conference 2021 (AEC-21)*, 1-18, Warsaw (Poland), 23-26 Nov 2021.
5. Martín-Neira, M., Scala, F., Zurita, A., Suess, M., De Wilde, D., Piera, M., Duesmann, B., Colombo, C., Closa, J., Gandini, E., Diez Garcia, R., Oliva, R., Corbella, I.. The TriHex mission concept. In *SMOS-HR workshop*, Paris (France), 28-29 Nov 2022.
6. Martín-Neira, M., Piera, M., Scala, F., Colombo, C., Zurita, A., Duesmann, B.. Formation Flying L-Band Aperture Synthesis Mission Concept. In *IGARSS 2022-2022 IEEE International Geoscience and Remote Sensing Symposium*, (pp. 7325-7328). IEEE, Kuala Lumpur (Malaysia), 17-22 Jul 2022.
7. Piera, M., Zurita, A., Scala, F., Colombo, C., Duesmann, B., Martín-Neira, M.. Satellite Design for a Formation Flying L-band Aperture Synthesis mission. In *ESA Living Planet Symposium 2022*, Bonn (Germany), 23-27 May 2022.

8. Piera, M., Scala, F., Colombo, C., Zurita, A., Martín-Neira, M., Duesmann, B.. Formation Flying L-Band Aperture Synthesis Mission Concept. In *In 7th Workshop on RF and Microwave Systems, Instruments & Sub-systems+(5th Ka-band Workshop)* (pp. 1-8), ESTEC-Noordwijk (The Netherlands), 10-12 May 2022.

9. Rizzieri, L., Scala, F., Colombo, C.. Precise Relative Motion and Control Strategy in the J22 Perturbed Geostationary Environment. In *11th International Workshop on Satellite Constellations & Formation Flying (IWSCFF 2022)* (pp. 1-15), Milan (Italy), 7-10 Jun 2022.

1.5 Structure of the thesis

The thesis is organised into five main chapters.

Chapter 2 presents the main considerations for the design of Earth observation missions carrying active and passive interferometry. An important part of the chapter is dedicated to the preliminary modelling of distributed systems with passive interferometry. This provides the improvement in payload performances (i.e. spatial resolution and coverage) for different geometries and number of spacecraft.

Chapter 3 describes the reference system used in the dissertation and provides the models for the absolute and relative dynamics of spacecraft under the typical perturbations of the LEO environment. This chapter presents the natural solution of the classic relative motion to understand how they can be exploited for remote sensing purposes.

Chapter 4 presents the method and algorithms developed for the definition of guidance and control. This chapter proposes a novel approach to design delta-v optimal manoeuvre in terms of the ROEs framework. Moreover, the LQR and the MPC algorithms are presented and tested over uncertainties in the initial conditions.

Chapter 5 presets the GNC framework developed to simulate the performances of the navigation and control for multi-spacecraft formation. This framework has been essential for the simulation of the operational phases of FFLAS study and has been applied to various test cases in this dissertation.

Chapters 6 and 7 presents the results and the simulation for different scenarios. Specifically, the result chapter has been divided into two parts. The first part in Chapter 6 presents the design and the trade-off analysis performed to set up distributed systems for active and passive interferometry. Then, Chapter 7 focuses on the simulation of different operational phases (from launch to off-nominal) of the FFLAS study.

CHAPTER 2

Earth Observation missions design

It's surely our responsibility to do everything within our power to create a planet that provides a home not just for us, but for all life on Earth.

— David Attenborough

THE design of missions for Earth Observation (EO) is motivated by the need to improve our knowledge of natural events and cycles on planet Earth. The sensor technology selected for EO greatly influences the design procedure of the mission itself. As discussed in Chapter 1, the importance of formation flying and relative motion to improve the current state of the art is relevant, and this thesis deals with spacecraft carrying *microwave* antennas, both active and passive, in the L-band range. This chapter presents a description of the current missions performing passive interferometry in L-band, as well as highlights performances and techniques for active L-band SAR from available studies in the literature (e.g. [16, 33]). Given the lack of research on passive L-band in distributed systems, the core of this chapter is dedicated to developing a model of a passive interferometer applicable to arbitrarily distributed systems. This tool is essential to characterise proper geometries for defining mission scenarios described in this thesis. Specifically, the interferometer model has been carried out in the context of FFLAS study, together with Dr. Manuel Martín-Neira (ESA, Radio Frequency Payloads & Technology Division) and Dr. Albert Zurita (Airbus Defence and Space SAU, Earth Observation).

This chapter defines the test cases selected in this dissertation and assesses the preliminary performances of the related instruments, taking advantage of the developed model of the interferometer instrument. Specifically, it is organised with an initial overview of current and future EO missions involving single and multiple spacecraft. Then, the applicative scenarios are defined in terms of requirements and design parameters of the active or passive microwave payloads. Next, the modelling of the passive radiometer to perform interferometric radiometry with both single and multiple platforms is presented. To conclude, the final part addresses the definition of different geometries for passive L-band formations that comply with the outcomes of the payload model.

2.1 Basics of active and passive radiometers

This section addresses the need to define the basics of SAR and passive interferometry, which will be used later in the chapter. Specifically, the antenna pattern, the types of antenna arrays, and the satellite's image resolution are described [33, 47].

Antenna pattern. The antenna pattern represents how an antenna radiates or receives electromagnetic energy in space [33]. The pattern is typically three-dimensional and can be described via portions of the patterns called lobes. The lobe is a part of the pattern surrounded by relatively weaker radiation. For SAR and passive radiometers, it is essential to identify the main and the sides lobes, as different energy levels characterise them. The main lobe identifies the maximum radiated power and the principal direction of the antenna. Specifically, the direction of the main lobe, for which the radiation pattern is maximum, is also called the boresight direction. Generally, the boresight direction corresponds to the symmetry axis of the antenna. Another important direction for antenna pattern in EO is the nadir, which is the direction pointing vertically below the antenna, toward the ground. The vertical direction of the nadir corresponds to the segment connecting the spacecraft to the centre of the Earth [33, 47].

Antenna array. An antenna array comprises multiple antennas working together for the same purpose. The corresponding combined interferometry in EO employs multiple platforms carrying an antenna. Therefore, we can select different relative geometries to produce an electromagnetic antenna pattern [47]. First, the antenna elements can be placed along a straight line, resulting in a linear array. Similarly, we obtain a planar array when the antenna elements are placed on the same plane facing the Earth. Finally, considering natural relative orbits, the antenna elements are placed in a non-planar configuration. This case is called staggered arrays, leading to a more challenging combined interferometry procedure [47]. In all previous configurations, the antennas belong to the same plane called Array Plane. This plane is used to identify the characteristics and the performances of a multi-satellite antenna array. Additionally, depending on the selected geometries and application, the antenna array could require continuous corrective thrust to maintain the correct relative position. This latter aspect is discussed later in the thesis.

Satellite's image resolution. Four main types of resolution of a satellite image are typically considered [33]. First, the *spatial resolution* describes the level of detail the sensor can provide. For optical sensors, it directly corresponds to the pixel size on the ground. Smaller pixel size produces a finer resolution and vice-versa. Second, the *temporal resolution* describes the time to revisit the same area. Most EO missions have a revisit time in the order of a few days. Third, the *spectral resolution* refers to the information on the spectral bands. A higher number of spectral bands are typically measured by multi-spectral or hyper-spectral sensors, providing more accurate information on the observed area. Finally, the *radiometric resolution* better differentiates the different objects. A finer sensor can distinguish more radiometric values emitted or reflected from Earth targets.

Following the introduction of basic terminology for microwave antennas, the following section presents an overview of the current microwave missions and studies for EO.

2.2 Microwave missions and studies for EO

This section recalls the primary missions' most relevant features and achievements for active and passive EO monitoring.

2.2.1 Passive microwave missions

In the passive microwave framework, the SMOS (Soil Moisture and Ocean Salinity) and SMAP (Soil Moisture Active and Passive) missions demonstrated the importance of passive radiometry for different applications. The main achievements and limitations are summarised in the following. Moreover, a single satellite study (i.e. SMOS-HR) is briefly described in the context of future missions.

SMOS mission The SMOS mission was designed and launched as part of an Earth Explorer mission by ESA, in collaboration with Centre National d'Études Spatiales (CNES) and CDTI (Centro para el Desarrollo Tecnológico Industrial). As mentioned in Chapter 1, it provides global information on soil moisture and ocean salinity. SMOS consists of a single spacecraft carrying a Y-shaped L-band passive antenna, the MIRAS instrument, capable of performing multi-spectral radiometry. MIRAS can provide a spatial resolution of about $40\,\mathrm{km}$ in boresight and $30\,\mathrm{km}$ in nadir, and a radiometric resolution of 0.8 to $2.2\,\mathrm{K}$. The operational frequency of the instrument is $1.4\,\mathrm{GHz}$, corresponding to a wavelength of about $21\,\mathrm{cm}$. The sensor consists of three arms in a Y-shaped configuration, equally distributed with an angular separation of $120\,\mathrm{deg}$, with 69 interferometer elements. The operational orbit is an SSO with a mean altitude of about $750\,\mathrm{km}$, a Local Time of the Ascending Node (LTAN) at $6\,\mathrm{a.m.}$ and a repeat cycle of 149 days [15, 46]. The SMOS satellite has been operative since 2009 and provides fundamental insight into the water cycle assessment, the carbon cycle, and forest degradation. Initially designed for a nominal operational lifetime of three years, SMOS is still currently providing scientific data. Given its longevity and the fact that it is already in the extended phase of the mission, future studies to replace and improve its performances have acquired more and more importance. Specifically, this thesis presents a study to improve the spatial resolution with formation flying means as a possible future development of the current state of the art. Differently from other studies developed in the last few years, as the SMOS-HR, the aim is to replace a single satellite carrying a large synthetic beam with multiple smaller spacecraft flying together to obtain a larger virtual aperture than the monolithic approach.

SMAP mission A second L-band microwave mission was designed by NASA and CSA: the Soil Moisture Active/Passive (SMAP) mission. It comprises a single satellite carrying a passive radiometer and a SAR instrument. It was launched in 2015 and is expected to continue providing observation data until September 2023 Similarly to SMOS, SMAP data support weather and climate forecasting, monitoring of droughts and floods, agricultural productivity, and human health. The passive radiometer consists of a circular reflector of $6\,\mathrm{m}$ diameter, operating at $1.4\,\mathrm{GHz}$. It provides a spatial resolution of $40\,\mathrm{km}$ and a radiometric resolution of $1.5\,\mathrm{K}$. The active radar works with two different frequencies, 1.26 and $1.29\,\mathrm{GHz}$, achieving a spatial resolution of 3 to $10\,\mathrm{km}$ [17, 46]. The operational orbit is a SSO at the mean altitude of about $680\,\mathrm{km}$, with an LTAN of $6\,\mathrm{p.m.}$ and a repeat cycle of 8 days. As for SMOS, SMAP reflector is a large instrument that requires a complex procedure to stow and deploy the antenna. An extendable mechanism was successfully designed to deploy the boom and reflector separately. This level of criticality of the satellite structure makes it evident that future missions to replace the SMAP spacecraft will envision miniaturised platforms to remove the deployment mechanism and reduce possible failure, complex flexible dynamics and satellite behaviours in orbit. Instead, a large aperture can be obtained by implementing a distributed system carrying L-band passive radiometer, as described in this chapter.

The outcome of both SMOS and SMAP shows the potentiality that an increase in spatial resolution would enable. Achieving a resolution of the passive L-band radiometry of 1 to $10\,\mathrm{km}$, instead of the $40\,\mathrm{km}$ of SMOS and SMAP, would allow studying new natural processes. As described in [26], a higher resolution enables measurements of values and variation of salinity properties of coastal areas, Arctic and Antarctic regions, and ice-sheets movements, which are only observable with a resolution of $10\,\mathrm{km}$ or better.

SMOS-HR study A first effort to improve the spatial resolution for L-band radiometers is the SMOS-HR (high-resolution) study, proposed and carried out by CNES. It foresees a single satellite carrying a large antenna with four arms of $12\,\mathrm{m}$ length for a total of 231 antennas [26]. The spatial resolution is estimated to be about $10\,\mathrm{km}$ with a radiometric sensitivity similar to the SMOS one. Nevertheless, this breakthrough in spatial resolution suffers from similar challenges as the SMOS and SMAP, where the instrument requires a carefully designed deployment mechanism. The phase A study mainly focused on this challenge and the improvement of the post-processing algorithms of remote sensing data [26].

To conclude, Figure 2.1 summarises the improvement in spatial resolutions proposed by SMOS-HR compared to SMOS and SMAP. In addition, resolution figures of merit are reported for both the nadir and boresight directions. The former is the nadir direction (i.e. from the instrument to the Earth's centre), while the latter is the direction of the peak gain of the antenna. As mentioned above, the SMOS and SMAP provide similar performances, around 30 to $40\,\mathrm{km}$ resolution. On the other hand, the SMOS-HR study estimates a resolution down to 10 to $15\,\mathrm{km}$, with a significant improvement in the performances. Aiming at achieving the feature of 1 to $10\,\mathrm{km}$ resolution, this thesis investigates the distribution of passive microwave instruments among several - definitely simpler - satellites. Section 2.4 presents the methodology for a preliminary design of a microwave radiometer and the effect of combining multiple distributed antennas from the coverage and impulse response points of view.

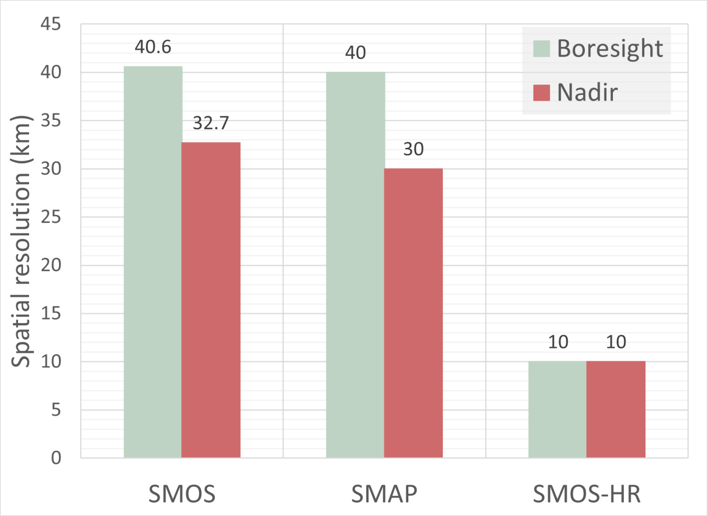

Figure 2.1: *Spatial resolution for the SMOS and SMAP missions and the SMOS-HR study, for both nadir and boresight directions.*

2.2.2 Active microwave missions

In addition to the operation of SMAP in L-band, several SAR missions have already been mentioned in Chapter 1. In this section, we want to provide insight into the most relevant missions involving formation flying with SAR instrument, namely the TDX/TSX mission.

TerraSAR-X - TanDEM-X mission TDX/TSX has been conceived, designed and funded by German Aerospace Center (DLR) and Airbus Defence and Space Germany. It consists of two spacecraft flying in close formation mounting an X-band radar sensor, capable of providing a flexible resolution from $25\,\mathrm{cm}$ to $40\,\mathrm{m}$ in both cross and along-track directions for different operational modes. The antenna operates in a bandwidth range of 150 to $300\,\mathrm{MHz}$. The two spacecraft fly at a few hundred meters separation in a helix formation (see Section 3.3), and they alternate bistatic and mono-static acquisition modes. The nominal orbit of TSX is SSO with a mean altitude of $515\,\mathrm{km}$ and LTAN at 6 p.m.. The size of the helix in cross-track direction is determined by imposing to TDX a given separation in Right Ascension of the Ascending Node (RAAN), to correspond to a baseline between 200 and $3000\,\mathrm{m}$ The maximum vertical separation in the helix is achieved by imposing a given relative shift between the eccentricity vectors of two satellites. The key peculiarity of the TSX/TDX formation is the implementation of a safe motion through relative eccentricity/inclination vectors' separation [67, 74]. This methodology ensures passive safety in case of failures or non-nominal scenarios among the platforms, with great advantages in terms of effort and cost of operations of the satellites' formation. As mentioned in Chapter 1, this methodology builds upon the operational experience gained during the swap of the GRACE satellites, performed in 2005 [20, 49].

Most of the current studies for distributed SAR missions are based on the lesson learnt from TSX/TDX mission, which provides essential considerations on both SAR baseline design and formation geometry.

2.3 Selection of formation flying scenarios

This section presents the formation geometry concept considered in this dissertation for performing EO. The thesis focuses on formation geometries for passive interferometric radiometry, in the direction of future missions for high-resolution measurements in L-band, as a continuation of the SMOS and SMAP missions. In addition to such main objectives, two mission concepts for SAR interferometry through formation flying are proposed to demonstrate the flexibility of the developed GNC framework, which indeed can support a variety of multi-satellite missions.

2.3.1 Multiple-satellite for interferometric radiometer

The scientific data from SMOS and SMAP provided global maps of soil moisture and sea surface salinity with an average resolution of $40\,\mathrm{km}$. In this context, future missions in passive L-band radiometry shall achieve a spatial resolution of 1-$10\,\mathrm{km}$, to enable key improvements of meteorological and climate monitoring and prediction (see Chapter 1).

Objective of the research This dissertation proposes a design strategy for formation geometry selection for innovative future missions in L-band. The main idea is to enlarge the aperture size of a single instrument with a cluster/formation of multiple platforms working as distributed nodes of a sensor in a network. The investigation originates from the Formation Flying L-band Aperture Synthesis (FFLAS) study - contextually performed during this PhD and in collaboration with ESA and Airbus

D&S Madrid - that considered a triangular formation of three spacecraft. Subsequent analyses have been performed in this dissertation to analyse different scenarios and multiple spacecraft formations for passive L-band purposes. Specifically:

- Three to twelve identical platforms are envisioned in different formation geometries in LEO.

The main objective is to evaluate the feasibility and the performances from the GNC point of view for future multiple spacecraft formation for remote sensing. This thesis considers the requirements and the performances of the combined interferometry payload, as well as the operational constraints typical of space missions, which are strictly related to safety policies for close satellites formations.

Requirements of L-band interferometric radiometry Regarding passive L-band interferometry, it is important to analyse the main requirements from the payload point of view. In continuity with technologies employed in SMOS and SMAP, the instrument main requirements are [120–122]:

(RP1) The N-arrays in the formation shall operate as a single aperture synthesis radiometer.

(RP2) The L-band arrays of different spacecraft shall belong to the same plane, called the Array Plane or Aperture Plane, and the array phase centre shall be the geometric centre of each individual array.

(RP3) The relative distance and orientation (attitude) among the platforms in the formation shall be maintained fixed, to allow a correct reconstruction of the combined synthetic beam.

(RP4) The relative position between the phase centres of any pair of antenna elements, belonging to the same array or different arrays, shall be controlled to be within $\pm 10\,\mathrm{cm}$ (1 sigma) from the nominal values.

(RP5) Considering a baseline of $10\,\mathrm{to}\,20\,\mathrm{m}$, the real-time relative position between the phase centres of any pair of antenna elements, belonging to the same array or different arrays, shall be known to $\pm 2\,\mathrm{cm}$ (1 sigma).

(RP6) The ground reconstruction of the relative position between the phase centres of any pair of antenna elements, belonging to the same array or to different arrays, shall be known within $\pm 2\,\mathrm{mm}$ (1 sigma).

Where 'RPX' stands for: R - requirement, P - passive, and X is the number of the requirement. (RP1), (RP2), and (RP3) directly influence the design of the geometry of the cluster of satellites. Particularly, (RP3) drives the selection of the relative dynamic. On one hand, concerning the relative attitude, this work assumes that the on-board actuators can satisfy this requirement. On the other hand, to maintain a fix and rigid distance among the vehicles, the on/board system should work against the natural oscillation of the relative motion and at the same time should compensate for the external perturbations. Consequently, a continuous forced motion is require to keep the correct geometry. This is an important difference compared to the active SAR technology, where a variation or drift in the relative motion could be used to achieve different baseline in time (see TDX/TSX). The selection of continuous propulsion system for orbit control is the direct result of these considerations. Passing to (RP4), it is valid for any possible geometry. To keep this requirement, the relative displacement of each antenna in terms of real-time relative control is obtained from (RP5). This considerations are valid for a tight baseline, when the vehicles are about $10\,\mathrm{to}\,20\,\mathrm{m}$ apart. Since an accurate control of the relative motion is required, the dynamic description of the orbital motion shall include the most relevant perturbation of the LEO environment At the same time, continuous control techniques are preferred over impulsive one, to continuously compensate in real-time over small baseline variation. Finally, the navigation technology has been selected among the GNSS-based techniques, which has already been implemented in real mission scenario (see Section 1.3). The last requirement, (RP6), is connected to precise position determination for high-quality data in post-processing (on-ground).

Design parameters From the requirements (RP1) to (RP3), we define the main parameters for the design of the cluster geometry.

- Number of spacecraft n_{sat}.
- Orientation of the Array Plane (x_a, y_a, z_a) in the relative frame (see Figure 2.2): yaw angle γ, pitch angle δ, and roll angle ϕ, respectivly assumed positive according to the convention defined in Figure 2.2.

A first possibility is to impose a null pitch and roll angle and modify the Array Plane's yaw angle, which describes a rotation on the plane orthogonal to the radial direction toward the Zenith. As a result, the (x_a, y_a) and (y, z) planes coincide. For the scenario of a planar Array Plane, this dissertation proposes two test cases:

(SP1) Planar Array Plane with 3 spacecraft: Formation Flying L-band Aperture Synthesis (FFLAS) study.

(SP2) Planar Array Plane with 4 to 12 spacecraft: FFLAS follow-on study.

Where 'SPX' stands for: S - scenario, P - passive (i.e. antenna technology), and 'X' number of the test case. A second possibility is to employ generic constant angles γ, δ, ϕ, so that the Array Plane has a generic orientation in the relative frame. Note that the inclination of the (x_a, y_a) plane influences the payload performances, as discussed in Section 6.5. We propose one test case for non-planar Array Plane:

(SP3) Non-planar Array Plane with 3 spacecraft: Three Hexagonal (TriHex) study.

Finally, the case of time-varying angles γ, δ, ϕ is not feasible for passive interferometry since it interferes with the duplicability of the data product over several orbit passages on the same location. Furthermore, a time-varying angle produces data results with different orientations over the global coverage (over different locations). For these reasons, this possibility has not been investigated.

2.3.2 Multiple satellites for synthetic aperture radar

Differently from the passive interferometer case, formation flying for SAR has been studied in the literature, and there exist some examples of missions launched for this purpose, such as TDX/TSX or *GRACE*. An example of research activity focused on the behaviour of distributed radar sensors is provided in [33].

Objective of the research The development and support of future activities of active L-band SAR is part of the expansion of the ESA's Copernicus program [123]. Accordingly, part of the research - carried out during the visiting period in ESA/ESTEC - focused on developing techniques suitable for two different SAR missions. The first one, named "Radar Observing System for Europe" (ROSE-L), is composed of two satellites flying in formation [124]; the second, "HARMONY", consists of three spacecraft in formation [125]. As for these study cases, bi/multi-static SAR has been considered, with independent satellites pointing simultaneously to a given target utilising synchronised antennas.

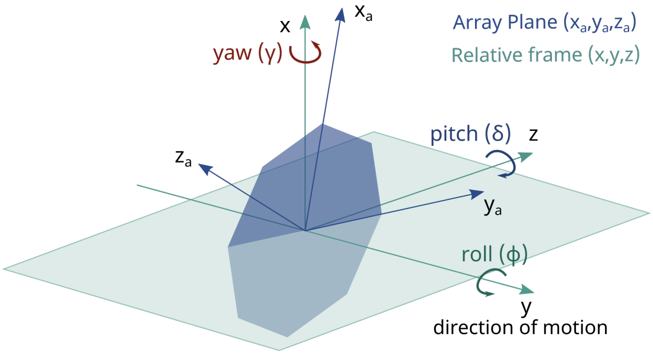

Figure 2.2: *Orientation of the Array Plane in the reference frame, with yaw γ, roll ϕ, and pitch δ angles.*

Two-satellite SAR The two-satellite SAR concept is applied to developing the ROSE-L mission for land monitoring and emergency management services. It exploits two identical satellites flying in a tandem configuration, following the seminal approach of the TDX/TSX mission. The formation concept is shown in Figure 2.3, where the relative trajectory of the deputy around the chief satellite is depicted. ROSE-L implements a bi-static single pass SAR interferometer. The scope of the study in the context of this thesis is to assess the feasibility of formation control with different control algorithms and methodologies.

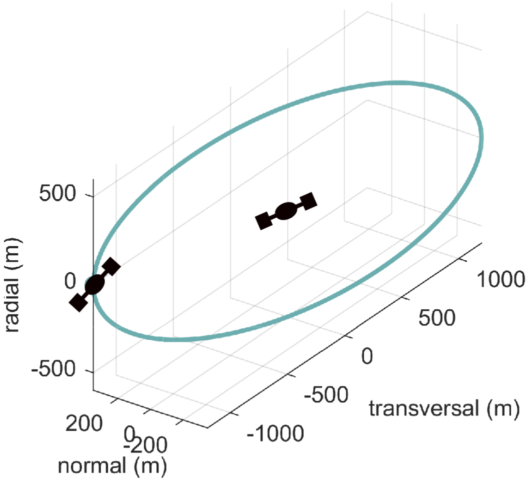

Figure 2.3: *Two-satellites tandem configuration for the ROSE-L study.*

Three-Satellite SAR The three-satellite SAR concept is applied to the development of the HARMONY mission for observing ocean surfaces, glaciers, and ice sheets. HARMONY aims to improve the information gathered by Sentinel-1 by combining the observation with two other spacecraft flying in formation. The operations consist of two different configurations. A first stereo configuration where the three spacecraft fly in a symmetrical leading/trailing formation, and a second cross-track interferometry configuration where two out of three spacecraft perform a closer relative motion in a helix geometry. Consequently, this second option implements a bi-static SAR interferometry. The scope of the activity in the context of this thesis is to assess the geometry of the formation and to evaluate the feasibility of using different control methodologies.

Requirements of SAR After defining the formation configuration for the SAR analysis, we defined the main requirements from the payload point of view that influence the formation flying design. First, an important definition is needed. For distributed SAR systems, the payload baseline is typically defined as the vector from the transmitter to the receiver in classic bistatic radar [33]. Then, based on past SAR missions, the instrument main requirements are [16, 33]:

(RA1) The multiple SAR antennas shall operate in a bi-static across-track configuration.

(RA2) Depending on radar wavelength, a proper effective baseline shall be selected for the payload as a linear combination of the radial and cross-track baseline.

(RA3) Multiple payload baselines in across-track direction are required for global data acquisition, imposing a RAAN shift among the satellites' orbits.

(RA4) The reference orbit shall be maintained within an orbit tube of diameter $\pm\ 120\,\mathrm{m}$ (3 sigma) (Earth-fixed).

(RA5) The real-time knowledge of the relative state shall be known within $\pm\ 1\,\mathrm{m}$ (3 sigma).

The requirement on the baseline is fundamental in the active SAR analysis. The requirements on the payload baseline (RA1), (RA2), and (RA3) influence the design of the formation/swarm selection. The payload baseline should be maintained constant and well-controlled between the spacecraft. This aspect reflects in two configurations. When the spacecraft is placed in the same orbit with a small along-track separation, they perform along-track interferometry, and the control effort is required to avoid orbital drift that could cause collision situations. On the other hand, for cross-track interferometry, the control effort is required to keep the vertical and horizontal cross-track separation. For this case, the orbital motion naturally produces a continuous change of the effective baseline, which should be controlled against external perturbations. In many studies [16, 33], a commonly used baseline has a sinusoidal shape over the mean argument of latitude variation. Moreover, for collision avoidance purposes, the effective baseline shall never be generated by an along-track separation only, but a non-vanishing radial or cross-track separation shall be present. Consequently, in (RP4) and (RP5), the accuracy of the control for both absolute and relative states is provided. The typical procedure to keep the reference orbit in a control tube is based on impulsive control. Whenever the reference orbit reaches one of the boundaries, an impulsive manoeuvre is performed to re-established the nominal trajectory. Similarly, an error up to $\pm\ 1\,\mathrm{m}$ is typically considered for the relative state due to a different payload baseline than passive interferometry. For active SAR, the spacecraft separation typically varies between a few hundred to a few thousand meters. Requirement (RA5) is typically handled with an impulse control scheme, resulting in about 2 manoeuvre per day to keep the baseline. The research in this thesis wants to investigate a different approach, applying continuous control schemes for formation maintenance purposes of active SAR distributed systems. Finally, similarly to the passive interferometry case, a GNSS-based navigation technique is typically enough to provide accurate position determination.

Design parameters From the requirements (RA1) to (RA3), the main design parameters are connected to the effective baseline of the SAR:

- Number of spacecraft n_{sat}.
- Different payload effective baselines are required for different mission phases, depending on the acquisition mode. For example, for ice or soil acquisition, the effective baseline changes.

Different baselines can be obtained by imposing a RAAN drift and changing the initialisation parameters of the relative motion. For ROSE-L and the cross-track interferometry configuration of HARMONY, the relative motion is initialised, imposing small variation in the orbital elements to obtain a combination of pendulum and cartwheel relative motion, also called helix configuration, which are better discussed in Section 3.3.

2.4 Modelling of passive interferometric radiometry

This section provides an overview of the methodologies and techniques for modelling interferometric radiometry. As discussed in the introduction paragraph of Chapter 2, techniques and algorithms for describing payload performances in clusters of active SAR have already been developed in several studies in the literature (e.g. [16,33]). The lack of research on passive radiometer systems requires the development of a model for arbitrarily distributed systems to assess the improvement in the quality of scientific data. First, the methodology and main equations are described for defining the interferometry response for a single antenna array composed of multiple interferometer couples, starting from algorithms available in the literature. Then, the methodology is applied to single satellite geometries to evaluate and compare the performances of current interferometry missions, such as the SMOS satellite. Finally, the modelling is extended to a combination of multiple satellites in orbit, introducing the formation flying concept. The analyses in this section build on the study performed during the supervision of an MSc thesis for distributed passive interferometry during the second year of this PhD [112], and extend the methodology to several different geometries of distributed clusters.

2.4.1 Antenna working principle

Starting from the outcomes of [47, 112, 120, 121, 126], we identify the need to have an array of interferometer couples. In fact, to observe the Earth, a set of two-element interferometers is required to synthesise a continuous source of radiation. A couple of antennas is represented in Figure 2.4, where λ is the wavelength of the interferometer, θ is the incident angle with respect to the direction normal to the plane of the antennas, and B is the projected baseline between the antennas. These three parameters are correlated via the following expression [126]:

$$\theta = \sin^{-1} \frac{\lambda}{B} \tag{2.1}$$

Therefore, the angle θ represents the direction of the phase centre. The baseline B can be expressed from the difference in the Cartesian coordinates of each pair of antennas. Considering the possibility to synthesise an image with a number N_A of arrays, we can define the baseline between a couple of antennas i, j as $B_{ij} = (x_i - x_j;\ y_i - y_j;\ z_i - z_j)$. The geometry of a Y-shaped antenna array is shown in Figure 2.5a, where a blue circle represents each element. Note that the spacing B_{ij} between each antenna pair should be smaller than $\lambda/3$ for the Nyquist criterion [127, 128].

Now the visibility function can be obtained for an antenna array with N_A elements in the (u, v) plane, which represents the measurement points sampled at a certain snapshot of time. The (u, v) space is the Cartesian space normalised in wavelength λ. Considering an array with N_A two-elements interferometers and $(x_i;\ y_i;\ z_i)$ the Cartesian coordinates, the number of baseline samples are $N_A(N_A - 1)$. Once all the possible combinations of baseline couples have been computed, the components of the resulting baseline B_{ij} for each couple of antenna is normalised over the wavelength to pass in the (u, v) space:

$$B_{ij}^{uv} = \begin{bmatrix} u_{ij} \\ v_{ij} \\ w_{ij} \end{bmatrix} = \frac{1}{\lambda} \begin{bmatrix} x_i - x_j \\ y_i - y_j \\ z_i - z_J \end{bmatrix} \tag{2.2}$$

This procedure generates redundancies due to the symmetric case for B_{ij} and B_{ji}. The redundancies are removed for a correct representation of the baseline samples B_{ij}^{uv} in the (u, v) plane, referred to as the visibility space. The visibility samples are depicted in Figure 2.5b for a Y-shaped antenna array with five elements per arm. The total number of elements for this case is $N_A = 16$, corresponding to total baseline samples of 240 and a number of visibility samples in the u, v plane of 181. In this analysis, the wavelength is assumed to be $\lambda = 21.2\,\mathrm{cm}$ and the spacing between each antenna

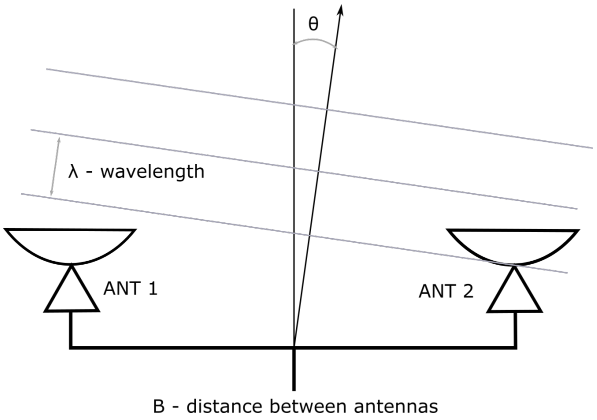

Figure 2.4: *Representation of an antenna couple at distance B, with incident wave from θ incident angle, with wavelength λ.*

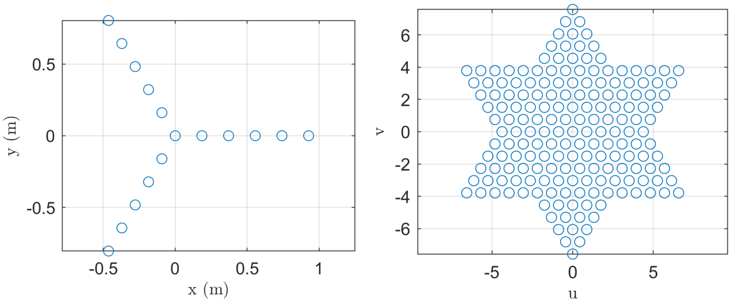

(a) *Geometry in Cartesian coordinates x, y*

(b) *Visibility samples in (u, v) plane.*

Figure 2.5: *Example of a Y-shaped antenna with 5 elements per arm.*

couple equal to 0.875λ, as in the SMOS study [120]. In agreement with the approach of [120, 121], for the visibility samples obtained from the array geometry, the full impulse response of the synthetic antenna array is simulated. Accordingly, the first step is the application of a windowing function $W(u_{ij}, v_{ij}, w_{ij})$ to weight the visibility samples, as explained in [47, 126]. This reduces the strength of the side lobes of the antenna response and widens the main lobe, increasing the efficiency of the main beam. Different methodologies exist to define a windowing function depending on the specific application [126]. One of the most used approaches in radiometry is the Blackman window, used for the MIRAS instrument of the SMOS mission [121], described by:

$$W(\rho_{ij}) = 0.42 + 0.5\cos\frac{\pi\rho_{ij}}{\rho_{\max}} + 0.08\cos\frac{2\pi\rho_{ij}}{\rho_{\max}} \tag{2.3}$$

where $\rho_{ij} = \sqrt{u_{ij}^2 + v_{ij}^2 + w_{ij}^2}$ and $\rho_{\max}$ is the maximum radius of the visibility samples in the (u, v) plane. The quantity ρ_{ij} represents the distance of each visibility sample from the origin. Similarly, the Hamming window, introduced in [129], is described by:

$$W(\rho_{ij}) = 0.54 + 0.46\cos\frac{\pi\rho_{ij}}{\rho_{\max}} \tag{2.4}$$

After applying the windowing function, we compute the full response of the synthetic antenna array, referred to as the Array Factor (AF). This is typically computed in terms of direction cosines angles of the signal source, identified by ξ, η [47], where $\xi = \sin\theta\cos\phi$ and $\eta = \sin\theta\sin\phi$, with ϕ and θ respectively azimuth and co-elevation angles. Finally, the AF is described by the visibility function in response to a point source in the field of view of the interferometer for each visibility sample [47]:

$$V(u, v, w) = e^{-2\pi i(u\xi_0 + v\eta_0 + w\sqrt{1-\xi_0^2-\eta_0^2})}, \tag{2.5}$$

where $(\xi_0,\ \eta_0)$ is the point source position. The AF is then computed as [47, 126]:

$$\mathrm{AF}(\xi, \eta, \xi_0, \eta_0) = \Delta s \sum_{m=1}^{N} W_m(\rho) V_m(u, v, w) e^{2\pi i(u_m\xi + v_m\eta + w_m\sqrt{1-\xi^2-\eta^2})}, \tag{2.6}$$

where N is the number of visibility samples, Δs is the term $\sqrt{3}/2d^2$, with d the spacing between each pair of antenna, and $W_m(\rho)$ is the windowing function for each visibility sample. Figure 2.6 shows an example of the AF for the geometry and the visibility samples in Figure 2.5. It represents the AF in logarithmic scale (dB) to better identify the main and the side lobe intensity. The corresponding contour plot in Figure 2.6b represents the AF in the ξ, η plane. The red central part identifies the main lobe, while the orange parts represent the side lobes, implying a level reduction of $\sim 20\,\mathrm{dB}$. To better understand the performances, the ξ and η cuts are represented in Figure 2.6c. As explained in [121], two important aspects are related to the AF plot::

- A broader main lobe corresponds to a reduced spatial frequency coverage, resulting in a loss of spatial resolution of the synthetic pattern.
- A wider decrease of the side-lobe level compared with the main lobe improves the synthetic images, reducing the impact of radio-frequency interference.

These two aspects are fundamental in evaluating the performances of different geometry and configuration of the antenna array: the more isolated and thin peak lobe the better the instrument's design.

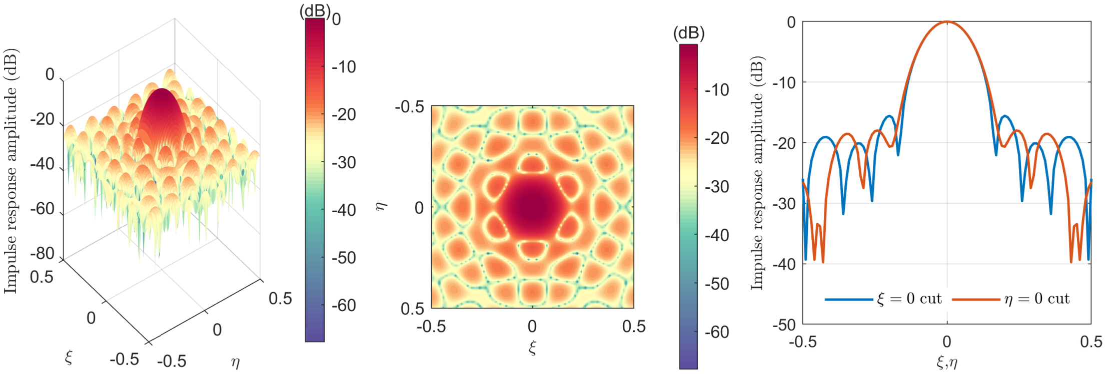

(a) *Full impulse response or array factor in ξ, η.*

(b) *Contour plot of the impulse response in ξ, η.*

(c) *Impulse response amplitude cut at $\xi = 0$ and $\eta = 0$.*

Figure 2.6: *Example of the array factor for a Y-shaped antenna with 5 elements per arm.*

2.4.2 Single-satellite interferometer

This section describes the visibility and full impulse response of a single satellite mission mounting an interferometry array. We took as a reference the mission SMOS, already studied and described in [120, 121], which mounts an L-band antenna (1400 till $1427\,\mathrm{MHz}$). Specifically, the original Y-shaped geometry of SMOS is presented, together with the follow-on hexagonal geometry, presented in [120], to improve the original performances. The work by [120] presents an extensive analysis of several different geometries and parameters to improve the current interferometry of the SMOS spacecraft. Specifically, exploiting a close geometry of the antenna array, such as a triangle or a hexagon, significantly improves spatial resolution. For this thesis, three cases have been selected from the analysis in [120]:

- The original SMOS configuration, with a Y-shaped antenna array with 23 antennas per arm.
- A modified SMOS configuration, with a Y-shaped antenna array with 50 elements per arm.
- An hexagonal antenna configuration, with 50 elements per each side.

The parameters for the computation of the visibility samples and the full impulse response are reported in Table 2.1 [120]. The wavelength, the total number of antenna elements, and the antenna spacings are the input parameters to compute the visibility samples and the full impulse response. Starting from the geometry and visibility samples results, Figure 2.7 shows the geometries and dimensions of the three antenna array cases. The SMOS case, with the smallest number of antennas, has a dimension of each arm of about $4\,\mathrm{m}$, while increasing the number of antennas per arm to 50, this dimension becomes

Table 2.1: *Parameters for the computation of visibility samples and full impulse response, for Y-shaped and hexagonal-shaped antennas [120].*

Parameter	SMOS	Y-shaped	Hexagonal-shaped
Wavelength λ (cm)	21.2	21.2	21.2
Antennas per arm (-)	23	50	50
Total no. of antenna arrays N_A (-)	69	151	300
Antenna spacing (m)	0.875λ	0.767λ	0.767λ

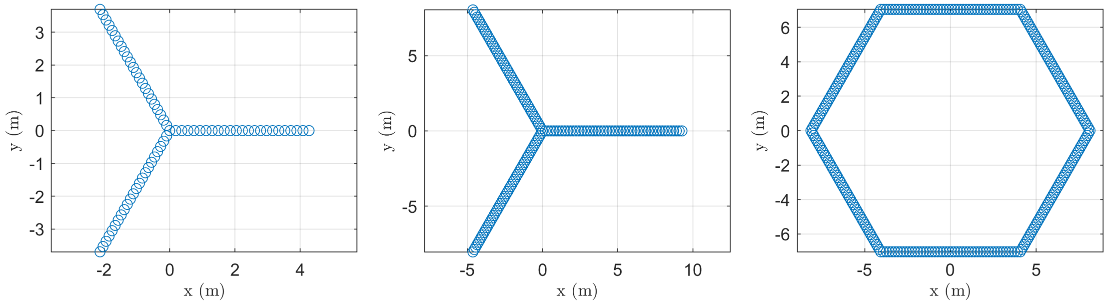

(a) *Y-shaped geometry with* $N_A = 69$.

(b) *Y-shaped geometry with* $N_A = 151$.

(c) *Hexagonal-shaped geometry with* $N_A = 300$.

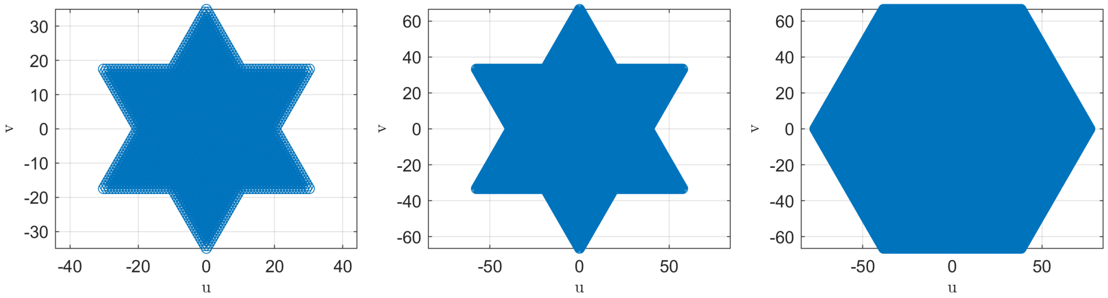

(d) *Visibility for Y-shaped with* $N_A = 69$.

(e) *Visibility for Y-shaped with* $N_A = 151$.

(f) *Visibility for Hexagonal-shaped with* $N_A = 300$.

Figure 2.7: *Geometry in Cartesian coordinates (top row) and visibility samples (bottom row) for different antenna shapes.*

circa $10\,\mathrm{m}$. The visibility samples for these two cases vary significantly, passing from coverage of a star inscribed in a circle with radius $u, v \sim 30$ to $u, v \sim 60$. This first improvement results in wider coverage and better performances at the cost of a larger number of antenna elements. Similarly, passing from the Y-shaped to the hexagonal-shaped cases, both with 50 elements per arm, the visibility samples are inscribed in a circle with radius $u, v \sim 60$. Moreover, as explained in [120, 129], the more the visibility samples represent a convex figure, the better the spatial resolution. In this case, the hexagonal shape performs better than the star distribution. As shown in Figure 2.8, the latter solution achieves both the improvements in the instrument performances recalled at the end of Section 2.4.1. Note that, as shown in Table 2.1, this improved solution exploits the largest number of antennas' arrays ($N_A = 300$).

Passing from the SMOS to the hexagonal-shaped case, the main lobe is sharper, indicating better spatial frequency coverage and better spatial resolution. At the same time, the side lobe level decrease is more significant in the hexagonal case, passing from $-13\,\mathrm{dB}$ to $-26\,\mathrm{dB}$ of the second lobe. This reduction corresponds to an improvement in spatial resolution of about $23\,\%$, and a better synthetic image and overall performances of the antenna. Finally, Figure 2.9 shows the full impulse responses and the respective contour plot for the three different cases. As mentioned, closed array configurations, particularly the hexagon shape, are responsible for larger u, v coverage and lower side lobe levels. The contour plot shows how the impulse response of the hexagon presents only 6 side-lobe tails at about $-30\,\mathrm{dB}$ to $-35\,\mathrm{dB}$ and the rest of the synthetic beam level around $-50\,\mathrm{dB}$.

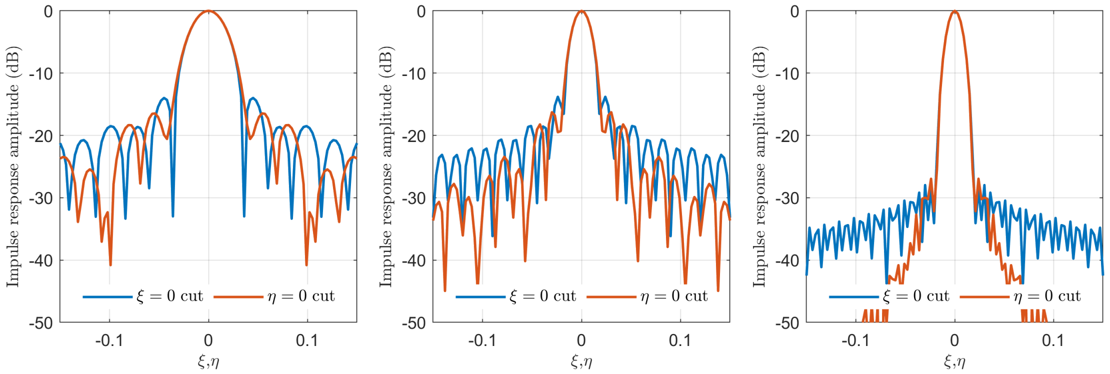

(a) *Y-shaped geometry with* $N_A = 69$.
(b) *Y-shaped geometry with* $N_A = 151$.
(c) *Hexagonal-shaped geometry with* $N_A = 300$.

Figure 2.8: *Full impulse response cut in the directrix directions* ξ *and* η *for different antenna shapes.*

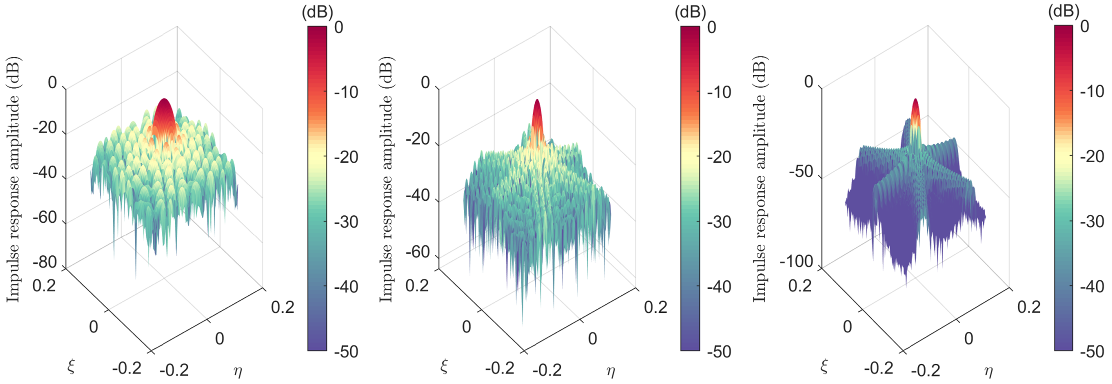

(a) *Y-shaped geometry with* $N_A = 69$.
(b) *Y-shaped geometry with* $N_A = 151$.
(c) *Hexagonal-shaped geometry with* $N_A = 300$.

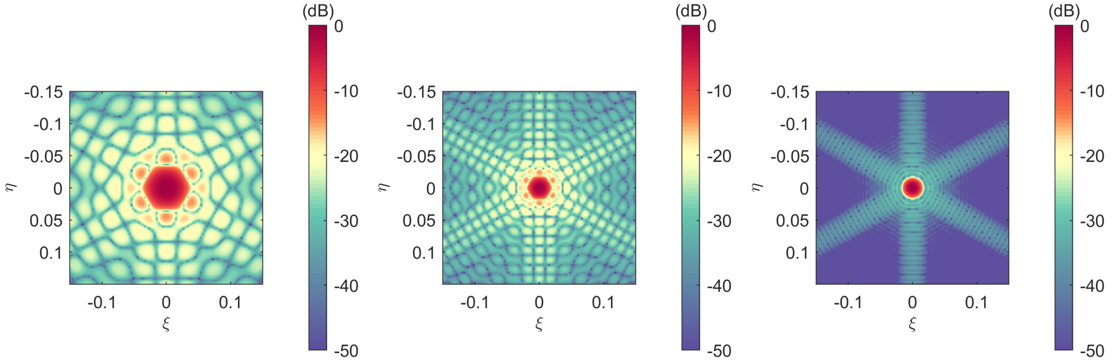

(d) *Y-shaped geometry with* $N_A = 69$.
(e) *Y-shaped geometry with* $N_A = 151$.
(f) *Hexagonal-shaped geometry with* $N_A = 300$.

Figure 2.9: *Impulse response (top row) and contour plot (bottom row) for different antenna shapes.*

To conclude, the performance of the antenna array improves with the close shape of the array and a higher number of antenna elements. However, the main drawbacks of this approach are:

- A larger and wider antenna array is required to perform better for future EO missions.
- A larger antenna array could be a critical point from the spacecraft design and launch points of view, requiring larger and heavy platforms: both the Y-shaped and hexagonal-shaped with $N_A = 151$ and 300 respectively results in an arm of about $10\,\mathrm{m}$ length.

This thesis aims to provide an alternative approach to improve the resolution and the performances of interferometer antenna arrays by combining the data from different platforms working as a distributed network of antennas. Specifically, in addition to optimising the antenna array design, the formation flying concept is exploited to enable larger and more flexible overall instrument configurations.

2.4.3 Multiple-satellites interferometer

This section describes the approach to obtain the visibility samples and the full impulse response for multiple satellite missions mounting interferometer arrays. The procedure is based on the preliminary analysis developed in [112]. In the case of multiple spacecraft, the antenna elements to be considered in the baseline equation (Equation (2.2)) are the sampled points of the overall distributed simple, instead of simply the number of the elements mounted on one single spacecraft. Once the baseline B_{ij}^{uv} in the u, v plane has been computed, the redundancies are removed to obtain the visibility samples, as performed for the single satellite case. Finally, the full response of the synthetic antenna array is computed through the windowing function.

The idea of exploiting multiple spacecraft for interferometry was proposed by Manuel Martín-Neira et al. in [27, 28], where a concept to pass from one single hexagon to three smaller hexagons was initially proposed. The small hexagons are located at three vertices of a larger hexagon as shown in Figure 2.10 (left). A hexagonal-shaped instrument with the same size as the larger hexagon of the distributed design is considered to compare the monolithic versus the distributed configuration. Accordingly, geometry and design parameters for the monolithic case are shown in Figure 2.7f and Table 2.1, respectively. As for the small hexagons, the main design parameters are: wavelength $\lambda = 21.2\,\mathrm{cm}$, number of receivers per arm equal to 17, and antenna spacing 0.767λ. The visibility function corresponding to the two configurations is computed and shown in Figure 2.10: central view for the multiple s/c options, right view for the single satellite case. The coverage geometry for the three-hexagon distributed configuration is not as convex as it is for the single satellite option: this worsens the performance in terms of coverage. Therefore it is essential to evaluate the full impulse response for the three satellite cases to assess the impulse response over the reduction of satellite dimensions. Figure 2.11 shows the full impulse responses of the formation (left) and the single satellite configurations (right). The side lobe level for the formation case is around $-20\,\mathrm{dB}$, which is slightly worst than the $-26\,\mathrm{dB}$ of the single hexagonal design. Nevertheless, compared to the initial SMOS performances, where the side lobe is $-13\,\mathrm{dB}$, the formation-flying design improves the performance of the instrument. As a result, the proposed formation-flying configuration improves the instrument spatial resolution of the $14\,\%$.

Once stated the improvement of the instrument performances through a distributed design, this thesis focuses on assessing the feasibility to realise a satellite's formation from the GNC point of view. Indeed, the size and masses of the single satellites composing the formation are smaller than the monolithic approach. Nonetheless, designing and operating a close formation of satellites poses several challenges to the relative GNC system. A set of convenient formation geometries is identified as the first step of the analysis. Section 2.5 addresses this topic in light of the achievable performances of the overall distributed instrument. The so-identified formations constitute the test cases analysed in this dissertation.

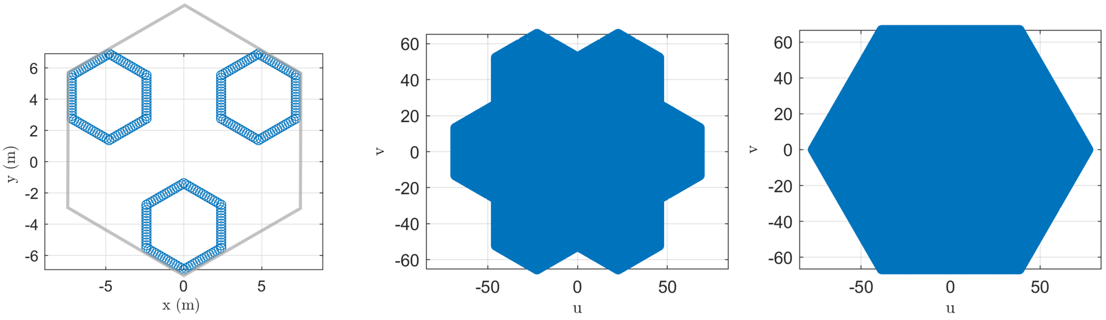

(a) *Three hexagonal-shaped array in Cartesian coordinates.* **(b)** *Visibility samples for the combined three hexagonal-shaped array.* **(c)** *Visibility samples for a single haxagonal-shaped array.*

Figure 2.10: *Comparison between multiple and single hexagonal antenna arrays.*

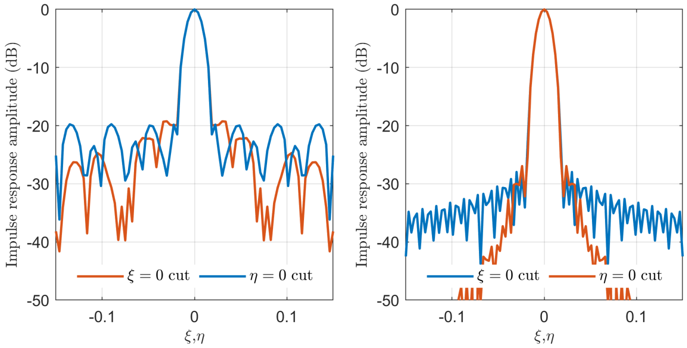

(a) *Three hexagonal-shaped arrays.* **(b)** *Single hexagonal-shaped array.*

Figure 2.11: *Full impulse response cut in the directrix directions $\xi = 0$ and $\eta = 0$.*

2.5 Passive L-band scenarios

The analysis outcomes in Section 2.4 show that the hexagonal-shaped antenna outperforms the Y-shaped one, when arms of the same size and number of antennas per arm are considered. Based on these results, this section presents different geometries of the hexagonal-shaped antennas to perform interferometry, considering an increasing number of spacecraft, three to twelve, with different dimensions and a number of antenna elements.

The geometries and radiometer performances are provided in the array plane, which is fixed in the satellites' body-fixed frames, without introducing consideration of non-planarity with generic angles γ, δ, ϕ (see Section 2.3). The design of feasible relative trajectories for each configuration is later presented in Section 3.3, where the considerations on payload performances for non-planar Array Plane are introduced.

The following configurations, starting from the test cases introduced in Section 2.3 for passive interferometry, are analysed:

- Three-spacecraft geometry:
    - Formation Flying L-band Aperture Synthesis (FFLAS) study (SP1).
    - Three Hexagonal (TriHex) study (SP3).

- Four to twelve spacecraft geometry (SP2):
  - Four spacecraft study FFLAS-2 Lite 2 (FFLAS2-L2).
  - Six spacecraft study: FFLAS-2 (FFLAS2).
  - Twelve spacecraft study: FFLAS-2 Lite 3 (FFLAS2-L3).

The main design parameters for each case study are provided in Table 2.2. The first difference consists of the antenna spacing. For the FFLAS, FFLAS-2 and FFLAS-2 L3 cases, the antenna spacing is 0.707λ. This value is smaller than the one adopted in SMOS, to reduce the aliasing problems [27,130]. On the other hand, for the TriHex and the FFLAS-2 L2 cases, an alias-free payload was studied, with an even more reduced antenna spacing, namely 0.577λ [129]. A further important aspect that varies significantly is the spacecraft dimensions: the satellites of FFLAS have a hexagonal shape with an external diameter of about $8\,\mathrm{m}$.

A way to reduce the dimension of the spacecraft is to exploit the formation flying design in terms of the number and distribution of the (smaller) satellites. Examples are the TriHex and the FFLAS-2 L3 concepts, with platforms of 3 and $2.7\,\mathrm{m}$ diameter, respectively. Consequently, the dry mass is further reduced, passing from the $1200\,\mathrm{kg}$ of FFLAS to the $400\,\mathrm{kg}$ of FFLAS-2 L3, entering the small spacecraft category.

Table 2.2: *Parameters for the computation of visibility samples and full impulse response, for different scenarios of multiple hexagonal-shaped spacecraft.*

Parameter	FFLAS	TriHex	FFLAS-2 L2	FFLAS-2	FFLAS-2 L3
No. of satellites	3	3	4	6	12
Wavelength λ (cm)	21.2	21.2	21.2	21.2	21.2
Antennas per arm (-)	24	12	12	14	8
Antenna spacing (m)	0.707λ	0.577λ	0.577λ	0.707λ	0.707λ
Distance of phase centres (m)	12.4	5.2	5.3	7.3	4.2
Spacecraft diameter dimension (m)	8	3	3	4	2.7
Spacecraft dry mass (kg)	1200	450	450	700	400

2.5.1 Three-spacecraft geometry

The first geometry consists of three spacecraft flying in a triangular formation to obtain similar performances of a larger single hexagon. In this context, three identical spacecraft with hexagonal shapes are envisioned to accommodate the antenna array.

As described in Table 2.2, we considered two cases characterised by different numbers of antennas per arm, antenna spacing and, consequently, spacecraft dimensions are considered: FFLAS and TriHex. The former demands a unit of the large spacecraft class, with a mass over $1000\,\mathrm{kg}$; while the latter consists of small spacecraft with a dry mass smaller than $500\,\mathrm{kg}$. The second consept pursuits the miniaturisation concept, mentioned in Chapter 1, where formation flying can be applied to small spacecraft to reduce the mass and cost of the mission itself. Note that a critical role in attaining the reduction of the mass of the satellites is played by the type of relative motion between the formation elements (see Chapter 6).

FFLAS scenario Figure 2.12 shows the geometry, the visibility samples, and the full impulse response of the virtual interferometer made by the three spacecraft in the FFLAS configuration. The geometry is described by Figure 2.12a, where the three spacecraft are located at the vertex of a triangle with $12.47\,\mathrm{m}$ side. The visibility samples cover an area similar to the result obtained in Figure 2.10, but with smaller spacecraft (in FFLAS 24 antennas per arm are used - see Table 2.2 - instead of 50 - see Table 2.1). The impulse response shows the performances that this kind of configuration could achieve: the side lobes are below $-20\,\mathrm{dB}$ level, and at the same time, the aperture angle of the main lobe is smaller than the one in SMOS, resulting in a spatial resolution of the observations below $10\,\mathrm{km}$ [130] way better than the $40\,\mathrm{km}$ of SMOS.

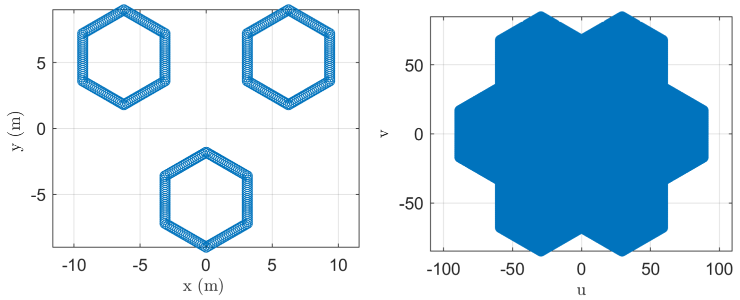

(a) *Formation geometry.* **(b)** *Visibility samples.*

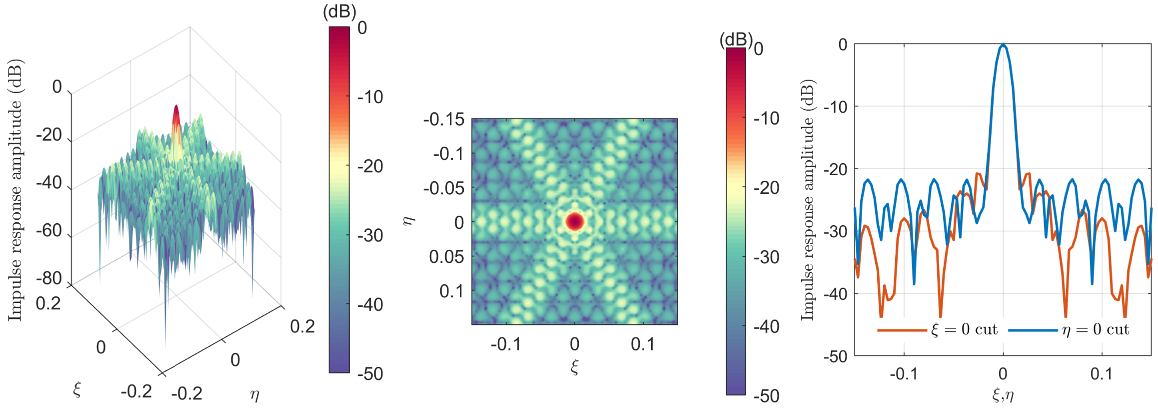

(c) *Full impulse response.* **(d)** *2D impulse response.* **(e)** *Impulse response cut in ξ, η.*

Figure 2.12: *Payload performances for the FFLAS geometry configuration.*

TriHex Scenario In this second scenario, priority has been given to reducing the dimensions and mass of the spacecraft to achieve good performances compared to the SMOS scenario. The formation configuration during the scientific phase is shown in Figure 2.13a, where the three spacecraft are placed at the vertex of a smaller triangle compared to the FFLAS case. This is required to obtain a continuous visibility sample without holes in the coverage, as in Figure 2.13b, considering that a smaller number of antennas per arm is used (i.e., 12 of TriHex instead of 24 of FFLAS).

As a drawback of this light design, the smaller dimensions of the antenna arrays and the lower number of antennas per arm (see Table 2.2), result in a smaller coverage area of the visibility samples. Moreover, analysing the impulse response of the combined array, we observe a larger aperture angle of the main lobe and a higher level of the side lobes (around $-15\,\mathrm{dB}$). This results in a spatial resolution

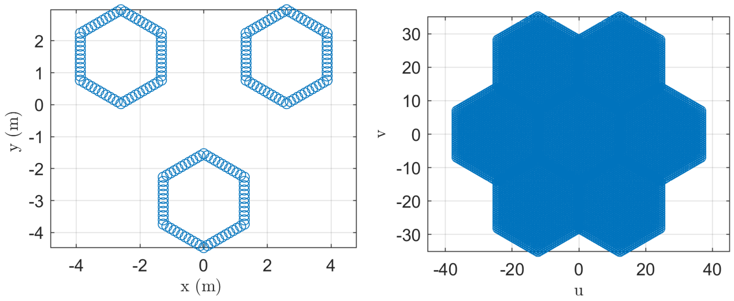

(a) *Formation geometry.* **(b)** *Visibility samples.*

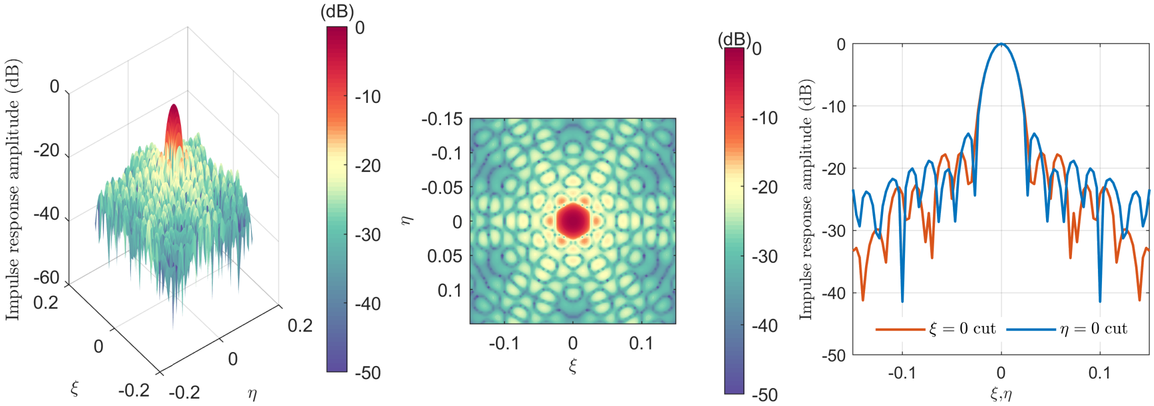

(c) *Full impulse response.* **(d)** *2D impulse response.* **(e)** *Impulse response cut in ξ, η.*

Figure 2.13: *Payload performances for the TriHex geometry configuration.*

of 15-20 km [129], thus slightly worse than the 10 km of FFLAS, but still way better than the original 40 km of SMOS.

Consideration on the spatial resolution Figure 2.14 shows the nadir and boresight spatial resolutions to compare the performances of single and multiple satellite architectures. One can note how the spatial resolution for the FFLAS and TriHex cases is significantly improved compared to the SMOS and SMAP cases. Moreover, FFLAS and TriHex provide similar values to the SMOS-HR case, which consists of a single large spacecraft. Consequently, this thesis proves that a three-satellite configuration can obtain a spatial resolution between 10 to 20 km.

Note that a further advantage of the distributed architecture is the possibility to reconfigure the spacecraft in case of failure or in case of formation extension with more platforms to improve the virtual payload aperture and, consequently, the spatial resolution [129].Moreover, fig. 2.15 compares the visibility and the impulse cut for the different geometries (SMOS, SMOS-Hexagonal, FFLAS and TriHex). The improvement in the spatial resolution is given by both the increase of visibility and the reduction of side lobe levels and width of the main lobe. Overall, SMOS-H and FFLAS has better performances and TriHex has intermediate performances compared to SMOS satellite mission.

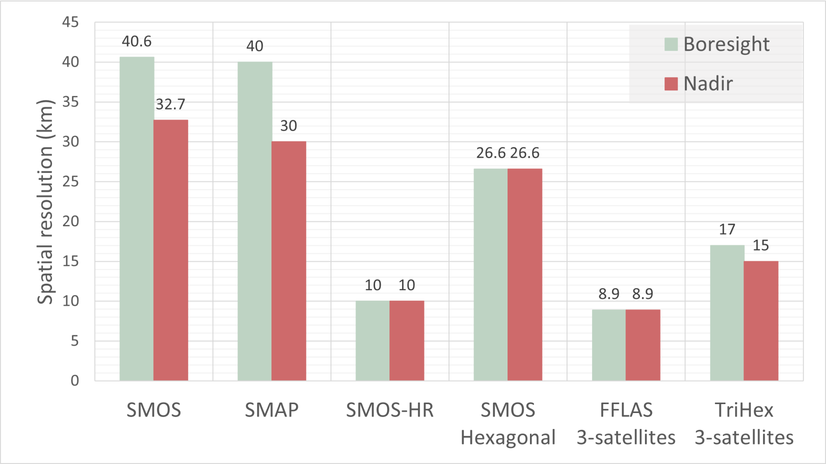

Figure 2.14: *Spatial resolution for both single satellites (SMOS, SMAP, SMOS-HR, SMOS hexagonal) and multiple satellites geometries (FFLAS and TriHex).*

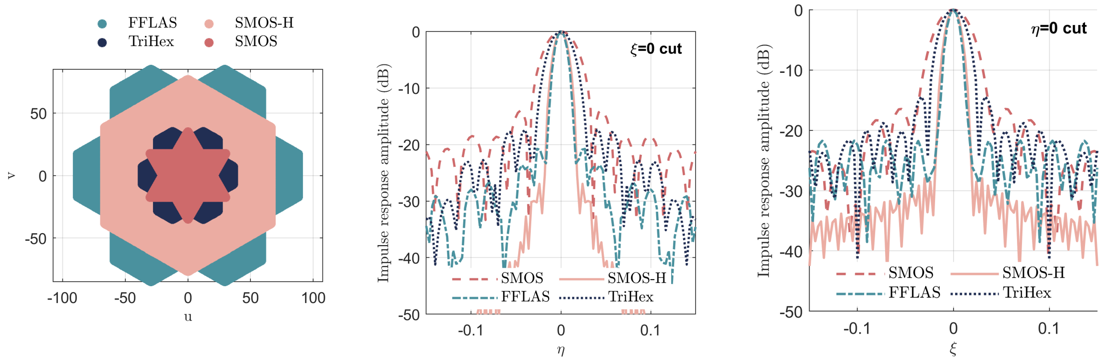

(a) *Visibility plot in u, v plane.* **(b)** *Impulse response cut in ξ.* **(c)** *Impulse response cut in η..*

Figure 2.15: *Comparison of visibility and impulse response for single and multiple satellites geometries.*

2.5.2 Four-spacecraft geometry

Similarly to the TriHex configuration, we investigated how beneficial it could be the inclusion of an additional antenna array in the central position through small spacecraft (see Table 2.2). The different geometry of the formation results in a different visibility sample coverage, as in Figure 2.16b. The corresponding impulse response shows similar performances, with a slightly smaller aperture angle of the main lobe. Nevertheless, the side-lobe level remains the same as in the TriHex scenario. The complexity of having an additional satellite does not result in a significant performance improvement from the payload point of view. Therefore, the TriHex solution is preferred to the four satellites.

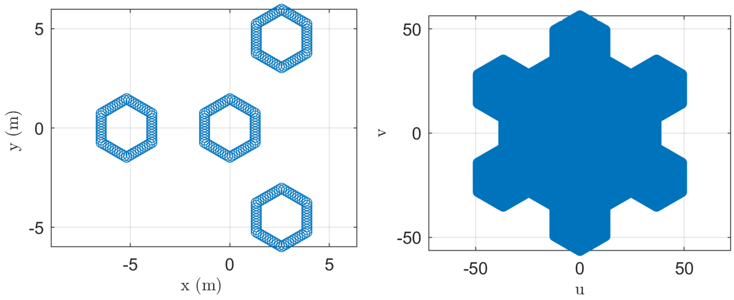

(a) *Formation geometry.* **(b)** *Visibility samples.*

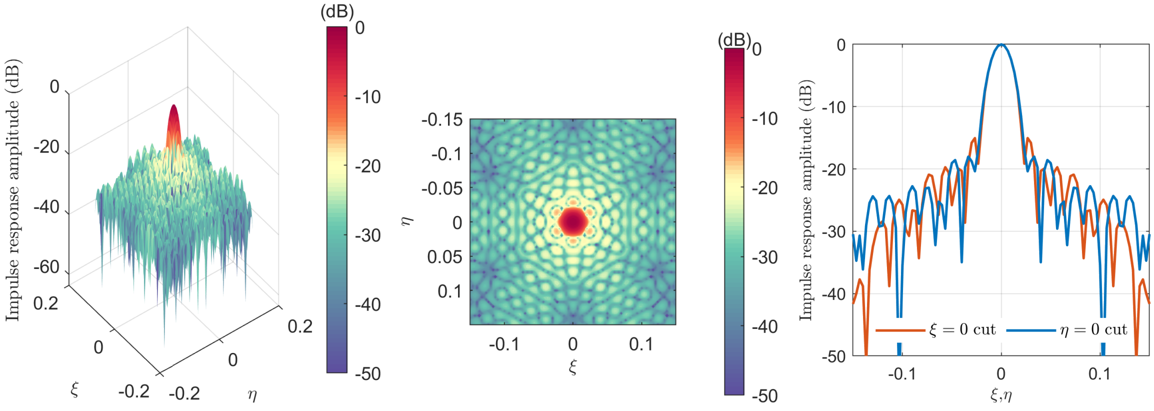

(c) *Full impulse response.* **(d)** *2D impulse response.* **(e)** *Impulse response cut in ξ, η.*

Figure 2.16: *Payload performances for the FFLAS-2 L6 geometry configuration.*

2.5.3 Six-/Twelve-spacecraft geometry

Apart from reducing the platform's dimensions, we also investigate the possibility of increasing the number of antennas array to six and twelve, respectively.

Six-spacecraft For the configuration with six spacecraft, the platform is located at the vertex of a hexagon with a distance centre to centre of about $4\,\mathrm{m}$, as in Figure 2.17a. It results in an equivalent aperture of $60\,\mathrm{m}$ diameter for the visibility sample (Figure 2.17b), similar to the FFLAS case. The impulse response produces a side-lobe level of $-16.4\,\mathrm{dB}$ and a narrow main lobe. Compared with the FFLAS case, the platform has a smaller size and mass, but the performance from the payload point of view is slightly worsened due to a higher side-lobe level. Furthermore, dealing with 6 spacecraft at such short separation is much more complex from an operational point of view than the three-satellite configuration. Consequently, the FFLAS and TriHex solutions are preferred in this thesis.

Twelve-spacecraft geometry Finally, the last case under analysis consists of twelve spacecraft with $2.7\,\mathrm{m}$ external diameter. Together with the TriHex case, this corresponds to the smallest platform analysed in this work, with a spacecraft dry mass of $400\,\mathrm{kg}$. Figure 2.18 shows the performances from the visibility samples and the impulse response point of view. The coverage of the overall formation is shown by the visibility samples in Figure 2.17b, producing similar results of the FFLAS and the six-spacecraft cases, with smaller platforms.

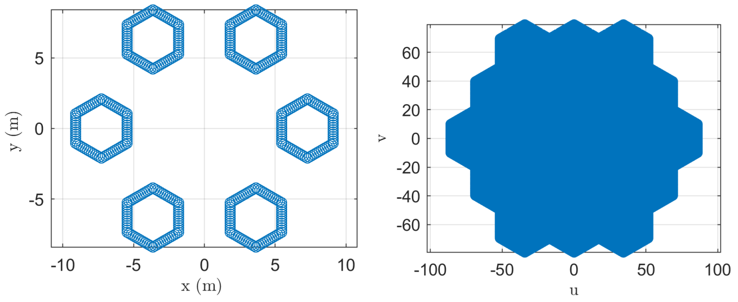

(a) *Formation geometry.* **(b)** *Visibility samples.*

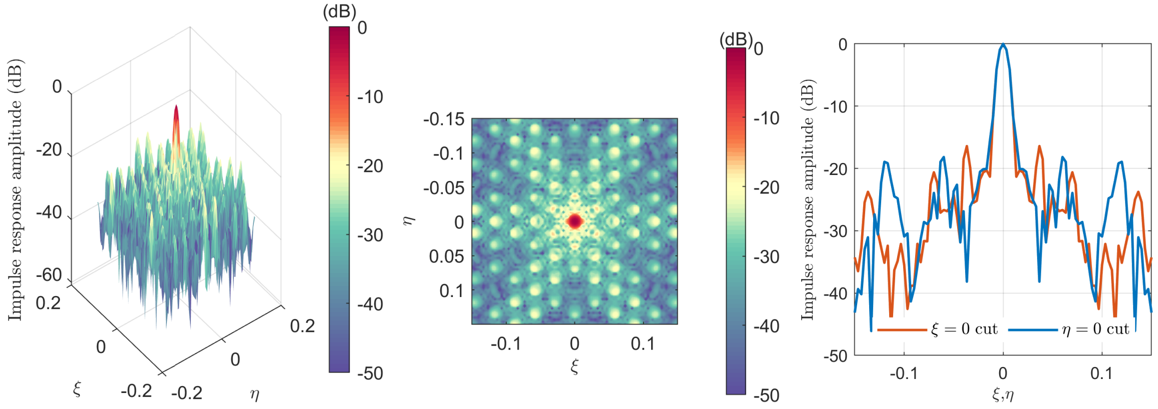

(c) *Full impulse response.* **(d)** *2D impulse response.* **(e)** *Impulse response cut in ξ, η.*

Figure 2.17: *Payload performances for the FFLAS-2 geometry configuration.*

For the ξ and η cut, the side-lobe level is in the order of $-28\,\mathrm{dB}$ for the first side lobe, and $-16\,\mathrm{dB}$ for the secondary side lobes, producing intermediate results between the three and the six satellite cases. Nevertheless, similarly to the six-satellite situation, operating 12 platform flying in such close formation and under forced motion is highly complex compared to the three-satellite case. Consequently, due to the operational complexity compared to previous FFLAS and TriHex solutions, this case is not further analysed in this dissertation.

2.6 Chapter conclusion

This chapter discusses the requirements and design parameters of active and passive microwave interferometers, including scenarios definition for the test cases in this dissertation. As for active SAR applications, two possible missions employing multiple active antennas operating in bi-static configuration have been proposed. ROSE-L exploits two spacecraft in tandem configuration: the control analyses exploiting impulsive and continuous manoeuvres are later presented in Section 6.1. HARMONY foresees three spacecraft to realise leader-follower and helix configurations: the main features and characteristics of these configurations are reported in Section 6.2.

On the other hand, the basic equations to model the passive L-band antennas have been provided to understand the potential of distributed systems with different payload characteristics and geometries. First, a preliminary approach to model the instrument has been presented, focusing on the most important criteria for performance assessment. The visibility plot and the full impulse response (i.e. width

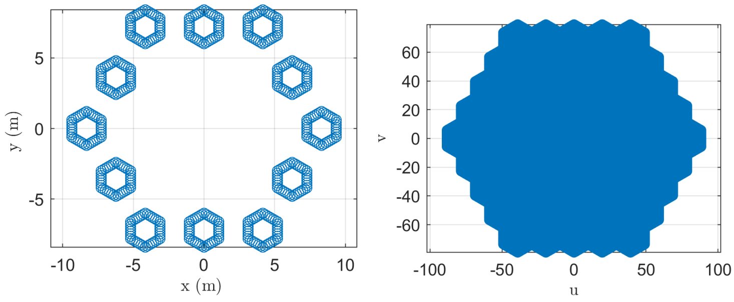

(a) *Formation geometry.* **(b)** *Visibility samples.*

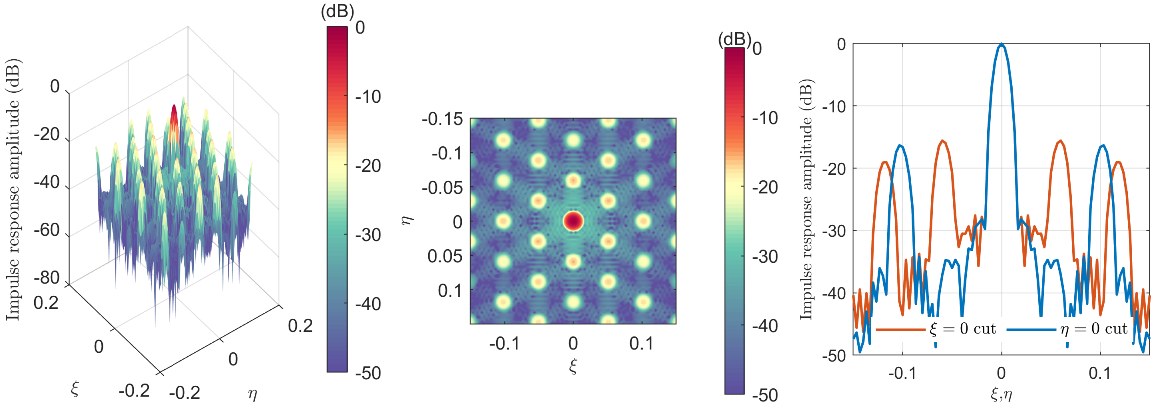

(c) *Full impulse response.* **(d)** *2D impulse response.* **(e)** *Impulse response cut in* ξ, η.

Figure 2.18: *Payload performances for the FFLAS-2 L3 geometry configuration.*

of the main lobe and level of the side lobes) provide criteria to evaluate the spatial resolution of the interferometers. A first analysis of the difference between open and closed geometry demonstrates how a hexagonal-shaped antenna has a better visibility function and a full impulse response with a narrow main lobe and lower side lobes. This improves the spatial resolution by a factor of 4. An important consideration for closed antennas is the number of elements per segment: closed geometries generally require more elements than open ones. To properly select the formation's geometry, the single units' dimensions and their number should be considered. The comparison among geometries with three to six spacecraft is based on the overall performances of the virtual synthetic aperture. The analyses demonstrated how, from the instrument point of view, the most promising are the three-satellite configurations: FFLAS and TriHex. They result in a better spatial resolution of a factor of 4 and 2.5, respectively, than SMOS. The main limitation of the larger number of spacecraft relies on the higher complexity of the operations for 6 to 12 vehicles at close distances. Furthermore, the spatial resolution performance is almost equivalent to the three-satellite case for the geometries analysed. The following part of the thesis focus on the development of guidance and control techniques to assess the feasibility of the most promising solutions (i.e. FFLAS and TriHex), considering a GNSS-based navigation.

The feasibility analysis results for passive and active interferometry distributed systems are described in Chapters 6 and 7. Specifically, given the mission scenarios and the payload performances, the next question is how to realise and design such formations and which Guidance, Navigation, and Control algorithms and techniques can be applied.

CHAPTER 3

Absolute and Relative Dynamics Framework

There is no figure left for the orbit of the planet but a perfect ellipse.

— Johannes Kepler

THIS chapter presents physical and numerical models to describe the absolute and the relative equations of motion of spacecraft around the Earth. To start, the definition of time and reference systems is essential for a rigorous implementation of dynamical models and orbital representations. The methodology for the derivation of spacecraft absolute motion in the LEO environment is presented, including the main orbital perturbations and disturbing forces. This model is validated against a commercial available tool, the General Mission Analysis Tool (GMAT), developed by NASA to support space mission design. Moreover, the relative equations of motion are presented in both unperturbed and perturbed environments. The former model is implemented to derive an analytical close form solution of the relative motion, useful for preliminary formation design. Then disturbing forces are added to the relative motion, to assess the effect of different perturbations on the relative orbit.

3.1 Definition of Reference Systems

This section provides the reference systems defined and used in this dissertation. We introduce absolute, relative, and temporal coordinate systems for a proper description of the GNC models.

3.1.1 Temporal Reference Systems

This section describes the temporal variables of importance in the modelling of spacecraft's orbits [131, 132].

Terrestrial Time The terrestrial time was introduced in 1991 to be consistent with the International System second definition and the General Theory of relativity. The Astronomical Almanac uses Terrestrial Time (TT) for its tables of positions (ephemerides) of the Sun, Moon and planets as seen from Earth. In this role, TT continues Terrestrial Dynamical Time (TDT or TD), which succeeded Ephemeris Time (ET). TT was introduced to remove the dependency on the irregularities in the rotation of Earth. It differs from the International Atomic Time (TAI) of about $32.184\,\mathrm{s}$:

$$TT = TAI + 32.184\,\mathrm{sec} \tag{3.1}$$

International Atomic Time The International Atomic Time is defined as the weighted average of the time kept by about 200 atomic clocks in over fifty national laboratories worldwide. Its epoch is defined at 1958 Jan 1, as for the Universal Time. While the stability of TAI is achieved by this weighted average, the accuracy of TAI is derived from data from primary frequency standards, which are clocks built at several national metrology institutes. TAI is computed by the International Bureau of Weights and Measures (BIPM) located in Paris, France.

Coordinated Universal Time The Coordinated Universal Time (UTC) was introduced in 1972, and it differs from TAI by an integral number of seconds. When needed, leap seconds are added to keep the difference between UTC and Universal Time (UT) less than $0.9\,\mathrm{s}$. This correction keeps UTC in conjunction with the apparent position of the Sun and the stars, and it is the standard used for all general timekeeping applications[1]. The time-of-day expressed by UTC is the time at the prime meridian (0 deg longitude) located near Greenwich, England. The time in local time zones is expressed as an offset from UTC.

Global Positioning System Time GPS is a constellation of satellites each carrying multiple atomic clocks. The time on each satellite is derived by steering the onboard atomic clocks to the time scale at the GPS Master Control Station, which is monitored and compared to UTC. Since Global Positioning System Time (GPS-Time) does not adjust for leap seconds, it is ahead of UTC by the integer number of leap seconds that have occurred since January 6, 1980 plus or minus a small number of nanoseconds. However, the time offset from UTC is contained in the GPS broadcast message and is usually applied automatically by GPS receivers. The GPS time differs from the UTC of $13\,\mathrm{s}$ on January 1st, 2000, and its epoch is defined at midnight (00:00) UTC on 1980-01-06. The differences between GPS-Time and TAI are constant at the level of some tens of nanoseconds:

$$GPS = TAI - 19.0\,\mathrm{sec} \tag{3.2}$$

On the contrary, the difference between GPS-Time and UTC changes in increments of seconds each time a leap second is added to the UTC scale[2].

---

[1] From NST announcements, website: `https://www.nist.gov/pml/time-and-frequency-division/time-realization/leap-seconds`

[2] From IERS Bullettins (Bulletin C), website: `https://www.iers.org/IERS/EN/Publications/Bulletins/bulletins.html`

Modified Julian Date The Modified Julian Date (MJD) gives the number of days since midnight on November 17, 1858. This date corresponds to $2\,400\,000.5\,\mathrm{d}$ after day 0 of the Julian calendar. MJD is still in common usage in tabulations by the U. S. Naval Observatory. Care is needed in converting it to other time units, however, because of the half-day offset (unlike the Julian date, the modified Julian date is referenced to midnight instead of noon) and because of the insertion of semi-annual leap seconds (which are inserted at midnight).

3.1.2 Absolute Reference Systems

This section describes the absolute reference systems of importance in the modelling of spacecraft's orbits around the Earth [131, 132].

Earth Mean Equator and Equinox of J2000 The Earth Mean Equator and Equinox of J2000 (EME2000) reference frame is the standard inertial frame, defined by the Eart's mean Equator and the Equinox as of 12:00 Terrestrial Time on January 1st, 2000. The Earth's equator and equinox is determined from observations of planetary motions and stars at the reference epoch. The right-hand side frame is defined by:

- The x-axis X_{EME} of the frame is aligned with the intersection of the equatorial plane and the ecliptic plane (i.e. vernal equinox) at the reference epoch.
- The z-axis Z_{EME} is aligned with the normal to the mean equator at the reference epoch and it is approximately directly as the Earth rotation axis.
- The y-axis Y_{EME} completes the right-hand side frame.

The dynamical propagation of the absolute state of the satellites is typically performed in EME2000, to include the major sources of perturbation of the orbital region. This orbital frame is used to describe the absolute position and velocity. The reference orbit, which denotes the orbit of the chief satellite of a formation, is identified with subscript $\bullet_c$ in the state vector:

$$\mathbf{X}_c = \left\{ \begin{array}{c} \mathbf{r}_c \\ \mathbf{v}_c \end{array} \right\} \tag{3.3}$$

with $\mathbf{r}_c$ and $\mathbf{v}_c$ being the position and velocity vectors of the reference orbit respectively. Considering a formation flying of N satellites, the absolute state of a generic j deputy spacecraft, with $j = 1, ..., N$, is defined as $\mathbf{r}_j, \mathbf{v}_j$, with $\mathbf{r}_j$ and $\mathbf{v}_j$ being the position and velocity vectors of the j-th satellite respectively. From the absolute state vector $\mathbf{x}$, it is possible to compute the Keplerian orbital elements of the reference orbit and the formation flying satellites. The set of classic osculating Keplerian elements of the reference orbit is denoted as $\boldsymbol{oe} = \{a_c,\, e_c,\, i_c,\, \Omega_c,\, \omega_c,\, f_c\}$, and it is composed of the semi-major axis, the eccentricity, the inclination, the right ascension of the ascending node, the argument of perigee, and the true anomaly, respectively. Similarly for a generic deputy satellite j in the formation, we define the osculating Keplerian elements as $\boldsymbol{oe}_j = \{a,\, e,\, i,\, \Omega,\, \omega,\, f\}_j$ for $j = 1 : N$. The osculating elements' set oe defines the real orbit of a spacecraft, and it is typically used to include the perturbation effects, such as nonspherical Earth, atmospheric drag, sun and moon gravity, and solar radiation pressure. On the other hand, to remove the fast motion of the $\boldsymbol{oe}$ over one orbital period, the mean orbital elements can be introduced. They are computed by introducing the mean anomaly M instead of the true anomaly f of the spacecraft, and by averaging over one orbital revolution of

M. The mean elements are identified by the vector $\boldsymbol{\alpha} = \{a,\, e,\, i,\, \Omega,\, \omega,\, M\}$. The mean elements are typically used by the two-line element set to describe the orbital elements of an Earth's orbiting object at a given time instant, and are widely used to predict in-orbit risk from space debris and collision avoidance manoeuvre. At the same time, mean elements are commonly used for the assessment of long-term effects on the spacecraft's orbit, since they do not include the fast dynamic of the vehicle along the orbit.

True-Of-Date Coordinate System The True of Date (ToD) reference frame is introduced to include the effects of nutation and precession of the Earth's motion, that is neglected in the EME2000 frame. It is referred to the current epoch, thus the coordinates system axes are time-dependent. The ToD frame is defined by:

- The x-axis X_{ToD} of the frame is aligned with the true vernal equinox at the current epoch.
- The z-axis Z_{ToD} is aligned with the true Earth rotation axis at the current epoch.
- The y-axis Y_{ToD} completes the right-hand side frame.

As described in [131, 132], the ToD and the EME2000 frame are related by a rotation matrix, named $\boldsymbol{R}_{eme2tod}$, which conveys the transformation from the EME2000 to the ToD:

$$\boldsymbol{R}_{eme2tod} = \boldsymbol{N}_{nut} \cdot \boldsymbol{P}_{prec}, \tag{3.4}$$

where $\boldsymbol{N}_{nut}$ and $\boldsymbol{P}_{prec}$ are the nutation and precession matrixes. The former one depends on the mean obliquity of the ecliptic ϵ and the nutation angles:

$$\boldsymbol{N}_{nut} = \boldsymbol{R}_x(-\epsilon_N - \Delta\epsilon)\boldsymbol{R}_z(-\Delta\psi_N)\boldsymbol{R}_x(\epsilon), \tag{3.5}$$

where the nutation angles are defined as: $\epsilon_N + \Delta\epsilon$ the change of the obliquity of the ecliptic over the 18.6-year nodal period of the Moon, and $\Delta\psi_N$ the periodic shift of the vernal equinox. The mean obliquity of the ecliptic depends on the time difference T between the current and the J2000 epoch:

$$\epsilon = 0.4090928 - 2.2696 \cdot 10^{-4} T. \tag{3.6}$$

The precession matrix, instead, is defined by the precession angles $z,\, \theta,\, \zeta$:

$$\boldsymbol{P}_{prec} = \boldsymbol{R}_z(-z)\boldsymbol{R}_y(\theta)\boldsymbol{R}_z(-\zeta) \tag{3.7}$$

International Terrestrial Reference Frame The International Terrestrial Reference Frame (ITRF) provides the realisation of the International Terrestrial Reference System for the definition of an Earth-fixed reference frame. It is computed from the ToD by adding the effects of the sidereal time and the polar motion. It is a rotating reference frame and aligns the x-axis with the apparent Greenwich location. At the same time, it includes the effect of the polar motion. It can be considered constant over one week of propagation, while for longer times it requires an update. The ITRF is computed from the ToD with a rotation matrix $\boldsymbol{R}_{tod2itrf}$:

$$\boldsymbol{R}_{tod2itrf} = \boldsymbol{P}_{pm} \cdot \boldsymbol{S}_{st}, \tag{3.8}$$

where $\boldsymbol{P}_{pm}$ and $\boldsymbol{S}_{st}$ are the sidereal time matrix and the polar motion matrix, respectively. The sidereal time matrix depends on the Greenwich apparent sidereal time ($GAST$), which depends on the current epoch [132].

$$\boldsymbol{S}_{st} = \boldsymbol{R}_z(GAST) \tag{3.9}$$

$$GAST = GMST + \Delta\psi_N \cos\epsilon, \tag{3.10}$$

where $GMST$ is the Greenwich Mean Sidereal Time, $\Delta\psi_N$ is the periodic shift of the vernal equinox, and ϵ is the obliquity of the ecliptic. On the other hand, the polar motion matrix is a combination of two rotations of the pole, called x_p and y_p:

$$\boldsymbol{P}_{pm} = \boldsymbol{R}_y(-x_p)\boldsymbol{R}_x(-y_p). \tag{3.11}$$

Note that the coordinates x_p, y_p depends on 16 free parameters that are obtained from the polar motion data of the past six years, [132].

Osculating/Mean orbital elements transformation The typical set up used for on-board algorithms is based on both mean and osculating elements, specifically:

- The navigation set up based on GNSS sensors provides the absolute position of a satellite as osculating state $\boldsymbol{X}$ in the EME2000 frame.
- The core part of the on-board algorithms is based on mean elements of the satellite, therefore:
  - First, the osculating state $\boldsymbol{X}_{eme}$ is transformed in the ToD reference frame $\boldsymbol{X}_{tod}$.
  - Second, the state in the ToD is transformed into the osculating orbital elements $\boldsymbol{oe}$.
  - Finally, the osculating/mean conversion is performed to obtain the mean orbital elements $\boldsymbol{\alpha}$.
- The mean orbital elements are used for the on-board propagation of the relative trajectory in ROEs.

This approach generates accurate orbital elements from the approximate description of an orbit. In this work, the approach used for this transformation is based on the Lie transform for the J_2 Earth's oblateness Hamiltonian problem (see [78]). This approach can be only applied to LEO orbits, where first $f^{(1)}$ and second $f^{(2)}$ order corrections are accurate to the $J_2\, e^3$ and $J_2^2\, e$ order, respectively. The osculating $\boldsymbol{oe}$ to mean $\boldsymbol{\alpha}$ transformation is the following [78]:

$$\begin{aligned}
\tilde{\boldsymbol{\alpha}} &= \boldsymbol{oe} - f^{(1)}_{\text{parallax}}(\boldsymbol{oe}) + 0.5g^{(2)}_{\text{parallax}}(\boldsymbol{oe}) \\
\hat{\boldsymbol{\alpha}} &= \tilde{\boldsymbol{\alpha}} - f^{(1)}_{\text{delaunay}}(\tilde{\boldsymbol{\alpha}}) + 0.5g^{(2)}_{\text{delauny}}(\hat{\boldsymbol{\alpha}}) \\
\boldsymbol{\alpha} &= \hat{\boldsymbol{\alpha}} - f^{(1)}_{\text{perigee}}(\hat{\boldsymbol{\alpha}}) + 0.5g^{(2)}_{\text{perigee}}(\hat{\boldsymbol{\alpha}})
\end{aligned} \tag{3.12}$$

Where the parallax and Delaunay transformations are fully described in the supplemental appendix of [78], and $g^{(2)}$ is the inverse second order correction. The authors in [78] demonstrated the accuracy level of this approach for LEO orbits.

3.1.3 Relative Reference System

This section describes the framework used in this thesis to model the relative motion between spacecraft orbiting around the same attractor.

Local Hill orbital frame The local Hill orbital frame or local-vertical local-horizontal, also called Radial-Transversal-Normal (RTN), is used to describe the relative motion of two or more satellites. It is commonly used in the representation of the formation flying relative motion, to visualize the relative trajectory as seen from the chief satellite. The frame is centred on the reference satellite and it is defined by:

- The x-axis x_{rtn} of the frame is aligned with radial direction of the reference orbit, pointing from the centre of the Earth towards the satellite.
- The z-axis z_{rtn} is aligned with the angular momentum of the reference orbit.
- The y-axis y_{rtn} completes the right-hand side frame

From the absolute inertial state, the unit vectors' triad of the relative frame in computed as:

$$\begin{aligned} \boldsymbol{x}_{rtn} &= \tfrac{\boldsymbol{r}_c}{r_c} \\ \boldsymbol{z}_{rtn} &= \tfrac{\boldsymbol{r}_c \times \boldsymbol{v}_c}{|\boldsymbol{r}_c \times \boldsymbol{v}_c|} \\ \boldsymbol{y}_{rtn} &= \boldsymbol{z}_{rtn} \times \boldsymbol{x}_{rtn} \end{aligned} \tag{3.13}$$

Where $\boldsymbol{r}_c$ and $\boldsymbol{v}_c$ are the position and velocity vectors of the reference satellite in the absolute coordinate frame. As a result, the RTN frame is not an inertial system, but rotates in time, depending on the mean motion n of the reference satellite. The angular velocity of this rotating synodic frame is defined as $\boldsymbol{\omega} = n\boldsymbol{e}_z$. Figure 3.1 represents the Hill orbital frame, where the mean position of the deputy with respect to the chief spacecraft is identified by the vector $\boldsymbol{\rho}$. The value θ_c is the true argument of latitude of the chief $\omega_c + f_c$, where f_c denotes the true anomaly of the spacecraft.

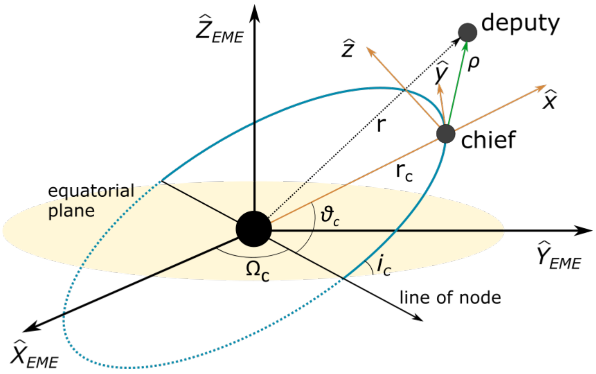

Figure 3.1: *Graphical representation of the local Hill orbital frame for a couple of chief-deputy satellites.*

Relative Orbital Elements framework The ROEs framework was introduced in [133] for easier inclusion of the orbital perturbation in the modelling of the relative motion, for formation flying application. The ROEs are function of the orbital elements of each satellite in the formation (deputies) and of the reference orbital elements (chief). They allow a semi-analytical representation of the dynamical model, with a deep insight into the geometry of the relative trajectory, and an easy representation of the inter-satellite collision avoidance approach based on the eccentricity-inclination vector separation [74]. Starting from the classical orbital elements mean $\boldsymbol{\alpha}$ or osculating $\boldsymbol{oe}$, we define the absolute orbit in terms of modified elements $\{a;\ u;\ e_x;\ e_y;\ i;\ \Omega\}$, where $u = \omega + M$ is the mean argument of latitude; while the eccentricity vector components e_x and e_y are defined as $e\cos\omega$ and $e\sin\omega$, respectively. The dimensionless ROEs vector denoted as $\delta\boldsymbol{\alpha}$, is defined as [133]:

$$\delta\boldsymbol{\alpha} = \begin{Bmatrix} \delta a \\ \delta\lambda \\ \delta e_x \\ \delta e_y \\ \delta i_x \\ \delta i_y \end{Bmatrix} = \begin{Bmatrix} (a - a_c)/a_c \\ u - u_c + (\Omega - \Omega_c)\cos(i_c) \\ e\cos(\omega) - e_c\cos(\omega_c) \\ e\sin(\omega) - e_c\sin(\omega_c) \\ i - i_c \\ (\Omega - \Omega_c)\sin(i_c) \end{Bmatrix}, \tag{3.14}$$

Where the subscript $\bullet_c$ denotes the Chief satellite. The terms are called the relative semi-major axis δa, the relative mean longitude $\delta\lambda$ and the relative eccentricity δe and inclination δi vectors respectively. Considering a Keplerian motion, the only term subject to time variation is the mean argument of latitude, with $\dot{u} = \sqrt{\mu/a_c^3}$.

3.2 Perturbed Orbital Dynamics

In literature, there are three different approaches for including the effect of orbital perturbations in the absolute spacecraft dynamics [131]. The so-called "special perturbation techniques" requires the numerical integration of the equation of motions. This approach provides quite accurate results, but suffers from numerical errors due to truncations during the integration. A second option are the "general perturbation techniques" that are based on an analytical description of the equation of motion, which then allows analytical propagation of the motion. The drawback of this approach is the accuracy of the achievable approximate or general solution. Nonetheless, the existence of an analytical formulation enables a better understanding of the physics behind each perturbing effect. Finally, the two previous methodologies can be combined to obtain "semi-analytical techniques", which aims at merging the convenient aspects from the two aforementioned approaches.

In this work, we implement a numerical methods to include an arbitrary perturbation effect in the orbital dynamics, when the high-fidelity simulation environment is regarded. This framework, in fact, provides the *true* orbit of a spacecraft, and therefore the better achievable accuracy is sought. As described in [131], the Cowell's formulation of the equation of motion allows the inclusion of perturbing accelerations to the two-body description of motion:

$$\ddot{\boldsymbol{r}}(t) = -\frac{\mu_\oplus}{r^3}\boldsymbol{r}(t) + \boldsymbol{a}_{\text{perturbation}}(t), \tag{3.15}$$

where $\mu_\oplus$ is the Earth's gravitational constant, $\boldsymbol{r}$ is the spacecraft position vector, while $\boldsymbol{a}_{\text{perturbation}}$ is the acceleration on the spacecraft due to external forces. As for the external environment, there are different orbital perturbation effects, such as the non-sphericity of the Earth's gravity field, the atmospheric drag, the third body effects, and the solar radiation pressure. Moreover, in case the spacecraft is equipped with a propulsive system, the acceleration due to the control action is included in the second member of Equation (3.15).

Since this thesis focuses on the LEO region, the equation of motions includes only the main effects typical of this region: the non-spherical Earth's gravity field, the atmospheric drag, and the solar radiation pressure, as well as the thrust action. The effects of third body perturbation (due to Sun or Moon), or tides and other perturbing forces are not included in the dissertation, given their negligible impact on the application under study. Consequently, the equation of motion, in the Cowell's formulation, becomes:

$$\boldsymbol{a}_{s/c}(t) = -\frac{\mu_\oplus}{r^3}\boldsymbol{r}(t) + \boldsymbol{a}_{\text{grav}}(t) + \boldsymbol{a}_{\text{drag}}(t) + \boldsymbol{a}_{\text{srp}}(t) + \boldsymbol{a}_{\text{cmd}}(t), \tag{3.16}$$

where $\boldsymbol{a}_{\text{grav}}$ accounts for the non-sphericity of the Earth's gravity field, $\boldsymbol{a}_{\text{drag}}$ the atmospheric drag effect, $\boldsymbol{a}_{\text{srp}}$ the solar radiation pressure, and $\boldsymbol{a}_{\text{cmd}}$ the control action.

3.2.1 Modelling of Disturbing forces

This section provides the mathematical model of the disturbing forces to be include in Equation (3.16).

Aspherical gravity field To correctly describe the gravitational effect due to the non-sphericity of the Earth, the acceleration effect is computed as the gradient of the potential associated to the non uniform distribution of the mass of the body. The gravitational potential function U can be modified through the zonal, tesseral and sectorial harmonics [131, 132]:

$$U = \frac{\mu_\oplus}{r} \cdot \left[1 + + \sum_{l=2}^{\infty}\sum_{m=0}^{l}\left(\frac{R_\oplus}{r}\right)^l P_{l,m}\left[\sin\phi_{gc}\right] \cdot \left\{C_{l,m}\cos m\lambda_{sc} + S_{l,m}\sin m\lambda_{sc}\right\}\right], \tag{3.17}$$

where $R_\oplus$ is the reference Earth's radius, $P_{l,m}\left[\sin\phi_{gc}\right]$ are the Legendre polynomial, with degree l and order m in the geocentric latitude ϕ_{gc} of the spacecraft. The coefficients $C_{l,m}$ and $S_{l,m}$ convey the Earth potential distribution when modelled through spherical harmonics, and λ_{sc} is the geocentric longitude of the spacecraft. The zonal harmonics express the contributions of an axial-symmetrical body and are typically described with the "J_l" notation, where $-C_{l,m} = -Cl, 0 = J_l$. By adopting such notation, Equation (3.17) becomes:

$$\begin{aligned} U = \frac{\mu}{r} \cdot \Bigg[1 - \sum_{l=2}^{\infty} J_l \left(\frac{R_e}{r}\right)^l P_l\left[\sin\phi_{gc}\right] + \\ + \sum_{l=2}^{\infty}\sum_{m=1}^{l}\left(\frac{R_e}{r}\right)^l P_{l,m}\left[\sin\phi_{gc}\right] \times \left\{C_{l,m}\cos m\lambda_{sc} + S_{l,m}\sin m\lambda_{sc}\right\}\Bigg]. \end{aligned} \tag{3.18}$$

The zonal harmonic part includes the Earth's oblateness (i.e. the J_2 term) and axial-symmetrical mass distribution at different bands of latitude, and are described by zeroth order ($m = 0$). The sectorial effect, instead, is described by terms with equal order and degree ($l = m$), and conveys the effect at different bands of longitude. Finally, the tesseral harmonics describes the asymmetries at certain band of latitude and longitude, characterised by ($l \neq m \neq 0$). Furthermore, the coefficients $P_{l,m}$, $C_{l,m}$ and $S_{l,m}$ can be normalised to get a more uniform magnitude and a lower variation in terms of l, m. Figure 3.2 provides a graphical representation of these terms on the Earth's globe, adapted from the representations in [131].

From the definition of the gravitational potential functions, the acceleration vector is obtained by computing the gradient of the function U with normalised coefficients [132]:

$$\boldsymbol{a}_{\text{grav}} = \nabla U = \nabla\frac{\mu}{r}\sum_{l=0}^{\infty}\sum_{m=0}^{l}\left(\frac{R_e}{r}\right)^l \bar{P}_{l,m}\left[\sin\phi_{gc}\right] \times \left\{\bar{C}_{l,m}\cos m\lambda_{sc} + \bar{S}_{l,m}\sin m\lambda_{sc}\right\}. \tag{3.19}$$

where the symbol ∇ indicates the gradient operator. Specifically, the gradient is computed in the body-fixed frame ITRF, with $\boldsymbol{r} = r_I\boldsymbol{I}, r_J\boldsymbol{J} + r_K\boldsymbol{K}$ to comply with the actual distribution of the mass in

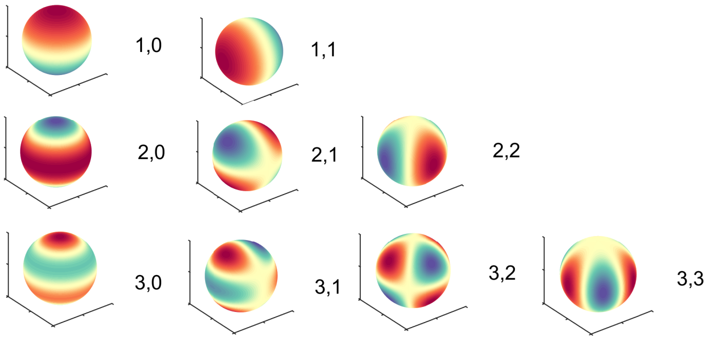

Figure 3.2: *Graphical representation of the zonal ($l, 0$), sectoral ($l = m$), and tesseral ($l \neq m \neq 0$) harmonics for degree l and order m up to 3.*

geocentric coordinates. The numerical integration of the satellite's motion is performed in the inertial EME2000 frame instead. The acceleration terms in Cartesian coordinate are the following, depending on the spherical coordinates of Lagrange functions (r, ϕ_{gc}, λ):

$$\begin{aligned}
a_I &= \left\{ \frac{1}{r}\frac{\partial U}{\partial r} - \frac{r_K}{r^2\sqrt{r_I^2 + r_J^2}}\frac{\partial U}{\partial \phi_{gc}} \right\} r_I - \left\{ \frac{1}{r_I^2 + r_J^2}\frac{\partial U}{\partial \lambda_{sc}} \right\} r_J - \frac{\mu_{\oplus} r}{r^3}, \\
a_J &= \left\{ \frac{1}{r}\frac{\partial U}{\partial r} - \frac{r_K}{r^2\sqrt{r_I^2 + r_J^2}}\frac{\partial U}{\partial \phi_{gc}} \right\} r_J + \left\{ \frac{1}{r_I^2 + r_J^2}\frac{\partial U}{\partial \lambda_{sc}} \right\} r_I - \frac{\mu_{\oplus} r}{r^3}, \qquad (3.20) \\
a_K &= \frac{1}{r}\frac{\partial U}{\partial r} r_K + \frac{\sqrt{r_I^2 + r_J^2}}{r^2}\frac{\partial U}{\partial \phi_{gc}} - \frac{\mu_{\oplus} r}{r^3},
\end{aligned}$$

where r_I, r_J, r_K and r are the components and the norm of the spacecraft position vector $\boldsymbol{r}$. The operator $\partial \bullet$ indicates the partial derivation of the variable, and in this case it is applied to the gravitational potential function U.

Finally, the computation of the a_{grav} acceleration requires the knowledge of the $\bar{C}_{lm}$ and $\bar{S}_{lm}$ terms (see Equation (3.19)). These are normalised coefficients function of the actual distribution of the Earth mass and have to be determined indirectly from satellite tracking, surface gravimetry, or altimeter data.

Different gravitational models are currently available to precisely model the orbital environment. Different Global Geopotential Models (GGM) have been developed over the years, based on satellites measurements. Particularly, the GRACE mission provided a fundamental contribution in the model developments. As an example, the GRACE gravity model, called GGM02S, has been developed in 2005 [134] and it provides geopotential coefficients in a normalised form up to degree/order 160, and includes the permanent tide effect in the $\bar{C}_{2,0}$ term. GGM02s improved the modelling accuracy to that time, compared against the previous Earth Gravitational Model EGM96. A subsequent model, called Earth Gravitational model EGM2008 [135], has been developed in 2008, as an improvement for the previous EGMN96. It consists of a least square combination of the GRACE gravitational model and its covariance matrix. It merged this model with terrestrial, altimetry, and airborne gravity data, complementing the model for coefficients up to degree/order 2159. As a result, it provides an improvement over a factor of six in resolution in comparison with the EGM96 model.

For the purpose of this work, the geopotential coefficients of the GRACE GGM02S model has been considered accurate enough for the absolute dynamic description, since in close-formation flying applications a natural cancellations of terms occurs, making negligible high order effects. Specifically, a maximum degree/order of 10 is considered in most of the analyses.

Atmospheric drag perturbation The atmospheric drag effect is the second main perturbation affecting spacecraft in the near Earth region. Moreover, this phenomenon has seasonal variations, due to the interaction of the Sun with the upper part of the atmosphere and the influence of the Earth's magnetic field. Since the drag is a non-conservative force, it is typically introduced in the dynamic equations of motion via the following acceleration term [131]:

$$\boldsymbol{a}_{drag} = -\frac{1}{2}\frac{c_D\,A_{cs}}{m}\rho\,v_{rel}^2\frac{\boldsymbol{v}_{\text{rel}}}{|\boldsymbol{v}_{\text{rel}}|}, \tag{3.21}$$

where c_D is the dimensionless drag coefficient of the spacecraft, A_{sc} is the spacecraft cross-sectional area in the velocity direction, m is the mass of the satellite, $\boldsymbol{v}_{\text{rel}}$ is the spacecraft velocity vector relative to the rotating atmosphere, and ρ is the atmospheric density. The typical value of the drag coefficient for spacecraft in the upper atmosphere varies in the range $c_D \approx 2.0\,\text{to}\,3.0$, for a preliminary analysis. Note that we define the ballistic coefficient BC as $\text{BC} = m/(c_D A_{sc})$, where m is the mass of the satellite, A_{sc} is the spacecraft cross-sectional area, c_D is the dimensionless drag coefficient: if BC is low, the drag effect on the spacecraft is high, and vice-versa. The relative velocity vector expresses the velocity of the spacecraft relative to the rotating atmosphere in Cartesian components. Its value depends on the Earth's rotation rate $\omega_\oplus$ [131]:

$$\boldsymbol{v}_{\text{rel}} = \frac{\mathrm{d}\boldsymbol{r}}{\mathrm{d}t} - \omega_\oplus \times \boldsymbol{r}, \tag{3.22}$$

where $\boldsymbol{r}$ represents the spacecraft position vector. Finally, the atmospheric density ρ can be computed following various models, with different region of validity and accuracy.

The exponential model, valid for altitude range in 0 to $100\,\text{km}$, assumes that the atmospheric density varies exponentially with the altitude, according to:

$$\rho = \rho_0\,\mathrm{e}^{-\left[\frac{h_{\text{ellp}}-h_0}{H}\right]}, \tag{3.23}$$

where ρ_0 and h_0 are the reference density and altitude respectively, h_{ellp} is the actual altitude, and H is the scale height. Both the reference values and the scale height are tabulated values, depending on the actual altitude of the spacecraft [131].

Another commonly used model is the one developed by Jacchia-Roberts, valid in the altitude range 70 to $2500\,\text{km}$ [136]. This is an analytical atmospheric model developed in 1970s widely used for reentry applications in low orbit regions [136]. This model accounts for the effects of the temperature and molecular mass profile for the altitude region below $125\,\text{km}$ altitude. For higher altitude, it provides a model to include the main constituents of the atmosphere (nitrogen, argon, helium, oxygen, and hydrogen) to derive the actual atmospheric density.

An additional model is the NRLMSISE-00, which is based on incoherent radar scatter and it is valid for altitudes in the range of 0 to $2000\,\text{km}$ [137]. Since it is an empirical model, it is based on mass density values given by satellite accelerometers, temperature from incoherent scatter radar, and molecular oxygen number density. The results from the model provide a density value with a smaller standard deviation interval in comparison with the Jacchia-Roberts one, as shown in [137]. In this dissertation, we employ in the absolute orbital dynamics the NRLMSISE-00 atmospheric density model.

Solar Radiation Pressure Similarly to aerodynamic drag, solar radiation pressure is a non-conservative force, and it is more relevant at higher altitudes. It is correlated to solar cycles and solar activities, and requires the computation of the sun-shadow condition for the spacecraft. The first important parameter is the solar-radiation constant or solar flux (SF) at Earth's mean distance from the Sun, which is equal to SF = $1367\,\mathrm{W\,m^{-2}}$. A more accurate computation is obtained considering the actual Earth-Sun distance throughout the year [131]:

$$SF = \frac{1358}{1.004 + 0.0334\cos D_{\text{aphelion}}}\frac{\mathrm{W}}{\mathrm{m}^2}, \tag{3.24}$$

where D_{aphelion} is 2π times the number of days passed from the aphelion condition of the Earth on its orbit, as a fraction of the whole year. From the SF value, we can compute the solar pressure p_{srp} per unit area:

$$p_{\text{srp}} = \frac{SF}{c}\frac{\mathrm{W/m^2}}{\mathrm{m/s}}, \tag{3.25}$$

where c is the speed of light equal to $3 \times 10^8\,\mathrm{m\,s^{-1}}$. As a result, the expression of the acceleration vector due to the solar radiation pressure is computed as:

$$\boldsymbol{a}_{\text{srp}} = -\frac{p_{\text{srp}} c_R A_\odot}{m}\frac{\boldsymbol{r}_{sc\odot}}{|\boldsymbol{r}_{sc\odot}|}, \tag{3.26}$$

where c_R is the reflectivity coefficient, which can vary in the interval 0.0-2.0, $A_\odot$ is the area of the satellite exposed to the Sun, and $\boldsymbol{r}_{sc\odot}$ is the vector connecting the spacecraft to the Sun.

3.3 Unperturbed Relative Motion

This section presents the dynamical equations of the relative motion among different satellites, under the hypothesis of no external perturbations. The description in both Cartesian coordinates and in ROEs is provided, as well as analytical solutions of the relative motions for designing close and stable relative trajectories. The notation used for the derivation of the equations of motion for a generic number N of satellites flying in formation is the following:

- The chief could either be a spacecraft or a virtual reference point for the formation.
- The parameters associated to the chief satellite are denoted with the subscript $\bullet_c$.
- The ROEs of the generic j-th deputy vehicle are denoted by $\delta\boldsymbol{\alpha}$, removing the subscript j for simplicity of notation.

Furthermore, the following assumptions have been considered in the derivation:

- No external perturbations are included: pure Keplerian motion for both chief and deputies satellites.

- Quasi-circular orbit of the chief. This assumption is based on the scientific applications of microwave interferometry, where the reference orbit should be circular to guarantee observations at constant altitude all over the globe.

- The separation among the deputies and the chief is negligible when compared to the absolute spacecraft positions in the absolute frame:
  - For active SAR the baseline for the separation among the spacecraft is typically in the order of tens of kilometre.
  - For passive microwave the baseline for the separation is in the order of few tens of meters.

3.3.1 Description in Cartesian coordinates

The non-linear equations of motion of a deputy around a chief satellite can be recovered from the Cartesian two body problem. The inertial equations of motion for a generic body around a planet is given by Equation (3.15), and the position vector of the deputy with respect to the chief spacecraft is given by:

$$\boldsymbol{\rho} = \boldsymbol{r} - \boldsymbol{r}_c \tag{3.27}$$

Where $\boldsymbol{\rho}$, $\boldsymbol{r}$, and $\boldsymbol{r}_c$ are represented in Figure 3.1. The non-linear equations of motion of a deputy around a chief becomes:

$$\ddot{\boldsymbol{\rho}} = -\ddot{\boldsymbol{r}}_c - \mu\frac{\boldsymbol{r}_c + \boldsymbol{\rho}}{|\boldsymbol{r}_c + \boldsymbol{\rho}|} \tag{3.28}$$

In the local Hill orbital frame, the components of the relative position vector are $\boldsymbol{\rho} = \{x, y, z\}$. Given the assumptions of Keplerian motion and quasi-circular reference orbit, Equation (3.28) can be linearised to obtain the well-known Hill-Clohessy-Wiltshire (HCW) equations [65,66]:

$$\begin{cases} \ddot{x} - 3n^2x - 2n\dot{y} = 0 \\ \ddot{y} + 2n\dot{x} = 0 \\ \ddot{z} + n^2z = 0 \end{cases} \tag{3.29}$$

Since the coefficients in the HCW equations are constant, the analytical solution can be computed:

$$\begin{cases} x(t) = \frac{\dot{x}_0}{n}\sin nt - \left(3x_0 + \frac{2}{n}\dot{y}_0\right)\cos nt + 4x_0 + \frac{2}{n}\dot{y}_0 \\ y(t) = 2\frac{\dot{x}_0}{n}\cos nt - 2\left(3x_0 + \frac{2}{n}\dot{y}_0\right)\sin nt - 3\left(2nx_0 + \dot{y}_0\right)t + y_0 - \frac{2}{n}\dot{x}_0 \\ z(t) = \frac{\dot{z}_0}{n}\sin nt + z_0\cos nt \end{cases} \tag{3.30}$$

All the three components (x, y, z) oscillate with a frequency function of the mean motion n, which is constant within the assumptions stated. Also, only the y component directly depends on time t, with a linear growth. Thus, to eliminate the drift between deputy and chief and, therefore, to guarantee a bounded motion, the term $(2nx_0 + \dot{y}_0)$ shall be set to zero during the design of the relative motion. As pointed out when dealing with the absolute dynamics, the Cartesian representation uses fast-varying parameters since all components vary with the one-orbital period frequency. At the same time, the HCW equations describe a motion under the linearisation and the quasi-circular assumptions, providing a precise description of the dynamics when the spacecraft separation is limited to few kilometres distance.

State-Space representation The linearised HCW equations (see Equation (3.29)) can also be rearranged in the state-space representation, introducing the state vector $\boldsymbol{x}_{rtn} = \{x,\, y,\, z,\, \dot{x},\, \dot{y},\, \dot{z}\}'$:

$$\dot{\boldsymbol{x}}_{rtn}(t) = \boldsymbol{A}_{hcw}\boldsymbol{x}_{rtn} = \begin{bmatrix} \mathbf{0}_3 & \boldsymbol{I}_3 \\ \boldsymbol{G} & \boldsymbol{H} \end{bmatrix} \boldsymbol{x}(t) \tag{3.31}$$

Where $\boldsymbol{A}_{hcw} \in \mathbb{R}^{6\times 6}$ is the plant matrix, $\boldsymbol{I}_3$ is the identity matrix, and the matrix $\boldsymbol{G}$ and $\boldsymbol{H}$ are defined as:

$$\begin{bmatrix} \boldsymbol{G} & \boldsymbol{H} \end{bmatrix} = \begin{bmatrix} 3n^2 & 0 & 0 & 0 & 2n & 0 \\ 0 & 0 & 0 & -2n & 0 & 0 \\ 0 & 0 & -n^2 & 0 & 0 & 0 \end{bmatrix} \tag{3.32}$$

The solution can then be written using the state transition matrix representation:

$$\begin{aligned} \boldsymbol{x}_{rtn}(t) = {} & \boldsymbol{\Phi}_{hcw}(t, t_0 = 0)\boldsymbol{x}_{rtn}(0) \\ = {} & \begin{bmatrix} 4 - 3\cos u & 0 & 0 & \frac{\sin u}{n} & \frac{2(1-\cos u)}{n} & 0 \\ -6(u - \sin u) & 1 & 0 & \frac{-2(1-\cos u)}{n} & \frac{4\sin u - 3u}{n} & 0 \\ 0 & 0 & \cos u & 0 & 0 & \frac{sinu}{n} \\ 3n\sin u & 0 & 0 & \cos u & 2\sin u & 0 \\ -6n(1-\cos u) & 0 & 0 & -2\sin u & -3 + 4\cos u & 0 \\ 0 & 0 & -n\sin u & 0 & 0 & \cos u \end{bmatrix} \boldsymbol{x}_{rtn}(0) \end{aligned} \tag{3.33}$$

Where $\boldsymbol{\Phi}_{hcw}(t, t_0 = 0)$ is the STM of the linear dynamic system, and $u = nt$ is the argument of latitude.

3.3.2 Description in Relative Orbital Elements

The description of the relative motion in terms of orbital elements provides some advantages, since the latter are integration constants of the orbital dynamics. In absence of external perturbations, the absolute motion is characterised by the only variation of the angular position of the spacecraft along the orbit, described by the mean anomaly $\dot{M} = 1$ (when using dimensionless variables), while the other Keplerian elements $\{a, e, i, \omega, \Omega\}$ remain constant. Furthermore, the linear equations of the relative dynamics are derived by linearising with respect to the orbital elements. As such, this modelling is accurate for neighbouring orbits, allowing for larger inter-satellite distance (especially in along-track) with respect to the Cartesian formulation. Moreover, working with oe, it becomes more straightforward the inclusion of orbital perturbations. The latter, in fact, consideration introduce a slow variation in the Keplerian elements. Starting from the Gauss' variational equations, it is possible to express the solution of the HCW in terms of ROEs. In fact, the Gauss' equations are expressed in the co-rotating RTN frame as function of the acceleration vector $\boldsymbol{d} = \{d_x, d_y, d_z\}$. The only hypothesis considered in this derivation is the assumption a non-equatorial reference orbit. As described in Section 3.1.3, the set of ROEs is defined in terms of non-linear functions of the difference of Keplerian elements:

$$\begin{aligned} \delta\boldsymbol{\alpha} &= \left\{ \begin{matrix} \delta a & \delta\lambda & \delta e_x & \delta e_y & \delta i_x & \delta i_y \end{matrix} \right\} \\ &= \left\{ \begin{matrix} \Delta a/a_c & \Delta u + \Delta\Omega\cos(i_c) & \Delta e_x & \Delta e_y & \Delta i & \Delta\Omega\sin(i_c) \end{matrix} \right\}, \end{aligned} \tag{3.34}$$

and we use these elements to write the Gauss' equations in terms of variation of orbital elements [133]:

$$\begin{Bmatrix} \Delta a/a_c \\ \Delta u \\ \Delta e_x \\ \Delta e_y \\ \Delta i \\ \Delta\Omega\sin(i_c) \end{Bmatrix} = \begin{bmatrix} 0 & 2 & 0 \\ -2 & 0 & -\sin u/\tan i_c \\ \sin u & 2\cos u & 0 \\ -\cos u & 2\sin u & 0 \\ 0 & 0 & \cos u \\ 0 & 0 & \sin u \end{bmatrix} \begin{Bmatrix} \Delta v_x \\ \Delta v_y \\ \Delta v_z \end{Bmatrix} \tag{3.35}$$

Where $\Delta v_x, \Delta v_y, \Delta v_z$ is the instantaneous variation of the velocity in RTN frame, and $u = nt + u_0$. At this point, the six integration constants $a_1, ...a_6$ of the HCW in Equation (3.30) can be written as function of the relative state at time $t = 0$ with $\boldsymbol{\rho} = 0$:

$$\begin{Bmatrix} a_1 \\ a_2 \\ a_3 \\ a_4 \\ a_5 \\ a_6 \end{Bmatrix} = \begin{bmatrix} 0 & 2 & 0 \\ -2 & 0 & 0 \\ \sin u_0 & 2\cos u_0 & 0 \\ -\cos u_0 & 2\sin u_0 & 0 \\ 0 & 0 & \cos u_0 \\ 0 & 0 & \sin u_0 \end{bmatrix} \begin{Bmatrix} \dot{x} \\ \dot{y} \\ \dot{z} \end{Bmatrix} \tag{3.36}$$

Comparing Equations (3.35) and (3.36), the similarity is evident, and the work in [133] suggested to adopt as integration constant of the HCW the dimensionless ROEs of the relative motion. These results explain why ROEs are a particularly convenient among the oe-based parametrisations. Although ROEs are defined using the spherical trigonometry and the oe of the absolute orbit, they can be related to the integration constants of the linearised relative motion parametrised in the Cartesian relative state. Accordingly, a set of linear relations between Cartesian and ROEs, characterised by periodic terms ($\sin(\bullet)$, $\cos(\bullet)$) and offsets are obtained:

$$\begin{cases} x/a_c = \delta a - \delta e_x \cos u - \delta e_y \sin u \\ y/a_c = \delta\lambda_0 - \frac{3}{2}\delta a(u - u_0) - 2\delta e_y \cos u + 2\delta e_x \sin u \\ z/a_c = -\delta i_y \cos u + \delta i_x \sin u \\ \dot{x}/v_c = -\delta e_y \cos u + \delta e_x \sin u \\ \dot{y}/v_c = -\frac{3}{2}\delta a + 2\delta e_x \cos u + 2\delta e_y \sin u \\ \dot{z}/v_c = \delta i_x \cos u + \delta i_y \sin u \end{cases} \tag{3.37}$$

Where v_c is the velocity of the chief on the circular orbit of radius a_c, and the mean argument of latitude u conveys the time variation. The term $\delta\lambda_0 - \frac{3}{2}\delta a(u - u_0)$ corresponds to the relative variation of the mean longitude in time $\delta\lambda$. The independency of the in-plane and out-of-plane motion of HCW reflects also in Equation (3.37). The in-plane dynamics depends on the variations in the semi-major axis, in the eccentricity and in the mean argument of latitude (δa, δe, $\delta\lambda$); on the other hand, the out of plane motion is driven by the relative inclination difference ($\delta\boldsymbol{i}$). In both x and y components of the relative motion, an offset term is present connected to the semi-major axis difference, and specifically, the the motion is not bounded if $\delta a \neq 0$. The eccentricity and inclination vector differences instead, cause a periodic behaviour in the relative motion.

Finally, the Equations (3.35) to (3.37) can provide a tool for a direct linear mapping of Hill's Cartesian coordinates into ROEs at a generic time instant defined by the mean argument of latitude u:

$$\begin{Bmatrix} \delta a \\ \delta\lambda \\ \delta e_x \\ \delta e_y \\ \delta i_x \\ \delta i_y \end{Bmatrix} = \begin{bmatrix} 4 & 0 & 0 & 0 & 2 & 0 \\ 0 & 1 & 0 & -2 & 0 & 0 \\ 3\cos u & 0 & 0 & \sin u & 2\cos u & 0 \\ 3\sin u & 0 & 0 & -\cos u & 2\sin u & 0 \\ 0 & 0 & \sin u & 0 & 0 & \cos u \\ 0 & 0 & -\cos u & 0 & 0 & \sin u \end{bmatrix} \begin{Bmatrix} x/a_c \\ y/a_c \\ z/a_c \\ \dot{x}/v_c \\ \dot{y}/v_c \\ \dot{z}/v_c \end{Bmatrix} \tag{3.38}$$

This transformation can be written in a more compact form as $\delta\boldsymbol{\alpha}(t) = \boldsymbol{T}(t)\boldsymbol{x}_{rtn}(t)$, with $\boldsymbol{T}$ the fist-order matrix for the linear matrix.

State-Space Representation The solution of the linearised equations of the relative dynamics in ROEs can be also written in terms of the STM. In particular, for the Keplerian motion, the plant matrix in ROEs is nil-potent of order 2. Accordingly, the STM becomes simply $\Phi_{ROE}(t, t0) = I + A_{ROE} * (t - t0)$ [138]. Starting from the relation in Equation (3.38), describing the linear mapping of the Hill Cartesian coordinates into ROEs, in the Keplerian motion assumption, a Lyapunov transformation relates the Cartesian and the ROEs variables. Accordingly the STM of the linearised equations either expressed in Cartesian relative state or in ROEs can be related to each other, obtaining:

$$\delta\boldsymbol{\alpha}(t) = \boldsymbol{T}(t)\boldsymbol{\Phi}_{rtn}(t, t_0)\boldsymbol{T}^{-1}(t)\delta\boldsymbol{\alpha}(0) \tag{3.39}$$

Because the change of variables is time-varying, it matches the fact that ROEs derive from expanding the orbital elements of the reference absolute orbit (which are defined in an inertial frame), whereas the Cartesian relative state is defined into the local Hill frame (which rotates at the rate of the mean motion).

3.3.3 Harmonic solutions

Starting from Equation (3.37), three main harmonic solutions can be identified by properly selecting the geometry of the formation: Helix-, Cross-Track pendulum- and Cartwheel-shaped formations. The analysis reported in this section is based on the results in [33, 133].

Helix formation The peculiarity of this solution is the passive safety characteristic. The relative eccentricity and inclination vectors are selected anti-parallel to each other, so that the cross-track and the radial separation never vanish at the same time [133]. The helix formation is based on the following assumptions:

- Same orbital plane: no inclination difference.
- Same semi-major axis, but different relative mean longitude $\delta\lambda$, depending on the application.
- Parallel relative eccentricity and inclination vectors.

The main advantage of this configuration is the cross-track baseline that never nullifies. The corresponding ROEs for initializing an helix-shaped formation are the following [133].

$$\delta\boldsymbol{\alpha} = \{0, \quad \delta\lambda, \quad 0, \quad \pm\delta e, \quad 0, \quad \pm\delta i\} \tag{3.40}$$

This kind of formation configuration was adopted for the TDX/TSX mission [37], with $\delta\lambda \neq 0$. This term introduces a separation in the along-track direction, between the chief and the deputy, generating a translation in the relative trajectory. This is implemented to generate different baselines for SAR observation. Figure 3.3 shows the natural orbit in the local orbital frame and the time evolution depending on the orbital position in time, parametrised in mean argument of latitude, considering a $\delta\lambda = 0$. The latter represents an helix-shaped evolution of the three deputies.

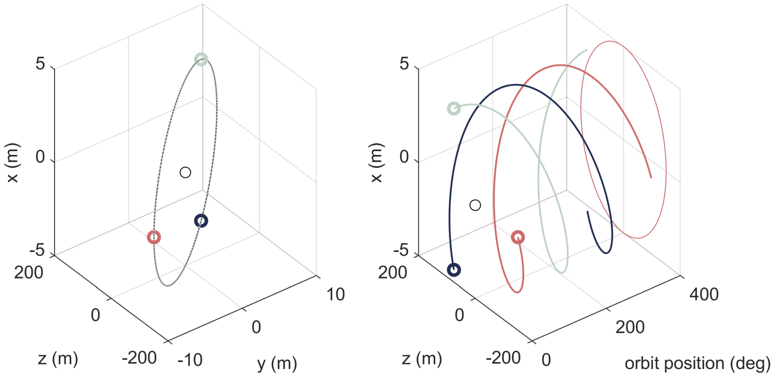

Figure 3.3: *Helix harmonic solutions of the unperturbed HCW relative motion.*

Cross-track pendulum formation This solution is characterised by small differences in inclinations and/or RAAN. As explained in [139], inclination differences are highly affected by the J_2 precession, and consequently, the pendulum is typically realised with a separation of RAAN $\Delta\Omega$. Moreover, a null relative eccentricity is set for all the spacecraft around the chief. To avoid collision, it is important to introduce a variation in the relative argument of latitude among the deputies. The corresponding ROEs for initialising a cross-track pendulum are the following:

$$\delta\boldsymbol{\alpha} = \{0, \quad \delta\lambda, \quad 0, \quad 0, \quad 0, \quad \Delta\Omega sin(i_c)\} \tag{3.41}$$

With these initial condition, the motion is bounded in the transversal-normal $(y - z)$ plane, with no components in the radial direction. Figure 3.4 shows the natural orbit in the local orbital frame and the time evolution depending on the orbital position in time, with a pendulum-like behaviour in the local frame.

Cartwheel formation In this configuration the variation of the baseline is generated by imposing an eccentricity vector separation among chief and deputy, which generates an harmonic variation in the radial-transversal $(x - y)$ plane [139]. At the same time the inclination vector separation is set to zero, as well as the semi-major axis difference. The ROEs for the initialisation of a cartwheel formation are the following:

$$\delta\boldsymbol{\alpha} = \{0, \quad 0, \quad \delta e_x, \quad \delta e_y, \quad 0, \quad 0\} \tag{3.42}$$

Figure 3.5 shows the natural orbit in the local frame and the time evolution depending on the orbital position in time. One can observe an oscillatory motion in the $y - z$ plane along the orbital revolution.

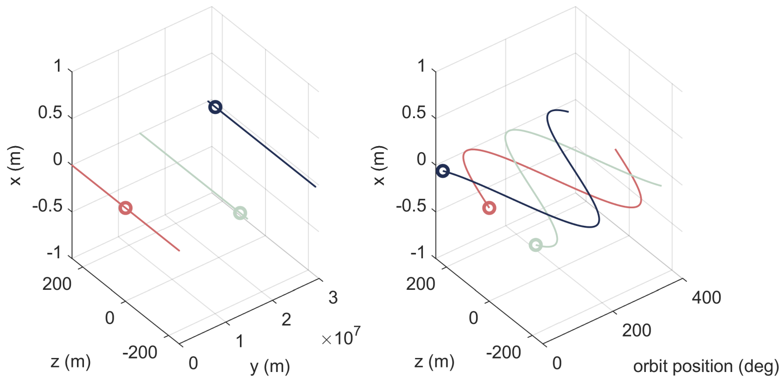

Figure 3.4: *Cross-track pendulum harmonic solutions of the unperturbed HCW relative motion.*

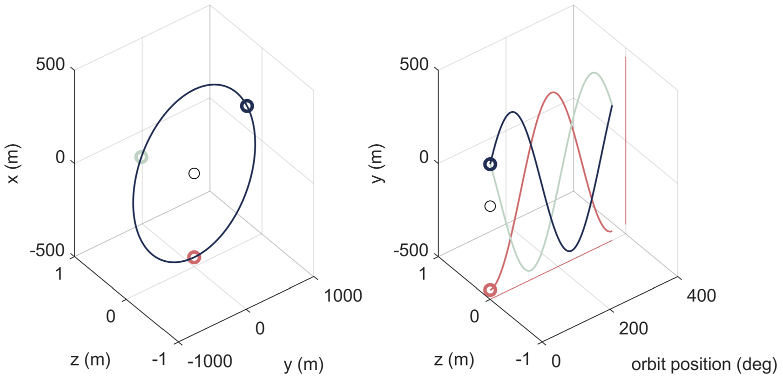

Figure 3.5: *Cartwheel harmonic solutions of the unperturbed HCW relative motion.*

3.3.4 Closed-form solutions

The design of a close and stable relative trajectory is based on the analytical solutions of the unperturbed relative motion. Similar to the work in [82], we start from the analytical solution of the linearised Hill equations to compute bounded periodic solution. Differently from other works in literature [33, 68, 82], we express the periodic solutions in terms of ROEs, instead of the Cartesian coordinates or orbital elements differences. First, to obtain a periodic solution, the secular terms are eliminated by imposing $\dot{y}(0) = -2\,n\,x(0)$. At this point, the solution of the unperturbed HCW in Equation (3.30), can be expressed in terms of amplitude and phase angle, using the equality $a \sin t + b \cos t = \sqrt{a^2+b^2}\cos\left(t - \arctan\left(a/b\right)\right)$:

$$\begin{cases} x = \rho_x \sin(u+\alpha_x) \\ y = \rho_y + 2\rho_x \cos(u+\alpha_x) \\ z = \rho_z \sin(u+\alpha_z) \\ \dot{x} = \rho_x \cos(u+\alpha_x) \\ \dot{y} = -2\rho_x \sin(u+\alpha_x) \\ \dot{z} = \rho_z \cos(u+\alpha_z) \end{cases} \tag{3.43}$$

Where ρ_x and ρ_z are the amplitude of motion in the x and z direction, while ρ_y represents the bias in the along-track direction. The angles α_x and α_z are the phase angles. The amplitudes ρ_x, ρ_y, ρ_z and the phases α_x, α_z are defined as:

$$\begin{array}{lll} \rho_x = \sqrt{(\dot{x}_0/n)^2 + (3x_0 + 2\dot{y}_0/n)^2} & \alpha_x = \arctan\left(\frac{\dot{x}_0/n}{3x_0+2\dot{y}_0/n}\right) & \rho_y = y_0 - 2\dot{x}_0/n \\ \rho_z = \sqrt{(\dot{z}_0/n)^2 + z_0^2} & \alpha_z = \arctan\left(\frac{\dot{z}_0/n}{z_0}\right) & \end{array} \tag{3.44}$$

Combining the Equation (3.43) and Equation (3.38), we obtain the relative equation of motion in amplitude-phase form based on ROEs:

$$\begin{cases} \delta a = 0 \\ \delta\lambda = \rho_y/a_c \\ \delta e_x = -\rho_x/a_c \sin\alpha_x \\ \delta e_y = -\rho_x/a_c \cos\alpha_x \\ \delta i_x = \rho_z/a_c \cos\alpha_z \\ \delta i_y = -\rho_z/a_c \sin\alpha_z \end{cases} \tag{3.45}$$

The parameters ρ_x, ρ_y, ρ_z, α_x and α_z can be tuned to obtain particular geometries of the relative trajectory. Specifically, three main particular solutions have been identified [33, 68, 82]. The first corresponds to a circular relative orbit of the deputy around the virtual reference point, the second to a relative orbit with a circular projection, and the last one to a leader-follower configuration.

General circular orbit The relative circular orbit of the deputy around the reference point is called General Circular Orbit (GCO). It is obtained by imposing the relative trajectory to be a circle. The corresponding parameters to tune the initial conditions of Equation (3.45) are the following:

$$\rho_x = \frac{1}{\sqrt{3}}\rho, \qquad \rho_y = 0, \qquad \rho_z = \rho, \qquad \alpha_x = \alpha_z. \tag{3.46}$$

Where ρ represents the radius of the relative circular orbit of the deputy about the chief. An example of a GCO trajectory is shown in Figure 3.6 with six deputies and a central virtual chief. On the left, the three-dimensional representation of the orbit is provided in the Hill plane, while on the right, the magnitude of the radius of the relative orbit is shown in time. Since the relative trajectory is a circular orbit, it results in a constant distance among the satellites during the unperturbed dynamical evolution.

Projected circular orbit The second case corresponds to a relative orbit with a circular projection on the transversal-normal $(y - z)$ or on the radial-normal $(x - z)$ plane, and it is called Projected Circular Orbit (PCO). Depending on the selection of the parameters it can be obtained the former or the latter solution, respectively:

$$\begin{array}{lllll} \mathrm{y-z\ PCO:} & \rho_x = \rho, & \rho_y = 0, & \rho_z = 2\rho, & \alpha_x = \alpha_z \\ \mathrm{x-z\ PCO:} & \rho_x = \rho, & \rho_y = 0, & \rho_z = \rho, & \alpha_x = pi/2 + \alpha_z. \end{array} \tag{3.47}$$

An example of the $y - z$ PCO case is shown in Figure 3.7 with six deputies. On the left, the three-dimensional representation of the orbit is shown, while on the right the magnitude of the relative orbit radius and the $y-z$ projected orbit radius are provided. The latter is constant in time in the unperturbed environment.

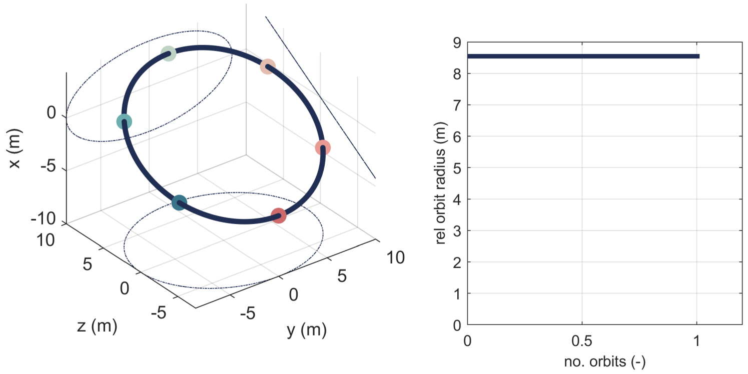

Figure 3.6: *Example of a GCO formation of six deputies. On the left, the three-dimensional representation is shown, while on the right the magnitude of the relative orbit radius is represented.*

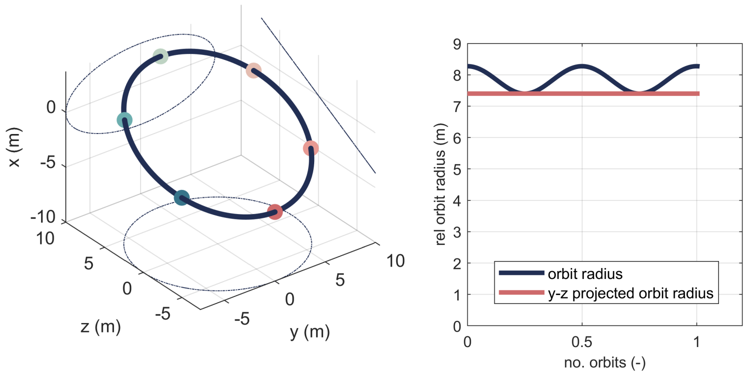

Figure 3.7: *Example of a y-z PCO formation of six deputies. On the left the three-dimensional representation, while on the right the magnitude of the radius of both the relative and y-z projected orbit.*

Leader-follower configuration The final solution corresponds to a formation where the deputy follow or precede the chief by a constant separation in the along-track direction (y). This solution is obtained imposing both ρ_x and ρ_z to be null, while $\rho_y = d$, with d constant value.

3.3.5 Operational Considerations

Following the analysis in Section 2.3, depending on the payload technology, different configuration and separation baseline are required. First, for SAR applications, helix-shaped configurations can guarantee both safety and imaging constraints, as proven in the TDX/TSX mission [133]. On the other hand, the cartwheel configuration has no cross track drift, which results in a baseline in the x, y plane. Finally, the cross-track pendulum configuration is the most common in SAR applications, since it guarantees constant along-track baseline, but when the relative motion is initialised with a separation in the RAAN, the secular effect of J_2 generates across and along-track drift over the orbital revolution.

Distributed systems for passive interferometry, as described in Section 2.4.3, require fix and rigid baseline. From the analysis in Chapter 2, the geometry of the distributed system is not compatible with the leader-follower configuration, as triangular or hexagonal formations are required. This aspect can be provided by the GCO solution, which guarantees a fixed relative distance among the vehicles. On the other hand, the other analytical solutions presented above, instead generates a time-varying baseline and are not suitable for passive interferometry. It should also be considered that the plane of the relative circular orbit does not lie on the transversal-normal ($y - z$) plane, but it is inclined by a positive rotation of $+30$ deg with respect to the direction of motion $+y$ (i.e. the transversal direction). Further analysis to assess the impact of this angle on both the operations and the microwave synthetic aperture are provided later in Section 6.5.

3.4 Perturbed Relative Motion

This section presents the effects of the external perturbations on the unperturbed relative motion of Section 3.3. First, the effect of the major environmental perturbation of LEO is considered, with the introduction of the dominant main J_2 zonal effect and differential drag. Then, the extension to higher order and degree contributions of the Earth gravitational perturbations is discussed. Perturbing effects are added to the linearised relative natural dynamics with a superposition approach. For the analysis of the precise relative motion, the osculating elements are regarded, to focus on the true actual positions of the satellites. As consequence of the action of the perturbations, the osculating orbital elements present short-, long-term, and secular variations. In the development of guidance and control algorithms for formation flying applications, it is convenient to work with mean (i.e., one-orbit time averaged) orbital elements, since they retain the main characteristics of the perturbed dynamics with reduced complexity and computational time. Note that, for very close formation flying, as for example in passive interferometry, the contributions of short- and long-term oscillations cancels out naturally, due to position/velocity differencing between neighbouring satellites. In this work, we consider three models for the perturbed relative motion:

1. Description in relative Cartesian state, including Earth's oblateness and differential drag.
2. Description in ROEs, including Earth's oblateness and differential drag.
3. Description in ROEs, including full gravitational harmonic terms.

These model have been used in the development of the guidance and control techniques. Specifically, the first two models, in relative Cartesian state and ROEs, have been employed in the derivation of a Convex Optimal Control Problem (COCP) for the design of delta-v optimal manoeuvre for formation reconfiguration (see Section 4.1). The performances of the COCP are compared for the two description in RTN and in ROEs. Moreover, the dynamical description in relative Cartesian state was implemented in the LQR control algorithm developed for the closed-loop simulations (see Section 4.2). Finally, the Model Predictive Control (MPC) algorithm for manoeuvre design and formation maintenance has been developed with a convex description of the dynamics based on the ROEs description of the relative motion including the including Earth's oblateness and differential drag. The last model has been developed to include in the dynamical description higher order effects of the gravitational perturbation. It is useful to understand the effect on the relative dynamics compared to the only J_2 case.

One important consideration is on the effect of external atmospheric drag perturbations on the relative motion. First, differently from the absolute dynamics, the main contribution is given by the differential effects of the perturbations. Specifically, the magnitude of the effect is typically smaller than on the absolute trajectory and depends on the difference in the orbital elements, mass and physical properties of the vehicles, and the attitude. As an example, in a two satellite formation, the atmospheric drag influences both dynamics. When the focus is on the relative effect, depending on the spacecraft separation, mainly in terms of altitude and spacecraft properties (i.e. mass, cross section, C_D), a difference in the magnitude of the drag effect may be present. We have two situations for the cases under analysis:

- For active SAR, the spacecraft are typically separated of few hundreds to few thousands meters. Nevertheless, the formation is generally initialised with a null separation in terms of semi-major axis: the differential drag effect is mainly caused by different ballistic coefficients of the satellites.

- For passive interferometry, the formation is designed with a spacecraft separation of few tens of meters. Also in this case the formation is initialised with a null semi-major axis, to reduce the potential drift due to the differential drag. Moreover, the platform have all the same physical properties (i.e. mass, cross section and attitude): the differential drag is almost negligible for these particular case.

To conclude, the differential drag has been included in the model to consider the second most important effect in LEO region, after the Earth's oblateness. Nonetheless, for the applications in this dissertation, its effect is relatively small whenever similar spacecraft have been considered. At the same time, the selection of dawn-dusk SSO orbits reduces the effect of the atmospheric drag in the absolute orbit due to the day-night variation, thanks to the reduced number of eclipses per year.

3.4.1 STM with Earth Oblateness and differential drag in Cartesian Coordinates

The model adopted to describe the relative dynamics under the Earth's oblateness and differential drag effects on the Cartesian relative state is based on the model derived by [71]. This work starts from the HCW representation of the relative motion (see Equation (3.30)), under the hypothesis of quasi-circular orbit. The plant matrix $\boldsymbol{A}_{rtn,J2+Drag}$ is included in the state-space representation:

$$\dot{\tilde{\boldsymbol{x}}}_{rtn} = \boldsymbol{A}_{rtn,J2+Drag}(t)\tilde{\boldsymbol{x}}_{rtn}(t) = \begin{bmatrix} 0 & 0 & 0 & 1 & 0 & 0 & \\ 0 & 0 & 0 & 0 & 1 & 0 & \\ 0 & 0 & 0 & 0 & 0 & 1 & \\ a_{41} & a_{42} & a_{43} & a_{44} & 2\omega_z & 0 & a_{47} \\ a_{51} & a_{52} & a_{53} & -2\omega_z & a_{55} & 2\omega_z & a_{57} \\ a_{61} & a_{62} & a_{63} & 0 & -2\omega_z & a_{66} & 0 \\ 0 & 0 & 0 & 0 & 0 & a_{77} & \end{bmatrix} \tilde{\boldsymbol{x}}_{rtn}(t) \quad (3.48)$$

Where the state $\tilde{\boldsymbol{x}}_{rtn}$ is composed by $\tilde{\boldsymbol{x}}_{rtn}(1:6) = \boldsymbol{x}_{rtn}$ and $\tilde{\boldsymbol{x}}_{rtn}(7) = -(\beta_d - \alpha_d)\omega_z$. The drag coefficient are defined from the chief's and deputy's drag coefficients C_D, cross-sectional area A_c, spacecraft mass M and the atmospheric density ρ_{atm}: $\alpha_d = \frac{1}{2}\frac{\rho_{atm}C_D A_c}{M}|X_c|$ for the chief satellite and $\beta_d = \frac{1}{2}\frac{\rho_{atm}C_D A_c}{M}|X_d|$ for the deputy's satellite. The coefficients of the plant matrix are defined as [71]:

$$
\begin{aligned}
&K = \frac{6J_2\mu R_e^2}{r^5} \qquad a_{41} = \omega_z^2 + 2\frac{\mu}{r^3} + K(1 - 3\sin^2 i \sin^2 u) \\
&a_{42} = \dot{\omega}_z + K\left(\sin^2 i \sin 2u\right) + \beta_d\omega_z^2 \qquad a_{43} = -\omega_x\omega_z + K\left(\sin 2i \sin u\right) \\
&a_{44} = -\beta_d\omega_z \qquad a_{47} = \dot{r} \qquad a_{51} = -\dot{\omega}_z + K\left(\sin^2 i \sin 2u\right) - \beta_d\omega_z^2 \\
&a_{52} = \omega_x^2 + \omega_z^2 - \frac{\mu}{r^3} + K\left(-\frac{1}{4} + \sin^2 i\left(\frac{7}{4}\sin^2 u - \frac{1}{2}\right)\right) \\
&a_{53} = \dot{\omega}_x + K\left(-\frac{1}{4}\sin 2i \cos u\right) + \beta_d\omega_x\omega_z \qquad a_{55} = -\beta_d\omega_z \qquad a_{57} = r\omega_z \\
&a_{61} = -\omega_x\omega_z + K\left(\sin 2i \sin u\right) \qquad a_{62} = -\dot{\omega}_x + K\left(-\frac{1}{4}\sin 2i \cos u\right) - \beta_d\omega_x\omega_z \\
&a_{63} = \omega_x^2 - \frac{\mu}{r^3} + K\left(-\frac{3}{4} + \sin^2 i\left(\frac{5}{4}\sin^2 u - \frac{1}{2}\right)\right) \\
&a_{66} = -\beta_d\omega_z \qquad a_{77} = -(\beta_d - \alpha_d)\dot{\omega}_z
\end{aligned}
\tag{3.49}
$$

The performances of this model were tested in [71], and demonstrated quite accurate results. The test with a formation of two spacecraft with a separation of about $10\,\mathrm{km}$ results in an error of the model compared to the non-linear propagator of about $0.25\,\mathrm{km}$ after one day of propagation, when same physical properties of the spacecraft are considered (when $\alpha_d = \beta_d$). This case corresponds to equal physical parameters of the spacecraft and therefore no differential drag effect. Furthermore, the following accuracy level have been reached in [71]:

- First case: a formation of two spacecraft with initial conditions $x_{rtn}(0) = [5,\ 0,\ 2.5,\ 0,\ -10n,\ 0]$ (km, km/sec) and a reference circular orbit at mean altitude of $622\,\mathrm{km}$, inclination of 97.87 deg. When only the J_2 perturbation is considered, a percentage error of the relative state with respect to the non-linear model below $10\,\%$ over 15 orbits is obtained.

- Second case: a formation of two spacecraft with $x_{rtn}(0) = [0,\ 500,\ 0,\ 0.026,\ -5.6e-4,\ 0.52]$ (m, m/sec) and a reference orbit at mean altitude of $722\,\mathrm{km}$, inclination of 70 deg and eccentricity 0.005. When only the J_2 perturbation is considered, a percentage error of the relative state with respect to the non-linear model below $5\,\%$ over 15 orbits is obtained.

- Third case: a formation of two satellites with initial conditions $x_{rtn}(0) = [0,\ 1,\ 0,\ 0,\ 0,\ 0]$ (km, km/sec) and a reference orbit at mean altitude of $722\,\mathrm{km}$, inclination of 70 deg and eccentricity 0.005. When the J_2 and differential drag perturbations are considered, a percentage error of the relative state with respect to the non-linear model below $5\,\%$ over 15 orbits is obtained. In this case a ballistic coefficient of $\alpha_d = \beta_d/2$ has been considered.

The results obtained with this model are accurate enough to model a preliminary guidance and control algorithm for the relative motion manoeuvres. Specifically, this model has been used to derive the convex optimal problem for delta-v optimal manoeuvre design based on the RTN representation of the dynamics. For most of the case under analysis in this thesis, the platforms have similar physical performances, from mass, cross sectional area and drag coefficient point of view. This is valid mainly for the cases of passive distributed interferometry, as the FFLAS and TriHex cases. Consequently, when $\alpha_d \approx \beta_d$, the effect of the differential drag is reduced compared to the J_2 perturbation. This is valid in the case of small spacecraft separation (below $2\,\mathrm{km}$), as for the passive interferometry formation flying.

3.4.2 STM with Earth's oblateness and differential drag in Relative Orbital Elements

The model adopted in this dissertation is based on the model developed for the AVANTI experiment carried out in 2016 [75,90]. It has been chosen to include both the effects of Earth's oblateness and of the differential atmospheric drag in the ROEs description. This work implements the state transition matrix of the relative dynamics, including the change in both relative mean longitude and relative inclination vector due to the mean J_2 effect and the differential drag. The state vector is augmented by introducing the time variation of the relative semi-major axis and the relative eccentricity components: $\delta\dot{\boldsymbol{\alpha}} = \{a\delta\dot{a}, a\delta\dot{e}_x, a\delta\dot{e}_y\}$. Considering the state vector as $\boldsymbol{x} = (a\delta\boldsymbol{\alpha}, a\delta\dot{\boldsymbol{\alpha}})'$, the state at a generic time t is computed from the initial conditions as:

$$\boldsymbol{x}(t) = \boldsymbol{\Phi}(t,t_0)\boldsymbol{x}(t_0) = \begin{bmatrix} \boldsymbol{\Phi}_{HCW}(t,t_0) + \boldsymbol{\Phi}_{J2}(t,t_0) & \boldsymbol{\Phi}_{dd}(t,t_0) \\ \boldsymbol{0}_{3\times 6} & \boldsymbol{I}_{3\times 3} \end{bmatrix} \tag{3.50}$$

Where $\boldsymbol{\Phi}(t,t_0)$ is the state transition matrix, including the terms for the differential drag $\boldsymbol{\Phi}_{dd}(t,t_0)$, the HCW contribution in $\boldsymbol{\Phi}_{HCW}(t,t_0)$, and the J_2 mean effect of the Earth's oblateness $\boldsymbol{\Phi}_{J2}(t,t_0)$. The overall state transition matrix is defined as [90]:

$$\boldsymbol{\Phi}(t,t_0) = \begin{bmatrix} 1 & 0 & 0 & 0 & 0 & 0 & dt & \frac{2}{n}su & -\frac{2}{n}\left(1-cu\right) \\ (\mu_A - 0.5n)dt & 1 & 0 & 0 & \mu_I dt & 0 & \frac{1}{2}\left(\nu+\mu_A\right)dt & -\frac{3}{n}\left(1-su\right) & 3dt + \frac{3}{n}su \\ 0 & 0 & cp & -sp & 0 & 0 & \frac{1}{n}su & dt + \frac{1}{n}cu\,su & \frac{1}{n}su^2 \\ 0 & 0 & sp & cp & 0 & 0 & \frac{1}{n}\left(1-cu\right) & \frac{1}{n}su^2 & dt - \frac{1}{n}cu\,su \\ 0 & 0 & 0 & 0 & 1 & 0 & 0 & 0 & 0 \\ \lambda_A dt & 0 & 0 & 0 & \lambda_I dt & 1 & \frac{1}{2}\lambda_A dt & 0 & 0 \\ 0 & 0 & 0 & 0 & 0 & 0 & 1 & 0 & 0 \\ 0 & 0 & 0 & 0 & 0 & 0 & 0 & 1 & 0 \\ 0 & 0 & 0 & 0 & 0 & 0 & 0 & 0 & 1 \end{bmatrix} \tag{3.51}$$

With coefficients:

$$\begin{aligned} & dt = (t-t_0) \qquad \nu = -\frac{3}{2}n_c \qquad n_c = \sqrt{\frac{\mu_\oplus}{a_c^3}} \qquad \gamma = \frac{J_2 R_\oplus^2}{2a_c^2\eta^4} \qquad \eta = \sqrt{1-e_c^2} \\ & \mu_A = -\frac{21}{4}n\gamma\left(3\cos^2 i_c - 1\right)(\eta+1) \qquad \mu_I = -\frac{3}{2}n\gamma\sin^2 i_c(3\eta+4) \\ & \lambda_A = \frac{21}{4}n\gamma\sin 2i_c \qquad \lambda_I = 3n\gamma\sin^2 i_c \qquad \dot{\phi} = \frac{3}{2}n\gamma\left(5\cos^2 i_c - 1\right) \\ & cp = \cos\left(\dot{\phi}(t-t_0)\right) \qquad sp = \sin\left(\dot{\phi}(t-t_0)\right) \\ & su = \sin\left(u-u_0\right) \qquad cu = \cos\left(u-u_0\right) \end{aligned} \tag{3.52}$$

The time evolution of the spacecraft relative dynamics, mainly depends on the characteristics of the reference absolute orbit (a_c, n_c, e_c, i_c). At the same time the effect of J_2 - expressed by the parameter γ - affects the relative eccentricity and inclination vectors components $\delta\boldsymbol{e}$ and $\delta\boldsymbol{i}$. It is also important to observe how the relative e/i vectors are decoupled in the relative dynamics, and the relative eccentricity vector rotates in its plane with the rate of $\dot{\phi}$, which depends only on quantities of the absolute orbit. The effect of the differential aerodynamics drag is present as a drift of the relative orbit, influencing the terms $a\delta\dot{a}, a\delta\dot{e}_x, a\delta\dot{e}_y$. The differential drag causes a linear variation in time of the relative semi–major axis, and at the same time a shift in the $\delta\lambda$. specifically, considering different mass and area properties of the satellites, the term $a\delta\lambda$ is a quadratic function of time. From the analysis in [75], the mean time variation of the in-plane elements are computed as:

$$\begin{aligned} a\delta\dot{a} &= 2/n\,C \\ a\delta\dot{e}_x &= 1/n\,A \\ a\delta\dot{e}_y &= 1/n\,B \end{aligned} \tag{3.53}$$

where the coefficients A, B, C depends on the effect of the differential drag. The perturbing acceleration due to the differential drag can be expressed in the local RTN frame as function of the difference of the ballistic coefficients of the chief and deputy:

$$\boldsymbol{d}_{dd} = \begin{pmatrix} 0 \\ -\frac{1}{2}\rho v^2 (BC_d - BC_c) \\ 0 \end{pmatrix} = \begin{pmatrix} 0 \\ A\cos nt + B\sin nt + C \\ 0 \end{pmatrix} \tag{3.54}$$

where BC_d and BC_c is the ballistic coefficient of the deputy and chief satellites, respectively. It is computed as $\frac{A_c C_D}{M}$, with A_c the cross section area, C_D the drag coefficient, and M the spacecraft mass.

Effect of perturbation on natural motion This paragraph presents the application of the model in Equation (3.51) to an helix formation of two spacecraft. The aim of this analysis is to evaluate the effect of the perturbing environment varying the physical characteristics of the vehicles. Moreover, the results of the model are compared with the high-fidelity propagation in the absolute frame (of Section 3.2). The scenario considers a two-spacecraft helix formation, with a separation of about $40\,\mathrm{km}$. To better assess the effect of the differential atmospheric drag, the reference orbit has been selected as a SSO with mean altitude of $500\,\mathrm{km}$, and an eccentricity of 0.0012. The initial condition for the mean ROEs of the formation were selected as:

$$a\delta\boldsymbol{\alpha}_{IC} = \{0.0151, \quad 0, \quad 0.12, \quad 40, \quad -0.10, \quad -35\}\ (\mathrm{m}) \tag{3.55}$$

Then, the following situations are analysed:

1. Both chief and deputy have the same physical properties: $BC_d = BC_c = 0.023\,\mathrm{m}^2\,\mathrm{kg}^{-1}$. This corresponds to platform of $130\,\mathrm{kg}$, a cross section area of $1\,\mathrm{m}^2$, and a drag coefficient of $C_D = 3$. Two analysis are performed in this case:
    - Propagation under the effect of the mean J_2 only, for both the high-fidelity model and Equation (3.51).
    - Propagation under the effect of the mean J_2 and differential drag, for both the high-fidelity model and Equation (3.51).
2. Chief and deputy have different physical properties. The propagation under the effect of the mean J_2 and differential drag, for both the high-fidelity model and Equation (3.51) is performed.
    - The chief is a large spacecraft, with mass $1150\,\mathrm{kg}$ and cross section area $6.5\,\mathrm{m}^2$: $BC_c = 0.0089\,\mathrm{m}^2\,\mathrm{kg}^{-1}$. The deputy is a smallsat with $BC_d = 0.023\,\mathrm{m}^2\,\mathrm{kg}^{-1}$ (as in case 1.).

- The chief is slightly larger than the deputy, with mass $230\,\mathrm{kg}$ and cross section area $2\,\mathrm{m}^2$: $BC_c = 0.026\,\mathrm{m}^2\,\mathrm{kg}^{-1}$. The deputy is a smallsat with $BC_d = 0.023\,\mathrm{m}^2\,\mathrm{kg}^{-1}$ (as in case 1.).

The results for the case 1. are depicted in Figure 3.8. The upper graph, Figure 3.8a shows the time evolution of ROEs elements under the effect of mean J_2 only. Three propagations are reported: *HF osculating* and *HF mean* are the osculating and mean evolution of the ROEs computed from the propagation of the absolute dynamics, with the models described in Section 3.2; *AVA mean* describes the time propagation of the mean ROEs, using the model of Equation (3.51). One can observe a good correspondence of the time evolution among the three different models. A small discrepancy is present in the $a\delta\lambda$ and in the δi_x components. Subsequently, the same case is tested including the differential drag when the ballistic coefficient of the vehicles are equivalent. In this case, given the short separation among the spacecraft (about $40\,\mathrm{m}$), the effect of the differential drag is almost negligible, as shown in Figure 3.8b. The most relevant effect in this case is still the mean J_2 perturbation, and the two plots in Figure 3.8. This behaviour is possible due to the following aspect: the two vehicles are at close distance ($40\,\mathrm{m}$ separation) and the difference in the semi-major axis is almost zero ($a\delta a = 0.0151\,\mathrm{m}$). Moreover, the equivalence of $BC_d = BC_c$ results in the same effect of the atmospheric drag on both vehicles, resulting in a null differential drag (see Equation (3.54)).

Passing now to the results for case 2., the situation with different ballistic coefficients for deputy and chief spacecraft is shown in Figure 3.9. In the first scenario, Figure 3.9a, significantly different physical properties are considered. In this example, the chief weights 10 more than the deputy, and, thus, also its cross sectional area is larger. Consequently, even if initially the difference in the semi-major axis is small ($a\delta a = 0.0151\,\mathrm{m}$), the difference in BC causes a different effect of the drag on the two vehicles. Following the relation in Equation (3.54), the differential effect is larger when the difference between the ballistic coefficient is higher. In this case, one can observe a shift in the along-track separation of about $a\delta\lambda = 3\,\mathrm{km}$ after 15 orbital periods. A more significant effect is also present in the other components of the ROEs: the relative semi-major axis is subject to a variation in the order of -40 m, at the same time the relative eccentricity and inclination vector are subject to a variation.

The most important consideration is that the analytical model of Equation (3.51) do not correctly estimate the variation in the x component of both the relative eccentricity and inclination vectors. This is mainly due to the different drag model used in the analytical and in the high-fidelity propagation. Similar results are obtained when a smaller difference is present in the ballistic coefficients of the spacecraft. Figure 3.9b shows the results for the case of $BC_c = 0.026\,\mathrm{m}^2\,\mathrm{kg}^{-1}$ and $BC_d = 0.023\,\mathrm{m}^2\,\mathrm{kg}^{-1}$. As expected, the effect of the differential drag is smaller, as the difference in the ballistic coefficient is lower. Also in this case the analytical model do not accurate predict the evolution of the x-component of both relative eccentricity and inclination vectors. An important observation is on the variation of the along track coordinate, about $600\,\mathrm{m}$, which is significantly lower than the case in Figure 3.9a.

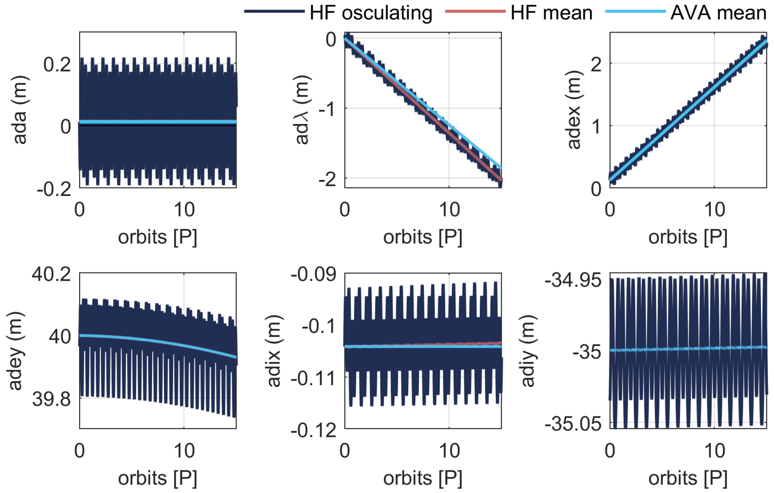

(a) *Time propagation under mean J_2 only perturbation.*

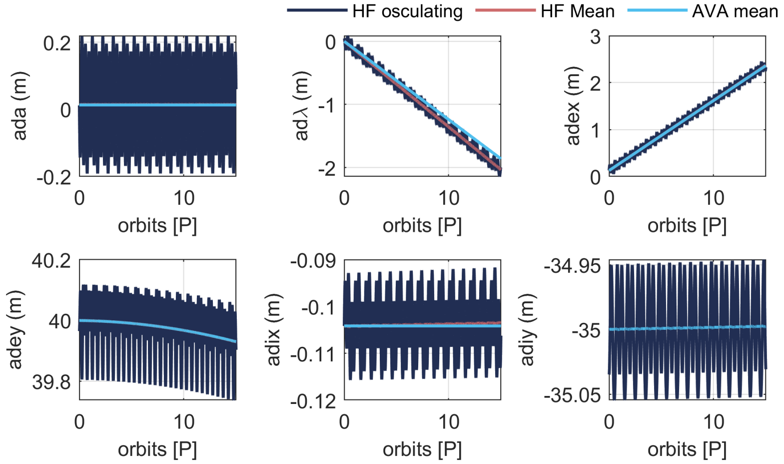

(b) *Time propagation under mean J_2 and differential drag with $BC_d = BC_c = 0.023\,\mathrm{m}^2\,\mathrm{kg}^{-1}$.*

Figure 3.8: *Comparison of time propagation of helix-shaped formation under J_2 and J_2+differential drag perturbed dynamics in ROEs framework with same physical properties of chief and deputy.*

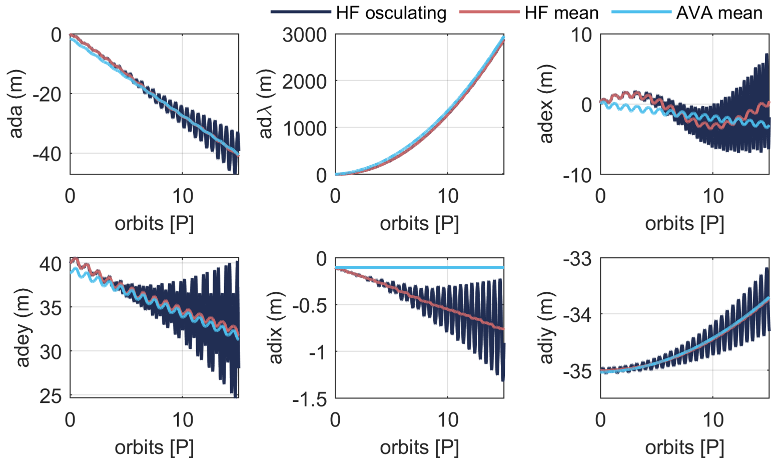

(a) *Time propagation under mean J_2 and differential drag with $BC_c = 0.0089\,\mathrm{m}^2\,\mathrm{kg}^{-1}$ and $BC_d = 0.023\,\mathrm{m}^2\,\mathrm{kg}^{-1}$.*

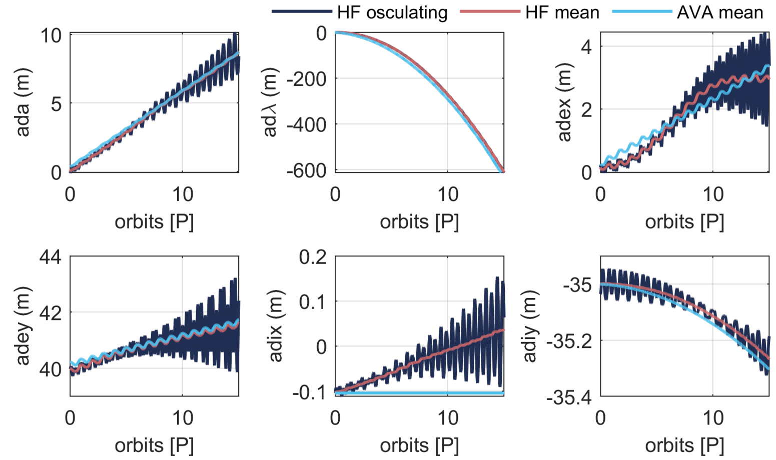

(b) *Time propagation under mean J_2 and differential drag with $BC_c = 0.026\,\mathrm{m}^2\,\mathrm{kg}^{-1}$ and $BC_d = 0.023\,\mathrm{m}^2\,\mathrm{kg}^{-1}$.*

Figure 3.9: *Comparison of time propagation of helix-shaped formation under J_2+ differential drag perturbed dynamics in ROEs framework with different physical properties of chief and deputy.*

As a final consideration, it is important to specify how the test cases analysed in this thesis are more similar to the one in Figure 3.8b, when ballistic coefficient are almost the same. Specifically, for the passive interferometer cases, the platform are designed to have same mass and dimensions. Combining this aspect with the short separation among the spacecraft (10 to $20\,\mathrm{m}$), the effect of the differential drag is significantly smaller than the Earth's oblateness perturbation. Nonetheless, the differential drag effect is included in most of the simulations, for a more accurate representation of the orbital environment.

3.4.3 STM with full gravitational harmonics

A different model is introduced to include the effect of higher order gravitational harmonics in the STM. The model is based on the work and derivation in [78], that derives a state transition matrix for the relative motion in mean elements. Considering the state vector as the ROEs vector $\delta\boldsymbol{\alpha}$, the state at a generic time t is defined by:

$$\delta\boldsymbol{\alpha}(t) = \boldsymbol{\Phi}(\boldsymbol{\alpha}_0, \Delta t)\delta\boldsymbol{\alpha}(0) \tag{3.56}$$

Where $\boldsymbol{\alpha}_0$ is the vector of the initial mean absolute Keplerian elements of the chief satellite, and $\Delta t = t - t_0$, being t_0 the initial time. The STM is defined as [78, 115]:

$$\Phi(\bar{\boldsymbol{\alpha}}_0, \Delta t) =$$
$$\begin{bmatrix} 1 & 0 & 0 & 0 & 0 & 0 \\ a\Delta t \sum_p g_a^{(p)} & 1 & \Delta t \sum_p g_{e_x}^{(p)} & \Delta t \sum_p g_{e_y}^{(p)} & \Delta t \sum_p g_i^{(p)} & 0 \\ a\Delta t A_1 \sum_p \dot{\omega}_a^{(p)} & 0 & C + \Delta t A_1 \sum_p \dot{\omega}_{e_x}^{(p)} & -S + \Delta t A_1 \sum_p \dot{\omega}_{e_y}^{(p)} & \Delta t A_1 \sum_p \dot{\omega}_i^{(p)} & 0 \\ a\Delta t A_2 \sum_p \dot{\omega}_a^{(p)} & 0 & S + \Delta t A_2 \sum_p \dot{\omega}_{e_x}^{(p)} & C + \Delta t A_2 \sum_p \dot{\omega}_{e_y}^{(p)} & \Delta t A_2 \sum_p \dot{\omega}_i^{(p)} & 0 \\ 0 & 0 & 0 & 0 & 1 & 0 \\ a \sin i \Delta t \sum_p \dot{\Omega}_a^{(p)} & 0 & \sin i \Delta t \sum_p \dot{\Omega}_{e_x}^{(p)} & \sin i \Delta t \sum_p \dot{\Omega}_{e_y}^{(p)} & \sin i \Delta t \sum_p \dot{\Omega}_i^{(p)} & 1 \end{bmatrix} \tag{3.57}$$

Where p is the index of the zonal harmonics' contribution of the set J_0, J_2, J_2^2, J_4, J_6. The notation $\bullet_x^{(p)}$ denotes the partial derivative of the quantity $\bullet$ generated by the $J\{p\}$ contribution with respect to the x quantity. Moreover, the following quantities are considered:

$$\begin{aligned} S &= \sin\left(\textstyle\sum_p \dot{\omega}^{(p)}\Delta t\right) & C &= \cos\left(\textstyle\sum_p \dot{\omega}^{(p)}\Delta t\right) \\ A_1 &= -(S e_{x0} + C e_{y0}) & A_2 &= (C e_{x0} - S e_{y0}) \\ g &= \dot{\omega} + \dot{M} + \dot{\Omega}\cos(i) \end{aligned} \tag{3.58}$$

Where $\dot{\omega}$ and $\dot{\Omega}$ are the time derivatives of the argument of perigee and the right ascension of the ascending node. The state transition matrix $\Phi(\bar{\boldsymbol{\alpha}}_0, \Delta t)$ can be used to express the relative motion with whatever order of the zonal harmonics' geopotential, and it is valid for a generic eccentric reference orbit, without any further approximation. The STM in Equation (3.57) represents the first-order approximation of the state transition tensor. As discussed in [78], this provides a good approximation of the relative motion when the separation distance is not too large (> $10\,\mathrm{km}$). In this work, we consider for the passive interferometry application a separation distance in the order of few tens of meter, remaining well below that threshold. For cases with large separation, instead, a second order approximation of the STM is required to guarantee a correct approximation of the relative motion.

Effect of higher order gravitational harmonics This paragraph presents the effects of higher order terms of the aspherical gravitational perturbation. The same scenario of the test case 1. of Figure 3.8 is considered. For the case of same ballistic coefficient for deputy and chief spacecraft, the drag effect can be neglected. The results of the analyses are reported in Figure 3.10, where we compare the following models propagating for 5 days (about 75 orbital periods):

- High-fidelity model from the absolute propagation of Section 3.2, considering the gravitational model up to degree and order 6 × 6. Both osculating and mean effects are studied: *HF Osc J2-J6* and *HF Mean J2-J6*.
- STM in ROEs considering only the J_2 effect, of Equation (3.51): *mean J2*.
- Higher order model in ROEs up to degree and order 6 × 6 of Equation (3.57): *mean J2-J6*.

One can observe that the mean effect of higher order terms is similar to the one with only J_2. Consequently, the major contribution to the perturbed relative motion is given by the mean J_2 effect. This is a quite important consideration for the work developed in this thesis. For the development of the guidance and control techniques, the models used to implement the relative motion only considers the effects of J_2 and differential drag. Furthermore, for most of the test cases, the ballistic coefficients of the spacecraft in the formation (e.g. FFLAS and TriHex), the differential drag has a negligible influence on the relative motion. Higher order terms of the gravitational perturbation have only been considered in the GNC analyses of Chapter 7, to better model the orbital environment during the study of different mission operations.

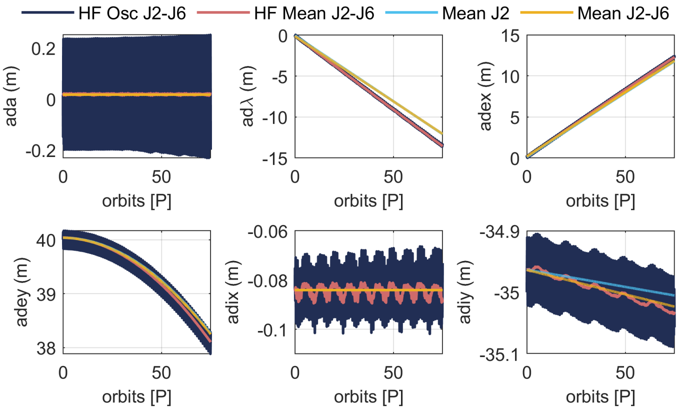

Figure 3.10: *Time propagation of helix-shaped formation with J_2 to J_6 terms of gravitational perturbation in ROEs.*

CHAPTER 4

Relative Guidance and Control

No great discovery was ever made without a bold guess.

— Isaac Newton

MODELLING algorithms and techniques for relative guidance and control is essential to support the design of formation flying mission concept. Specifically, for the case under analysis in this thesis, the accurate control of formation geometry and manoeuvre assessment is critical due to the short separation among the spacecraft for the passive interferometry application (i.e., in the order of few tens of meters). The aim of this chapter is to provide a computationally light and accurate control technique in both open- and closed-loop that could be implemented on-board the platform for autonomous operations in orbit. This aspect is of primary importance for future space application, due to the limited availability of ground support and the need of prompt response to non-nominal situations, as failures and collision avoidance procedure.

The chapter is organised in three main parts, and the control technique is based on a continuous thrust approach. First, the methodologies for open-loop control are proposed. After an initial description of formation maintenance for two different operational scenarios, driven by the payload functioning. An optimal control problem is developed to support formation reconfiguration phases. This is based on convex optimisation and is able to deal with the most relevant constraints for the application in study, namely: collision avoidance and thrust limitation. Differently from previous works [57, 87, 91], the methodology is based on the dynamical description of the relative motion in ROEs framework, paving the way to the exploitation of the developed algorithms beyond the scenario of microwave interferometry. For what regards the dissemination, this part of the work has been successfully published in two journal papers, [113, 115]. Note that a decentralised architecture has been selected to improve the efficiency of the algorithms as well as to reduce the computational time to solve it. The second part of the chapter presents the closed-loop strategies developed to feedback the control error taking also into account external uncertainties. Initially an adaptive Linear Quadratic Regulator (LQR) algorithm is designed to track the (previously computed optimal) open-loop trajectory. Its behaviour has been tested over several phases foreseen in the operations: from formation maintenance to formation reconfiguration. Then, the impact of uncertainties on the initial condition of the relative motion is investigated. A Monte Carlo (MC) analysis is presented for one case scenario, to assess the robustness of the adopted control techniques.

The third and last part of the chapter focuses on a Model Predictive Control (MPC) algorithm, that is developed to perform fuel-optimal formation reconfigurations. Differently from previous works [91], the MPC presented in this thesis is based the optimal convex problem developed for the open-loop algorithm in ROEs framework, including in the relative dynamics the mean J_2 perturbation. As a result, this algorithm provides real-time collision free trajectory for formation reconfiguration.

4.1 Open-loop strategy

This section describes models and methodologies employed to design the low thrust open-loop trajectories for formation keeping and formation reconfiguration.

As for formation keeping, two application scenarios have been targeted: the maintenance of a close rigid formation (see Chapters 2 and 3) and the maintenance of the GCO natural solution of the unperturbed linearised motion (see Chapter 3). In the first case, the nominal control acceleration values are computed from the forced dynamics of the HCW equations, since the rigid formation is conveniently described in terms of the Cartesian relative state. In the second application, the nominal control profile is computed for the natural closed-form solutions of the linearised unperturbed relative motion. In both cases, the computed nominal accelerations serve as (open-loop) reference control command to perform trajectory tracking (i.e., formation keeping). The control loop is then closed using LQR feedback techniques.

As for formation reconfiguration, an optimal convex problem based on relative dynamics in ROEs is developed. The analysis foresees the transformation of the classical optimal control problem into a convex formulation. The convexification of the problem grants the existence of a unique solution of the problem, and it does not require several iterations to converge to the optimal solution [91]. An approach, relying on convex formulation, has already been discussed in previous studies for relative motion manoeuvre [89, 91, 103]. With respect to such works, the algorithm here developed proposes a novel description in the ROEs framework and at the same time deals with the design of different phases of the mission, including specific constraints for collision avoidance and thrust level. Specifically, first the algorithm has been developed in the RTN frame to tackle the formation establishment problem after the satellites in-orbit injection by the launcher, and it has been presented in a conference proceedings [114]. Subsequently, the it has been extended to the ROEs framework, where the discretisation and convexification procedure were applied to the Optimal Control Problem (OCP). This model has been presented in two journal publications [113, 115] and it employs the algorithm to design the optimal guidance for close formations. The collision-avoidance constraint becomes fundamental for the application under analysis, as spacecraft are few meters apart. On the contrary, previous works have dealt with spacecraft separation in the order of kilometre range, making less critical the collision risk. The nature of the convex representation allows a simple immediate discretisation of the system dynamics, including the effect of the control action. As described in [91], the reduced computational effort required by this approach makes it suitable for an implementation on-board the satellites, which have reduced computational capability. The solution of the convex optimisation problem provides the thrust level for the guidance of the optimal reconfiguration manoeuvre of the spacecraft. Within this framework, a reconfiguration manoeuvres can be the solution of a global time-optimal or a fuel-optimal problem.

As for what this dissertation concerns, a fixed end-time is assumed and the reconfiguration minimises the propellant consumption. Such choice is driven by, the fact that, on the one hand, space operations are eased in the presence of well defined timing of the activities. On the other hand, for microwave passive interferometry the minimisation of the masses of the spacecraft is of primary importance (see Section 2.3). Afterwards, the fuel-optimal problem is cast into a convex form, requiring the discretisation of the entire control problem, cost function and constraints acting on the system.

4.1.1 Analytical forced motion

This section describes an analytical procedure to compute the reference control required to perform relative motion keeping. The first case analysed considers the unperturbed HCW equations and the acceleration terms required to maintain the initial condition of the formation to keep it rigid. As such this situation corresponds to a pure forced motion, where the engines provides a control to counteract the natural dynamics of the relative motion. This approach allows assessing the magnitude of the control accelerations required to keep a rigid and fixed formation as needed to perform passive interferometry (see Section 2.4.3). The second case, instead, presents a control profile to perform formation maintenance of the closed-form natural solution of the relative motion under the presence of the mean J_2 perturbation.

Control matrix in ROEs

To include a control term in the relative motion, a control matrix is defined in the system dynamics. As introduced in Chapter 3, the linearised equation of the relative motion can be written as:

$$\delta\dot{\boldsymbol{\alpha}}(t) = \boldsymbol{A}\delta\boldsymbol{\alpha}(t) + \boldsymbol{B}(t)\boldsymbol{u}(t) \tag{4.1}$$

Where $\boldsymbol{A}$ and $\boldsymbol{B}(t)$ are the plant and input control matrices, respectively, while the term $\boldsymbol{u}$ is the control variable in RTN frame, including the components of the acceleration in the three directions. Section 3.3 (i.e., unperturbed motion) is computed from the plant matrix through the expression $\Phi(t, t0) = I + A(t - t0)$. The STM of the perturbed motion of Section 3.4.2 has been computed by integrating the plant matrix obtained with a first-order Taylor expansion of the time derivatives of the mean OEs of the reference orbit [76–78]. Whereas the STM of Section 3.4.3 has been obtained directly expanding the perturbed mean orbital elements of the chief's orbit. Under the assumptions of quasi-circular orbit of the chief, the control matrix $\boldsymbol{B}(t)$ is obtained from Equation (3.35), using the definition of the ROEs components. Its expression is given by:

$$\boldsymbol{B}(t) = \frac{1}{na}\begin{bmatrix} 0 & 2 & 0 \\ -2 & 0 & 0 \\ \sin u & 2\cos u & 0 \\ -\cos u & 2\sin u & 0 \\ 0 & 0 & \cos u \\ 0 & 0 & \sin u \end{bmatrix} \tag{4.2}$$

To derive the corresponding control matrix to be included in the linear dynamics model of the analytical solution in ROEs (of Section 3.4), the convolution matrix $\hat{\boldsymbol{B}}(t, t_0)$ is computed. Following the linear dynamics system theory [115, 140], and assuming a constant control over the time step $[t_0, t]$, the matrix $\hat{\boldsymbol{B}}(t, t_0)$ is:

$$\hat{\boldsymbol{B}}(t, t_0) = \int_{t_0}^{t} \boldsymbol{\Phi}(t, \tau)\boldsymbol{B}(\tau) d\tau, \tag{4.3}$$

and the corresponding linear system becomes:

$$\delta\boldsymbol{\alpha}(t) = \boldsymbol{\Phi}(t, t_0)\delta\boldsymbol{\alpha}(t_0) + \hat{\boldsymbol{B}}(t, t_0)\boldsymbol{u}(t) \tag{4.4}$$

Depending on the selected dynamical model, the matrix $\hat{\boldsymbol{B}}(t, t_0)$ has different expression.

Control matrix in RTN

A similar approach can be used when the dynamics is parametrised by the relative Cartesian state in the RTN frame. In this case the linearised equations of motion have the following expression:

$$\dot{\boldsymbol{x}}(t) = \boldsymbol{A_{rtn}}\boldsymbol{x}(t) + \boldsymbol{B}_{rtn}\boldsymbol{u}(t) \tag{4.5}$$

Where $\boldsymbol{A}_{rtn}$ and $\boldsymbol{B}_{rtn}$ are the plant and control matrices of the linear time invariant system, respectively, while the term $\boldsymbol{u}(t)$ is the control variable in RTN frame. The expression of the control matrix is trivially given by, since it provides control acceleration in the three direction of the local orbital frame:

$$\boldsymbol{B}_{rtn} = \begin{bmatrix} 0 & 0 & 0 & 1 & 0 & 0 \\ 0 & 0 & 0 & 0 & 1 & 0 \\ 0 & 0 & 0 & 0 & 0 & 1 \end{bmatrix}'. \tag{4.6}$$

Close and rigid formation keeping

Starting from the linear description of the relative motion in the local orbital frame (see Section 3.3), the control acceleration can be included in the dynamics, as in Equation (4.5). Considering as acceleration components the vector $\boldsymbol{u} = [u_x,\ u_y,\ u_z]$ in the RTN frame, the HCW equations in Equation (3.29) becomes:

$$\begin{cases} \ddot{x} - 3n^2x - 2n\dot{y} = u_x \\ \ddot{y} + 2n\dot{x} = u_y \\ \ddot{z} + n^2z = u_z \end{cases} \tag{4.7}$$

By assuming that the control acceleration components are constant in time. Equation (4.7) can be integrated in closed form and its general solution of is:

$$\begin{cases} x(t) = \frac{-\cos u(u_x+n(3nx_0+2\dot{y}_0))+u_x+2n(u_yt+2nx_0+\dot{y}_0)+(n\dot{x}_0-2u_y)\sin u}{n^2} \\ y(t) = \frac{-2n(2u_xt+n(6ux_0+3t\dot{y}_0-y_0)+2\dot{x}_0)+4\sin u(u_x+n(3nx_0+2\dot{y}_0))+u_y\left(8-3n^2t^2\right)+(4n\dot{x}_0-8u_y)\cos u}{2n^2} \\ z(t) = \frac{-u_z\cos u+u_z+n^2z_0\cos u+n\dot{z}_0\sin u}{n^2} \end{cases} \tag{4.8}$$

Where $[x_0,\, y_0,\, z_0,\, \dot{x}_0,\, \dot{y}_0,\, \dot{z}_0]$ are the initial conditions of the relative state. Solving Equation (4.8) in terms of control components results in:

$$\begin{cases} u_x = & \frac{-n^2\left(15n^2t^2x_0+6nt^2\dot{y}_0+8t\dot{x}_0+48x_0\right)+n\cos u\left(n\left(x_0\left(48-9u^2\right)-6nt^2\dot{y}_0+8t\dot{x}_0\right)+32\dot{y}_0\right)}{5u^2+(3u^2-16)\cos u-16u\sin u+16} \\ & \frac{nu\sin u(3u\dot{x}_0+48nx_0+28\dot{y}_0)-32n\dot{y}_0}{5u^2+(3u^2-16)\cos u-16u\sin u+16} \\ u_y = & \frac{2n((\cos u-1)(u\dot{y}_0-4\dot{x}_0)-2u\dot{x}_0\sin u)}{5u^2+(3u^2-16)\cos u-16u\sin u+16} \\ u_z = & n^2 z_0 \end{cases} \tag{4.9}$$

where the rigid formation conditions of $x(t) = x_0$, $y(t) = y_0$, and $z(t) = z_0$ have been imposed. To compute the effort of the control to keep the initial condition of the formation, we evaluate Equation (4.8) over one orbital period. This corresponds to an averaging procedure over one revolution of the relative state $\boldsymbol{x} = \{x,\, y,\, z\}$:

$$\bar{\boldsymbol{x}} = \frac{n}{2\pi}\int_0^{\frac{2\pi}{n}} \boldsymbol{x} \tag{4.10}$$

With this procedure and imposing $x(t) = x_0$, $y(t) = y_0$, and $z(t) = z_0$, we obtain the following control effort over one orbital period:

$$\begin{cases} u_x = -\frac{n\left(3\pi^2nx_0+6nx_0+2\pi\dot{x}_0+\pi^2\dot{y}_0+4\dot{y}_0\right)}{2+\pi^2} \\ u_y = -\frac{\pi n\dot{y}_0-2n\dot{x}_0}{2(2+\pi^2)} \\ u_z = n^2 z_0 \end{cases} \tag{4.11}$$

The magnitude of the control accelerations depends on the initial conditions in relative position and velocity. Moreover, thanks to the uncoupled dynamics of the in-plane and out-of-plane motion, the C_z component only depends from the coordinate in the normal direction. Evaluating the control effort to keep a rigid formation is essential for the test case under analysis of passive interferometry. In fact, for this situation, the geometry of the formation should be maintained rigid and fixed. As an example, for the FFLAS study, a continuous forced motion is implemented to perform formation maintenance (see Chapter 7 for the results of the analysis), and the control acceleration components of Equation (4.9) is used to provide the reference control law to the closed-loop framework for trajectory tracking.

General Circular Orbit formation keeping

In this work, the relative motion can be described by the system $\dot{\boldsymbol{x}} = f(\boldsymbol{x}, \boldsymbol{u})$, with $\boldsymbol{x}$ the relative state of the satellite in terms of position and velocity, and $\boldsymbol{u}$ the control action. From the analysis in Section 3.3, a set of feasible trajectories is identified as $(\boldsymbol{x}_d, \boldsymbol{u}_d)$. For the GCO case, the desired trajectory $\boldsymbol{x}_d$ is defined by combining in Equation (3.45) with the corresponding parameters to tune the initial conditions in Equation (3.46). In previous literature works as [33, 83], a feasible control term $\boldsymbol{u}_d$ is identified to counteract the mean J_2 induced acceleration for the GCO case. The control components in the RTN frame are [83]:

$$\begin{aligned} &u_{x_d} \approx 0, \\ &u_{y_d} \approx -0.5\rho_x\, n(\dot{\omega} + \dot{\alpha_x})\cos\left(u + \alpha_x + (\dot{u} + \dot{\alpha}_x)\, t\right), \\ &u_{z_d} \approx -2\, n\, \dot{\alpha}_x\, \rho_z \sin\left(u + \alpha_x + (\dot{u} + \dot{\alpha}_x)\, t\right) + 2\, \rho\, k\, n\, \sin^2 i_c \cos\alpha_x \sin u. \end{aligned} \tag{4.12}$$

Where α_x and u are the phase angle and the argument of latitude respectively, and $\dot{\alpha}_x$ and $\dot{u}$ are their variation in time due to the J_2 effect [33]:

$$\begin{aligned}\dot{\alpha}_x &= \tfrac{1}{17}(8\,k\sin^2 i_c - \dot{\omega})\\ \dot{u} &= n - n\,J_2\tfrac{3\,R_e^2}{4\,a_c^2\eta^4}(\eta(1-3\cos^2 i_c) + (1-\cos^2 i_c)).\end{aligned} \tag{4.13}$$

Where $\eta = \sqrt{1-e_c^2}$, and the parameter $k = -1.5\,n\,J_2\left(\frac{R_e}{a_c}\right)^2$ introduces the dependence on the Earth's oblateness term.

4.1.2 Convex Optimal Problem for formation reconfiguration

This section deals with the computation of the open-loop guidance for the formation reconfiguration. Starting from the classical definition of Optimal Control Problem (OCP), the discretisation procedure is the first step to write an optimal control problem in a convex form. A Convex Optimal Control Problem (COCP) can be efficiently solved with different methods, such as the interior-point methods [141]. Thanks to the sparsity of the matrices involved, it is typically very time efficient and can handle large problems up to thousands of variables and constraints. The most challenging part to deal with the convex formulation is the transformation of the OCP into a convex form. Three main requirements are posed for a convex problem: both the objective and the inequality constraint functions must be convex, and the equality constraints must be affine [141]. The main advantage of a COCP is the equivalence among local and global optimal points.

Optimal Control Problem.

The fuel-optimal reconfiguration manoeuvre can be defined under the classical OCP formalism. The control system is described by an ordinary differential equation for the j-th satellite in the formation. The notation in both RTN and ROEs is provided in the following analysis:

$$\begin{aligned}\dot{\mathbf{x}}_j(t) &= f\left(t, \mathbf{x}_j, \mathbf{u}\right) = \mathbf{A}_{rtn_j}\mathbf{x}_j(t) + \mathbf{B}_{rtn_j}\mathbf{u}_j(t)\\ \delta\dot{\boldsymbol{\alpha}}_j(t) &= f\left(t, \delta\boldsymbol{\alpha}_j, \mathbf{u}\right) = \mathbf{A}_j\delta\boldsymbol{\alpha}_j(t) + \mathbf{B}_j\mathbf{u}_j(t)\end{aligned} \tag{4.14}$$

where $\mathbf{u}_j = \left\{u_{x_j},\, u_{y_j},\, u_{z_j}\right\}^T$ is the control input vector , and t is the time. The matrices $\mathbf{A}$ and $\mathbf{A}_{rtn}$ represents the natural relative motion under the influence of external perturbations, and $\mathbf{B}$ and $\mathbf{B}_{rtn}$ are the control input matrices. The time dependency in $\mathbf{A}$ and $\mathbf{A}_{rtn}$ is due to the effect of orbital perturbations. The matrix $\mathbf{A}_{rtn}$ is taken from Section 3.4.1 for the description in relative Cartesian coordinates; while $\mathbf{A}$ from Section 3.4.2 for the description in ROEs. The low thrust control is introduced in the dynamical system as a continuous effect on the natural dynamics. The matrix $\mathbf{B}$ relates the control term to the acceleration components in the system dynamics. The objective of the analysis is to find the optimal control input $\mathbf{u}(t)$, such that the performance index, or cost function, is minimised. The performance index for this fuel-optimal control problem is defined for each j-th satellite as following:

$$J = \int_t \left\|\mathbf{u}_j(t)\right\|_1 dt \tag{4.15}$$

The 1-norm is used in the cost function to minimise the sum of the magnitude of the control components in the RTN directions, to properly account for the three directional manoeuvring capability of the spacecraft. This corresponds to the minimisation of the propellant mass for the manoeuvre; the control effort is related to the propellant mass via the spacecraft wet mass and the engine thrust level: $\mathbf{T}_j = m_{s/c_j} \cdot \mathbf{u}_j$, where m_{s/c_j} is the mass of the j-th spacecraft. The initial and final conditions of the dynamic system in Equation (4.14) influence the dynamics with the following relations:

$$\text{RTN}: \begin{cases} \mathbf{x}_j(t_0) = \mathbf{x}_{0,j} \\ \\ \mathbf{x}_j(t_f) = \mathbf{x}_{f,j} \end{cases} \qquad \text{ROEs}: \begin{cases} \delta\boldsymbol{\alpha}_j(t_0) = \delta\boldsymbol{\alpha}_{0,j} \\ \\ \delta\boldsymbol{\alpha}_j(t_f) = \delta\boldsymbol{\alpha}_{f,j} \end{cases} \tag{4.16}$$

where $\bullet_{0,j}$ is the initial state of the $j-th$ satellite and $\bullet_{f,j}$ is the final (or boundary) condition. Finally, the problem is subject to some constraints on the collision avoidance and the maximum available thrust. Thus, at any time instant, the maximum thrust limitation translates into a limitation in the maximum acceleration possible $T_{max} = m_{s/c_j} \cdot \mathbf{a}_{max_j}$. The collision avoidance constraint is expressed in terms of minimum distance between the j-th and i-th satellites to guarantee a safe flight.

$$\text{RTN}: \begin{cases} \|\mathbf{u}_j(t)\| \leq \mathbf{a}_{\mathbf{max}j} \\ \\ \|\mathbf{C}\left(\mathbf{x}_j(t) - \mathbf{x}_i(t)\right)\|_2 \geq d_{thr} \end{cases} \qquad \text{ROEs}: \begin{cases} \|\mathbf{u}_j(t)\| \leq \mathbf{a}_{\mathbf{max}j} \\ \\ \|\mathbf{D}(t)\delta\boldsymbol{\alpha}_j(t) - \mathbf{D}(t)\delta\boldsymbol{\alpha}_i(t)\|_2 \geq d_{thr} \end{cases} \tag{4.17}$$

where $\mathbf{a}_{\mathbf{max}j}$ is the maximum acceleration that the thruster can provide, $\mathbf{C} = [\mathbf{I}_{3\times3} \quad \mathbf{0}_{3\times3}]$ is the matrix to retain only the position components in the state vectors $\mathbf{x}_j(t)$ and $\mathbf{x}_i(t)$, and d_{thr} is the minimum safe distance to avoid inter-satellite collision. The matrix $\mathbf{D}(t)$ corresponds to the first three rows of the relations in Equation (3.37), which provides the first-order mapping of $\delta\boldsymbol{\alpha}(t)$ in the Cartesian relative position of the satellite w.r.t. the virtual point of the formation.

Control system in Convex form.

The first step to convert an OCP in classical form into a convex formulation is the discretisation of both the objective and the constraint functions.

Discretization procedure. The approach followed for discretising the system is based on the Laplace transformation of the state equations [142]. The time is divided into K finite time instants, each representing the sample interval for the state $\mathbf{x}$ and the update interval for the control term $\mathbf{u}$. Moreover, the zero-order-hold approach is considered, with the control term piecewise constant in each time instant k [91]. For the procedure, we consider:

- Time discretization: $k = 1, ..., K$ (where $t_{k=1} = t_0$ and $t_{k=K} = t_f$)
- Time interval: $\Delta t = t_{k+1} - t_k$
- Total time: $T = (K-1)\Delta t$
- Number of satellites in the formation: $j = 1, ..., N$

The discretization of Equation (4.14) requires the solution of the non-homogeneous system, via the Laplace transformation. This procedure leads to an expression that includes the convolution integral for the control effort [88]. Starting from the dynamical representation in RTN, the following relation is obtained:

$$\mathbf{x}_j[k+1] = e^{\mathbf{A}_{rtn}\Delta t}\,\mathbf{x}_j[k] + \int_0^{\Delta t} e^{\mathbf{A}_{rtn}\tau} d\tau\,\mathbf{B}_{rtn}\,\mathbf{u}_j[k] \tag{4.18}$$

Where $e^{\mathbf{A}_{rtn}\Delta t}$ represents the state transition matrix $\mathbf{\Phi}_{rtn}$, and the second term $\int_0^{\Delta t} e^{\mathbf{A}_{rtn}\tau} d\tau\, \mathbf{B}_{rtn}$ is the convolution matrix $\hat{\mathbf{B}}_{rtn}$. Note that the assumption of $\mathbf{A}_{rtn}$ time invariant over the k-th interval is introduced. The approximation is acceptable, since the effects produced by the orbital perturbations over Δt is negligible. The term $e^{\mathbf{A}_{rtn}\Delta t}$ can be expanded in series as up to the second term: $\mathbf{I} + \mathbf{A}\Delta t + \mathbf{A}^2\Delta t^2$. For nil-potent matrices of order 2, as for the plant matrix in ROEs, the second order term ($\mathbf{A}^2$) is zero, and the approximation $\mathbf{\Phi}_{rtn} = \mathbf{I} + \mathbf{A}_{rtn}\Delta t$ is valid. On the other hand, the $\mathbf{A}_{rtn}$ do not have the nil-potent property. However, for the case under analysis, the first order truncation has been considered under the assumption of small time step Δt. In this specific case, the truncation provides accurate results as the time step is much lower than the typical frequencies of the orbital dynamics. The following expression is obtained for each j-th satellite:

$$\mathbf{x}_j[k+1] = (\mathbf{I} + \mathbf{A}_{rtn}\Delta t)\; \mathbf{x}_j[k] + \hat{\mathbf{B}}_{rtn}\, \mathbf{u}_j[k] = \mathbf{\Phi}_{rtn}\, \mathbf{x}_j[k] + \hat{\mathbf{B}}_{rtn}\, \mathbf{u}_j[k] \tag{4.19}$$

Note that the matrix $\mathbf{A}_{rtn}$ represents the plant matrix of the linearised relative motion parametrised in Cartesian coordinates. Similarly, for the ROEs representation, the dynamic system can be written in a discrete form, introducing the STM $\mathbf{\Phi}$ and the convolution matrix for the control term $\hat{\boldsymbol{B}}$ (see Equation (4.4)):

$$\delta\boldsymbol{\alpha}_j[k+1] = \mathbf{\Phi}\, \delta\boldsymbol{\alpha}_j[k] + \hat{\mathbf{B}}\, \mathbf{u}_j[k] \tag{4.20}$$

In this representation $\mathbf{\Phi}$ is the STM, and, if the time step is sufficiently small (Δt), it is equivalent to the expression $\mathbf{I} + \mathbf{A}\Delta t$. The STM for this description has been selected from Equation (3.50), when only the J_2 perturbation is included. Similarly, for the description in RTN, the plat matrix of Equation (3.48) is adopted, considering only the J_2 perturbing effect.

The description in relative orbital elements is included to get an easier convergence of the optimisation: the matrices in Equation (4.20) are highly sparse compared to the representation in Cartesian coordinates, improving the convergence time of the algorithm. For the case of satellite separation below 1 km, the linear mapping between RTN and ROEs (see Equation (3.38)) is accurate enough to provide a precise description of the relative motion. This case could be applied to the nominal operations required by a passive microwave formation, with vehicle's separation in the order of few tens of meters. On the other hand, for different mission scenarios (e.g. distributed SAR), the inter-satellite distance could be larger than 1 km. For this case, the linear mapping in Equation (3.38) is not accurate enough to provide a precise description of the motion. For this case, the relative elements $\delta\boldsymbol{\alpha}$ are used to compute the absolute elements of the deputies spacecraft $\boldsymbol{\alpha}_j$ based on the information of absolute chief elements $\boldsymbol{\alpha}_c$. Once know the absolute elements, the absolute states of the satellites are computed, and the relative Cartesian state is recovered from differencing these latter.

The objective function (or cost function) described in Equation (4.15) is dicretised thanks to the piecewise constant control property in each time interval:

$$J = \sum_{1}^{K} \|\mathbf{u}_j[k]\|_1 \tag{4.21}$$

where $j = 1, ..., N$ and the 1-norm is used again for an optimal solution with minimum fuel consumption.

The initial and final conditions of the system dynamics can be described as:

$$\text{RTN}: \begin{cases} \mathbf{x}_j[k=1] = \mathbf{x}_{0,j} \\ \mathbf{x}_j[k=K] = \mathbf{x}_{f,j} \end{cases} \qquad \text{ROEs}: \begin{cases} \delta\boldsymbol{\alpha}_j[k=1] = \delta\boldsymbol{\alpha}_{0,j} \\ \delta\boldsymbol{\alpha}_j[k=K] = \delta\boldsymbol{\alpha}_{f,j} \end{cases} \tag{4.22}$$

where the relation is valid for each satellite in the formation with $j = 1, ..., N$.
The maximum thrust limitation constraint in Equation (4.17) can be discretised as following:

$$\|\mathbf{u}_j[k]\| \leq a_{max_j} \tag{4.23}$$

where $j = 1, ..., N$ and the maximum bound is imposed so that at each time interval, the acceleration provided by the thrusters is bounded by the engine technological limit.
The minimum allowable distance between the j-th an i-th satellites (with $j \neq i$) requires a mode detailed discussion. First, the expression in Equation (4.17) is discretised as follows:

$$\begin{aligned} \text{RTN} : \left\|\mathbf{C}\left(\mathbf{x}_j[k] - \mathbf{x}_i[k]\right)\right\|_2 \geq d_{thr} \\ \text{ROEs} : \left\|\mathbf{D}[k]\delta\boldsymbol{\alpha}_j[k] - \mathbf{D}[k]\delta\boldsymbol{\alpha}_i[k]\right\|_2 \geq d_{thr} \end{aligned} \tag{4.24}$$

where $j = 1, ..., N-1$ and $i \neq j$. To guarantee that the collision avoidance constraint is satisfied on $(t_k,\, t_{k+1})\,\forall k$, and to prepare the relation for a correct convexification, the expression in Equation (4.24) is transformed in the following relation [91]:

$$\begin{aligned} &\text{RTN} : \left(\bar{\mathbf{x}}_j[k] - \bar{\mathbf{x}}_i[k]\right)^T \mathbf{C}^T\mathbf{C}\left(\mathbf{x}_j[k] - \mathbf{x}_i[k]\right) \geq d_{thr}\left\|\mathbf{C}\left(\bar{\mathbf{x}}_j[k] - \bar{\mathbf{x}}_i[k]\right)\right\|_2 \\ &\text{ROEs} : \left(\mathbf{D}[k]\delta\bar{\boldsymbol{\alpha}}_j[k] - \mathbf{D}[k]\delta\bar{\boldsymbol{\alpha}}_i[k]\right)^T\left(\mathbf{D}[k]\delta\boldsymbol{\alpha}_j[k] - \mathbf{D}[k]\delta\boldsymbol{\alpha}_i[k]\right) \geq d_{thr}\left\|\mathbf{D}[k]\delta\bar{\boldsymbol{\alpha}}_j[k] - \mathbf{D}[k]\delta\bar{\boldsymbol{\alpha}}_i[k]\right\|_2 \end{aligned} \tag{4.25}$$

for $i \neq j$ and $j = 1, ...N-1$, where the $\bar{\bullet}_j[k]$ and $\bar{\bullet}_i[k]$ represents an initial guess of the optimal trajectory followed by the spacecraft. The idea behind Equation (4.25) is to approximate the original concave constraint with a surface described by affine constraints. Accordingly, the closer the initial guess is to the actual trajectory, the more accurate the convex program solution will be. In this work, the initial guess is selected as the result obtained from a first running of the convex problem, without collision avoidance constraints. Then, the collision avoidance is added to the problem formulation and the initial guess is refined with the resulting trajectory and control from the first running of the convex problem. Finally, this refined initial condition is used to obtain a refined solution. The expression in Equation (4.25) generates separating planes among the satellites, transforming the circular prohibited zone of Equation (4.24) into a suitable convex formulation. This formulation defines a collision-free zone with separating planes, ensuring a sufficient condition for the collision avoidance of the j-th and i-th satellite couple [91]. Note that with this formulation the collision avoidance is imposed only at k times, with no control of what happens during the k-th time interval. Nonetheless, given the hypothesis of Δt small enough, this approximation becomes acceptable despite the satellites are very close to each other in passive interferometry application.

Convex formulation. After the discretisation procedure, the system can be written in terms of a convex formulation. The derivation is provided for the description in RTN, but the same considerations are valid for the approach in ROEs framework. Following the approach described in [141], we want to express the control system in a convex formulation, with equality and inequality constraints:

$$\begin{aligned} \text{minimise} : \quad & f_0(x) \\ \text{subject to} : \quad & f_i(x) \leq 0 \quad i = 1, ..., m \\ & h_i(x) = 0 \quad i = 1, ..., p \end{aligned} \tag{4.26}$$

where $x \in \mathbf{R}^n$ is the optimisation variable, including the state vectors of all the satellites in the formation. The aim is to solve the optimisation problem for the overall formation to properly minimise propellant while dealing with the inter-satellite collision avoidance constraint. For each satellite j, with $j = 1, ..., N$, we define a column vector $\hat{\mathbf{x}}_j$, which includes the state vector and the control term at each time instant k:

$$\hat{\mathbf{x}}_j = \left\{ x_j^1 \quad \cdots \quad x_j^k \quad \cdots \quad x_j^K \quad u_j^1 \quad \cdots \quad u_j^k \quad \cdots \quad u_j^{K-1} \right\}^T \tag{4.27}$$

where $\hat{\mathbf{x}}_j$ is a $(6K + 3(K-1))$ size vector. For conciseness, we define $M = (6K + 3(K-1))$ the length of the decisional vector of each j-th satellite. For the whole formation, we define the full state column vector $\hat{\mathcal{X}}$ as the decisional vector, with size $(N \cdot M)$:

$$\hat{\mathcal{X}} = \left\{ \; \hat{\mathbf{x}}_1 \quad \cdots \quad \hat{\mathbf{x}}_j \quad \cdots \quad \hat{\mathbf{x}}_N \; \right\} \tag{4.28}$$

The relation in Equation (4.19) is now expressed in terms of the full state column vector $\hat{\mathcal{X}}$. For each j-th satellite, the discrete system dynamic at instant k is:

$$\mathbf{x}_j^{k+1} - (\mathbf{I} + \mathbf{A}\Delta t)\;\mathbf{x}_j^k - \hat{\mathbf{B}}\,\mathbf{u}_j^k = 0 \tag{4.29}$$

where $j = 1, ..., N$. Considering the k-th instant, in matrix form the system dynamics for satellite j are the following.

$$\mathbf{A}_{sd}\cdot\hat{\mathbf{x}}_j = [\mathbf{0}_{6\times 6(k-1)}, \quad -(\mathbf{I}_6 + \mathbf{A}\Delta t), \quad \mathbf{I}_6, \quad \mathbf{0}_{6\times 3(2K-k-3)}, \quad -\hat{\mathbf{B}}, \quad \mathbf{0}_{6\times 3(K-k-1)}]\cdot\hat{\mathbf{x}}_j = 0 \tag{4.30}$$

where the matrix that multiplies $\hat{\mathbf{x}}_j$ is called $\mathbf{A}_{sd}$. Thus, for the overall formation, the system dynamics can be expressed as:

$$\begin{bmatrix} \cdots & \cdots & \cdots \\ \mathbf{0}_{6(K-1)\times M(j-1)} & \mathbf{A}_{sd} & \mathbf{0}_{6(K-1)\times M(N-j)} \\ \cdots & \cdots & \cdots \end{bmatrix} \cdot \hat{\mathcal{X}} = 0 \quad \rightarrow \quad \hat{\mathbf{A}}_{sd}\,\hat{\mathcal{X}} = 0 \tag{4.31}$$

where $j = 1, ..., N$. Finally, the system dynamics in convex formulation for the overall formation is represented as $\hat{\mathbf{A}}_{sd}\,\hat{\mathcal{X}} = 0$, where the overall $\hat{\mathbf{A}}_{sd}$ matrix is of $6K \times (N \cdot M)$.

For the cost function, we define a matrix $\mathcal{H}$ to extract, from the state vector of each j-th satellite, the control terms $\mathbf{u}_j^k$:

$$\mathcal{H}_j\,\hat{\mathbf{x}}_j \;\; = \left[\mathbf{0}_{1\times 6K}, \quad \mathbf{I}_{1\times 3(K-1)}\right]\,\hat{\mathbf{x}}_j = \left[\mathbf{0}_{1\times 6K}, \quad \mathbf{u}_j^1, \quad \cdots, \quad \mathbf{u}_j^k, \quad \cdots, \quad \mathbf{u}_j^{K-1}\right]^T \tag{4.32}$$

where $j = 1, ..., N$. Finally, for the overall formation, the objective function including the contribution of each satellite becomes:

$$J = \left\| (\hat{\mathcal{H}}\,\hat{\mathcal{X}})\,\Delta t \right\|_1 \tag{4.33}$$

where $\hat{\mathcal{H}} = [\cdots, \quad \mathcal{H}_j, \quad \cdots]^T$ for every $j = 1, ..., N$. Note that the expression in Equation (4.33) is equivalent to the objective function defined for the classical control problem in Equation (4.15). In fact, it correspond to the sum of the norm-1 at each time instant k of the control effort $\mathbf{u}_j^k$. The value from the matrix multiplication is multiplied by the discretised time interval Δt, to recover the cost of the manoeuvre in the overall time interval ΔT.

The same procedure used for the system dynamics and the objective function is used to write the initial and final conditions in terms of the full state column vector $\hat{\mathcal{X}}$. The final result of the described procedure is the following relation:

$$\begin{cases} \hat{\mathcal{A}}_{IC}\,\hat{\mathcal{X}} = \mathbf{X}_0 \\ \hat{\mathcal{A}}_{FC}\,\hat{\mathcal{X}} = \mathbf{X}_f \end{cases} \tag{4.34}$$

where the matrices $\hat{\mathcal{A}}_{IC}$ and $\hat{\mathcal{A}}_{FC}$ are defined as:

$$\hat{\mathcal{A}}_{IC} = \begin{bmatrix} \cdots & \cdots & \cdots \\ \mathbf{0}_{M\times M(j-1)} & \mathcal{A}_{IC} & \mathbf{0}_{M\times M(N-j)} \\ \cdots & \cdots & \cdots \end{bmatrix} \quad \hat{\mathcal{A}}_{FC} = \begin{bmatrix} \cdots & \cdots & \cdots \\ \mathbf{0}_{M\times M(j-1)} & \mathcal{A}_{FC} & \mathbf{0}_{M\times M(N-j)} \\ \cdots & \cdots & \cdots \end{bmatrix} \tag{4.35}$$

For each row defined by $j = 1, ..., N$, where $\mathcal{A}_{IC}$ and $\mathcal{A}_{FC}$ are $(M \times M)$ matrices with only not-null components the $\mathcal{A}_{IC}^{(1:6,1:6)} = \mathbf{I}_6$ and $\mathcal{A}_{FC}^{(6K-5:6K,6K-5:6K)} = \mathbf{I}_6$ for each j-th satellite. While the $\mathbf{X}_0$ and $\mathbf{X}_f$ terms are $(6KN)$ column vectors for the initial/final conditions of the overall formation, defined as:

$$\mathbf{X}_0 = [\mathbf{x}_{0,1} \quad \cdots \quad \mathbf{x}_{0,j}, \quad \cdots \quad \mathbf{x}_{0,N}]^T \tag{4.36}$$

$$\mathbf{X}_f = [\cdots \quad \mathbf{x}_{f,1} \quad \cdots \quad \mathbf{x}_{f,j}, \quad \cdots \quad \mathbf{x}_{f,N}]^T \tag{4.37}$$

For the thrust limitation, the relation is defined for multiple thrusters, i.e. each satellite j could provide a thrust in a generic direction along the relative RTN frame. The maximum thrust given by the on-board engine poses a limit in both positive and negative directions of the firings. The relation in Equation (4.23) is manipulated in the matrix form in terms of the full state column vector as follows:

$$\hat{\mathcal{A}}_{th}\, \hat{\mathcal{X}} \leq \mathbf{a}_{max}\, \hat{\mathcal{B}}_{th} \tag{4.38}$$

where the matrix $\hat{\mathcal{A}}_{th}$ is defined for the multiple thruster case to extract from the full state column vector the control components u_j^k for each $j = 1, ..., N$ and for each $k = 1, ..., K$.

$$\hat{\mathcal{A}}_{th} = \begin{bmatrix} \cdots & \cdots & \cdots \\ \mathbf{0}_{6(K-1)\times M(j-1)} & \mathcal{A}_{th} & \mathbf{0}_{6(K-1)\times M(N-j)} \\ \cdots & \cdots & \cdots \end{bmatrix} \tag{4.39}$$

where $\mathcal{A}_{th} = \left[\tilde{\mathcal{A}}_{th}; -\tilde{\mathcal{A}}_{th}\right]$, and for each satellite j, the matrix to extract the control component from the state vector is $\tilde{\mathcal{A}}_{th}(:, 6K+1 : M) = \mathbf{I}_{3(K-1)}$. Finally the column vector $\hat{\mathcal{B}}_{th}$ is defined depending on the thruster configuration:

$$\begin{aligned} &\text{In RTN}: && \hat{\mathcal{B}}_{th} = \mathbf{I}_{6N(K-1)\times 1} \\ &\text{In TN only}: && \hat{\mathcal{B}}_{th} = [0,\ 1,\ 1,\ \cdots\ 0,\ 1,\ 1]^T \end{aligned} \tag{4.40}$$

In particular, the solution with the thrust in the radial direction is suboptimal, as it results in an expensive manoeuvre and variation in along track directions can be obtained with a thrust in transversal direction only, thanks to the natural dynamics. Furthermore, the solution in TN is of importance for one of the applications in Chapter 6. The FFLAS mission concept envision the possibility to have the control only in transversal and normal direction.

When dealing with formation flying, the collision avoidance constraint is of utmost importance to ensure safety, since it provides a collision-free zone for the optimal manoeuvre. As defined in Equation (4.25), the relation could be converted in matrix form with the full state column vector $\hat{\mathcal{X}}$ for each pair of satellites j and i with $j = 1, ..., N-1$ and $i > j$ as:

$$\hat{\mathcal{B}}_{CA}\left(\left(\hat{\mathcal{A}}_{CA}\,\bar{\mathcal{X}}\right)^T \cdot \left(\hat{\mathcal{A}}_{CA}\,\hat{\mathcal{X}}\right)\right) \geq d_{thr}\, \hat{\mathcal{C}}_{CA} \tag{4.41}$$

where $\bar{\mathcal{X}}$ is the matrix form of the initial guess of the optimal trajectory $\bar{\mathbf{x}}_j[k]$. The matrix $\hat{\mathcal{A}}_{CA}$ is defined to extract the term $\mathbf{x}_j[k] - \mathbf{x}_i[k]$ from the full state vector $\hat{\mathcal{X}}$ and from the initial guess $\bar{\mathcal{X}}$ at each time step k. The generic formulation of $\hat{\mathcal{A}}_{CA}$ for the collision avoidance constraint of satellite i and j is the following:

$$\hat{\mathcal{A}}_{CA} = \begin{bmatrix} \vdots \\ \mathcal{A}_{CA}^{i,j}[k] \\ \vdots \end{bmatrix} \tag{4.42}$$

$$\mathcal{A}_{CA}^{i,j}[k] = \begin{bmatrix} \mathbf{0}_{3,6(k-1)} & \mathbf{I}_3 & \mathbf{0}_{3,3(3K-2)} & -\mathbf{I}_3 & \mathbf{0}_{3,3(6K-2k-1)} \end{bmatrix} \tag{4.43}$$

for $k = 1, ..., K$ and $j = 1, ..., N-1$, $i > j$. The matrix $\hat{\mathcal{B}}_{CA}$ is introduced to extract the quadratic form of the inter-satellite distance between satellite j and satellite i. Similarly, the matrix $\hat{\mathcal{C}}_{CA}$ is selected to represent in quadratic form the component $\mathbf{C}\left(\bar{\mathbf{x}}_j[k] - \bar{\mathbf{x}}_i[k]\right)$ of Equation (4.24) at each time instant k from the initial state $\bar{\mathcal{X}}$. The quadratic form of the collision avoidance constraint grants the convexity of the formulation, and the closer the initial guess is to the actual optimal trajectory, the more easily the optimal control problem will converge to the solution.

Disciplined Convex Programming

The disciplined convex programming was introduced by the work in [143]. The terminology "disciplined" is related to a set of rules and convention to set up convex optimization programs. The set provide a unique and rigorous methodology to properly manipulate the problem for an automatic solution. As specified in [143], a problem based on the set of rules is automatically convex. This set is divided into two components, *athoms* and *rule-set*. The former provides a set of functions with specific properties, as convex, concave or affine, monotonicity and validity range. The latter is a set of principles for the combination of variables, parameters, and numeric values to produce convex formulation. As an example, it provides a set of rules for the definition of the cost function and the constraints. Similarly, the affine property of the convex functions are incorporated in a number of composition rules [143].

In this work, the disciplined convex programming is derived under these assumptions and is used to solve the convex optimal problem defined by Equation (4.33) subject to the constraints in Equation (4.30), Equation (4.34), Equation (4.38), and Equation (4.41). Both the objective and the inequality constraints are expressed in convex formulation, while the equality constraints are affine. There exist different software for the resolution of disciplined convex problems. An example is the *SeDuMi* software, which can be employed to solve a problem involving linear and quadratic equations and inequalities, developed by [144]. A second example is the semidefinite program solver *SDPT3*, an infeasible path-following algorithm for semidefinite-quadratic-linear programming developed by [145]. Finally, a third similar approach is the *GuRoBi* for linear and non-linear mathematical optimisation problems [146]. We take advantage of the sparse properties of the matrices defined in the convex problem, for a more computationally efficient resolution. Moreover, we use the *CVX* Matlab® based software from [147] and [148], which allows to solve a convex problem in a simple formulation, with the possibility to select either the *SDPT3*, *SeDuMi* or *GuRoBi* solvers. The input specifications of the *CVX* software are shown in Algorithm 1.

As described in [148], the *SeDuMi* solver is faster for most of the applications and supports linear, quadratic, quadratically constrained quadratic, second order cone, and semi-definite programming. However, it generates low reliability results compared to other solvers. One solution is the *SDPT3*

Algorithm 1: Convex optimal problem for formation reconfiguration in *CVX* format

```
Data: Initial and final state of each satellite $X_0$ and $X_f$;
      Maximum acceleration from the thrusters $\mathbf{a}_{max}$;
      Minimum inter-satellite distance $d_{thr}$;
Initialisation;
  $n = N \cdot (6K + 3(K-1))$;
  $\Delta t = t^{k+1} - t^k$;
cvx_begin
    cvx_solver      sdpt3 (or sedumi or gurobi);
    cvx_precision   best;
    variable        X(n);
    minimise$\left(\mathrm{norm}\left(\left(\hat{H}\,X\right)\Delta t, 1\right)\right)$;
    subject to;
        $\hat{A}_{sd}\,X = 0$;
        $\hat{A}_{IC}\,X = X_0$;
        $\hat{A}_{FC}\,X = X_f$;
        $\hat{A}_{th}\,X \leq \mathbf{a}_{max}\,\hat{B}_{th}$;
        $\hat{B}_{CA}\left[\left(\hat{A}_{CA}\,\bar{X}\right) \cdot \left(\hat{A}_{CA}\,X\right)\right] \geq d_{thr}^2\,\hat{C}_{CA}$;
end
```

solver, it supports all the previous continuous models and produces more reliable results in most of the applications. Similarly, the *Gurobi* solver provide quite reliable solutions and also support integer constraints. on the other side, it is not compatible with semi-definite programming. The performances of each solver are application dependant, and should be tested for the cases under analysis. For the case in this work, the *SDPT3* was preferred for a more stable and reliable solution, specifically when the collision-avoidance constraint is employed. The *SeDuMi* and *Gurobi* perform worst in terms of reliability and solving time when the number of spacecraft in the formation is increased (see the Figure 4.2). For an accurate and reliable solution, the tolerance level of the solver is set to [$\epsilon^{1/2}$, $\epsilon^{1/2}$, $\epsilon^{1/4}$], where the machine precision is $\epsilon = 2.22 \times 10^{-16}$. Note that the dimension of the problem should be defined before the call to the *CVX* solver. In this case, the dimension of the full state variable depends on the number of satellites N and on the number of time steps K. The simulation time is selected as a fraction of the orbital period of the reference orbit of the formation. It is important to consider a fraction of the orbital period to guarantee the convergence of the optimal problem. Moreover, for an accurate solution and to guarantee the convergence, the discretization for a manoeuvre in one orbital period should not be higher than $2°/n_c$, where n_c is the mean motion of the reference orbit [89].

Algorithm performances evaluation. The performances of the selected methodology based on disciplined convex programming are tested against a progressive number of satellites (from 2 to 12), to evaluate the computational time. The different solvers available for the *CVX* software are tested for performance evaluation. The test case presented in this section simulates a reconfiguration of a line to a PCO configuration [68], considering the simulation parameters reported in Table 4.1. The satellites are initially placed in a coplanar formation configuration along the transversal direction, with an initial inter-satellite distance of $50\,\mathrm{m}$. The final condition for each satellite j is selected as a PCO with a radius $\rho = 200\,\mathrm{m}$, using the procedure described in Section 3.3, based on magnitude-phase form of the relative motion.

Table 4.1: *Parameters for simulation setting.*

Properties		**Value**
SSO Keplerian elements	(m, -, deg,deg,deg)	$\{7.416e6\,,\,0,\,98.5\,,\,0\,,\,0\}$
Manoeuvring time	(s)	$3/4\,P$
Discretisation step	(s)	25
Minimum inter-satellite distance	(m)	45
Satellites Mass	(kg)	50
Maximum Thrust	(mN)	10

An example of the reconfiguration trajectory for the 10-satellites formation case is shown in Figure 4.1a. The solution is obtained imposing a first guess of the trajectory without collision avoidance constraint and then refining the solution with a second iteration of the optimisation. This procedure guarantees the correct inclusion of the collision avoidance constraint in the simulation. The first performance comparison is performed by solving the same optimal procedure using the optimisation algorithm first based on RTN and then on ROEs description of the COCP. The same trajectory is computed with the two approaches and slightly different performances in terms of solving time are identified. Figure 4.1b compares the solving time of the COCP algorithm for different number of spacecraft in the reconfiguration manoeuvre. The solver for the *CVX* is set equal to *SeDuMi* and the solving time is computed for both representations in RTN and in ROEs. The simulations have been run on a Windows computer with Intel(R) Core(TM) i7-4720HQ CPU @ 2.60 GHz at 2.59 GHz and a RAM of 16.0 GB. One can observe that the two algorithms performs similarly, as expected, and the ROEs-based algorithm preforms slightly better than the RTN description for higher number of spacecraft: for 12 spacecraft the former requires about 21 s, while the latter about 30 s. This time difference is mainly due to the description of the motion in ROEs coordinates, that significantly simplify the plant matrix of the dynamic system. On the other hand, for fewer spacecraft, the algorithms perform similarly, providing a solution in less than 10 s.

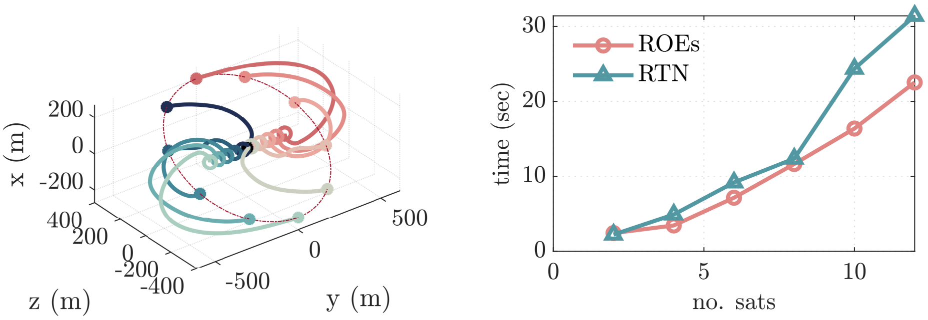

(a) *3d representation of the reconfiguration manoeuvre: lienar to PCO*

(b) *Computational time for CVX (sedumi) solver for the set up in RTN and in ROEs framework.*

Figure 4.1: *Performance of the coplanar to PCO reconfiguration for a 10-satellite formation.*

The second comparison is related to the time for the problem set up (i.e. the matrices computation in the convex formulation of the COCP) and the different available solvers for the *CVX*. Figure 4.2

show the performances of the algorithm against the number of satellites. Figure 4.2b represents the computational time to set up the matrices for the convex problem, which is required to initialised the *CVX* software. The behaviour is exponential with the increasing number of satellites, varying from a minimum of 2 seconds to a maximum of about 3 minutes for the 12-satellites case. This time is required only for the initialization of the convex problem and does not affect the *CVX* solver time. This exponential behaviour is connected to the code implementation, where the matrices have been computed through nested for loops. Figure 4.2a shows the computational time required by the *CVX* solver to provide the optimal solution, considering the three possible solvers of *CVX*, *GuRoBi*, *STDP3* and *SeDuMi*. In this case, the behaviour scales approximately linear with the number of satellites, with a maximum of about 30 seconds for the 12 satellites case. For the coplanar to PCO reconfiguration, the *STDP3* provides slightly better performances with a higher number of satellites.

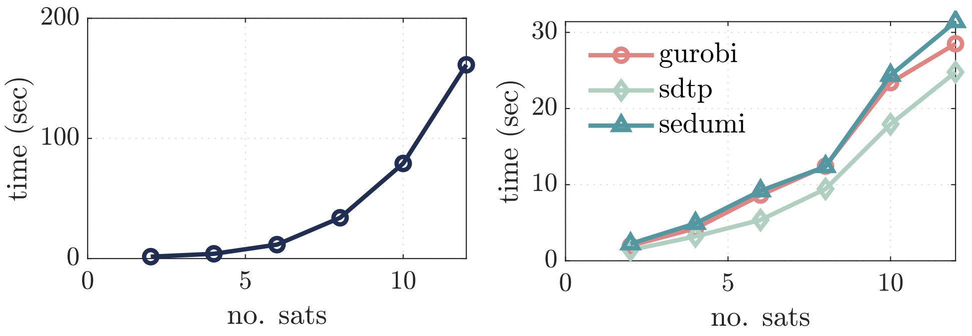

(a) *Computational time for setting up the simulation.*

(b) *Computational time for CVX solver.*

Figure 4.2: *Algorithm performance evaluation with 2 to 12 satellites formation.*

4.2 Closed-loop strategy

The methodology developed in Section 4.1.2 provide a delta-v optimal trajectory for formation reconfiguration. Nevertheless, no feedback on the actual error is included in the procedure, as an open loop strategy is considered. Moreover, only the secular perturbation due to Earth's oblateness is included in the relative dynamic description. To include uncertainties and external perturbations of the LEO region, a complete dynamic description is required and a closed loop control logic is implemented to perform trajectory tracking based on the error between the actual and the reference state. Two control techniques are considered in this work. First a LQR is implemented, based on the error with respect to the relative state in the RTN frame. It provides a feedback control to the dynamics for the trajectory tracking problem. Second, a MPC is developed in the ROEs framework to compute the control action to directly solve the optimal control problem in a closed-loop approach.

4.2.1 Linear Quadratic Regulator

This section describes the algorithms implemented for the closed-loop feedback control to maintain the formation geometry, based on an LQR controller. Linear quadratic controllers have been used in different works involving formation flying [94,97,149]. Moreover, this work includes the design of the onboard actuators to consider the uncertainties and limitations of a low-thrust engine. The following logic is considered:

- The open loop control methodology provides a reference trajectory and corresponding nominal control profile.
- The dynamical propagation of the distributed system is performed using a full description of the dynamics (see Section 3.2) and it is subsequently transformed into precise relative motion.
- The error between the actual and the reference relative state of the formation is computed.
- The error is used to compute the effort to keep the formation along the reference trajectory and provide a feedback commanded control to thruster.
- The thrusters are modelled including errors and uncertainties typical of an ion thruster. They provide the feedback control to the system dynamic of the formation.

The trajectory tracking problem is based on the design of a feedback compensator and a model of the low thrust engines.

Controller design. The design of the controller in the LQR based on the definition of an optimal control problem with specific assumptions on the system dynamics. In a general fashion, a control system is defined as

$$\begin{aligned} \dot{\boldsymbol{x}}(t) &= f(t, \boldsymbol{x}, \boldsymbol{u}) \\ \boldsymbol{x}(t_0) &= \boldsymbol{x}_0 \end{aligned} \tag{4.44}$$

Where $\boldsymbol{x}$ and $\boldsymbol{u}$ are the state and the control action respectively, and $\boldsymbol{x}_0$ is the initial condition. For this system, a generic cost functional can be derived in terms of running cost $\boldsymbol{L}$ and terminal cost $\boldsymbol{M}$:

$$\mathcal{J} = \int_{t_0}^{t_f} \boldsymbol{L}(t, \boldsymbol{x}, \boldsymbol{u})dt + \boldsymbol{M}(t_f, \boldsymbol{x}_f) \tag{4.45}$$

Where t_0 and t_f are the initial and final state, respectively, and $\boldsymbol{x}_f = \boldsymbol{x}(t_f)$ is the terminal state. For the problem under analysis in this work, the following assumptions have been considered:

- No terminal cost: $\boldsymbol{M} = 0$ (i.e. corresponding to the Lagrange problem).
- Linear system dynamics: $\dot{\boldsymbol{x}}(t) = \boldsymbol{A}(t)\boldsymbol{x}(t)$, including in the plant matrix the effects of the mean J_2 and the differential atmospheric drag (see Section 3.4.1).
- Quadratic cost function $\mathcal{J}$.
- Linear time-varying control system.

Under these assumptions, corresponding to a finite-horizon LQR, the feedback compensator is derived in terms of trajectory tracking: the aim of the controller is to minimise the error between the spacecraft actual and desired trajectories. This is expressed with the following relation:

$$\lim_{t \to \infty} \boldsymbol{x} - \boldsymbol{x}_d = 0 \tag{4.46}$$

Where $\boldsymbol{x}$ and $\boldsymbol{x}_d$ are the actual and desired state, respectively, and their difference is the error $\boldsymbol{e} = \boldsymbol{x} - \boldsymbol{x}_d$. The linear time varying control system is defined as:

$$\begin{aligned} \dot{\boldsymbol{x}}(t) &= \boldsymbol{A}_{rtn}(t)\boldsymbol{x}(t) + \boldsymbol{B}_{rtn}\boldsymbol{u}(t) \\ x(t_0) &= x_0 \end{aligned} \tag{4.47}$$

The feedback control term $\boldsymbol{u}(t)$ is computed from the dynamics of the error $\boldsymbol{e}$ and the desired control profile $\boldsymbol{u}_d$, under the relation $\boldsymbol{v} = \boldsymbol{u} - \boldsymbol{u}_d$. Following the procedure in [150], the feedback law has been obtained from the derivation of the dynamics of the error $\boldsymbol{e}$ as $\boldsymbol{v} = \boldsymbol{K}\boldsymbol{e}$, where $\boldsymbol{K}$ is the gain matrix. Substituting this relation in the definition of the control error $\boldsymbol{v}$, the solution in terms of a linear control law is derived around the desired equilibrium point:

$$\boldsymbol{u} = -\boldsymbol{K}(\boldsymbol{x} - \boldsymbol{x}_d) + \boldsymbol{u}_d \tag{4.48}$$

The gain matrix $\boldsymbol{K}$ depends on the solution of the optimal control problem. Specifically, from the hypothesis introduced above, the quadratic cost functional has been defined for a finite-horizon LQR, with no terminal cost, based on the state and control errors:

$$\begin{aligned} \text{minimise}: \quad & \mathcal{J} = \frac{1}{2}\int_{t_0}^{t_f} \left((\boldsymbol{e})^T \boldsymbol{Q}\,(\boldsymbol{e}) + (\boldsymbol{v})^T \boldsymbol{R}\,(\boldsymbol{v}) \right) dt. \\ \text{subject to}: \quad & \dot{\boldsymbol{e}}(t) = \boldsymbol{A}_{rtn}(t)\boldsymbol{e}(t) + \boldsymbol{B}_{rtn}\boldsymbol{v}(t), \quad e(t_0) = e_0 \end{aligned} \tag{4.49}$$

Where $\boldsymbol{Q} = \boldsymbol{Q}^T \succeq 0$ and $\boldsymbol{R} = \boldsymbol{R}^T \succ 0$ are the weight matrix of the error and control variable, respectively, defined as positive (semi-) definite and diagonal matrices. The cost function takes into account both the deviation of the actual state from the reference trajectory and the cost of the control. The rate of convergence depends on the balance between the weight matrices. The candidate for the optimal feedback law derives from the inspection of the necessary conditions for optimality under the maximum principle [150]. The derivation is based on the introduction of a Lagrange multiplier $\boldsymbol{p}(t)$, called costate. A new expression $\mathcal{L}$ is identified to include the cost function $\mathcal{J}$ and the error dynamic:

$$\mathcal{L} = \mathcal{J} + \int_{t_0}^{t_f} \boldsymbol{p}^T(t)\left(\boldsymbol{A}_{rtn}(\tau)\boldsymbol{e}(\tau) + \boldsymbol{B}_{rtn}\boldsymbol{v}(\tau) - \dot{\boldsymbol{e}}(\tau)\right) d\tau \tag{4.50}$$

First, this expression is used to derived the relation between the co-state $\boldsymbol{p}(t)$ and the control action $v(t)$, by computing the gradient of $\mathcal{L}$ with respect to the control action $\boldsymbol{v}$: $\nabla_{v(t)}\mathcal{L}$. The condition for optimality requires that $\nabla_{v(t)}\mathcal{L}|_* = 0$, and the following relation is recovered:

$$\boldsymbol{v}^*(t) = -\boldsymbol{R}^{-1}\boldsymbol{B}_{rtn}^T\boldsymbol{p}^*(t) \tag{4.51}$$

The second important relation is the gradient of $\mathcal{L}$ with respect to the error $\boldsymbol{e}(t)$. For the optimality condition, also this derivatives is set to zero: $\nabla_{e(t)}\mathcal{L}|_* = 0$. This expression is used to derive the dynamics of the co-state multiplier $\boldsymbol{p}(t)$:

$$\dot{\boldsymbol{p}}^*(t) = -\boldsymbol{A}_{rtn}^T\boldsymbol{p}^*(t) - \boldsymbol{Q}e^*(t) \tag{4.52}$$

From the previous optimality conditions (Equations (4.51) and (4.52)), one can note that there is a linear relation between the system state and the co-state ($\boldsymbol{e}(t)$ and $\boldsymbol{p}(t)$). Under these assumptions, and introducing a new matrix $\boldsymbol{P}$ related to the co-state, the linear relation can be expressed as:

$$\boldsymbol{p}^*(t) = \boldsymbol{P}\boldsymbol{e}^*(t) \tag{4.53}$$

Where the it can be demonstrated that the matrix $\boldsymbol{P}$ satisfy the co-state dynamical equation (Equation (4.52)). The matrix $\boldsymbol{P}$ can be computed as the solution of the Riccati equation (see Equation (4.55)). Now, combining the expression for the optimal control Equation (4.51) and the co-state Equation (4.53), the following relation is obtained, in the form of linear feedback law:

$$\boldsymbol{u}^*(t) = -\boldsymbol{R}^{-1}\boldsymbol{B}_{rtn}^T\boldsymbol{P}^T(\boldsymbol{x}^*(t) - \boldsymbol{x}_d) + \boldsymbol{u}_d \tag{4.54}$$

Note that generally, the feedback gain is time-varying, as $\boldsymbol{P} = \boldsymbol{P}(t)$ for a finite-horizon LQR. In this work, the weight $\boldsymbol{R}, \boldsymbol{Q}$ and the control input $\boldsymbol{B}$ matrices have been considered time invariant. The time-variation of the matrix $\boldsymbol{P}$ is expressed by the Riccati differential equation [150]:

$$\dot{\boldsymbol{P}}(t) = -\boldsymbol{P}(t)\boldsymbol{A}_{rtn}(t) - \boldsymbol{A}_{rtn}^T(t)\boldsymbol{P}(t) - \boldsymbol{Q} + \boldsymbol{P}\boldsymbol{B}_{rtn}\boldsymbol{R}^{-1}\boldsymbol{B}_{rtn}^T\boldsymbol{P}(t) \tag{4.55}$$

The time dependence for the case under analysis only depends on the time variation of the plant matrix of the relative motion, which includes the effects of differential drag and mean J_2 (see Section 3.4.1). In addition, for the case when also the matrix $\boldsymbol{A}_{rtn}$ can be considered constant in time, the LQR problem can be written in the infinite horizon version. For this case, the Equation (4.55) becomes a time-constant algebraic equation:

$$\boldsymbol{A}_{rtn}^T\,\boldsymbol{P} + \boldsymbol{P}\,\boldsymbol{A}_{rtn} + \boldsymbol{Q} - \boldsymbol{P}\,\boldsymbol{B}_{rtn}\,\boldsymbol{R}^{-1}\,\boldsymbol{B}_{rtn}^T\,\boldsymbol{P} = 0, \tag{4.56}$$

This relation has a unique static positive solution. In this work, the system dynamics is considered discretised during the simulations, and the matrix of the relative dynamics $\boldsymbol{A}_{rtn}$ can be considered constant over each time step. Consequently, for each time instant of the simulation, a unique solution $\boldsymbol{P}$ can be computed, resulting in an adaptive gain matrix $\boldsymbol{K} = \boldsymbol{R}^{-1}\boldsymbol{B}^T\boldsymbol{P}^T$. The controllability of the system is achieved if the rank of the controllability matrix is equal to the order of the system n_{sys}. The controllability matrix is defined as:

$$\boldsymbol{C} = \left[\begin{array}{cccccc} \boldsymbol{B} & \boldsymbol{A}_{rtn}\boldsymbol{B}_{rtn} & \boldsymbol{A}_{rtn}^2\boldsymbol{B}_{rtn} & \cdots & \boldsymbol{A}_{rtn}^{n_{sys}-1}\boldsymbol{B}_{rtn} \end{array}\right] \tag{4.57}$$

A final consideration is required for the solution of Riccati's equation. Different procedures and algorithms are available in various programming languages (as MATLAB® or Python). The time-variation of matrix $\boldsymbol{A}_{rtn}$ is accounted for at each time step, and it is due to the orbital perturbations included in the model (i.e. mean J_2 and differential drag). For slowly varying dynamics under external perturbations, the variation of matrix $\boldsymbol{A}_{rtn}$ could be negligible for several time steps. This behaviour varies depending on the application under analysis. For the case when the variation of $\boldsymbol{A}_{rtn}$ is negligible over a fraction of the orbital period, the logic on-board could rely on the solution of the gain matrix $\boldsymbol{K}$ only at specific times (i.e. not at every time steps) to update the previous value. This aspect could improve the computational effort of the on-board processor. However, this has yet to be considered in future development, as the gain matrix has been updated at each time step.

Feedback control architecture The architecture adopted for the LQR closed-loop control is shown in Figure 4.3. The desired trajectory $\boldsymbol{x}_d$ and control $\boldsymbol{u}_d$ are provided by the guidance block, that implements the convex optimisation algorithm for formation reconfiguration (see Section 4.1). The error $\boldsymbol{e}$ is computed from the knowledge of the actual state given by the system dynamics, and then the gain matrix $\boldsymbol{K}$ is evaluated. The system dynamic implemented in the controller is based on the J_2 and drag linear approximation of the relative motion (see Section 3.4.1). The control law is implemented depending on the LQR gain, on the trajectory error and the control term $\boldsymbol{u}_d$. Then it is provided to the model of the actuator, to include the noises, uncertainties and technological limitations, and finally feedback to the system dynamics.

Uncertain control analysis

For the purpose of this thesis, it is important to test the robustness of the control against uncertainties on the initial conditions of the actual relative state with respect to the desired state for trajectory

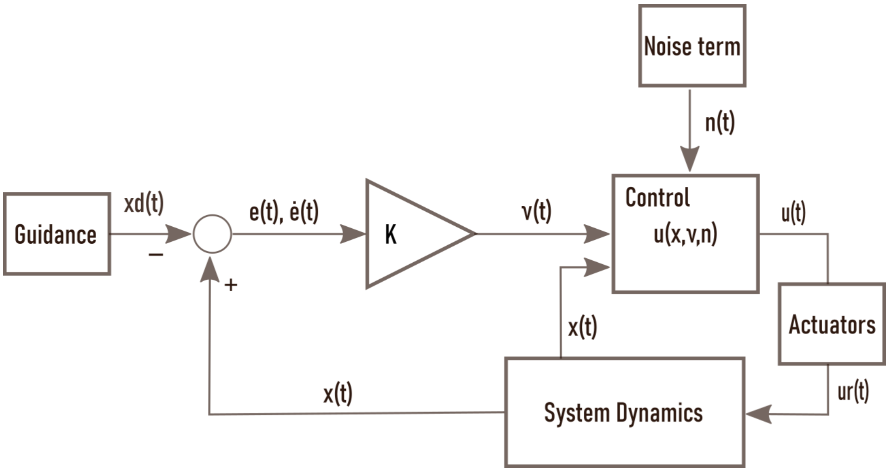

Figure 4.3: *Closed-loop guidance and control system architecture.*

tracking. Specifically this paragraph presents the results of the uncertainty analysis considering the current initial state of each spacecraft, defined by a mean value μ, perturbed with standard deviations σ. A MC analysis is run to test the performances of the control against uncertainties in the initial conditions. Specifically, the following logic has been considered starting from Figure 4.3:

- The desired relative trajectory of the *guidance* block is computed with the open-loop logic for the formation (either formation maintenance or delta-v optimal reconfiguration from Section 4.1).
- The model implemented in the *system dynamics* block is based on the absolute dynamics under external perturbations (atmospheric drag and aspherical gravity), developed in Section 3.2.
- The *actuator* block includes the noises and uncertainties of an ion thruster: internal delays, thrust magnitude and direction errors, thrust limitation (see Chapter 5 for more details).
- The *control* block is based on the optimal control in Equation (4.54).

For each spacecraft, actual initial condition is described by a mean and standard deviation. Specifically, the mean values is considered equal to the guidance reference, while the standard deviations account for initial uncertainties in the relative state knowledge. This uncertainty is representative to an error in the initial set up of the formation geometry with respect to the desired trajectory. The simulation aims at evaluating the robustness of the control in case of an initial error on the relative state with respect to the desired guidance. Specifically, the example of formation maintenance for a GCO trajectory (see Section 3.3) with three deputies is considered in the analysis. The chief spacecraft is considered equal to a virtual point at the centre of the circular relative trajectory. The initial conditions of the absolute reference orbit are reported in Table 4.2, while the value of initial parameters for the GCO initialisation are reported in Table 4.3. Considering an initial distribution of the initial conditions of 500 samples, the value of the standard deviation is selected to get an error in the order of $20\,\mathrm{cm}$ for the relative orbit radius ρ, and an error of 1 to 2 degrees on the phase angles. These values are considered representative of an error in the initial set up of the formation geometry. The distribution of the initial conditions in ROEs is reported in Figure 4.4. For each sample of the distribution of the initial conditions, the propagation is performed by the closed-loop in about $10\,\mathrm{s}$ seconds. This results in an overall MC running time of about $1\,\mathrm{h}$ and $20\,\mathrm{min}$. The specifications of the system machine for the simulation are 11th generation Intel(R) Core(TM) i7-1165G7, RAM of 16 Gb, and an operating system based on a 64-bit processor. The following weight matrices $\boldsymbol{Q}$ and $\boldsymbol{R}$ of the LQR control law are selected after a parametric analysis to ensure the convergence of the control during the formation maintenance for the GCO trajectory:

$$\begin{aligned}\boldsymbol{Q} &= diag[100,\ 100,\ 100,\ 1e6,\ 1e6,\ 1e6]\\ \boldsymbol{R} &= diag[10,\ 1,\ 1]1e9\end{aligned} \tag{4.58}$$

Table 4.2: *Initial condition for the reference orbit.*

Parameter	Value
$\boldsymbol{\alpha}_c$ (m, -, deg, deg, deg, deg)	$[7153.1,\ 0,\ 98.51,\ 270.83,\ 0,\ 0]$
Initial epoch	21 March 2025, 12:00:00
Step size	10 sec
Simulation time	2 orbital periods

Table 4.3: *Initial parameters in terms of mean and standard deviation.*

Parameter	Value
μ_ρ (m)	6.228
μ_α (deg)	$[30, 150, 270]$
σ_ρ	0.06
σ_α	0.01

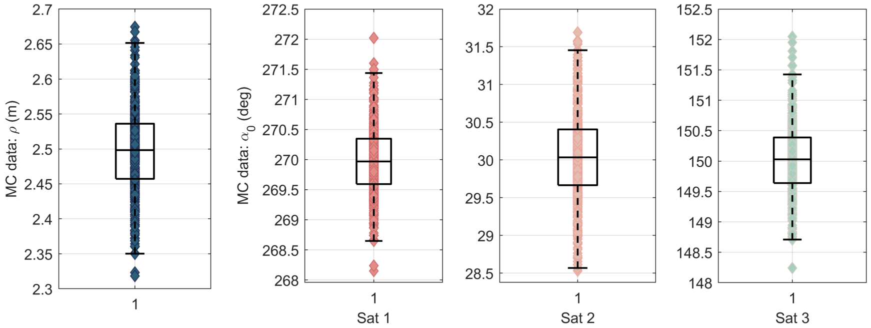

Figure 4.4: *Distribution of the initial conditions for ρ (first on the left) and α parameters (last three on the right). The mean and the standard deviation are represented with the box plot.*

The matrices $\boldsymbol{Q}$ and $\boldsymbol{R}$ are diagonal positive semi-definite matrices. The performances of the control are evaluated in terms of relative state accuracy in comparison with the guidance reference trajectory: $\text{error} = \text{current} - \text{desired}$. The control error is evaluated in terms of Cartesian state in RTN by the controller. Its mean value during the MC simulation is depicted in 4.5 for spacecraft 1, where the envelope of the error for the 500 runs is reported. Similar considerations are valid also for spacecraft 2 and 3. The bold line represents the mean value of the control error, that is bounded in

± 2 cm, considering the 500 MC runs. The uncertainty of the control, the envelope of the error, is represented by the shadow area in the graph. The uncertainty is higher in the first part of the simulation, where it can reach up to ± 10 cm of error. Then the uncertainty converges in time so that after less than half of the orbital period all the 500 MC runs converge to the mean value of the error. This behaviour is particularly important, demonstrating the robustness of the control against initial uncertainties. The corresponding error on the ROEs has been recovered from the absolute propagation of the absolute orbital elements of each satellite in the formation during the MC simulation. Figure 4.6 represents such behaviour for spacecraft 1 in terms of mean and standard deviation, which are represented as the bold line and the shadowed area, respectively. For the other two spacecraft the accuracy level is similar. The error on the relative semi-major axis $a\delta a$ has initially an uncertainty of ± $50\,\mathrm{cm}$, then it converges to the mean value in less than half an orbital period, remaining bounded in ± $10\,\mathrm{cm}$. Similarly, the relative argument of latitude $a\delta L$ has a mean value of the error in ± $10\,\mathrm{cm}$, while initially, the uncertainty can reach up to ± $20\,\mathrm{cm}$.

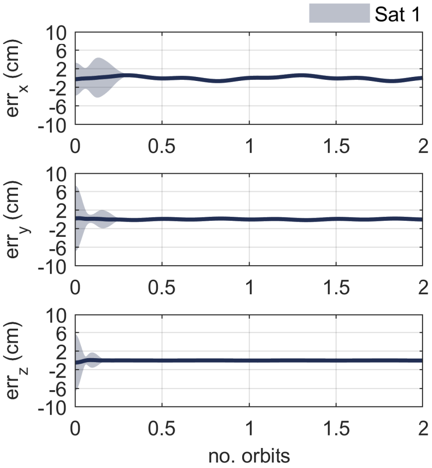

Figure 4.5: *Mean and standard deviation of the control error in the RTN frame for 500 MC runs.*

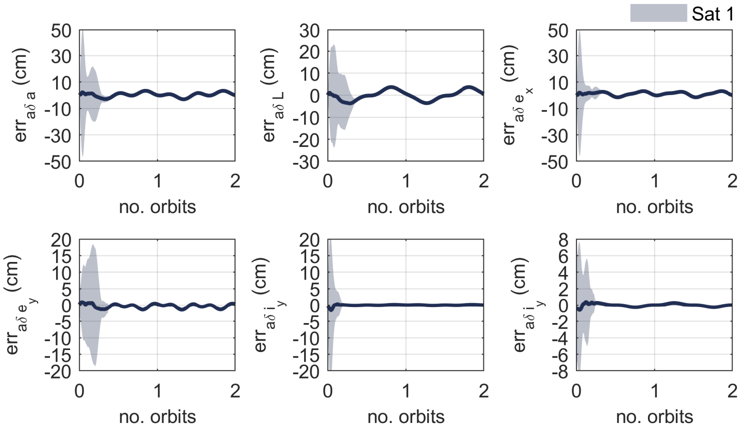

Figure 4.6: *Mean and standard deviation of the control error in the ROEs frame for 500 MC runs.*

4.2.2 Model Predictive Control in ROEs

This section presents the control model based on the Model Predictive Control (MPC) algorithm. The MPC has been of primary importance in the improvement of autonomous routine for trajectory optimization and guidance planning for distributed systems. In the space field, it has been applied to swarm and formation of multiple spacecraft to improve the autonomy and enhancing a decentralised architecture for trajectory computation [91,151,152]. One of the advantage of the MPC is the possibility to update the open-loop reference trajectory during the reconfiguration. This could be an important consideration when the formation starts from initial conditions significantly different from the desired state. Furthermore, considering a decentralised architecture, the MPC results in a reduction of size of the problem, even with the inclusion of collision avoidance constraints. This could be a relaxed condition for on-board computing, given the limitation of computational capability of medium to small spacecraft. The decentralised architecture have several advantages compared to the classic centralised one. For the situation under analysis, the decentralised approach have been considered (see Section 5.2.5 for more details). This management scheme gives each entity in the formation a certain level of autonomy in the decision. Each entity can receive and send information to the other entities in the formation. In a distributed system, typically, this exchange happens only among nearest vehicles. In this thesis, the informations are exchange all over the platform, so that the current relative state of each spacecraft is known by all the entity in the formation. Specifically, differently from the work in [91], the collision avoidance constraints are included in the MPC for all the vehicles of the formation, and not only for the closest one. In fact, thanks to the proximity of spacecraft for passive interferometry application (i.e. separation of few tens of meters), we assume for all the vehicles communication capability to exchange their current state. This assumption has an impact on the computational effort, that scales poorly with higher number of spacecraft. Nevertheless, for the case under analysis in this work, mainly formation composed by two to six spacecraft are considered, maintaining the number of vehicles small compared to the ones of a typical swarm.

The MPC is based on the computation of the current control action at each time instant $\boldsymbol{u}(t)$ by solving at each time instant an COCP. The controller is composed by:

- An *optimizer* to solve the COCP by minimising a cost function.
- A *plant model* to predict the evolution of the system.

Moreover, it produces as output the control action at each time step and takes as input the state estimation of the system dynamic. In this thesis, the optimal control variable $\boldsymbol{u}(t)$ is obtained by minimising a cost function for fuel optimal reconfiguration. The core of the *optimiser* is based on the COCP developed in open-loop (see Section 4.1). The dynamic of the distributed system in space is based on the STM matrix developed in Section 3.4.2, to include both J_2 and drag perturbations. The MPC is developed considering a fixed manoeuvre time and a receding horizon. The aim is the real-time design of reconfiguration manoeuvre for a swarm of spacecraft to reach a desired final configuration with minimum delta-v consumption. For the convergence of the MPC, it is essential to have terminal constraint for stability of the algorithm. The logic of the MPC is shown in Figure 4.7. Theoretically, the MPC algorithm solves the COCP at each time instant and this would require a high-frequency exchange of information. To relax this constraint, the solution is computed first at t_k and subsequence jumping at t_{k+2}, avoiding the solution of the problem at t_{k+1}. This approach relax the requirement on the communication exchange frequency and on the computational capability. With this approach, the MPC generates the control action for two successive time instants. At each step of the *optimizer* solve, the control action is given to the actuator models, that provides the real control to the *plant* *model*, composed by the system dynamics and the navigation algorithms (see Section 5.2). They provides the current state estimate representative of the state reconstruction on-board the spacecraft, which serves as an input for the next *optimizer* solve.

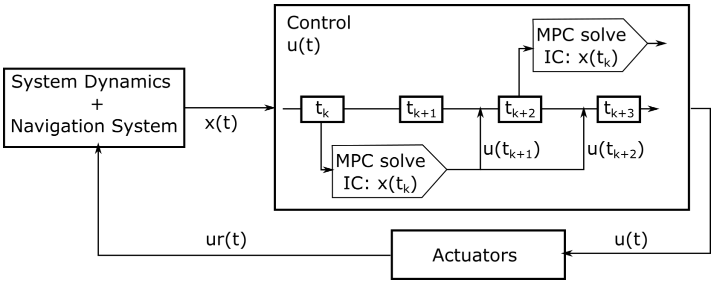

Figure 4.7: *Logic of the MPC control scheme.*

Receding horizon MPC Starting from the COCP presented in Section 4.1, the MPC algorithm (i.e. the optimizer) is developed. A receding horizon is considered without the need of adding a terminal cost to the objective function [91, 153, 154]. The concept of receding horizon refers to an algorithm that solves at each step k_0 an optimal control problem with a shorter time period. Specifically, for each optimal control problem, two different horizons can be identified. First, the input (or control) horizon, denoted with T_H, defines the time interval where the optimal control sequence is actually applied to the plant $k_0, k_0+1, \cdots, k_0+T_H$ (while the remaining optimal inputs are discarded). The second quantity is denoted as prediction (or output) horizon T. Its defines the terminal time of the horizon of the optimization, where the predicted outputs are computed by the MPC algorithm. Note that $T_H \leq T$. With the receding horizon approach, the MPC is implemented by reducing the horizon of the problem throughout the optimization [154]. At every new run, the initial time k_0 is increased and the previously computed outputs are applied to k_0+T_H, resulting in the so-called receding horizon. The optimization problem provides then the optimal trajectory until the final time T. The step-size of the simulation is identified with Δt. For the case under analysis, at each run, the optimal control of the previous step is applied to for two successive time instants (k_0+1 and k_0+2). The core of the algorithm is the COCP in ROEs formulation:

$$\begin{aligned}
\text{Minimize:}\quad & J = \sum_{j=1}^{N} \sum_{k=k_0}^{T-1} \left\| \mathbf{u}_j[k] \right\|_1 \Delta t \\
\text{Subject to:}\quad & \delta\boldsymbol{\alpha}_j[k+1] = \boldsymbol{\Phi}\delta\boldsymbol{\alpha}_j[k] + \mathbf{B}\,\Delta t\,\mathbf{u}_j[k] \\
& \delta\boldsymbol{\alpha}_j[k=k_0] = \delta\boldsymbol{\alpha}_{k_0,j} \\
& \delta\boldsymbol{\alpha}_j[k=T] = \delta\boldsymbol{\alpha}_{f,j} \\
& \left\| \mathbf{u}_j[k] \right\| \leq a_{max_j} \\
& \left(\mathbf{D}[k]\delta\bar{\boldsymbol{\alpha}}_j[k] - \mathbf{D}[k]\delta\bar{\boldsymbol{\alpha}}_i[k]\right)^T \left(\mathbf{D}[k]\delta\boldsymbol{\alpha}_j[k] - \mathbf{D}[k]\delta\boldsymbol{\alpha}_i[k]\right) \geq \\
& \qquad\qquad d_{thr} \left\| \mathbf{D}[k]\delta\bar{\boldsymbol{\alpha}}_j[k] - \mathbf{D}[k]\delta\bar{\boldsymbol{\alpha}}_i[k] \right\|_2
\end{aligned} \tag{4.59}$$

Where this is valid for all spacecraft: $\forall\, j = 1, \cdots, N$. The state $\delta\boldsymbol{\alpha}_{k_0,j}$ represents the current real time ROEs during the simulation. This value is updated every time MPC algorithm is rerun until the final position $\delta\boldsymbol{\alpha}_{f,j}$ is reached at $k = T$. At this point, the algorithm for the MPC is described in Algorithm 2. It relies on the numerical solution of the COCP in Equation (4.59). Once the optimal control is solved at the time step k, it is applied to the real system and the new state vector of the formation is computed. This value is then used as input for the next solution of the optimal control at updated time k_0. The STM $\mathbf{\Phi}$ considered in this algorithm is based on the model derived in Section 3.4.3, including the effects up to J_2 in the spherical harmonics. Moreover, the parameters for prediction and control horizon (as the simulation time), has been selected starting from the analysis performed with the open-loop convex algorithm (see Section 4.1.2). For the purpose of this study, no sensitivity analysis has been developed to optimise the MPC parameters.

Algorithm 2: Model Predictive Control Algorithm

```
Data: Initial and final state of each satellite $X_0$ and $X_f$;
      Maximum thruster acceleration $\mathbf{a}_{max}$ and minimum inter-satellite distance $d_{thr}$;
Initialisation;
  set state : $\delta\boldsymbol{\alpha}[\boldsymbol{t_k}]$;
  set time step : $\Delta t = t_{k+1} - t_k$;
  set initial time : $\Delta k = 0$;
  set input horizon : $T_H$;
while $k_0 \leq T$ do
    Optimize cvx_begin
        cvx_solver       sdpt3 (or sedumi or gurobi);
        cvx_precision    best;
        variable         X(n);
        solve            eq. (4.59);
        compute          u(n)
    end
    Update;
      $x_j[k]$ = state solution of optimizer;
      $u_j[k]$ = control solution of optimizer;
      update $k_0$;
end
```

Line to Circle reconfiguration with MPC. An example of a reconfiguration with the closed-loop MPC algorithm (Algorithm 2) is shown in Figure 4.8. Figure 4.8a shows the trajectory of the reconfiguration manoeuvre for two spacecraft flying in a leader-follower configuration to a circular GCO formation. At the initial time, the spacecraft has a separation of $150\,\mathrm{m}$, and after 1.5 orbital period they reconfigure with to a configuration with shorter separation (about $90\,\mathrm{m}$). A maximum thrust of $5\,\mathrm{mN}$ is imposed to the optimisation procedure, and a minimum separation of $80\,\mathrm{m}$ is required for safe operations. The real-time inter-satellite distance among the two spacecraft is shown in Figure 4.8b, where it can be observed how the safety threshold is always respected. For the simulation itself, similar computational time to the open-loop convex optimal control are required.

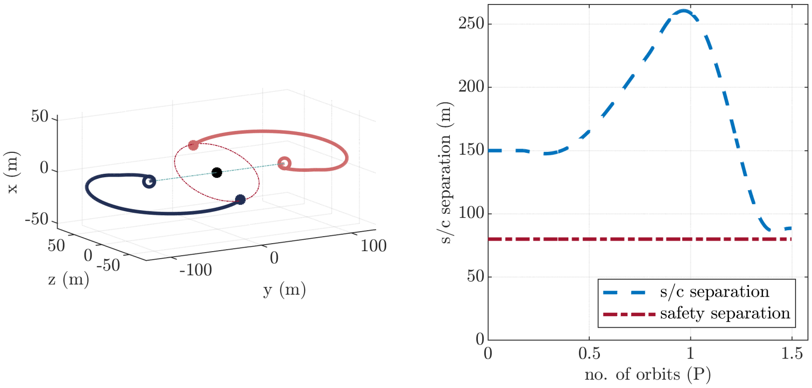

(a) *Trajectory reconfiguration in RTN frame.* **(b)** *Spacecraft separation in time.*

Figure 4.8: *Example of a reconfiguration of two spacecraft from a lead-follower configuration to the circular (GCO) formation using the MPC algorithm.*

CHAPTER 5

Guidance, Navigation, and Control Architecture

> *As our circle of knowledge expands, so does the circumference of darkness surrounding it.*
>
> — Albert Einstein

TIHS chapter presents the description of the architecture selected for the Guidance, Navigation, and Control (GNC) framework for multiple-satellites formation flying simulations, developed as part of PhD activities. First, an overview of the framework structure is presented, to address different operational needs. Then, the architecture of the algorithms and the closed-loop design is introduced and, finally, it is described how the algorithms for interferometry performances are included in the GNC framework. It has been developed as part of the ESA-funded FFLAS study and successfully presented at the final review of the project in November 2021. The current released is applied to relative motion in the LEO region, but it can be extended to other orbital region, by simply including the relevant orbital perturbations. The analyses presented in this document focus on the integration of guidance and control algorithms with GNSS-based navigation, to set-up a framework for the simulation of the main operational phases of a formation flying missions. The objective of the analysis is to assess the feasibility of different test case scenarios, by evaluating the control and navigation accuracy, as well as the delta-v budget and payload performances.

5.1 General System Structure

The design and development of the GNC framework for formation-flying simulation is based on the Matlab/ Simulink® environment. It integrates the techniques presented in Chapters 3 and 4 in a single closed-loop simulator, to model with high fidelity the formation flying behaviour during mission operations in an environment subject to orbital perturbations. The general architecture of the framework is shown in Figure 5.1.

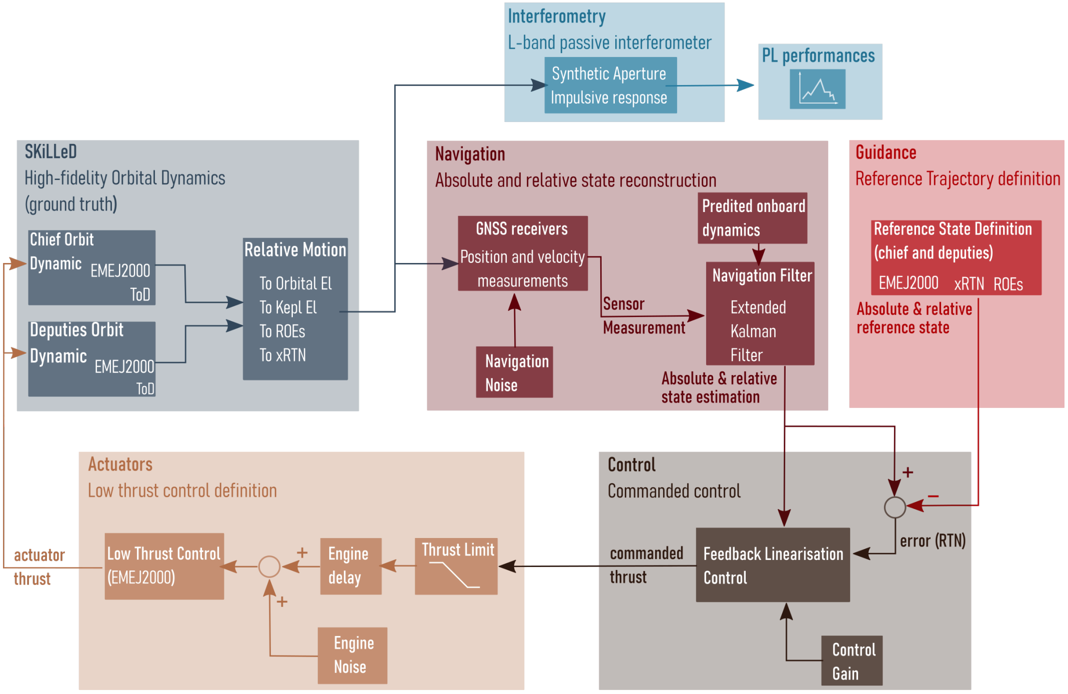

Figure 5.1: *Architecture of the GNC framework based on the Matlab/Simulink® environment.*

Six main blocks can be identified. The first block in blue represents the high-fidelity propagator for absolute and relative dynamics, representative of the ground truth implementation. It is based on an adaptation of the in-house Simulation Kit for Logic Layout Design of Formation Flying (SKiLLeD) [78]. Specifically, the absolute state of the chief and the deputies is computed first in the EME2000 and then in the ToD frames. The information on the state in the ToD is used to compute the relative motion in both RTN and ROEs representation. Moreover, the orbital elements are recovered during the propagation for further use. The state in ToD is taken as input in the navigation block. The second block in purple is dedicated to the GNSS-based navigation. The GNSS receiver is simulated adding noise to the ground truth dynamics, related to the actual receiver onboard the satellites. This is used to compute the absolute and relative state as measured by the GNSS receivers. The sensor measurements of the state together with the predicted onboard dynamics are used in the navigation filter, an Extended Kalman Filter (EKF), for absolute and relative state reconstruction. The dynamical model included in the filter includes the effects of the Earth's oblateness J_2 and the differential drag for the relative dynamics description. Similar assumption have been made for the absolute propagation of the state of each satellite for on-board reconstruction. The absolute and relative state estimation is important for the definition of the nominal control effort to be commanded to the actuators. The guidance trajectories are computed in the third block in red. It provides the reference trajectory, depending on the mission phase, based on the open-loop convex optimization problem for the relative motion and the analytical thrust profile for formation maintenance (see Section 4.1). The difference between the actual estimated relative state and the reference optimal state from the guidance algorithm represents the error in the relative trajectory, which is the input to control in the fourth block in brown. It implements closed-loop control techniques of Section 4.2. This provides the commanded control to the onboard actuators, the low thrust engine. The fifth block in orange implements the on-board thrusters, including the technological limitations of the engine. These are applied to the command, in terms of thrust limit, on-off delay, and thrust noise. From this analysis, the control provided by the low thrust engine is used as the input control law for the high-fidelity dynamic propagator, the first block. The last block, in light blue, consists of the interferometry model, that implements a simplified algorithm for a fast estimation of the payload performances during the simulation. Only the passive interferometry is considered in this block, for multiple passive L-band distributed antennas. Specifically, it provides an assessment of the synthetic aperture and impulsive response of the passive interferometer (see Chapter 2).

The main outcomes of the GNC framework are the accuracy in the control and in the navigation solution reconstruction that is achievable on-board by the implemented algorithms with respect to the ground truth trajectory. A key aspect is to assess that the overall GNC accuracy achievable during nominal operations is able to meet the requirements posed by the passive interferometry payload. This will support the feasibility of performing the main operational modes autonomously on-board, including the collision risk assessment and the eventual transition to a safe mode. So far, several missions demonstrated the feasibility of a precise millimetre and centimetre relative navigation in LEO, for the ground and onboard reconstruction, respectively, as discussed in [64].

5.2 Architecture of the GNC framework

This section provides the description of each part of the GNC framework, as well as the reference systems used and the initialisation procedure.

5.2.1 Reference systems

The GNC framework implements different reference systems, as already discussed in Section 3.1.3. It reports also the name and the acronym that is used in the parameters of the simulator.

Table 5.1: *Coordinates and Temporal systems used in the GNC framework.*

System	Acronym
Absolute reference frames	
Earth Mean Equator and Equinox of J2000	EME2000
True of Date	ToD
Osculating Keplerian coordinate frame	OSC_KEP
Relative reference frames	
Local Hill orbital frame	RTN
Relative Orbital Elements	ROEs
Spacecraft body frame	SC_B
Temporal	
International Atomic Time	TAI
Coordinated Universal Time	UTC
Terrestrial Time	TT
Global Positioning System Time	GPS-Time
Modified Julian Date	MJD

5.2.2 Framework initialisation

The GNC framework is initialised in MATLAB® with an input file to define the settings and the initial condition for the case scenario under analysis. The routine to set up the input file is standardised for an easy initialisation of different scenarios. The main parameters required to set up the input file are reported in Table 5.2. The gravity model file currently used can be selected among the Grace gravity file GGM01S, GGM02S and the JGM-2 gravity files. A comment is needed for the *Environment setting* parameter, the possible choices currently available in the simulator are the following:

- ’Keplerian’ for no perturbing effect in the simulation.
- ’J2 only’ or ’Drag only’ for including only the J2 or the drag effect.
- ’Mass’ to include the complete $\{l, m\}$ Gravity Model.
- ’Drag + Mass’ for the complete $\{l, m\}$ Gravity and Drag Models.

Moreover, the initialisation of the reference orbit (Chief orbit) and the relative state of the Deputies is essential to initialise the formation characteristics. The reference orbit can be provided with the Keplerian elements at the time t_0, while the relative state of the deputies could be provided in the RTN or ROEs format.

Table 5.2: *Parameters and description of the input file for the initialisation of the GNC framework.*

Parameter	**Symbol**	**Type**	**Description**
Gravity file	`NameGravityFile`	.dat	Gravity model file for the simulation
Environment Setting	`Environment`	string	Flag for the set up of the perturbations
Order l	`TransfOrder`	int	Order l of the gravity model
Degree m	`TransfDegree`	int	Degree m of the gravity model
Initial time	`TO_UTC`	vector	Initial UTC of the simulation
SC Mass	`mass`	float	Mass of the chief and deputies satellites
SC Area	`area`	float	Cross section area of the chief and deputies spacecraft
C_D	`CD`	float	Drag coefficient of the chief and deputies satellites
C_R	`CD`	float	SRP coefficient of the chief and deputies satellites
Reference orbit	`oeChief`	vector	Initial orbital elements of the chief satellite
Relative state	`xRTN` or `ROEqns`	vector	Initial relative state of the deputies
Simulation Step	`Step`	float	Step size for the simulation
Simulation time	`End`	float	Time duration of the simulation
No. of Deputies	`N_sat`	int	Number of deputies of the formation

Input pre-processing

After the definition of the input parameter, characterising a specific mission scenario, the data are pre-processed for inclusion in the Simulink® model. Four base quantities are defined to be used in Simulink®, as structure variables:

- `Simulation`: It includes all the parameters to initialise the simulation:
  - External files, such as gravity file.
  - Simulation constants, such as the Earth’s parameters.

  - Simulation date and time step.
  - The number of deputies of the formation.

- `TARGET`: It includes the physical and orbital information of the chief satellite.

- `CHASER`: It includes the physical and orbital information of the deputies satellite.

- `Relative`: It includes the relative orbital information of the deputies' satellites with respect to the chief satellite. Both ROEs and RTN representations are provided.

5.2.3 High-fidelity dynamical propagator

The in-house high-fidelity dynamical propagator, called SKiLLeD developed by Gaias [78], was adapted to the multiple-spacecraft formation environment in LEO. The absolute orbits of a chief and multiple deputies satellites are propagated in the EME2000 and then a conversion between osculating/mean elements is provided after the transformation into the ToD reference system. The conversion and the reference systems have been described in Chapter 3. The dynamical propagation is based on a C++ algorithm, which includes the main gravitational perturbations effects due to the gravitational terms. This work introduces some modification to the original code developed in SKiLLeD, as follow:

- Inclusion of the possibility to simulate simultaneously one chief satellite and up to N deputies' satellites, by vectorizing the C++ based functions.

- Development of a high-fidelity atmospheric drag model in the perturbing acceleration of the relative motion, in a separated C++ function, based on the NRLMSISE-00 model of [137].

The high-fidelity propagator is made of three main blocks for the computations of the main parameters of chief and deputies satellites. The schematics of the block is represented in Figure 5.2, where the *Orbital Dynamics* Block, *State Conversion EME2000 to ToD* Block, and *State Conversion absolute to relative* Block are represented. The input file is given by the initialisation of the problem in MATLAB®, as described in Section 5.2.2. Moreover, the information on the Atmospheric density is given at each time instant by a C++ based S-function, implementing the NRLMSISE-00 atmospheric model [137], and the geopotential gravity field implemented in the model is based on the GRACE Earth Gravity model 02 (GGM02S) [134]. The control thrust is given to the dynamical propagator by the Control block. Finally, the dynamical behaviour of the Chief and the deputies in terms of the absolute and relative state is provided as an input to the Navigation and Guidance blocks. The following subsections describe the models implemented in each block.

Atmosphere Block

The atmospheric block is based on the NRLMSISE-00 empirical atmosphere model developed by Picone et al. [137] It describes the natural temperatures and densities in the Earth atmosphere from ground level to thermosphere heights. The database of the empirical model includes the following data:

- Total mass density from satellite accelerometers and orbit determination, including the Jacchia and Barlier data.

- Temperature from incoherent scatter radar, and the molecular oxygen number density.

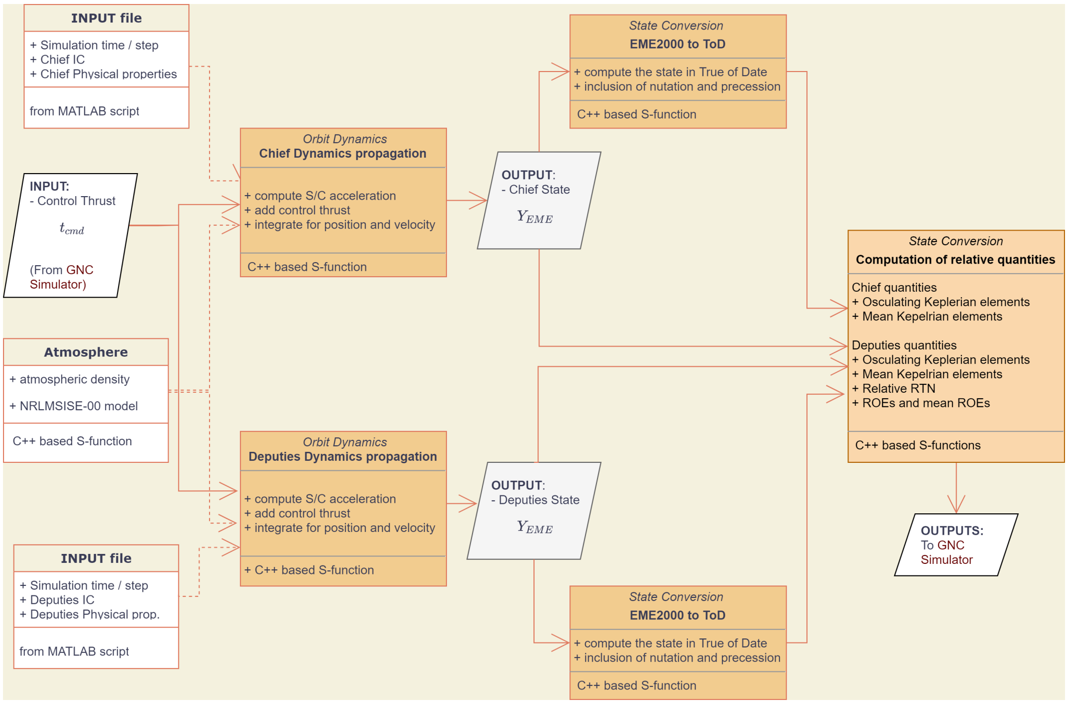

Figure 5.2: *Block diagram schematics of the high-fidelity dynamical propagator in the Simulink® environment.*

- Anomalous Oxygen component for appreciable O(+) and hot atomic oxygen contributions to the total mass density at high altitudes and applies primarily to drag estimation above 500 km.

The C++ function used in the propagator is based on the NASA distribution package of the FORTRAN model[1]. Thanks to the MEX wrapper for S-function, the C++ code is interfaced with the Simulink environment.

Orbital Dynamics Block

The Orbital Dynamics Block computes the acceleration of an Earth-orbiting satellite under the influence of:

- The Earth's harmonic gravity field.
- The atmospheric drag.
- The commanded thrust from the Actuator block.

The acceleration is computed in the EME2000 Orbital frame from the information on the position and velocity of a generic satellite at time t, as in Equation (3.16). The acceleration due to the harmonic gravity field is computed from the information on the position of the satellite at a generic time instant and the $\{l, m\}$ parameters.The GGM02S gravity model is based on the analysis of the in-flight data collected by GRACE during 363 days of measurements. It describes the gravitational field up to 160x160 degree order and includes the gravity anomalies over the surface of the Earth. Finally, the

---

[1] Package available at https://ccmc.gsfc.nasa.gov/pub/modelweb/

atmospheric drag contribution is provided by the Atmosphere Block, while the commanded acceleration imparted to the satellite is recovered from the control block. The function is implemented with a C++ based S-function, for an easier inclusion of the block in the Simulink environment via the MEX wrapper.

State Conversion EME2000 to ToD Block

The orbit dynamics is propagated in the EME2000 reference frame. Nevertheless, to include nutation and precession effect for a high-fidelity description of the dynamics, the satellite position and velocity are converted into the ToD orbital frame. The transformation is based on the rotation matrix $R_{eme2tod}$ (see Section 3.1), which includes both the effect of nutation and precession. This function is developed completely in the Simulink® environment and takes as input the information on the rotation matrix from the input file (see Section 5.2.2).

State Conversion absolute to relative

The state conversion block for relative quantities implements several S-function sub-blocks for the computation of relative and absolute state of the chief and the deputies:

- *Car2Kep Block*: implements the conversion between the inertial state to the orbital elements. It is implemented in a C++ function, taking as input the satellite state and the Earth's gravitational parameter.

- *Relative Cartesian Block*: implements the conversion from the inertial state (position and velocity) of two spacecraft to the Cartesian relative state (position and velocity), in the local Hill orbital frame of the chief satellite. It is implemented in a C++ function, taking as input the chief and the deputy inertial state.

- *ROE Block*: implements the conversion from the Keplerian elements of the chief and deputy satellites to the relative orbital element framework. It is implemented in a C++ function, taking as input the Keplerian elements of chief and deputies' satellites.

Outputs

The outputs of the high-fidelity propagator are reported in Table 5.3. The algorithms provide a high-fidelity ground truth base of the orbital dynamics of the formation flying. These values serve as inputs in the navigation algorithms for the formation performance definition.

Table 5.3: *Parameters and description of the input file for the initialisation of the GNC framework.*

Variable	Symbol	Unit	Description
EME2000 state	`yC_EME`, `yD_EME`	m, m/s	State vector of the chief and deputies satellites in EME2000 frame
ToD state	`yC_ToD`, `yD_ToD`	m, m/s	State vector of the chief and deputies satellites in ToD frame
Keplerian elements	αC, αD	m, -, rad	Osculating Keplerian elements of chief and deputies
RTN state	`yRTN`	m, m/s	Relative state vector of deputies satellites in RTN frame
ROEs state	$\delta\alpha$	-	Relative orbital element vector of deputies satellites in ROEs frame

5.2.4 Guidance

The Guidance Block is based on the analyses presented in Section 4.1. The block aims at providing a reference trajectory and control to the Control block, depending on the scenario to be simulated. This block has been developed in Simulink® environment, based on the algorithms for the definition of the optimal reference trajectory for different case scenarios. The inputs to the guidance block mainly depends on the test case scenario, the number of spacecraft, and the sample time. Specifically, it takes the reference trajectory designed with the convex optimization tool in open loop for different operation phases. This procedure is computed offline implementing the COCP, and then the resulting optimal trajectory and control profile are included in the guidance block. The reference trajectory can either be a maintenance of the operative orbit or the manoeuvre between two different formation configuration. The scheme of this block is reported in Figure 5.3. It shows that the outputs are used as input for the Control block. Specifically, it provides:

- Desired reference trajectory: `xRTN_des` or `ROEs_des`. It provides the desired trajectory for the relative motion of the deputies' satellites with respect to the chief, for the case scenario under study. It is provided both in RTN or ROEs framework.
- Reference control law: `uRTN_des`. It provides the reference continuous control law for the desired trajectory, in the RTN frame.

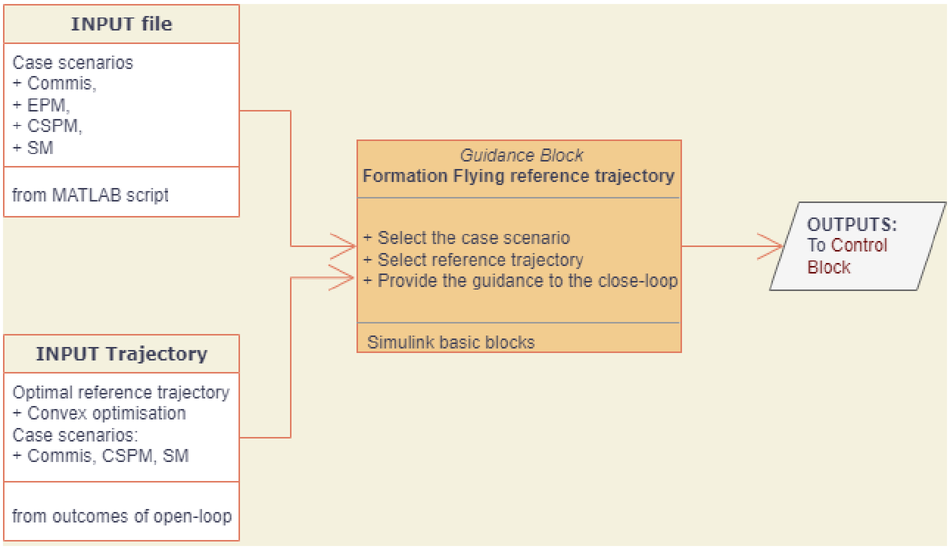

Figure 5.3: *Block diagram schematics of the guidance block in the Simulink® environment.*

5.2.5 Navigation Block

The Navigation block includes the procedures and algorithms necessary to estimate the absolute and the relative state of the satellites in the formation, based on GNSS navigation. In this dissertation, we consider a decentralized architecture, where each vehicle computes its relative state through a navigation filter. Specifically, the onboard sensors provide measurements on the position and velocity evolution of each satellite during the time. These measurements are subject to noise and disturbances, caused by the sensor's accuracy on the measures, and the navigation algorithms aim at filtering and processing such information, to generate a good estimation of the actual state of the satellite. The inputs to the Navigation block are reported in Table 5.4.

Table 5.4: *Parameters and description of the input variables for the navigation block.*

Variable	**Symbol**	**Unit**	**Description**
Sample time	`Step`	sec	Time step of the simulation
Number of satellites	`N_sat`	-	Number of deputies in the formation
Ground truth absolute state	`X_tod`	m, m/s	Ground truth absolute state of the deputy satellites in ToD
Ground truth relative state	`xRTN`	m, m/s	Ground truth relative state of the deputy satellites w.r.t. the chief
Onboard absolute state	`X`	m, m/s	Onboard absolute state of the deputy satellites
GNSS error in the position	`err_pos`	m	Absolute position navigation error from the GNSS receiver
GNSS error in the velocity	`err_vel`	m/s	Absolute velocity navigation error from the GNSS receiver
Carrier phase error	`err_cp`	-	Carrier phase error of the GNSS receiver
Code measurement error	`err_cm`	-	Code measurement error in the GNSS receiver

Decentralised architecture

A decentralized approach is selected for the possibility of an autonomous GNC management without the mediation from a specific satellite. Each spacecraft is supposed to have the same computational and data-handling capabilities and to autonomously elaborate their measurements. The continuous mutual exchange of GNSS navigation data enables the reconstruction of the absolute formation status at each time instant onboard each satellite. Moreover, each spacecraft could recover, from the information on the absolute formation status, its relative state associated with a virtual spacecraft at the centre of the formation. The elements of the virtual satellite are propagated in time thanks to the onboard dynamical propagator. The GNC algorithms are elaborated by each satellite of the formation in the reference frame of the virtual platform. This architecture is shown in Figure 5.4, where the virtual platform is identified by dashed contours, and the deputies are called 'A', 'B', 'C', and 'D' respectively. During the nominal phases of the mission, it is important the correct sharing of data among the satellites, to enable the autonomous navigation and path planning of the formation. The navigation logic for the exchange of data is selected as follow:

- Each satellite (A, B, C, or D) transmits the current state to the remaining satellites.
- Each satellite receives the data from the other platforms.
- Each satellite computes the current navigation state estimate in the local frame of the virtual satellite.

GNSS receivers block

The GNSS receivers can provide three different measures: the pseudo-range, the carrier phase, and the Doppler measurement. The former is the range between the GNSS satellite and the user, in our case one of the satellites of the formation. It is subject to some noises, the receiver clock error, the ionospheric error, and other sources. The second instead, measure the difference between the carrier phase of the GNSS and the receiver satellite, and the Doppler measurement provides information on the range rate [155]. In this simulator, information on the absolute position and velocity given by the GNSS receiver is obtained by perturbing the state of the satellites in ToD with a noise term. The high-fidelity propagation in ToD from the dynamical environment is considered representative of the

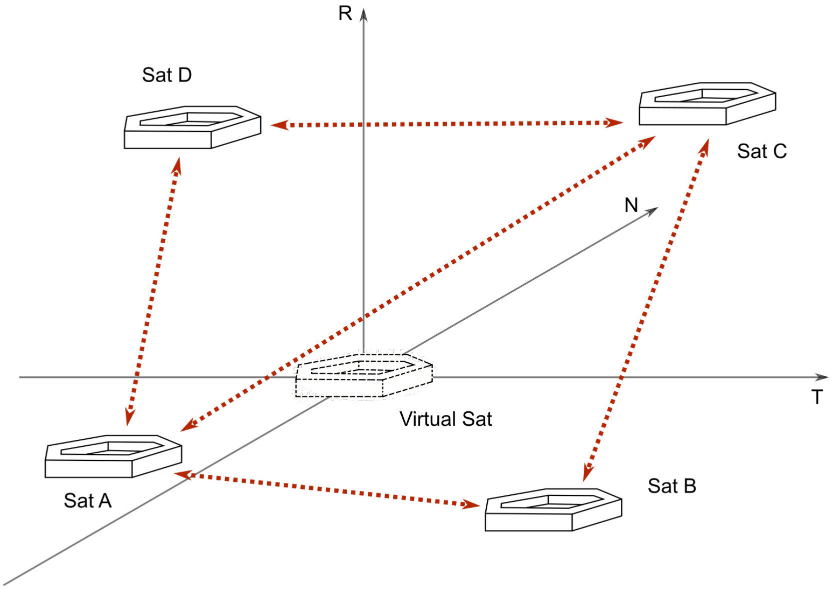

Figure 5.4: *Selected logic for the navigation system based on a decentralised approach.*

ground truth dynamics of the formation, whereas the noise term is representative of the sources of uncertainties in the signal received from the GNSS satellites. A zero-mean Gaussian noise used to perturb the ground truth propagation is selected according to the physical properties of the GNSS receivers. In this work, the GNSS error has been considered with no temporal correlation. This aspect must be included in a further development of the study, since the temporal dependency has an important contribution on the GNSS errors.

Extended Kalman Filter

The navigation system aims at estimating the absolute and the relative state of the satellites in the formation. The navigation algorithms are introduced to filter and process data from navigation sensors, to generate a good estimation of the actual state of the satellite. For space application, the typical filter used for absolute and relative state estimation is the Extended Kalman Filter [156]. It is an extension of the classical Kalman filter for non-linear dynamics representation. The general idea of the EKF is to provide a recursive estimate for the state in time by propagating the current estimate of the state and the error covariance matrix. At every time step, we assume the existence of a closed-form expression for the predicted state as a function of the previously estimated state $\boldsymbol{x}_k$, noise $\boldsymbol{w}_k$, control $\boldsymbol{u}_k$, and time t:

$$\boldsymbol{x}_{k+1} = f(\boldsymbol{x}_k, \boldsymbol{u}_k, t) + \boldsymbol{w}_k \tag{5.1}$$

Where the function $f(\boldsymbol{x}_k, \boldsymbol{u}_k, t)$ provides the state x_{k+1} as function of x_k, u_k, and t to the net of the noise contribution. The Jacobian of the predicted state is computed as the partial derivative over the previous state.

$$\boldsymbol{F}^x = \frac{\partial f(\boldsymbol{x}_k, \boldsymbol{u}_k, t)}{\partial \boldsymbol{x}_k} \tag{5.2}$$

The Jacobian can be used to predict the covariance estimate from the process noise covariance $\boldsymbol{Q}_k$:

$$\boldsymbol{P}_{k+1} = \boldsymbol{F}^x \boldsymbol{P}_k \boldsymbol{F}^{x'} + \boldsymbol{Q}_k \tag{5.3}$$

A similar procedure is applied to compute the update value of the measurements z_k:

$$z_{k+1} = h(\boldsymbol{x}_x, t) + \boldsymbol{v}_k \tag{5.4}$$

Where $h(\boldsymbol{x}_x, t)$ is the function to compute the measurement $\boldsymbol{z}$ from the state $\boldsymbol{x}_x$, and $\boldsymbol{v}_k$ is the measurement noise. The Jacobian of the measurement can e computed from the partial derivative of $h(\boldsymbol{x}_x, t)$ over the state: $\boldsymbol{H}^x$. Once the main correlation have been defined, the update of the state is computed at each time step with the following procedure, considering $\boldsymbol{R}_k$ the process noise covariance:

$$\begin{aligned}
\tilde{\boldsymbol{y}}_{k+1} &= \boldsymbol{z}_{k+1} - h(\boldsymbol{x}_k, t) \\
\boldsymbol{S}_{k+1} &= \boldsymbol{H}_{k+1}\boldsymbol{P}_{k+1}\boldsymbol{H}'_{k+1} + \boldsymbol{R}_k \\
\boldsymbol{K}_{k+1} &= \boldsymbol{P}_{k+1}\boldsymbol{H}_{k+1}\boldsymbol{S}'_{k+1} \\
\hat{\boldsymbol{x}}_{k+1} &= \boldsymbol{x}_{k+1} + \boldsymbol{K}_{k+1}\tilde{\boldsymbol{y}}_{k+1} \\
\hat{\boldsymbol{P}}_{k+1} &= (\boldsymbol{I} - \boldsymbol{K}_{k+1}\boldsymbol{H}_{k+1})\boldsymbol{P}_{k+1}
\end{aligned} \tag{5.5}$$

The estimate of the state $\hat{\boldsymbol{x}}_{k+1}$ is provided together with the covariance matrix $\hat{\boldsymbol{P}}_{k+1}$, which gives an idea of the level of uncertainty in the current estimate. Each term in the covariance matrix represents the square error between the real and the estimated state. The navigation system aims to obtain an accurate estimate of the relative state of the satellites from raw GNSS measurements.

Absolute and relative state estimation block

As explained above, the state estimation block is based on an Extended Kalman Filter (EKF), which processes the information from the GNSS satellites and the state variable connected to the other satellites in the formation. The inputs to the state estimation block are the satellite state computed from the GNSS sensors and the formation status. The latter is exchanged among the formation with the inter-satellite communication link. The initial covariance on the satellite state knowledge is given as a covariance matrix P_0. Moreover, an additive measurement noise with covariance R_0 is included in the model, as well as a measurement function to recover the state from the non-linear dynamics. In the estimation filter, the knowledge on the onboard non-linear dynamical propagator for the absolute state reference is the state transition value and it implements the main LEO perturbing effects. The algorithm includes both the mean J_2 contribution of the Earth's oblateness and the drag effects. Besides, to improve the performances of the state reconstruction, the Jacobian function of the dynamical propagator is included in the model. Finally, the process noise is included in the state transition value with the covariance matrix Q_0, which represents the additive process noise. The parameters used in the simulator to provide the absolute and the relative state estimation in the close-loop of the GNC simulator are used as input for the (EKF) to estimate the actual state from the GNSS sensor measurements. The variance of the position and velocity is selected according to the GNSS sensor characteristics [37, 110]:

- For the absolute estimation, an error in the sensor measurements in the order of $1\,\mathrm{m}$ and $0.2\,\mathrm{cm\,s^{-1}}$, for the position and velocity respectively, is considered in the variance definition.
- For the relative navigation estimation, an error in the sensor measurements in the order of $10\,\mathrm{cm}$ (σ) and $0.1\,\mathrm{mm\,s^{-1}}$ is considered for the position and velocity, respectively.

For both absolute and relative state estimation, the initial state estimation covariance matrix P_0 is selected for the initial step and then at each time is updated in the algorithm considering the residual error from the previous step. Consequently, an adaptive EKF is considered in the navigation block, to improve the state reconstruction performances. Particularly, the relative navigation after the filter reconstruction is below few centimetre accuracy. An important consideration is needed for the relative state reconstruction. The relative state is computed from the GNSS measurements between a couple of satellites in the formation. Between two receivers of two different satellites, i and j, the single difference carrier phase measurement can be computed as:

$$\rho_{sdcp}^{ij}(t) = \rho_{cp}^{j} - \rho_{cp}^{i} \tag{5.6}$$

This procedure can be applied to any couple of satellites in the formation. Similarly, a single difference among the Doppler measurement can be computed to provide the range-rate change in time:

$$\Delta\phi^{ij}(t) = \phi^{j} - \phi^{i} \tag{5.7}$$

The advantage of using the differential measurement is the cancelling of the ionospheric noise, which affects the accuracy of the GNSS measurements. Moreover, it provides a value with smaller uncertainties and external noises. Now the state vector for the formation can be computed at each time instant as:

$$x_{RTN} = \left\{ x_{ABS}^{i}, \qquad x_{rel}^{1i}, \qquad \dots \qquad x_{rel}^{ji}, \qquad \dots \qquad x_{rel}^{(N_{sat}-1)i} \right\} \tag{5.8}$$

Where the index i stands for the reference satellite in the formation and the index j represents the other satellites for $j = 1 : N_{sat} - 1$, with N_{sat} the number of vehicles in the formation. In this work, we start from the absolute state estimation in the ToD frame, and we recover the relative state of the satellite j of the formation with respect to the reference i satellite. The measurement vector is the relative state of the satellites in the formation corrupted by a zero-mean Gaussian noise. The relative navigation filter is used to estimate the relative position and velocities of the satellites in the formation from the noisy measurement.

Navigation error

The characterization of the estimation error is important to assess the performance of the navigation filter. The state estimation error can be computed at each time step by subtracting the actual $x(t)$ and the estimated state $\hat{x}(t)$:

$$e_{nav}(t) = x(t) - \hat{x}(t) \tag{5.9}$$

Another parameter to assess the performance of the state estimation is the standard deviation, from the filter covariance matrix P_k:

$$\sigma_k = \sqrt{P_k} \tag{5.10}$$

Both the navigation error and the standard deviation provide a performance of the navigation solution with respect to the actual state at each time instant. An example of the performances of the EKF for the relative navigation estimation is provided in Figure 5.5. The figure on the top (Figure 5.5a) shows the uncertain measurement form the on-board sensor, introducing an error of about 10 to $20\,\mathrm{cm}$ in the relative state. After the filter processing via the EKF, the uncertainty is reduced to a few centimetre level. This is displayed in the figure on the bottom (Figure 5.5b), and represent an example of the navigation error defined in Equation (5.9).

Block scheme

The scheme of the navigation block is described in Figure 5.6, where the receivers and the filter blocks are described.

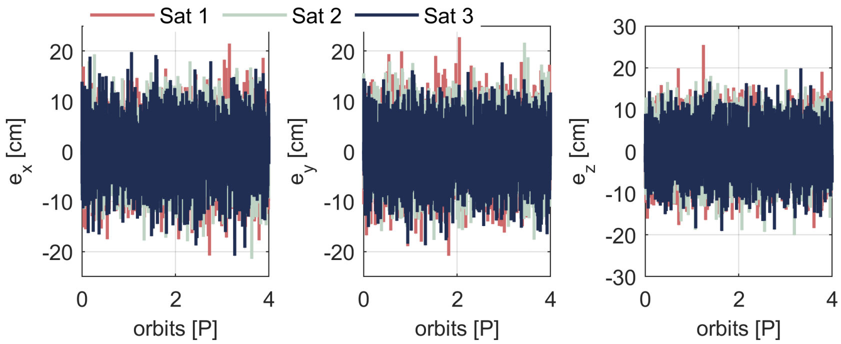

(a) *Uncertain measurement from the navigation sensor.*

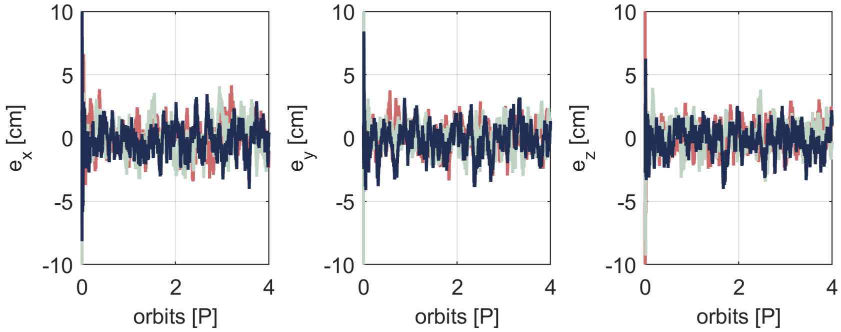

(b) *Accuracy of the on-board navigation reconstruction.*

Figure 5.5: *Example of the performances of the EKF for the on-board relative navigation estimation.*

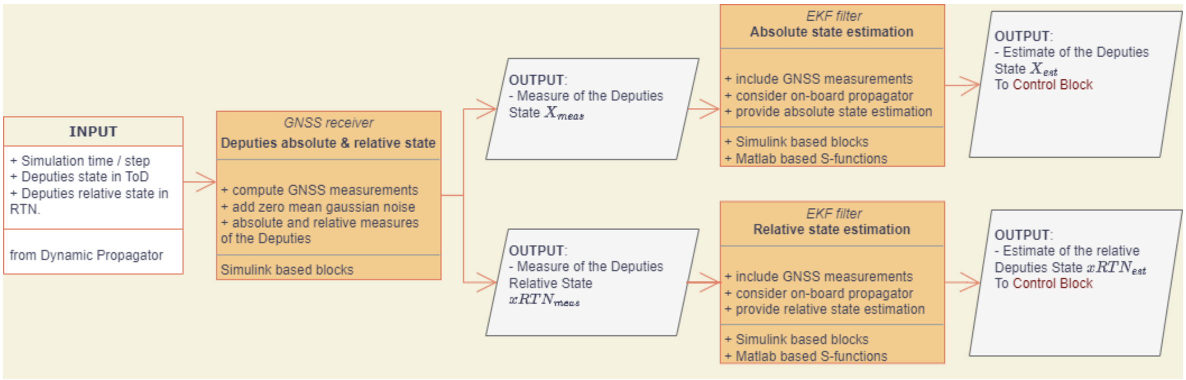

Figure 5.6: *Block diagram schematics of the navigation block in the Simulink® environment.*

Outputs

The navigation block provides as outputs the reconstruction for both the absolute and the relative sate of the vehicles in the formation. At the same time, the navigation error is computed as output of the block, to assess the accuracy of the navigation. The output parameters are reported in Table 5.5.

Table 5.5: *Parameters and description of the outputs for the navigation block.*

Variable	Symbol	Unit	Description
Estimated absolute state	`X_est`	m, m/s	Estimated absolute state from the navigation filter for deputies' satellites
Estimated relative state	`xRTN_est`	m, m/s	Estimated relative state for deputies' satellites w.r.t. the virtual chief
Navigation error	`err_nav`	m, m/s	Navigation error with respect to the ground truth

5.2.6 Control Block

The Control Block includes the procedures and algorithms necessary to provide a control thrust to the satellites in the formation. It takes both the information on the desired state from the Guidance Block and the estimated state from the Navigation Block. In this work we implements a continuous thrust architecture, based on ion thrust engines. The inputs of the control block are reported in Table 5.6.

Table 5.6: *Parameters and description of the input variables for the control block.*

Variable	Symbol	Unit	Description
Sample time	`Step`	sec	Time step of the simulation
Number of satellites	`N_sat`	-	Number of deputies in the formation
SC Mass	`M`	kg	Mass of the satellites
Desired relative state	`xRTN_des` or `ROE_des`	m, m/s, rad	Desired relative states of the deputies from the guidance block
Actual relative state	`xRTN_est` or `ROE_est`	m, m/s, rad	Estimated relative state of deputies from the navigation block
Actual absolute state	`X_est`	m, m/s	Estimated absolute state from the navigation block

The block diagram in Figure 5.7 describes the schematics of the control block. It is composed of two main blocks:

- Controller Block: provides the ideal control to the close-loop simulator from the error difference between the desired and the estimated satellites state.
- Actuator Block: implements the ideal control in the onboard thrusters, considering the technological limitations to provide the actual control to the close loop simulator.

It requires two inputs information: the desired relative state of the deputies, given by the Guidance block, and the estimated absolute and relative states of the deputies, given by the Navigation block. The following subsections describe the models implemented in each block of the Control algorithm.

Controller block

The control algorithm implements the manoeuvre commanded by the guidance algorithms and provides the command control to the actuators. It implements a control to minimize the error between the actual state and the desired state (see Section 4.2), from the navigation reconstruction and the guidance algorithms, respectively. The Controller Block implements a feedback control law for non-linear system dynamics and in particular a feedback linearisation of the system error. The following procedure is implemented:

- The system error is computed from the comparison between the desired and the estimated relative states of the Deputies:
  - RTN error: $e(t) = xRTN_{est} - xRTN_{des}$

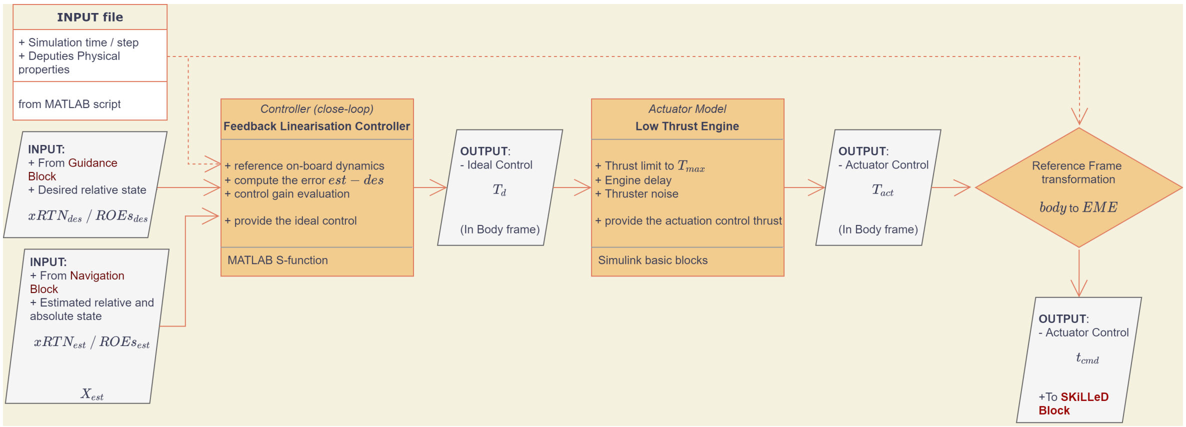

Figure 5.7: *Block diagram schematics of the control block in the Simulink® environment.*

  - ROEs error: $e(t) = ROE_{est} - ROE_{des}$

- Positive-definite control gain parameters (k_1 and k_2) are introduced to compute the equivalent input for ideal control definition.
- The onboard dynamics (J_2 and drag) is considered the reference for the deputies evolution.
- From the current state and the reference dynamic of the deputies, the commanded control is computed.

Finally, the commanded control law is provided as input to the Actuator Block.

Low thrust Actuator Model

After the definition of the ideal control law in the Controller block, it is important to characterise the actual control that the onboard thruster can provide. The deputies satellites are considered equipped with low-thrust engines, and specifically for the FFLAS case, the QinetiQ T5 are considered [157]. In this work, the commanded control is elaborated and transmitted by the propulsion control unit to the engine assembly, which has an intrinsic delay in the response time and saturation limits. Finally, noise terms and error terms are introduced on the thrust level, to account for the real behaviour of the engine, as well as to simulate errors in the attitude of the satellites. The following considerations are included in the Actuator block, to represent the real behaviour of the onboard actuators:

- Maximum thrust limitation: a saturation limit is implemented, to guarantee that the required thrust is below the technological limit.
  - $|T| \leq T_{max}$
- Control delay term: a real actuator will always introduce a delay in the ideal control, due to the intrinsic time delay in the actuator response.
  - The ideal control is elaborated and transmitted by the propulsion control unit to the engine assembly, which has an intrinsic delay in the response time.
- Thruster errors: noise terms, error terms, and attitude uncertainties are introduced on the thrust level, to account for the real behaviour of the engine.

- Aim at simulating a real scenario for the close loop implementation.

Outputs

The outputs of the Control block are reported in Table 5.7. The actuator thrust provided by the control block serves as input for the high-fidelity dynamical propagator, to include the control effort in the dynamics. For this purpose, the actuator control law is transformed in the absolute EME2000 frame before it can be used in the dynamical propagator block. Moreover, the control block provides a real-time assessment of the inter-satellite distance among the vehicles of the formation. This is essential for safety consideration of the formation, to ensure collision avoidance among the spacecraft. In case the minimum safety distance among the vehicle is not respected, a flag is introduced in the control and guidance block to switch the operation to the immediate transition to the safe mode configuration.

Table 5.7: *Parameters and description of the output variables for the control block.*

Variable	Symbol	Unit	Description
Actuator command thrust	`T_EME`	N	Thrust given by the onboard engines
Inter-satellite distance	`3D_ca`	m	Check on the real-time inter-satellite distance among the satellites

5.2.7 Payload Block

The paylaod block includes the procedure and algorithms necessary to estimate the antenna response of the L-band paylaod. The procedures developed in Section 2.4.3 is considered, and it takes as input the actual relative state of the formation. This block is only used during the simulation of the passive interferometry distributed systems to characterise the science phase. It takes as input the actual state from the propagator block of each satellite in the formation. Then it computes the visibility and the array factor functions, as described in Table 5.8. This block allows to compute the performances of the distributed paylaod, including the external uncertainties and the control accuracy. In this way we can assess how much the paylaod is affected by the error in the relative state over the simulation.

Table 5.8: *Parameters and description of the inputs/outputs for the payload block.*

Variable	Symbol	Unit	Description
Inputs			
Actual absolute state	`X`	m, m/s	Absolute state from the propagation block
Actual relative state	`xRTN`	m, m/s	Relative state from propagation block
Outputs			
Visibility function	`V`	-	Visibility function of the synthetic antenna array
Array Factor	`AF`	dB	Impulse response of the antenna array

5.3 Chapter conclusion

In this chapter, the GNC framework has been presented in detail. The closed-loop logic and the main building blocks are discussed in detail. First, the correct procedure to set up the initialisation file for the framework is presented, including all the input parameters to be provided in MATLAB/Simulink® environment. Then, block-by-block, the simulator is discussed. The high-fidelity simulator is presented, providing the input and output parameters and a detailed discussion on the model implemented for the computation of the absolute and relative dynamical evolution of the satellites in the formation. Then, a similar procedure is implemented to present the GNC part of the simulator. For each block the initial conditions, the algorithms used, and the expected outputs are presented. The analysis aims to provide an insight into the GNC simulator, understanding the potentiality to be exploited during the test case phase. In the subsequent part of the dissertation, the results of the simulation using the GNC framework are discussed, see Chapters 6 and 7. Specifically, the GNC framework has been applied to the FFLAS study to assess the performances of different operational phases (from launch to end-of-life) and the corresponding reconfiguration manoeuvres. The entire Chapter 7 is dedicated to the FFLAS analysis.

CHAPTER 6

Results Part I: Active and Passive Mission Scenarios

C'è un concetto di base nella scienza: ogni scoperta,
ogni invenzione è sempre il frutto di ricerche
precedenti che hanno preparato il terreno

— Alberto Angela

THE methodologies, algorithms, and framework described in the previous chapters have been designed to support performance analysis of distributed systems in LEO, carrying active or passive interferometer antennas. The theoretical derivation depends neither on the number of spacecraft nor the specific mission scenario. Still, it can be applied to a multitude of different cluster/formation concepts for optimal reconfiguration design and performance assessment of closed-loop relative GNC systems based on GNSS navigation.

Chapters 6 and 7 of this thesis are dedicated to the definition, design and numerical simulation of the test cases identified in Chapter 2. For clarity and organisational purposes, the numerical results are divided into two parts as follows:

1. Chapter 6 presents the design and simulation for the active SAR scenarios (SA1 - ROSE-L tandem study and SA2 - Harmony study), as well as the analysis and trade-off performed for the passive interferometer scenarios (SP1 - FFLAS, SP2 - planar array scenarios, and SP3 - non-planar array scenario).

2. Chapter 7 focuses on the main simulation scenario of this dissertation, the FFLAS study (SP1) for distributed passive interferometry, providing the analysis developed for the different operational phases of the mission.

Such an organisation of the achieved results reflects the development of the research activities. In fact, during the first year and a half of this PhD, the main focus was dedicated to the preliminary mission analysis and GNC architectural design and simulation for the ESA-funded FFLAS project, in collaboration with Airbus D&S Madrid. Accordingly, a detailed analysis has been carried out, including the design and simulation of the main operational phases of that formation flying mission, from launch to disposal.

This chapter starts by presenting active SAR scenarios. It reports the analyses carried out during the visiting period in the Mission Analysis Support section of the Earth Observation Program department (EOP-PES) in ESA-ESTEC under the supervision of Berthyl Duesmann and Dr Manuel Martin-Neira. The second part is dedicated to the trade-off analysis and geometry selection of the formation for the FFLAS study. Moreover, it provides follow-on investigations to deal with the limitations that arose within FFLAS. Specifically, it proposes planar and non-planar formation geometries to perform distributed passive interferometry.

6.1 SA1: Two-Satellites SAR

The two-satellites SAR concept is studied to support the development of the ROSE-L tandem mission study for land monitoring and emergency management services. The baseline of this concept relies on two identical satellites flying in a tandem configuration, following the lesson learnt from TDX/TSX mission. It was carried out during the research visiting period in ESA-ESTEC. The scope of study in the context of this thesis is to assess the feasibility of formation control with different GNC algorithms and methodologies.

The reference orbit for the tandem formation is the one of Sentinel 1: a SSO, with a mean altitude of $690\,\mathrm{km}$, and an LTAN at 18:01. For the simulation, the reference epoch is set equal to June 1st 2028 at midnight. Moreover, a frozen eccentricity condition is selected to comply with the SSO property. Table 6.1 shows the initial conditions employed in the simulations in terms of time (UTC), state of the absolute orbits (EME2000), and Keplerian osculating elements.

Table 6.1: *Initial conditions of the SA1 test case.*

Variable	Value
`UTC`	00:00 01/06/2028
`X_EME`	$\{6.967 \cdot 10^6,\ 1.238 \cdot 10^6,\ -19.17 \cdot 10^3,\ 0.198 \cdot 10^3,\ -1.052,\ 7.429 \cdot 10^3\}$ (m, m/s)
α	$\{7.080 \cdot 10^6,\ 0.00127,\ 98.202,\ 10.05,\ 68.77,\ 291.075\}$ (m,-,deg,deg,deg,deg)

6.1.1 Analysis on the altitude profile

The evolution of the altitude profile and the velocity magnitude over the latitude has been computed to assess the daily variation due to external perturbations: a 70×70 gravity field perturbation, the NRLMSISE-00 atmospheric model, and the spherical model of the Solar Radiation Pressure for a one-day propagation time. The results of the analysis are shown in Figure 6.1, under the hypothesis of no control of the absolute orbit. An altitude variation between $725\,\mathrm{km}$ and $697\,\mathrm{km}$ is present over one day period, which corresponds to a $0.02\,\mathrm{km\,s^{-1}}$ variation of the velocity magnitude over latitude. A small variability can be seen over any given latitude, reflecting the orbit's frozen SSO condition. This analysis is important to understand the variability in the SAR image acquisition at different latitudes from the absolute orbit point of view. A minimum variability is envisioned to improve the coherency among various observations. This analysis has been done a priori for selecting the frozen orbit condition.

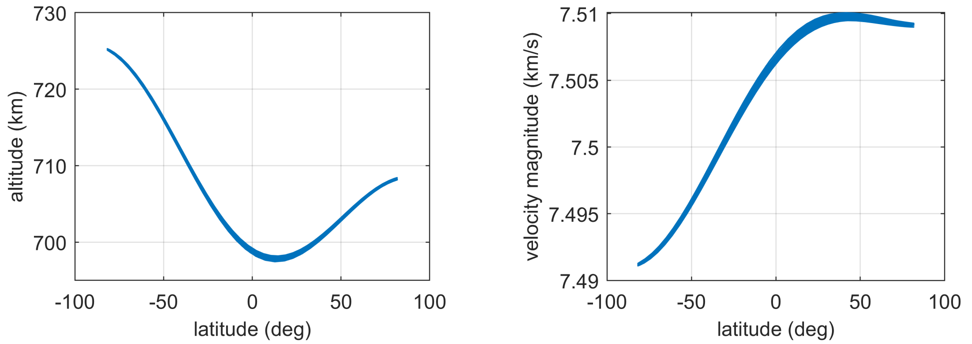

(a) *Evolution of altitude as function of latitude.* **(b)** *Evolution of velocity as function of latitude.*

Figure 6.1: *Altitude and velocity evolution under perturbed absolute dynamics for the frozen SSO.*

6.1.2 Relative motion

The requirements for the relative motion trajectory have been provided as input to this analysis from the "Mission Analysis Report" of the ROSE-L study. From this document, a helix formation has been selected (see Section 3.3). The formation consists of:

- Satellite 1 or Chief flying on the reference orbit. It is considered at the origin of the local orbital frame.
- Satellite 2 or Deputy flying in a helix trajectory, with a slightly different magnitude of the relative inclination and eccentricity vectors.

The analysis aims to set up a relative orbit with (anti-)parallel relative eccentricity/inclination vectors for passive safety purposes.

Relative Eccentricity/Inclination separation The initial conditions for the helix formation are chosen to establish a (anti-)parallel configuration of the relative eccentricity/inclination (e/i) vectors [74]. Accordingly, a relative helix trajectory is achieved, where the out-of-plane (horizontal) and radial (vertical) components never vanish simultaneously. Consequently, the relative orbit is designed so that the two spacecraft never cross to guarantee safe operations, also in the presence of large uncertainties in the along-track direction. To achieve such relative motion, the relative orbit shall guarantee [74]:

- A given (not null) magnitude of the relative inclination vector $\delta \boldsymbol{i}$, related to the maximum cross-track displacement.
- A given (not null) magnitude of the relative eccentricity vector $\delta \boldsymbol{e}$ related to the maximum in-plane relative displacement
- A $0 + k180$ deg separation in the phase angles of the relative eccentricity and inclination vector to maximise the minimum radial-normal inter-satellite separation.

These considerations derive from the correlation between ROEs and RTN described in Equation (3.37). In the case of a difference in the semi-major axes of the satellites, a mean, not null, separation in the radial direction is present, and the transversal separation varies over time. Regarding safety operations, it is important to recall that typically the uncertainties in the along-track are higher than in the radial and cross-track direction, and this impact the design of the mission profile. Specifically, from the analysis in [74], we get the following considerations:

- Setting a parallel or anti-parallel $\delta \boldsymbol{e}$ and $\delta \boldsymbol{i}$ or for values of the relative semi-major axis well smaller than $\boldsymbol{i}$ and $\delta \boldsymbol{e}$ guarantees a safe formation, and in particular, the spacecraft separation is never null:
    - A maximum radial separation Δx is present when the normal separation is $\Delta z = 0$.
    - A maximum normal separation Δz is present when the radial separation is $\Delta x = 0$.

Consequently, the following initial conditions have been selected for the deputy satellite:

$$a\delta\boldsymbol{\alpha}_0 = \{0, \quad 0, \quad 0, \quad 400, \quad 0, \quad -350\}\, m \tag{6.1}$$

An analysis to understand the effect of orbital perturbations also in the presence of uncertainties has been carried out to evaluate the nature of passive safety of the selected relative trajectory.

Effect of J2 perturbation The first analysis assessed the secular effect of the Earth's oblateness (J_2) on the relative motion over 1 and 15 days of propagation. The three-dimensional representation of the relative orbit for 1-day and 15-day propagation is shown in Figure 6.2. For the 1-day propagation, a small oscillation in the radial-normal plane is present in time but without making collide the two vehicles. Similar considerations apply for the 15-day propagation; the effect of the J_2 perturbation causes a drift in the relative trajectory but keeps the deputy far from the chief satellite. The time evolution of the relative eccentricity/inclination vector separation gives an immediate representation of the passive safety. As represented in Figure 6.3a, δe and δi vectors remain almost parallel even in the presence of Earth's oblateness since the initial conditions have been chosen with $\delta i_x = 0$. Nevertheless, increasing the propagation time to 15 days, it is possible to appreciate the rotation of the relative eccentricity vector, going toward the orthogonal unsafe condition at the rate of $\dot{\phi}$ of Equation (3.52).

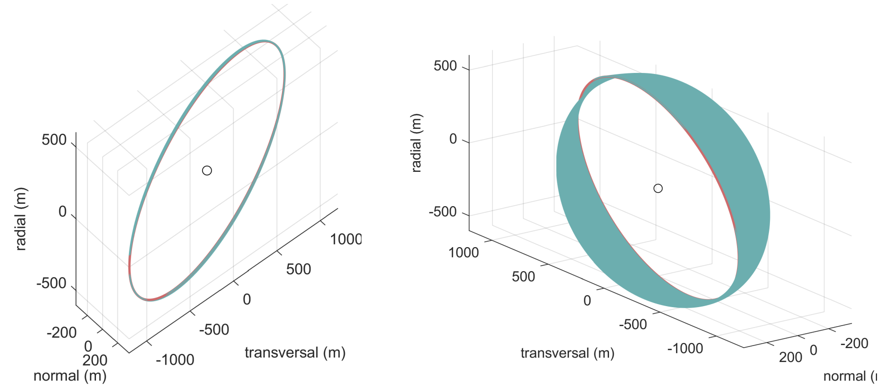

(a) *volution over 1-day period* **(b)** *volution over 15-days period*

Figure 6.2: *Evolution of the helix relative trajectory under Earth oblateness.*

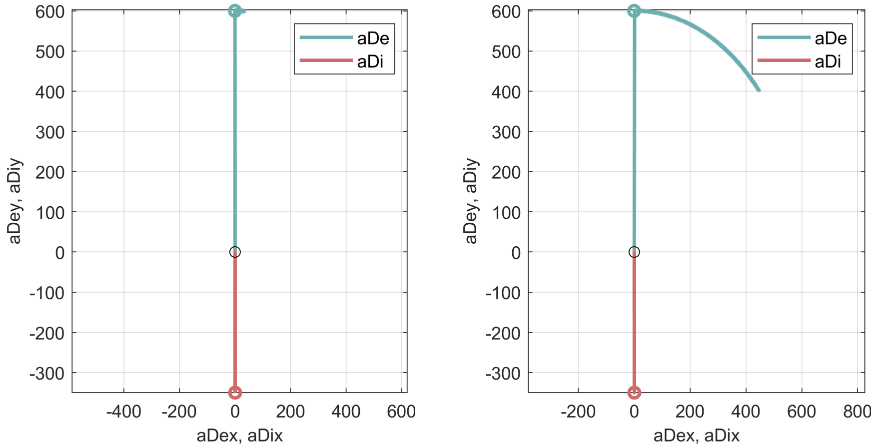

(a) *Evolution over 1-day period.* **(b)** *Evolution over 15-days period.*

Figure 6.3: *Evolution of the relative eccentricity/inclination vector under Earth oblateness.*

Effect of uncertainties in the relative semi-major axis The initial conditions of the helix relative trajectory are tested in the presence of an offset in the relative semi-major axis δa. This offset could be caused by uncertainties in the formation acquisition, the error in the relative navigation solution, and/or the relative control. Therefore, we impose a separation of $a\delta a\ = 1\,\mathrm{m}$ to the initial conditions. The relative motion is then propagated for 15 orbital periods to assess the effect of the Earth's oblateness perturbations. The results of the analysis are reported in Figure 6.4, showing no impact of such an error on the passive safety condition in the first 15 orbits. As for the minimum RN distance, provided a proper e/i phasing, the impact on the magnitude is negligible when $\|\delta a\| \ll \min\{\|\delta e\|, \|\delta i\|\}$. However, in the presence of a non-vanishing relative semi-major axis, the y-component of the relative inclination vector varies over time, contributing to the change of the e/i phasing w.r.t. the (anti-)parallel nominal condition.

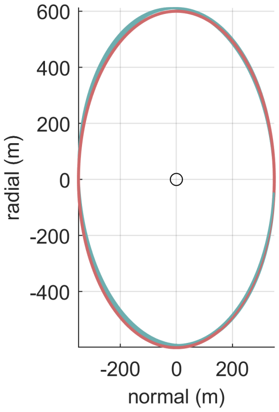

Figure 6.4: *Effect of the Earth's oblateness perturbation with a non-null relative semi-major axis offset.*

6.1.3 Impulsive vs continuous control strategy

After the analysis of the effect of the Earth's oblateness effect, it was required to study and compare different control strategies.

The study aims to perform a comparison between impulsive and continuous control approaches to identify the benefit and disadvantages of both strategies for formation maintenance.

Specifically, the ROSE-L study has been proposed under an impulsive control scheme (i.e. similar to the TDX/TSX mission). Therefore, the research question was to evaluate the feasibility of implementing a continuous control scheme (as derived in Chapter 5) in terms of fuel consumption to guarantee a control accuracy continuously over the mission timeline below $20\,\mathrm{m}$. The main requirements of the analysis are the following:

- The spacecraft separation varies from $400\,\mathrm{m}$ in normal direction to $600\,\mathrm{m}$ in radial.
- A daily variation of the relative eccentricity vector De_{daily} of about $-37\,\mathrm{m}$ is present under the J_2 perturbation (with respect to the nominal value), due to the change of phase (i.e. the magnitude remains constant).
- The control accuracy shall be within $\pm 20\,\mathrm{m}$.

Impulsive control The impulsive propulsion system consists of a pair of engines that can provide up to $1\,\mathrm{N}$ thrust. In the analysis, a satellite with the physical properties of Sentinel 1 satellite has been considered, with a mass of about $2000\,\mathrm{kg}$. The control strategy is based on the control of the eccentricity/inclination vector separation developed in [74]. Starting from the delta-v budget to compensate for the daily drift, we can assess the control effort for formation maintenance. Specifically, the impulsive delta-v correction is based on the relation in Equation (3.35) for orbital corrections and delta-v. First, in-plane manoeuvres can compensate for the drift in the relative semi-major axis and relative eccentricity vector. The in-plane relative motion can be maintained by two symmetric thrusts in the tangential direction, given a specific location in terms of the mean argument of latitude u. The magnitude of the delta-v is driven by the relative orbital elements corrections. The two in-plane impulses are computed as.

$$\Delta v_y^{(1),(2)} = \frac{v}{4}\left(De_{\text{daily}} - \frac{Da}{a}\right) \tag{6.2}$$

where De_{daily} is daily variation of the relative eccentricity vector and Da is the difference in the relative semi-major axis. The two manoeuvre are performed at $u^{(1)} = \arctan\left(\frac{De_y}{De_x}\right)$ and $u^{(2)} = u^{(1)} + \pi$. Note that the daily De_{daily} depends on the Earth's oblateness effect and, for our scenario, is equal to $-37\,\mathrm{m}$. Compensating twice per day, the maximum displacement is limited to about $20\,\mathrm{m}$, respecting the initial requirement. The corresponding delta-v in the along-track direction is:

$$\Delta v_y = \Delta v_y^{(1)} + \Delta v_y^{(1)} = 1.332\,\mathrm{cm/s} \tag{6.3}$$

And this corresponds to a yearly along-track velocity increment of $4.861\,\mathrm{m\,s^{-1}}$.

Continuous control A feasibility analysis has been implemented for the continuous control strategy for formation maintenance. The control is based on an ion thruster engine, with about $3000\,\mathrm{s}$ of specific impulse and a maximum thrust of $2\,\mathrm{mN}$. The control logic implements the LQR closed-loop technique described in Chapter 5. The thrust capability in the radial direction is removed to reduce fuel consumption during the formation maintenance. After a sensibility analysis of the gain matrices of the control, the following values are considered for the convergence of the methodology:

$$\boldsymbol{Q} = \begin{bmatrix} 10^{-5}\boldsymbol{I}_{3\times3} & \mathbf{0}_{3\times3} \\ \mathbf{0}_{3\times3} & 10^{-2}\boldsymbol{I}_{3\times3} \end{bmatrix} \qquad \boldsymbol{R} = 10^{8}\boldsymbol{I}_{3\times3} \tag{6.4}$$

The resulting control thrust and accuracy of the continuous approach are shown in Figure 6.5. The thrust in the transversal direction (y) is limited at $2\,\mathrm{mN}$, while the one in the normal direction (z) is far below $1\,\mathrm{mN}$. From the thrust evolution, it is possible to compute the delta-v budget for continuous formation maintenance. It results in about $3\,\mathrm{cm\,s^{-1}\,d^{-1}}$ in the normal direction and about $10\,\mathrm{cm\,s^{-1}\,d^{-1}}$ in the transversal direction. Concerning the control accuracy, the error with respect to the nominal trajectory is kept below $10\,\mathrm{m}$ in the along-track, $5\,\mathrm{m}$ in the radial, and $2\,\mathrm{m}$ in the cross-track direction, respecting the initial requirement of the study.

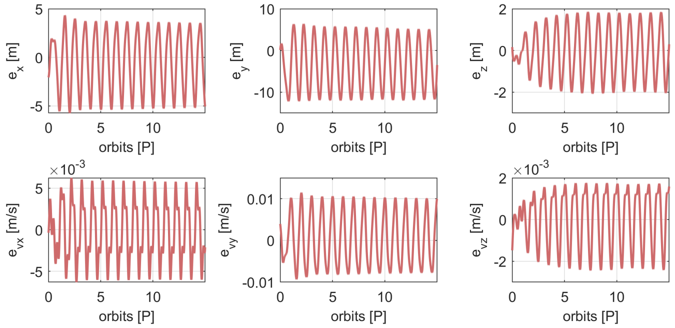

(a) *Control accuracy over 1-day period.*

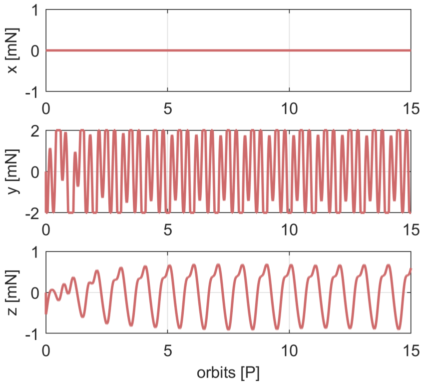

(b) *Thrust profile over 1-day period.*

Figure 6.5: *Continuous control performance over 1-day period.*

Conclusions In this analysis, two different control strategies (impulsive and continuous) have been implemented for the two-satellite formation ROSE-L. As for the impulsive approach, an in-plane control based on the methodology of [74] has been implemented, achieving results in terms of cost and accuracy in agreement with the ones obtained by the Mission Analysis Support Section (EOP-PES) of ESA/ESTEC. Instead, the continuous control approach has been implemented according to the methodologies developed in this research. The two strategies are intrinsically different. Impulsive control triggers an action only upon violation of the control accuracy threshold, leaving long intervals without interfering with the functioning of the scientific payload. Moreover, in this case, only in-plane corrections have been considered. Instead, the implemented continuous control continuously compensates for navigation and control errors in in- and out-of-plane components. This methodology is applicable when the payload is not disturbed by the accelerations produced by the control actions. The propellant mass can be computed from the delta-v analysis, knowing the specific impulse of the propulsion system in use. A hydrazine-based engine has been selected for the impulsive control, with a specific impulse of $226\,\mathrm{s}$. Instead, the specific impulse for the ion thrusters is $3000\,\mathrm{s}$. The computation is performed thanks to the Tsiolkovsky equation, which relates the delta-v and the propellant mass:

$$\Delta v = I_{sp} g \ln\left(\frac{m_0}{m_1}\right) \tag{6.5}$$

Where I_{sp} is the specific impulse of the engine, g is the standard gravity constant, m_0 is the initial mass, and m_1 is the new mass after the delta-v: $m_1 = m_0 - m_p$, with m_p the propellant mass used by the engine. This equation can be solved for m_p, providing the propellant mass required for formation maintenance. As a result, the comparison between the daily delta-v and propellant mass is possible:

- Impulsive control
  - Daily delta-v $1.332\,\mathrm{cm\,s^{-1}}$; propellant Mass $12\,\mathrm{g}$
- Continuous control
  - Daily delta-v $13\,\mathrm{cm\,s^{-1}}$; propellant Mass $9\,\mathrm{g}$

For the continuous control, the delta-v budget is higher, but thanks to the higher specific impulse, it corresponds to a smaller propellant mass than the impulsive strategy. Moreover, in both cases, the control accuracy is kept below $20\,\mathrm{m}$, as per the requirements of the study. In conclusion, both control technologies can meet the required control accuracies. However, the impulsive requires higher propellant mass (i.e. higher mass of the satellite) and performs the pair of tangential manoeuvres as soon the nominal trajectory exits the $20\,\mathrm{m}$ large error threshold. On the other hand, the continuous scheme uses less propellant mass and continuously compensates errors with respect to the nominal trajectory, keeping the overall control error below $10\,\mathrm{m}$ threshold.

6.2 SA2: Three-Satellites SAR

A three-satellites SAR concept is studied in support of the preliminary analysis for the Harmony mission study for improving the data quality of ocean, glaciers, and ice sheets. The baseline of this concept foresees two vehicles (in this analysis called M1 and M2) flying in formation with Sentinel-1 satellite. This study has been carried out as part of the research visiting period in ESA-ESTEC. It aims to evaluate the feasibility of a continuous control technique for formation maintenance.

The mission concept consists of three satellites in two different configurations. A first close formation is studied when only two out of three vehicles (i.e. M1 and M2) fly under a closer relative motion in a helix geometry. Then, a loose formation, where the three spacecraft (i.e. M1, M2 and Sentinel

1) fly in a symmetrical leading/trailing configuration. The reference orbit is a near-polar SSO with 12 day repeat cycle and 175 orbits per cycle. The LTAN is selected at $18{:}00$, and the mean equatorial altitude is $693\,\mathrm{km}$. Table 6.2 shows the initial UTC used for the simulations and the initial conditions employed in the simulations, in terms of time (UTC), state of the absolute orbits (EME2000), and Keplerian osculating elements.

Table 6.2: *Initial condition of the SA2 test case.*

Variable	Value
`UTC`	00:00 21/03/2028
`X_EME`	$\left\{-4.303\cdot10^4, 6.875\cdot10^6, -1.471\cdot10^4, 1.083\cdot10^3, 14.684, 7.538\cdot10^3\right\}$ (m,m/s)
α	$\left\{6.878\cdot10^6,\ 0.00118,\ 98.002,\ 90.756,\ 66.283,\ 293.713\right\}$ (m,-,deg,deg,deg,deg)

6.2.1 Relative motion

Two formation geometries are envisioned in this study to implement a bi-static SAR interferometry.

Close formation In the first configuration, M1 and M2 spacecraft fly in close proximity, while Sentinel 1 remains in a single satellite configuration. Precisely, M2 is placed on a helix formation around M1, which remains on the same reference orbit of Sentinel 1, but at a different argument of latitude u. The relative orbit is selected based on the following ROEs, where M1-M2 vehicles are in the chief-deputy configuration:

$$a\delta\boldsymbol{\alpha} = \{0, \quad 0, \quad 0, \quad 800, \quad 0, \quad 2260\}\ \text{(m)} \tag{6.6}$$

Similarly to the SA1 (ROSE-L) case, the initial condition is selected to get a parallel relative eccentricity/inclination vectors configuration for safety purposes. Figure 6.6 shows the nominal trajectory of the Harmony close configuration, presenting the trajectory in the three side views. The nominal distance among the spacecraft varies in the range 1000 to $2000\,\mathrm{m}$. When in the presence of external perturbation, the nominal trajectory is subject to drift and oscillations. In the Harmony study, an impulsive propulsion system was initially considered, based on Hydrazine propellant and providing $1\,\mathrm{N}$ thrust. Instead, the analyses in this dissertation aim to assess the feasibility of controlling the formation

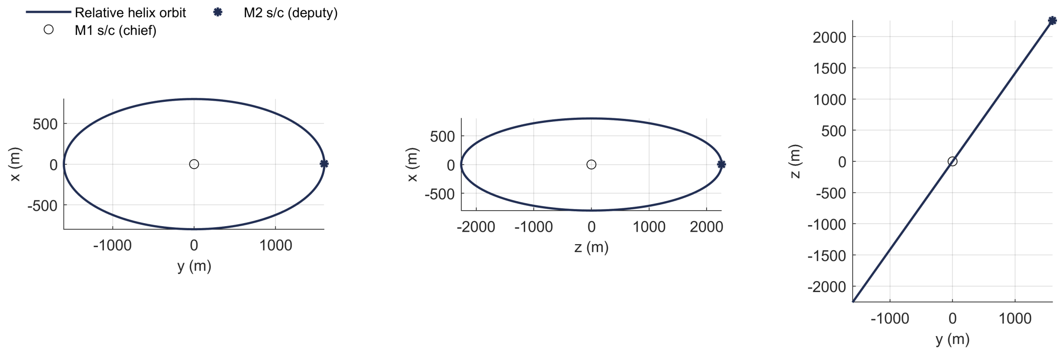

(a) *x-y view.* **(b)** *x-z view.* **(c)** *y-z view.*

Figure 6.6: *Nominal trajectory for the close formation of Harmony study.*

with a low-thrust technology. The low thrust control is based on an ion thruster with a specific impulse of $3000\,\mathrm{s}$. The control logic is based on the closed-loop GNC framework developed in Chapter 5 under the hypothesis of ideal navigation (no navigation error has been considered for this analysis). For the simulations, the dynamics include the effect of gravitational field up to 10×10 order and degree and the differential atmospheric drag. The latter has been modelled with the NRLMSISE model in Section 3.2, and a difference in the ballistic coefficient of 2% has been considered as a design input of the study. The gain matrices for the LQR control have been selected after a sensitivity analysis, as follows:

$$\boldsymbol{Q} = \begin{bmatrix} 10^{-4}\boldsymbol{I}_{3\times3} & \boldsymbol{0}_{3\times3} \\ \boldsymbol{0}_{3\times3} & 10^{-1}\boldsymbol{I}_{3\times3} \end{bmatrix} \qquad \boldsymbol{R} = 10^{8}\boldsymbol{I}_{3\times3} \tag{6.7}$$

Moreover, the thrust has been limited to $15\,\mathrm{mN}$, and the delays due to the engine mechanism have been set equal to $1\,\mathrm{s}$, driven by the requirements of the study. The effect of the control is reported in Figure 6.7. First, the variation due to external perturbation on the nominal relative trajectory is described in Figure 6.7a, where the error in terms of RTN parameters is reported. A drift in the three directions is present, with a magnitude of $\pm 50\,\mathrm{m}$ in the radial, $180\,\mathrm{m}$ in the along-track, and $\pm 250\,\mathrm{m}$ in the cross-track direction. The propagation is reported for $1\,\mathrm{day}$ period, corresponding to 15 orbits. The idea of impulsive control, as in ROSE-L, is to perform a couple of tangential manoeuvres per day

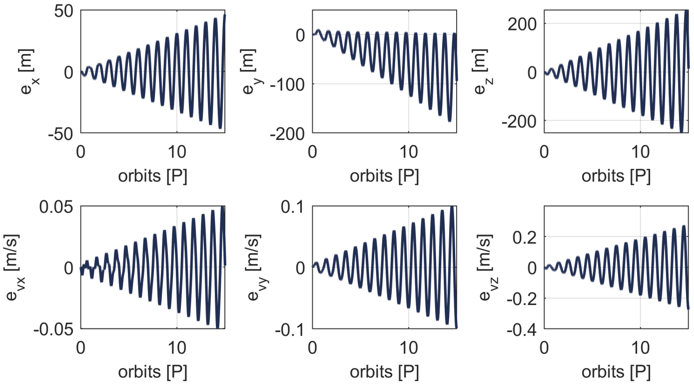

(a) *Natural drift of the nominal relative trajectory.*

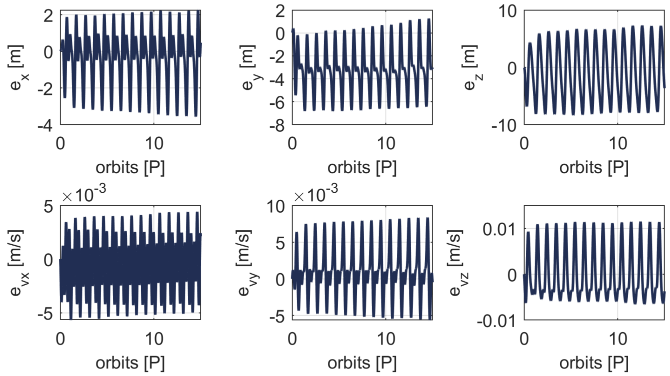

(b) *Error in the control under a continuous control scheme.*

Figure 6.7: *Continuous control analysis for the close formation of Harmony study.*

at a predefined true anomaly to compensate for the differential drag effect. Differently, the low-thrust control approach continuously compensates for the drift, keeping the error between the actual and the nominal trajectory below $\pm 10\,\mathrm{m}$ with a maximum thrust of $15\,\mathrm{mN}$. The error in the control is reported in Figure 6.7b, for the RTN components.

To conclude, this preliminary study serves as input for future analysis in terms of the feasibility of continuous control strategy for swarm mounting remote sensing instruments (e.g. active SAR). The advantage of continuous control is based on the capability to continuously compensate for external perturbation with lower propellant mass than an impulsive control scheme. This is due to the higher specific impulse of the technology. On the other hand, the main limitation of such engines is connected to the high power consumption, and further analyses are needed in future developments of the work to study the power budget of the platform for different operational phases.

Loose formation The second configuration consists of a three-satellite formation flying in a symmetric leader-follower configuration (see Section 3.3). To study the relative motion, the formation includes the two deputies and the Sentinel 1 spacecraft as the chief satellite at the origin of the local hill frame. The following configuration is imposed:

- The two deputies are at $800\,\mathrm{km}$ distance from each other along the orbit.
- Sentinel-1 spacecraft is in the middle, at $400\,\mathrm{km}$ separation from each deputy.

The first important analysis is the correct initialisation of the formation in terms of ROEs elements. An initialisation of the formation with a difference in the relative-semi-major axis causes an important drift in the other relative elements, particularly the mean argument of latitude $\delta\lambda$. This drift could significantly threaten the formation safety under the natural evolution due to the external perturbation of the LEO region. Two cases are analysed:

- Separation in semi-major axis $\delta a \neq 0$, due to an error in the formation set-up.
- Separation only in $\delta\lambda$.

The dynamic is propagated considering the atmospheric drag and gravitational perturbations up to degrees and orders 10×10, from the absolute dynamical model developed in Section 3.2. The case with $\delta a \neq 0$ is represented in Figure 6.8a, where the natural evolution is shown for 15 orbital periods. The δa error is set equal to $3\,\mathrm{km}$ (i.e. about 1% of the separation M1-Sentinel 1 and M2-Sentinel 1). A divergent evolution is present in most of the components of the ROEs elements; specifically, a significant drift affects the relative longitude $\delta\lambda$, making the deputies drift away from the chief in a few orbits. On the other hand, when no semi-major axis separation is present, the difference in the relative argument of latitude $\delta\lambda$ generates a variation in the ROEs that is bounded in time. The behaviour for only two orbital periods is represented in Figure 6.8b. Some oscillations are present in the dynamical evolution, but the separation along the orbit ($\delta\lambda$) remains constant. Thus, it is important to correctly set up the $800\,\mathrm{km}$ separation only along the orbit, minimising (i.e. $\delta a = 0$) the difference in the relative semi-major axis.

6.3 SP1: Formation Flying L-band Aperture Synthesis study

This section presents the analyses performed for the FFLAS study (SP1), the primary test case of this dissertation. First, the definition and scope of the study are outlined, together with the main mission

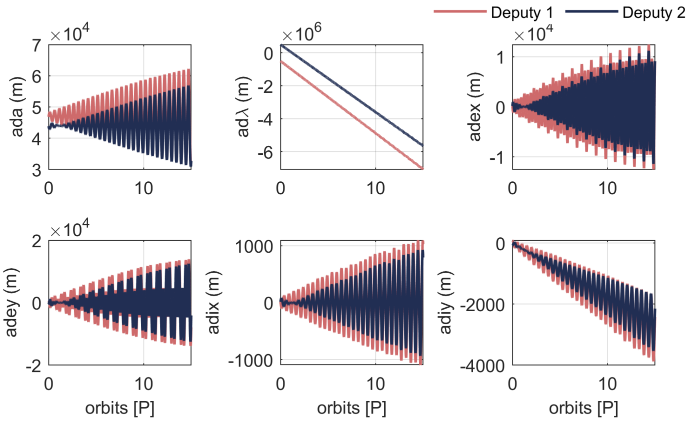

(a) *Natural drift for* $\delta a \neq 0$ *for* 1 *day.*

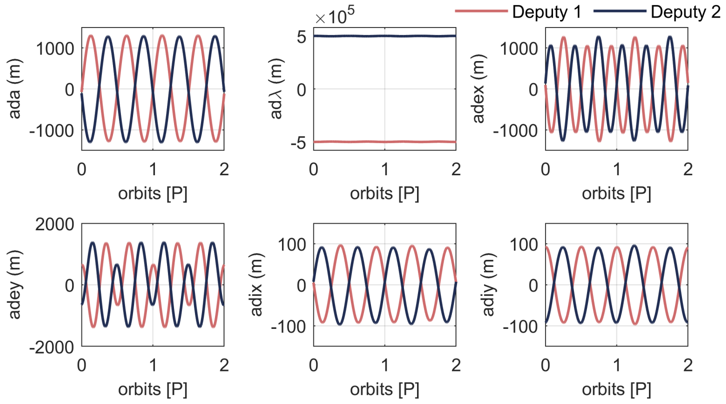

(b) *Natural drift for* $\delta a = 0$ *for* 2 *orbital period.*

Figure 6.8: *Natural drift for two different configurations of the Harmony case under external perturbation.*

requirements. Second, the chapter presents the trade-off analyses for the nominal geometry selection for scientific data acquisition, along with relative motion and payload considerations.

The context of the FFLAS study is based on the ESA's Soil Moisture and Ocean Salinity (SMOS) mission. Since November 2009, SMOS has been producing global maps of soil moisture and sea surface salinity with an average resolution of $40\,\mathrm{km}$. In the context of an incoming L-band mission, it is necessary to address the future needs for a range of applications over land and ocean that calls for much enhanced spatial resolution, down to 1 to $10\,\mathrm{km}$. With today's technology, the spatial resolution of a radiometer can be improved only by increasing its aperture size. In this context, the Formation Flying L-band Aperture Synthesis (FFLAS) study proposes aperture synthesis at L-band using formation flying as a potential way to significantly increase the spatial resolution, as described in Chapter 2. The FFLAS mission concept consists of 3 hexagonal arrays of about $8.2\,\mathrm{m}$ in diameter (slightly smaller size than SMOS), flying with their centres at the vertices of an equilateral triangle of about $13\,\mathrm{m}$ side. Such formation has a hexagonal receivers with external diameter of $8.2\,\mathrm{m}$, achieving an equivalent aperture of $21\,\mathrm{m}$. This produces a $9.84\,\mathrm{km}$ boresight spatial resolution with an effective sensitivity better than SMOS (see Section 2.3.1). The most relevant physical properties of the FFLAS concept are summarised in Table 6.3.

Table 6.3: *FFLAS spacecraft physical properties.*

Physical property	Value
Side of equilateral triangle	13 m
Satellite's diameter	8.2 m
Dry/Wet mass	1400 kg / 1600 kg

6.3.1 Requirements

Different class of requirements can be identified for the FFLAS study: functional, mission/operational, and physical. Apart from the requirements presented in Section 2.3 (RP1 to RP6), additional requirements specific to the FFLAS study are introduced in Tables 6.4 and 6.5, which presents the most relevant requirements divided into their class. The three spacecraft of FFLAS are identified as Satellites 1, 2, and 3, respectively.

Table 6.4: *FFLAS formation flying requirements divided into functional, and physical (Part I).*

Functional requirements
RP-F1 **Distribution of raw signal**
The raw measurements of satellites 1, 2 and 3 shall be sent to satellites 2, 3 and 1, respectively.
RP-F2 **Distribution of navigation signal**
The GNSS raw measurements shall be distributed among the 3 satellites to enable precise relative navigation.
RP-F3 **Pointing modes**
The formation shall have two pointing modes: Earth pointing and Cold Sky pointing. In both pointing modes the formation shall be capable of performing aperture synthesis. In Earth pointing the z-axis of the aperture plane shall be nadir oriented, to carry out nominal measurements. In Cold Sky pointing the z-axis of the aperture plane shall be in zenith direction, to carry out the cold sky calibration.
RP-F4 **Graceful degradation**
The satellite formation shall be designed in a way such that if one satellite fails the other two satellites can maintain full aperture synthesis capabilities as a two-satellite formation.
Physical requirements
RP-P1 **Type of formation**
The 3 satellites shall fly in rigid formation, i.e. a formation in which the relative distances and orientation among the satellites remain fixed.
RP-P2 **Aperture plane definition**
The 3 arrays shall lie on a plane orthogonal to the radial direction form the centre of the Earth (i.e. on the transversal-normal plane). The perpendicular to the aperture plane shall be pointed in nadir-zenith direction.

6.3.2 Selection of reference orbit

The reference orbit for the FFLAS formation has been selected starting from the operative orbit of SMOS. Thus, the reference orbit is a dusk-dawn orbit with a mean altitude of $775\,\mathrm{km}$. This requirement sets the launch parameters to meet the $6\,\mathrm{a.m.}$ - $6\,\mathrm{p.m.}$ condition. To obtain an ascending node of the reference orbit at dawn ($6\,\mathrm{a.m.}$), the satellites shall be launched southward at $6\,\mathrm{p.m.}$ Such orbit grants very favourable illumination conditions from the Sun. Specifically, the Sun's direction is in the negative normal direction of the local orbital frame (see Figure 6.9a), and the reference orbit undergoes eclipse phases mainly around the winter solstice. The peak duration of the eclipse is around $18\,\mathrm{min}$, providing a low load factor to the on-board batteries, as shown in Figure 6.9b.

Table 6.5: *FFLAS formation flying requirements divided in mission/operational (Part II).*

Mission/Operational requirements
RP-M1 Release
A release concept based on state-of-the-art shall be considered in combination with a spring element to push the satellites away from the adapter.
RP-M2 Formation Keeping - 1
The orbits of the three satellites shall be designed to enable the proposed formation flying and the formation keeping shall be able to maintain a rigid and fixed geometry among the spacecraft.
RP-M3 Formation Keeping - 2
The required sensors, actuators and control law shall keep the position requirements continuously
RP-M4 Collision Avoidance - 1
A collision risk algorithm shall be continuously running on each satellite with inputs from all local navigation sensors and the relative navigation information.
RP-M5 Collision Avoidance - 2
In case that relative positioning evolution showed any risk of collision, the system shall be designed to bring the satellites safely apart into a safe-mode flight formation.

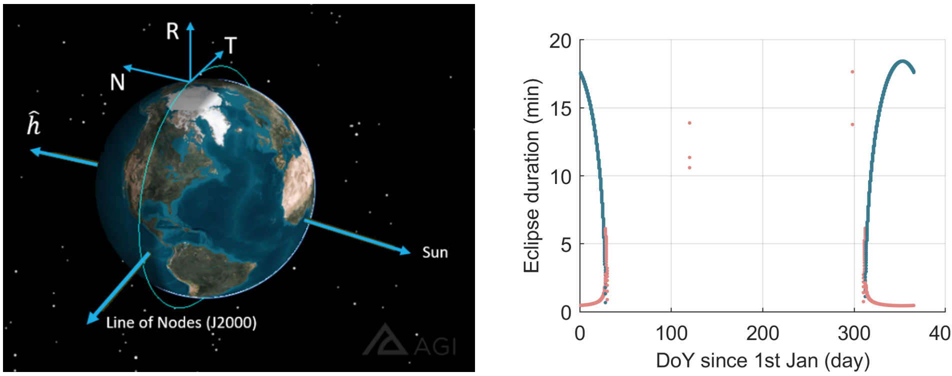

(a) *FFLAS reference Orbit in the J2000 Orbital frame. The figure shows the RTN frame orientation w.r.t. the Sun direction.*

(b) *Eclipse duration over one year for the SSO reference orbit: umbra (blue) and penumbra (red).*

Figure 6.9: *Reference orbit for the FFLAS study.*

6.3.3 Formation geometries and baseline selection

This section presents the analyses carried out to study admissible formation geometries. The analyses focus on the following tasks:

- A complete analysis of admissible formation geometries by exploiting the yaw parameter, the relative attitude profile, and the sun-angle in each body-fixed local frame.
- The definition of the strategies to realise a fuel consumption balancing among the FF satellites during nominal operations.
- The assessment of the inter-satellite collision risk (with and without the nominal continuous control) for the definition of the backup two satellite formation and the safe-mode geometry.

The generic baseline of the formation geometry is shown in Figure 6.10. The baseline triangle is centred at the origin of the RTN frame, and it has a generic orientation in the aperture plane (i.e.

transversal-normal) defined by the yaw angle γ of the formation, counter-clockwise (see Figure 2.2). In the plot, satellites are marked by a small circle at their centre of mass, and 3, and the larger circles represent the external envelope of the spacecraft to show the effective separations among the nodes of the distributed instrument. According to the scientific mission requirements, the equilateral triangle must remain fixed and rigid during the nominal operation of the mission. Therefore, the only degree of freedom for the design is given by the orientation of this triangle in the formation plane, parametrised in terms of the yaw angle γ. From geometric construction, the yaw angle of each j-th satellite is defined from the yaw angle of the formation γ, as $\gamma_j = \gamma + \frac{\pi}{6}(j-1)$. The length of the side of the equilateral triangle is denoted by l, and the distance of the centre of each satellite from the reference point O is $\frac{\sqrt{3}}{3}l$. The j-th satellite's coordinates in RTN orbital frame, with respect to the origin O, can be defined in a general way as:

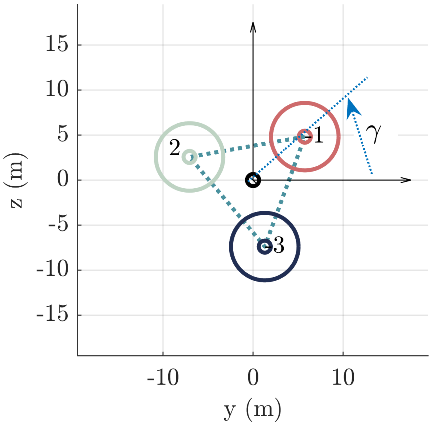

Figure 6.10: *Generic baseline geometry for FFLAS.*

$$\boldsymbol{x}_j = \left\{ 0, \quad \frac{\sqrt{3}}{3} l \cos\gamma_j \quad \frac{\sqrt{3}}{3} l \sin\gamma_j \right\}_{\text{rtn}} \tag{6.8}$$

where $\boldsymbol{x}_j$ represents the x, y, z coordinates of the generic j-th satellite with $j = 1, 2, 3$ in RTN.

6.3.4 Trade-off analyses

The requirement of maintaining a fixed relative position among the satellites demands a continuous forced motion to counterbalance the relative natural dynamic. In addition, the control is needed to keep the equilateral triangle formation geometry during the operations. The additional control cost related to the effect of the orbital perturbations can be minimised by initialising the formation at convenient values of the mean argument of the latitude of the reference orbit. Moreover, depending on the swarm configuration, we can identify different illumination conditions and self-shadowing effects. For a Sun-Synchronous orbit, the angle between the orbit's normal and the Sun is fixed in time. Still, the daily evolution of the spacecraft along its orbit produces a sinusoidal variation in the incidence angle on the solar panels. Moreover, since the spacecraft are flying at metre-level separation, large solar panels could generate self-shadowing effects among the vehicles of the formation. Finally, the use of continuous control to counteract the relative natural motion drives the selection of ion thruster technology. The resulting plume could generate self-impingement effects and cause degradation on the optical and electronic devices on-board. Specifically, these thrusters produce an ion discharge that can erode the external part of the satellites. The trade-off analysis aims to identify a proper γ angle and swarm configuration to optimise the considerations on the Sun illumination, as well as on the self-shadowing and thrusters' self-impingement. The analysis results drove the selection of the FFLAS configuration in terms of the yaw angle to minimise the possible secondary effect of the thruster plume in relation to the main firings in the normal direction.

Selection of the initial argument of latitude

A first analysis is performed on the initial mean argument of latitude u_0 to minimise the effect of the J_2 perturbation. The study is parametrised in terms of the yaw angle γ and u_0. The former defines the orientation of the formation in the transversal-normal plane and can vary in the interval $[0, 2\pi]$. The u_0 parameter, instead, describes the positioning of the central reference point of the formation along one orbit, and it is computed starting from the ascending node of the orbit. The effect of a different argument of latitude and yaw angle is evaluated for each satellite in the ROEs environment. The analysis focuses on the variations in the relative eccentricity and inclination vectors in time. As described by the STM in Equation (3.51), the mean Earth's oblateness produces sinusoidal oscillations on the natural motion (see the terms μ_A, μ_I, λ_A, λ_I). Specifically, the ROEs initial values that directly multiply the STM components that are affected by the secular J_2 effect are immediately identified, namely: $\delta a(0)$, $\delta e_x(0)$, $\delta i_x(0)$, and $\delta i_y(0)$. For the FFLAS configuration under analysis, we introduce the following assumptions:

- The relative semi-major axis is considered negligible: $\delta a(0) = 0$.
- The difference in the relative eccentricity is considered negligible $\delta e_x(0) = 0$ and $\delta e_y(0) = 0$.
- The non-null components in the initial ROEs are the relative inclination vector and the relative mean argument of latitude.

The variation in $\delta\lambda$ is a function of the difference on the initial argument of latitude u_0 and the initial RAAN. The latter term also influences the y-component of the relative inclination vector, and it cannot be set equal to zero due to the geometry constraints of the formation. Consequently, the reduction of the effect of J_2 on the natural ROEs evolution is studied by minimising the x-component of the relative inclination vector. The results of the parametric analysis for the δi_x component are shown in Figure 6.11. For an angle, γ of 0 deg or 180 deg, the difference in inclination is null, independently from the argument of latitude u_0. This situation corresponds to a formation flying initialised at the nodes. Finally, a u_0 equal to 90 deg or 270 deg results in a sinusoidal variation of the initial inclination separation modulus, reaching the maximum value of the modulus in correspondence of γ equal to 90 deg or 270 deg. Now for the FFLAS general configuration, the angular separation among the vehicles is of 120 deg. Consequently, selecting a γ_1 for the satellite $j = 1$ results in a yaw angle for the other two spacecraft ($j = 2, 3$) of γ_1+120 deg and γ_1+240 deg. The only condition that provides an initial null δi_x for all three satellites corresponds to an argument of latitude initialised at the nodes of the reference orbit: u_0 equal to 0 deg or 180 deg. Figure 6.12 shows the time propagation of the ROEs for both cases of $u_0 = 0$ deg (left) and $u_0 = 90$ deg (right), for the three FFLAS platforms. For the former case, the ROEs remain constant in time, resulting in an easier control from the formation maintenance point of view, compared to a time-varying propagation of the elements for the $u = 90$ deg case. Thus, as an outcome of this first analysis, the initial mean argument of latitude for the nominal operations of the formation is set at the nodes of the reference orbit.

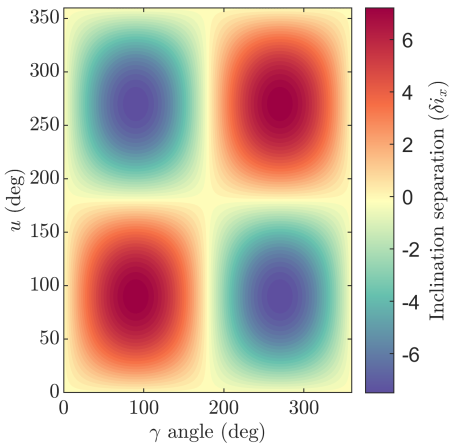

Figure 6.11: *Parametric analysis for the* δi_x *component under external* J_2 *perturbation for FFLAS.*

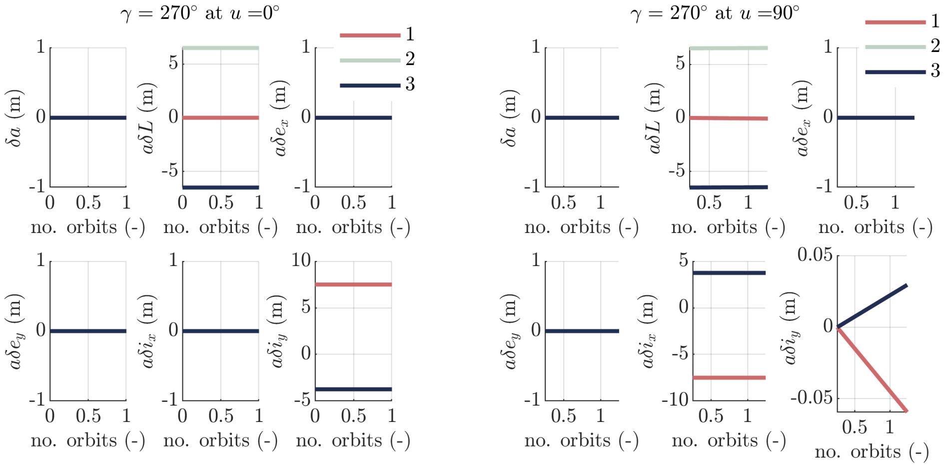

(a) $u_0 = 0$ *deg.*

(b) $u_0 = 90$ *deg.*

Figure 6.12: *Time propagation of ROEs for different initial mean arguments of latitude* u_0.

Sun angle analysis and self-shadowing effect

Proper analyses of the Sun direction are an important factor for the design of the mission operations of the formation. In the FFLAS study, the platform is equipped with deployable solar panels, and for power generation requirements, the solar panels are maintained in the Sun direction. Due to the solar panels' shape and the short separation among the spacecraft (about 13 meters), a possible self-shadowing effect could arise depending on the γ orientation of the formation in the normal-transversal plane with respect to the direction of the Sun, as in Figure 6.9. Figure 6.13 represents the shadow generated by the solar panel shape when the Sun is in the negative direction of the z axis. The condition with the yaw angle γ equal to 270 deg, minimises the self-shadowing effect. Moreover, Figure 6.14 shows the cone of the elevation angle over one year with respect to the negative normal axis. The maximum oscillation is about 30 deg, which ensures proper power generation over the year. The power budget is affected consistently by seasonal and orbital variations of the Sun elevation angle.

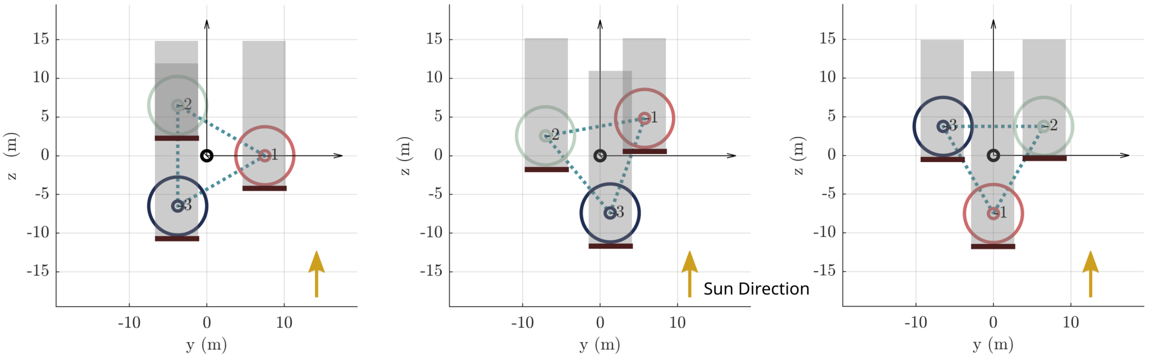

Figure 6.13: *Self-shadowing analysis for FFLAS with different γ angles: 0 deg, 40 deg, and 270 deg.*

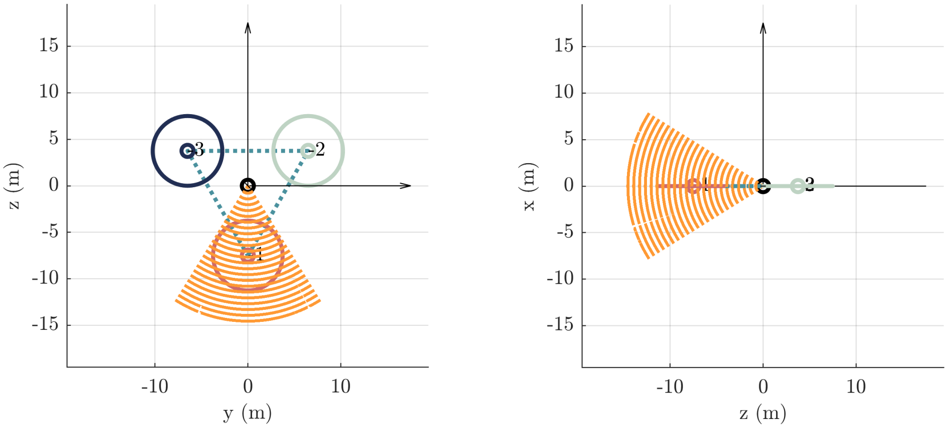

(a) *Sun cone projection in the y, z plane.*

(b) *Sun cone projection in the x, z plane.*

Figure 6.14: *Cone of the time evolution of the elevation angle of the Sun over one year.*

Plume impingement analysis

The analysis of the plume impingement is important to provide a preliminary assessment of the effect of the plume of an ion engine on the satellite's equipment. The FFLAS platforms are equipped with four low-thrust engines, as shown in Figure 6.19. The plume impingement from ion thrusters could generate severe degradation effects on satellite material and optical instruments. The plume can be modelled as a cone defined by the exit velocity and the semi-aperture angle. Depending on the orientation angle, the effect could be more severe. When two spacecraft are facing each other, as in Figure 6.15b, the plume of spacecraft 2 directly impacts the whole platform 3 , and vice-versa, causing a potential harness to electronics and optical instruments. Differently, the case in Figure 6.15a, with $\gamma = 270$ deg, avoids the direct impingement of the plume on the satellite's body. Then, the actual effect due to the semi-cone aperture angle depends on the thrust level with an inversely proportional law. Considering the QuinetiQ T5 engine [1], the cone semi-angle can vary between 12 deg

---

[1] `https://www.qinetiq.com/en/what-we-do/services-and-products/solar-electric-propulsion`, last access on 14/02/2023

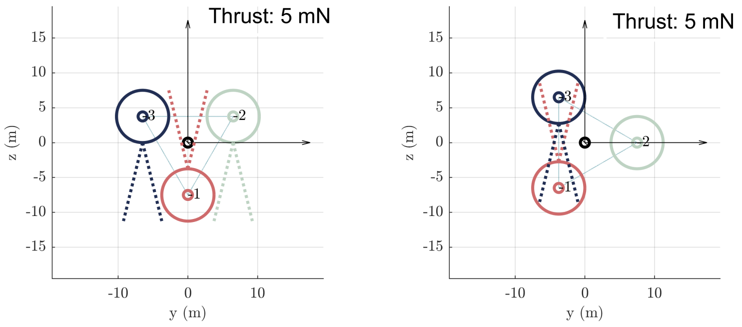

(a) *Orientation angle* $\gamma = 270$ *deg.* **(b)** *Orientation angle* $\gamma = 0$ *deg.*

Figure 6.15: *Plume impingement effect for different orientation angle* γ.

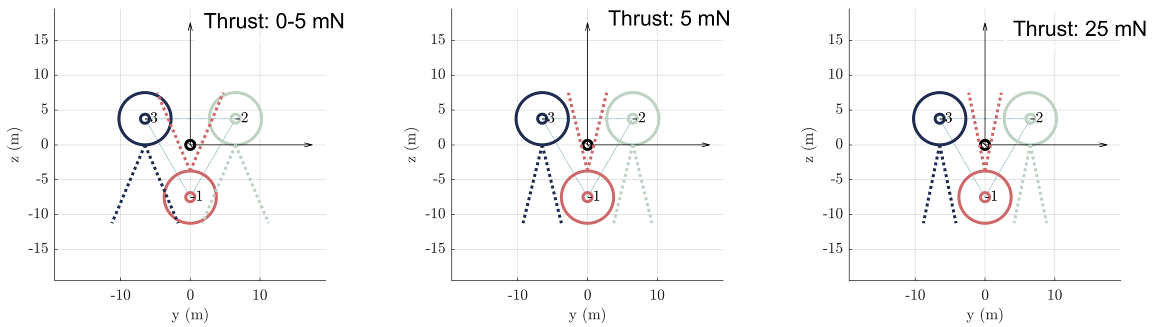

(a) *Thrust level* $0-5$ *mN.* **(b)** *Thrust level* 5 *mN.* **(c)** *Thrust level* 25 *mN.*

Figure 6.16: *Plume impingement effect for different thrust level for* $\gamma = 270$ *deg.*

and $25\,\mathrm{deg}$ when the thrust is $25\,\mathrm{mN}$ and $1\,\mathrm{mN}$, respectively. Performing an extrapolation, the plume impingement effects for three different level of thrust is reported in Figure 6.16, with γ =$270\,\mathrm{deg}$.

Fuel consumption analysis

As described in Section 4.1.1, a forced motion is required to keep the triangular formation. Specifically, the control effort is proportional to the displacement in the normal direction (see Equation (4.9)). This paragraph briefly presents the results of two investigations: first, a parametric analysis over γ angle of the j-th spacecraft is presented to assess the normal (cross-track) displacement δN; second, the delta-v effort for formation maintenance is proportional to the amplitude of the normal displacement. For this reason, the analysis aims at finding a configuration in terms of the γ angle, which provides a similar oscillation amplitude for the three satellites. Figure 6.17a shows the normal displacement in time for different initial γ angles of the satellites. In addition, two peculiar configurations are reported: FF-B1 represents a formation with a γ angle of $270\,\mathrm{deg}$ for satellite 1; FF-B2 represents a formation with a γ angle of $0\,\mathrm{deg}$ for platform 1. Configurations FF-B1 and FF-B2 are quite peculiar because they represent two opposite situations. The former corresponds to the most balanced situation that can be obtained with three platforms with an angular separation of $120\,\mathrm{deg}$: the spacecraft with

γ =30 deg and 150 deg have the same normal displacement evolution in time, while the spacecraft with γ =270 deg is subject to a larger oscillation. For the latter configuration (FF-B2), instead, one platform (with γ =0 deg) has a null cross-track displacement, while the other two spacecraft have a non-null displacement, resulting in a completely unbalanced delta-v budget for formation maintenance. The most promising scenario corresponds to FF-B1, where the γ angles of the formation are $270 + 120(j - 1)$ with $j = 1 : 3$. Nonetheless, the normal displacement is still not balanced. To solve this issue, triangular formations with the centre in a reference point that has some non-vanishing normal displacement are analysed. Introducing a displacement ΔN of the barycentre of the equilateral triangle with respect to the origin of the local orbital frame can produce configurations balanced in the normal direction. Specifically, the ΔN is chosen to have an equal displacement out-of-plane (δi_y) of all the three satellites of the formation. Recall that δi_x is null as all formations are initialised at the nodes of the reference orbit, Figure 6.17b shows this configuration with a ΔN =1.875 m. This value ensures that $|z_1| = |z_2| = |z_3|$. At this point, the assessment of the preliminary delta-v budget to keep

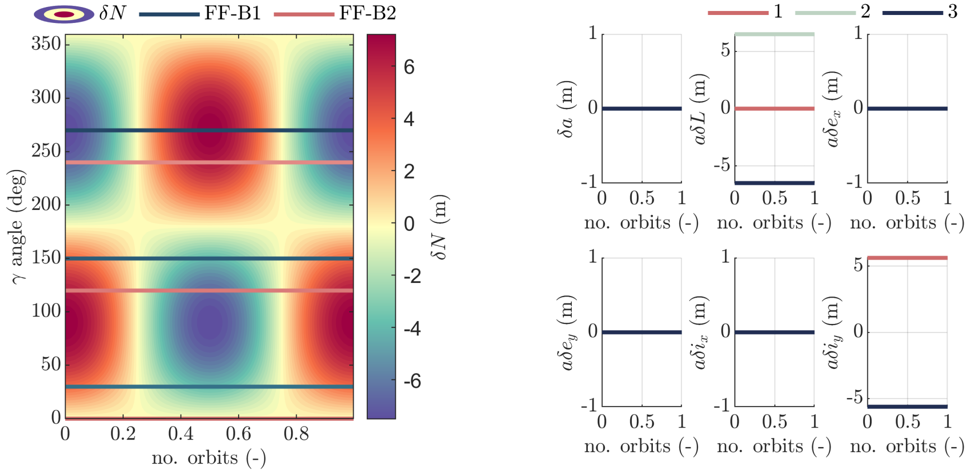

(a) *Parametric analysis for normal displacement.* **(b)** *Balanced configuration with $\Delta N = 1.875$ m.*

Figure 6.17: *Fuel balancing analysis for FFLAS.*

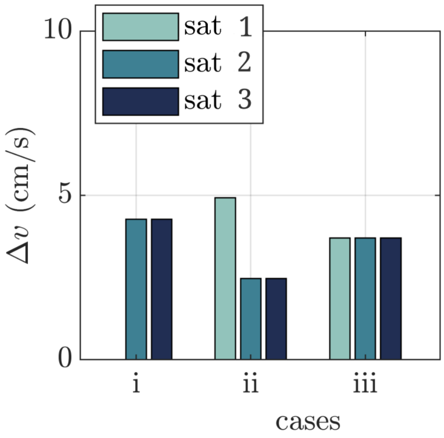

Figure 6.18: *Delta-v budget analysis over one orbital period for different formation configurations.*

the formation is computed from the solution of the forced motion in Section 4.1.1. The delta-v budget is evaluated over one orbital period for the following geometries: *i.* FF-B2; *ii* FF-B1; *iii* FF-B1 with ΔN =1.875 m. The results of the analyses are reported in Figure 6.18. The first case is completely unbalanced, as satellite 1 requires no delta-v to maintain the initial relative state. The third case is preferred over the second one, resulting in a completely balanced scenario. The normal-displaced condition assures an equal delta-v budget among the satellites for the nominal operations. An important consideration is needed to conclude the delta-v analysis. Due to configuration and instrument constraints, the spacecraft could not be rearranged to balance the fuel consumption of cases *i* and *ii* by simply moving the position of $1-2-3$ into $2-3-1$ or similar. This could have been the case for configuration *i*, where time to time, the spacecraft could have been swapped. Nevertheless, this operation is not compatible with the deployable solar panels and the optical link connection, as the formation is required to be fixed in terms of attitude and geometry. Consequently, the configuration *iii* is the only one possible to realise fuel balancing. This analysis set the formation configuration with an N-displacement of 1.875 m and a preferred γ =270 deg.

6.3.5 FFLAS baseline selection

Section 6.3.4 presented a trade-off analysis to set up the nominal formation configuration in the hill orbital frame to obtain a balancing of the delta-v budget, the best conditions to avoid/minimise self-shadowing and plume impingement, and minimise the effect of the external mean J_2 disturbance. Table 6.6 shows the best configurations for the different analyses. Consequently, the baseline is selected with an initial mean argument of latitude equal to 0 or 180 deg (formation initialised at the nodes), and a γ angle equal to 270 deg with a normal displacement of the barycentre of the formation of 1.875 m. The corresponding formation geometry is shown in Figure 6.19. The platforms have a hexagonal shape and can communicate with each other with an optical IInter-Satellite Link (ISL), as well as a radio frequency antenna. The relative distance among the spacecraft is driven by the payload characteristics, which requires a distance from centre to centre of about 12 m to correctly perform interferometry (see Section 2.4.3).

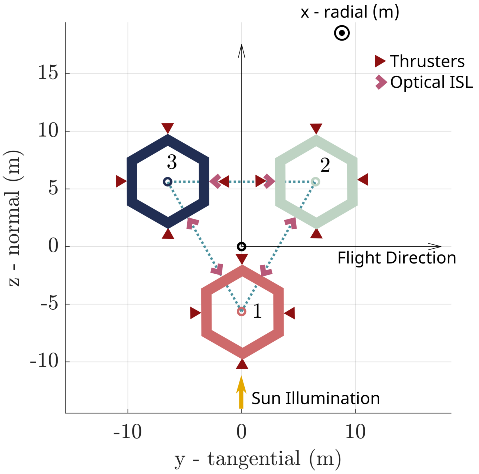

Figure 6.19: *Triangular formation configuration in the relative frame for the scientific phase of FFLAS study. The thrusters are shown by the red triangles, while the pink arrows represent the optical inter-satellite link.*

Table 6.6: *Results of the trade-off analyses for the FFLAS distributed system of three spacecraft.*

	Trade-off analysis			
Variable	Argument of laitude u_0	Self shadowing	Plume impingement	Fuel balancing
γ angle (deg)	any	270	270	270
u_0 (deg)	0 or 180	any	any	any
ΔN (m)	-	-	-	1.875

6.3.6 Safety considerations

The inter-satellite collision risk for the formation is evaluated over one orbital period for uncontrolled propagation. After the propagation of the relative position under the effect of the mean J_2 perturbation, two quantities are evaluated to assess the inter-satellite collision risk:

- The three-dimensional distance among each couple of satellites in the RTN frame is evaluated.
- The two-dimensional inter-satellite distance is evaluated in the radial-normal plane.

For the analysis, an initial mean argument of latitude u_0 is set to $0\,\mathrm{deg}$. Since the external diameter of the hexagonal satellites is $8.2\,\mathrm{m}$, the threshold to considered a collision among two vehicles is set equal to $8.2\,\mathrm{m}+20\%$ margin. As shown in Figure 6.20a, the natural motion of the formation lead to the collision of the satellites in less than one orbital period. The second information on the radial-normal separation provides information on passive safety. The results are shown in Figure 6.20b. Since the geometrical constraints demand a null relative eccentricity vector, no passive safety can be achieved, and we should implement the following considerations. First, the formation must fly under a continuously forced motion, to control the relative satellite position accurately at any time instant. Second, a robust formation safety policy should be implemented to minimise the inter-satellite collision risk in case of a failure of the on-board engine, as well as an autonomous procedure to have safety policies also in case of no contact with the ground station.

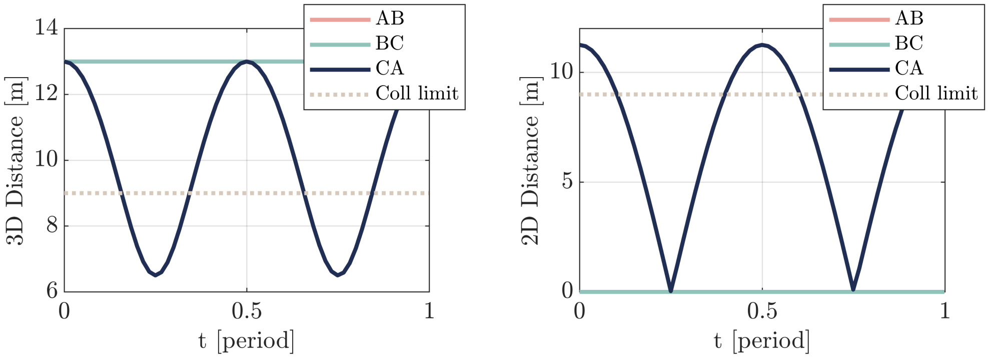

(a) *Three-dimensional speacraft's separation in RTN frame.*

(b) *Two-dimensional speacraft's separation in transversal/normal plane.*

Figure 6.20: *Natural evolution of the spacecraft separation for the FFLAS formation, under relative dynamics.*

6.3.7 Forced motion for formation maintenance

For the FFLAS formation, a continuous forced motion is required to counteract the natural evolution of the relative dynamics. Starting from the analysis in Section 4.1.1, we can identify the continuous control law and the delta-v budget to keep the formation under the unperturbed dynamics. First, the conditions of the relative state for the triangular geometry are the following:

- The formation lies on the transversal-normal plane, i.e. the x-coordinate of the RTN frame is zero, as well as the velocity in the radial direction:$x_j(0) = 0$, $\dot{x}_j(0) = 0, \forall j = 1, ..., 3$.
- The relative coordinates in the transversal and normal directions are shown in Figure 6.19: $y_j(0)$ and $z_j(0)$.
- The relative velocity is zero in the y-z plane to have a rigid formation: $\dot{y}_j(0) = 0$, and $\dot{z}_j(0) = 0$.

The corresponding control law to keep the rigid formation is (from Equation (4.9)):

$$\begin{cases} u_{jx} = & 0 \\ u_{jy} = & 0 \\ u_{jz} = & n^2 z_j(0) \end{cases} \tag{6.9}$$

Thus, the control to keep the triangular formation only depends on the z coordinate of the relative state in RTN. The delta-v budget for the FFLAS selected baseline is around $4\,\mathrm{cm\,s^{-1}}$ over one orbital period. This is a significant control effort to be maintained over the mission lifetime, as it results in about $60\,\mathrm{cm\,s^{-1}}$ for one day of formation maintenance. Moreover, this value considers only the natural motion and should be complemented with the required control to counteract the effect of external orbital perturbations.

6.4 SP3: FFLAS follow-on analysis

This section presents the follow-on analysis performed at the end of the FFLAS study. Most of this section has been presented at the International Astronautical Congress 2022 in Paris [118]. The aim of this section is to focus on two different questions:

- From the outcome of the FFLAS study, how can we design formation with three to twelve satellites and realise fuel balance among the platform?
- Given the importance of natural solution for active SAR, can we exploit those trajectories for passive interferometry application?

The analysis starts from the outcome of Section 2.4, where three to twelve-satellite formations have been proposed to realise high-resolution L-band passive interferometry. Both planar and non-planar geometries are analysed to obtain fuel balancing among the platforms. Given the similarity of the formation geometry of FFLAS and the four spacecraft cases (see Figure 2.16), it is not analysed in this dissertation. Moreover, the six and twelve spacecraft cases are analogous, thus, only the six-spacecraft case is discussed in detail. The section is organised as follows:

- The first part of the section focuses on the planar six-spacecraft case, providing different analyses to realise fuel balancing during the formation maintenance.
- The second part focus on the possibility to exploit the natural solution of the relative motion to realise a non-planar formation of three and six spacecraft.

6.4.1 Planar Geometry: Six-spacecraft case

The relative geometry for performing passive interferometry with six spacecraft and its implication on payload performance have been presented in Figure 2.17. In this first scenario, the configuration is analogous to the FFLAS study, and the Aperture Plane of the formation is coincident with the transversal-normal ($y - z$) plane. In this way, the normal to the antenna can be directed in the nadir direction, facing the Earth's surface.

As described in Table 2.2, the idea is to increase the number of spacecraft to obtain a similar spatial resolution of FFLAS, but with smaller platforms, since its reduction in terms of platform dimension and mass brings several advantages compared to the FFLAS study. First, considering a platform with $3\,\mathrm{m}$ diameter removes the need for having a deployable structure of the spacecraft as in FFLAS, reducing the complexity and improving the robustness of the mission. Second, smaller launchers (e.g. Vega launchers) can be employed for orbit insertion, reducing the overall cost of the mission if compared with bigger launchers (e.g. Ariane 6).

Parametric analysis of the yaw angle As described in Figure 2.2, the yaw angle describes the orientation of the Array Plane on the transversal-normal plane. The generic formation geometry for the six-satellite configuration is shown in Figure 6.21. Following a similar approach of Section 6.3.4, it is possible to compute the relative eccentricity/inclination separation with different yaw angles γ and initial mean argument of latitude u_0. The results of this analysis are reported in Figure 6.22. Specifically, we can observe how an initialisation of the formation at the ascending/descending node of the orbit (i.e. $u = 0$ deg or $u = 180$ deg) minimised the separation along the x-component of e/i vectors and maximises the y-component. Setting an initial mean argument of latitude at the nodes minimises the effect of the Earth's oblateness perturbation. However, for formation keeping purposes, we should translate this analysis in terms of transversal and normal displacement under natural motion. This is represented in Figure 6.23, where FF-B1 is a configuration initialised with a generic 30 deg yaw angle and FF-B2 is initialised with 0 deg yaw angle. For the six spacecraft geometry, it is not possible to obtain the same magnitude of displacement in the normal direction. As for the FFLAS case, this is the driver in the computation of the delta-v for formation maintenance. The normal displacement has an oscillatory motion in time, and the amplitude depends on the initial yaw angle, while the transversal displacement remains constant in time for different satellites.

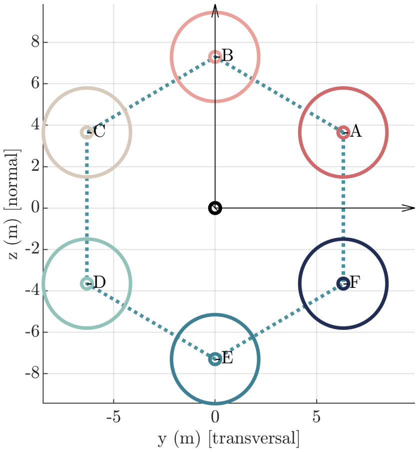

Figure 6.21: *Generic formation configuration with six spacecraft in planar geometry.*

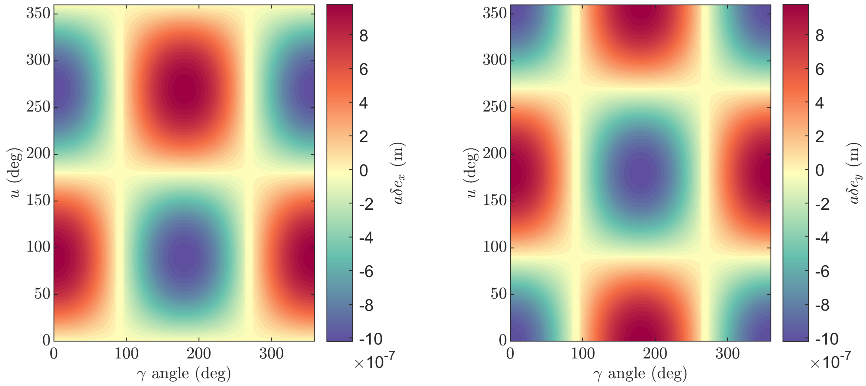

(a) *Parametric analsyis for δe_x.*

(b) *Parametric analsyis for δe_y.*

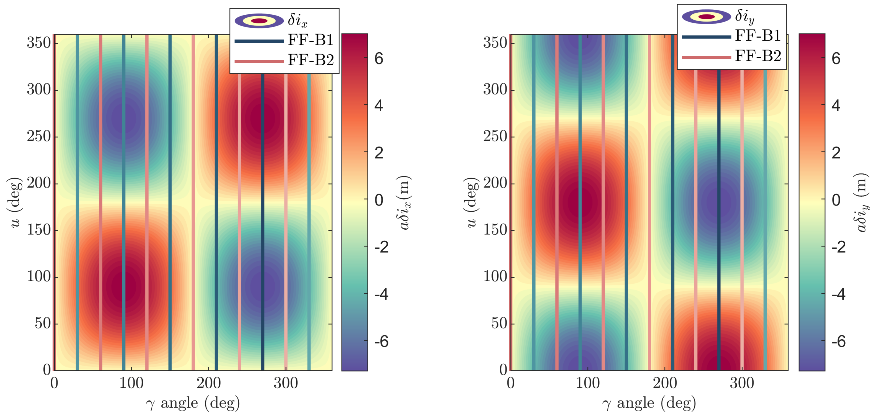

(c) *Parametric analsyis for δi_x.*

(d) *Parametric analsyis for δi_y.*

Figure 6.22: *Parametric analysis of the relative e/i vector with varying yaw angle and initial mean argument of latitude.*

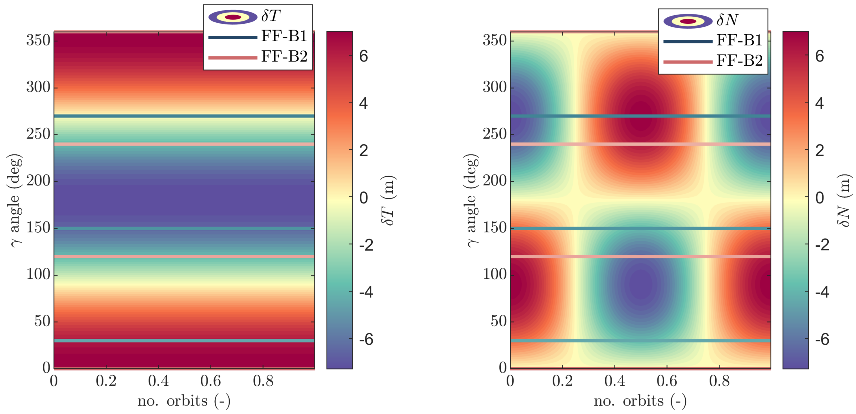

(a) *Transversal separation.*

(b) *Normal separation.*

Figure 6.23: *Parametric analysis of the relative transversal and normal separation with varying yaw angle in time.*

An active control strategy to perform simultaneously formation keeping and fuel balancing is then required. At the end of this first analysis, the main outcome is the identification of the initial argument of latitude at the ascending/descending node of the reference orbit.

Uncertainty analysis on the initial conditions In the previous paragraph, we set the initial argument of latitude to $u = 0$ deg. Nevertheless, during the formation establishment, an error in the initial condition could generate a variation of the ROEs under the effect of the Earth's oblateness. This paragraph presents an uncertain analysis considering as initial conditions a Gaussian distribution of 1000 points centred in $u = 0$ deg. A maximum deviation of 5 deg is imposed with respect to the initial conditions, to represent the error in the formation establishment. The initial distribution is reported in Figure 6.24. The initial distribution is propagated for 3 orbital periods and the temporal evolution of ROEs is evaluated in terms of mean and standard deviation (σ and 2σ). The results are reported in Figure 6.25 for three different initial conditions of yaw angle in the transversal-normal plane: 0

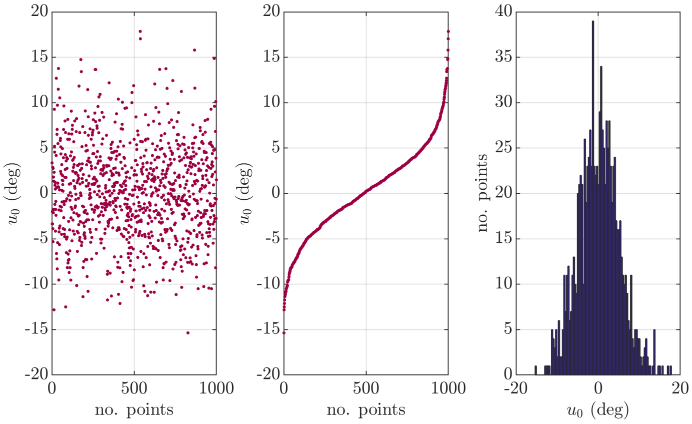

Figure 6.24: *Gaussian distribution of the initial conditions for the six-satellite formation: for* 1000 *points.*

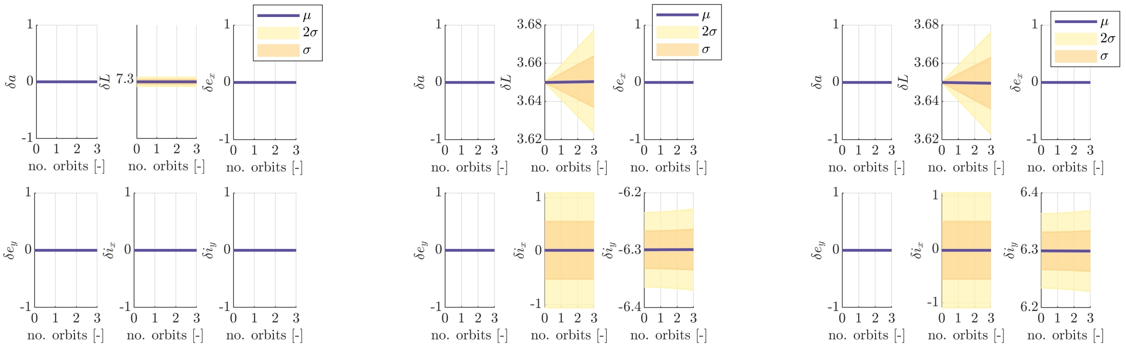

(a) *Uncertain propagation for* $\gamma = 0$ *deg.*

(b) *Uncertain propagation for* $\gamma = 60$ *deg.*

(c) *Uncertain propagation for* $\gamma = 300$ *deg.*

Figure 6.25: *Uncertain analysis for an initial Gaussian distribution of 1000 points with different* γ *angles.*

deg, 60 deg, 240 deg. For the spacecraft with $\gamma = 0$ deg, the uncertainty in the initial condition has the smallest effect in terms of dispersion and standard deviation in time. On the other hand, the cases with $\gamma = 60$ deg or $\gamma = 240$ deg, are affected by a significant variation in terms of $\delta\lambda$ component, for which the standard deviation linearly increases in time. Also, the relative inclination vector component is affected in both cases, with a non-null standard deviation. This behaviour could affect the stability and the safety of the formation. Specifically, it is important to properly initialise the formation reducing the error in terms of initial condition u_0.

Nominal delta-v budget for formation maintenance The two configurations, FF-B1 and FF-B2 are represented in Figure 6.26. For both cases, the ISL in the hexagonal formation is based on a dual link, to connect each entity with the other two vehicles of the formation. Differently from the FFLAS case, the solar panel constraint has been removed, considering body-mounted cells, and the selected configuration allows for a reorganisation of the satellites (i.e. a swap in position), without loss in the optical link and in the power budget.

The delta-v budget for the pure forced motion is reported in Table 6.7 for both configurations: FF-B1 and FF-B2. It has been computed using the equation of the pure forced motion (see Section 4.1), to recover the corresponding acceleration value. In the nominal geometry, the delta-v budget is unbalanced among the vehicles of the formation, and the implementation of specific control strategies is required to balance the situation. Consequently, two approaches have been implemented to realise fuel balancing: the first one consists in implementing a rotation of the geometry around the radial direction, and the second in a translation in the normal direction.

Table 6.7: *Delta-v budget for formation maintenance of FF-B1 and FF-B2. The values are computed over one orbital period.*

delta-v (cm/sec)	s/c 1	s/c 2	s/c 3	s/c 4	s/c 5	s/c 6
FF-B1	0	4.12	4.12	0	4.12	4.12
FF-B2	2.34	4.83	2.34	2.34	4.83	2.34

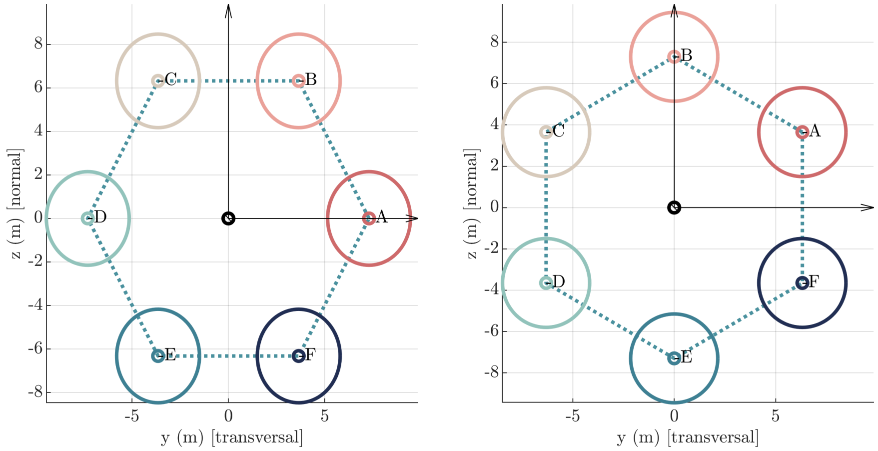

(a) $\gamma = 0$ *deg.* **(b)** $4\gamma = 30$ *deg.*

Figure 6.26: *Six-spacecraft formation geometry for yaw angles of 0 deg and 30 deg.*

Fuel balancing with complete rotation The idea of this first approach is to perform a 180 deg rotation in three steps of the formation geometry around the radial direction. Under this strategy, at each step, the configuration is rotated by a 60 degree angle. It has been assumed that the full rotation is completed over a period of six months, to impact less on the L-band data acquisition. Note that this strategy requires the spacecraft to have solar panels on all six sides of the platform, to provide power in any of the six configurations, differently from FFLAS study (which has only one deployable solar panel not orientable). The delta-v budget is reported in Table 6.8, where the delta-v is reported for each step over one orbital period for simplicity. This approach results in a balancing of the duel consumption over a science phase of 6 months.

Table 6.8: *Delta-v budget for formation maintenance of the rotation strategy. The values are computed over one orbital period as a reference.*

delta-v (cm/s)	s/c 1	s/c 2	s/c 3	s/c 4	s/c 5	s/c 6
Step 1	0	4.12	4.12	0	4.12	4.12
Step 2	4.12	4.12	0	4.12	4.12	0
Step 3	4.12	0	4.12	4.12	0	4.12
Total	8.24	8.24	8.24	8.24	8.24	8.24

Fuel balancing with translation The main idea of the first study case is to study the possibility of balancing fuel consumption by implementing two subsequent translations in the normal direction. The idea is to have:

Step 1 Up translation as in Figure 6.27a. Satellites 5 and 6 do not need any control for formation maintenance, while 1,2,3,4 will consume some fuel: s/c 2 and 3 will consume more than s/c 1 and 4.

Step 2 Down translation, as in Figure 6.27b. Satellites 2 and 3 do not need any control for formation maintenance, while 1,4,5,6 will consume some fuel: s/c 5 and 6 will consume more than s/c 1 and 4.

The idea of the fuel balance strategy is based on the hypothesis of 1 year of scientific observation. Every 3 or 6 months, a manoeuvre should be implemented to modify the configuration from step 1 to step 2 geometry. Alternating the configurations allows for fuel balancing. In the following study, it is important to assess the delta-v for the manoeuvre and then proceed with the frequency and operations consideration. An assessment of the delta-v budget for the formation keeping is provided for steps 1 and 2 in Table 6.9. Note how the delta-v required is higher for the satellites with the higher displacement in the normal direction. In fact, they undergo an oscillation with a wider amplitude, and consequently, a higher delta-v is required to maintain the relative position.

Table 6.9: *Delta-v budget for formation maintenance of the translation strategy. The values are computed over one orbital period as a reference.*

delta-v (cm/s)	s/c 1	s/c 2	s/c 3	s/c 4	s/c 5	s/c 6
Step 1	4.12	8.24	8.24	4.12	0	0
Step 2	4.12	0	0	4.12	8.24	8.24
Total	8.24	8.24	8.24	8.24	8.24	8.24

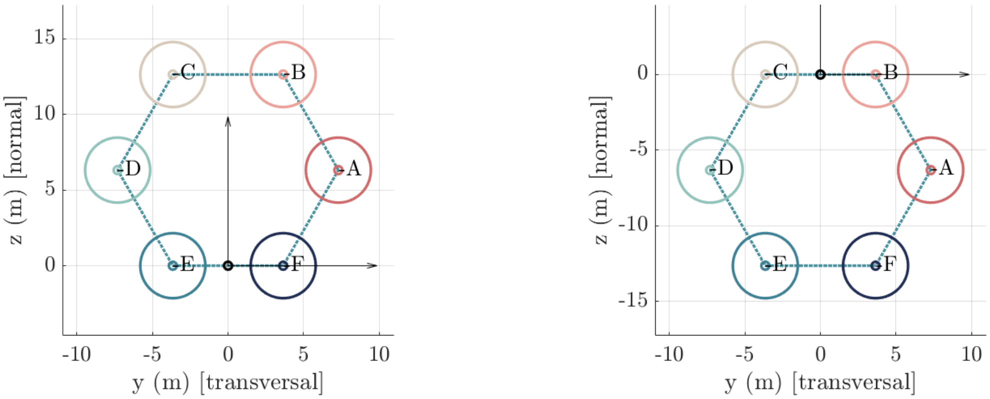

(a) *Step 1 - up translation.*

(b) *Step 2 - down translation.*

Figure 6.27: *Up and down translation in the normal direction for the six-spacecraft formation.*

Conclusion To conclude, this analysis demonstrates the feasibility of keeping a hexagonal formation of six spacecraft with balanced fuel consumption. This is essential for the symmetrical design of each platform. Moreover, a difference in the spacecraft mass affects the ballistic coefficient for calculating the effect of the atmospheric drag. It is reasonable to maintain the mass of the platforms more similar as possible to reduce the differential drag effect.

6.4.2 Non-planar Geometries

This section analyses the possibility of exploiting natural solutions of the relative motion for combined interferometry. Starting from the FFLAS study, three- and six-spacecraft cases are considered in the analysis. The main requirement for passive interferometry is the constraint on the relative distance and attitude of the formation. Specifically, the relative distance and attitude among the platform in the formation shall be kept fixed, to allow a correct reconstruction of the combined synthetic beam. As a consequence, from the analysis of natural solutions in Section 3.3, only the General Circular Orbit (GCO) solution provides a fixed separation among the spacecraft. Differently from active SAR cases, where helix or pendulum geometries were adopted, the GCO is exploited for the first time for distributed passive L-band purposes. Differently from planar geometries, the formation on a GCO rotates around the central virtual point and requires a particular design of the attitude control, to keep the relative geometry and the relative attitude fixed in time.

In the context of this thesis, the idea of employing a GCO trajectory was proposed at the conclusion of the nominal phase of FFLAS for a possible reduction of the delta-v budget for formation maintenance, during the extended operational life. In fact, given the periodic nature of the solution, the control should only compensate for external perturbations typical of the LEO environment. This is an important difference from the FFLAS or the planar case with six to twelve spacecraft, where a fully forced motion was required to keep the formation rigid and fixed. Differently from previous studies, the GCO can naturally maintain the correct configuration for combined interferometry. The possibility of reducing the delta-v for formation maintenance has been of primary importance in the identification of possible strategies for the mission extension phase of FFLAS, as well as for new mission concepts.

As shown in Section 3.3, the geometry of the solution is such that the inclination of the array plane is around 30 deg around the direction of motion of the RTN frame. This is a consequence of

Equation (3.43) for the GCO case. Moreover, the natural solution of the relative motion is a stable orbit, and the control action required for formation maintenance when considering a perturbed environment is relatively small. At the same time, the stable nature of the analytical solution guarantees more robust collision avoidance in case of failure of the control, compared to the FFLAS case. The external perturbations lead to an unsafe situation over one day period, leaving the possibility to implement correction manoeuvre even from ground control. Nevertheless, robust planning of the safe mode transition is essential for safe operations. A final advantage of this solution is that the external perturbations similarly affect the spacecraft, resulting in a balanced delta-v consumption for formation maintenance. Figure 6.28 represents the GCO configuration for a three- and six-spacecraft formation.

The relative trajectory has been initialised to guarantee a correct distance among the distributed antenna array to perform combined interferometry. Therefore, different formation geometry can be obtained depending on the spacecraft dimensions and mass, as described in Table 6.10. The *case-1: FFLAS-FO* and the *case-3: Six-Spacecraft case* are described in this section, while the *case-2: TriHex* is described in Section 6.5.

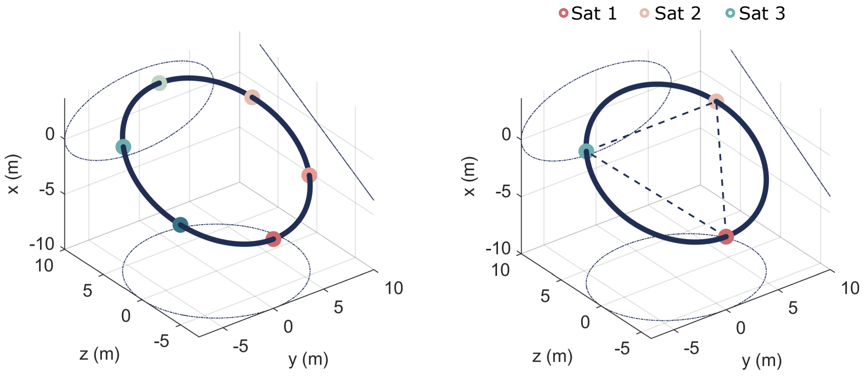

(a) *GCO configuration for 6-satellites formation.*

(b) *GCO configuration for 3-satellites formation.*

Figure 6.28: *General Circular orbit configuration for FFLAS follow on and the six-spacecraft case.*

Table 6.10: *Initial condition for different GCO configurations.*

Parameter	case-1: FFLAS-FO	case-2: TriHex	case-3: Six-Spacecraft case
No. of spacecraft	3	3	6
Dry Mass (kg)	1200	450	450
Spacecraft diameter (m)	8	3	3
GCO radius ρ (m)	6.228	5.0	8.5

FFLAS-FO For the FFLAS-FO case, the reference orbit of the formation is the one for the FFLAS study in section 6.3, i.e. the orbit of the SMOS satellites. The idea is to reconfigure the triangular formation in the GCO natural orbit, to reduce the fuel consumption for formation maintenance. Specifically, this study envisions the possibility of moving the distributed system to a more advantageous orbit at the end of the nominal science operation for the extension phase of the mission. In this way, the formation can still provide scientific data even in a different configuration.

First, to assess the feasibility of the mission extension phase for the FFLAS study, it is important to design the reconfiguration manoeuvre between the planar triangle and the GCO configuration. The manoeuvre is designed based on the closed-loop MPC, in ROEs framework. The initial condition of the formation is the nominal triangular geometry of FFLAS during the science phase (see Section 6.3.5). The final condition for the reconfiguration is the GCO trajectory with radius $\rho = 6.228\,\mathrm{m}$. Moreover, the analysis considers the mean J2 Earth's oblateness effect to design the manoeuvre, and the thrust is limited in the normal and transversal direction only, as the main requirements of FFLAS spacecraft. A maximum thrust of $5\,\mathrm{mN}$ and a reconfiguration period of about $3/4$ of the orbital period is imposed. Finally, for collision avoidance purposes, a minimum relative distance threshold is considered equal to 11 m among the centre of the spacecraft. Figure 6.29 shows a three-dimensional representation and the control thrust level for the reconfiguration manoeuvre. The reconfiguration is achieved in less than 1 orbital period. The manoeuvre requires a delta-v budget for each spacecraft of about $7\,\mathrm{cm\,s^{-1}}$, confirming the feasibility of the approach for the FFLAS follow-on phase.

Second, a feasibility analysis is performed to assess the delta-v budget required to keep the GCO relative trajectory and a sensitivity analysis is executed to test the robustness of the control against uncertainty in the reconfiguration manoeuvre. The simulation is completed with the GNC framework presented in Chapter 5. Table 6.11 reports the initial conditions to initialise the simulation in terms of mean Keplerian elements, initial epoch, simulation step and simulation time. The orbit radius of the GCO is set equal to $6.228\,\mathrm{m}$ to keep the spacecraft separation equal to $13\,\mathrm{m}$. The three spacecraft are placed on the GCO equally spaced, resulting in a phase angle of 30 deg, 150 deg, and 270 deg.

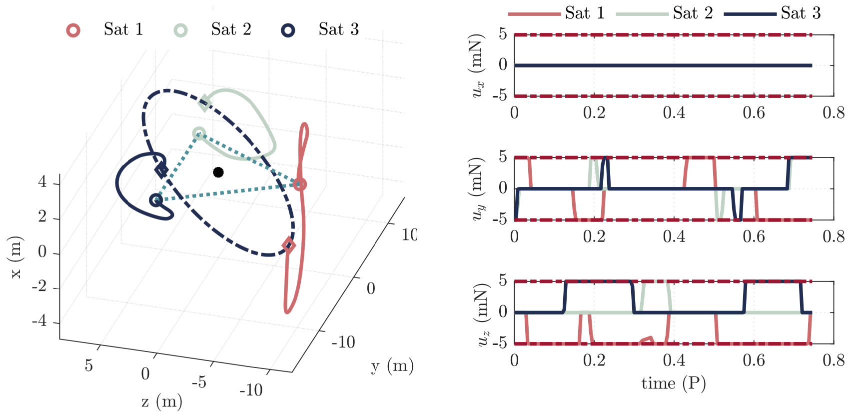

(a) *Reconfiguration manoeuvre for the triangular to GCO configuration.* **(b)** *Thrust profile for the triangular to GCO configuration.*

Figure 6.29: *Reconfiguration between triangular and GCO formations and control profile.*

Table 6.11: *Initial condition for the simulation and mean Keplerian parameters of the reference orbit.*

Parameter	**Value**
Mean Keplerian elements (m,-,deg)	$\{7153.1,\ 0,\ 98.51,\ 270.83,\ 0,\ 0\}$
Initial epoch	21 March 2025 12:00
Step Size (sec)	10
Simulation Time	15 orbital periods (1 day)
GCO radius (m)	6.228

The selected initial conditions have been tested against uncertainties in the relative state. Specifically, a Monte Carlo (MC) analysis has been carried out to assess the feasibility of on-board control capability against possible error in the reconfiguration from the triangular to the GCO. For the analysis, 500 random sample points have been considered under Gaussian distribution, considering mean and standard deviation for the radius of the GCO, ρ, and the phase angles, as reported in Table 4.3. The uncertain control analysis connected to this situation has already been presented in Section 4.2.1, where the initial conditions for the set-up of the 500 MC runs have been presented. From the analyses shown in Section 4.2.1, the uncertainty in the formation maintenance of the GCO trajectory converges to an error in the control of $\pm\ 2\,\mathrm{cm}$ (in terms of relative states in RTN) in less than half of an orbital period for all the 500 samples points. For completeness, in Figure 6.30 is reported the error in the control in terms of relative states for the three satellites for one sample of the MC run. Moreover, Figure 6.30b shows the thrust profile required to keep the formation. As for the technological limitation, the thrust on the third axis (radial direction) is not considered in the simulation, as the spacecraft can control only in the transversal and normal directions. Moreover, the thrust was limited to $25\,\mathrm{mN}$, as from the limitation of the FFLAS thrusters (see Section 6.3). The corresponding delta-v budget over one day of operations for each spacecraft is reported in Table 6.12.

The total delta-v budget for each spacecraft is around $0.8\,\mathrm{cm\,s^{-1}\,d^{-1}}$, which is significantly lower than the nominal delta-v to keep the FFLAS triangular geometry (i.e. about $60\,\mathrm{cm\,s^{-1}\,d^{-1}}$, see Section 6.3.7). Furthermore, the fuel consumption is almost balanced among the platforms, providing naturally a good solution also from this point of view. To conclude, the total delta-v budget is essen-

Table 6.12: *Daily delta-v budget for formation maintenance of the FFLAS-FO configuration.*

Spacecraft	**Radial**: Δv_x	**Transversal**: Δv_y	**Normal**: Δv_z
Spacecraft 1 (cm/s)	0	0.72	0.11
Spacecraft 2 (cm/s)	0	0.56	0.10
Spacecraft 3 (cm/s)	0	0.61	0.12

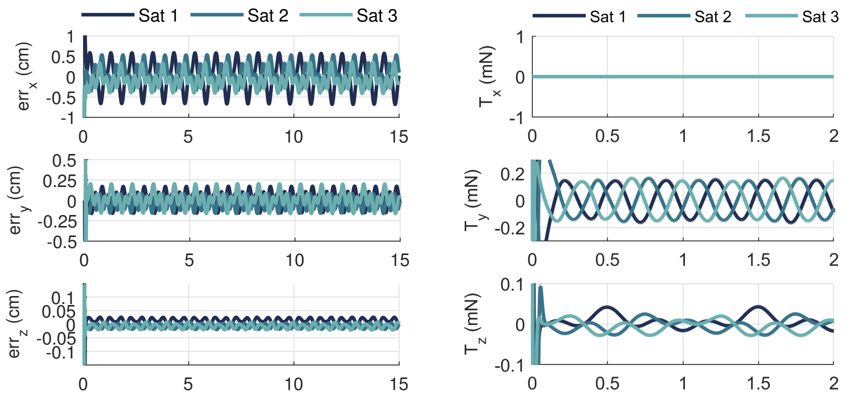

(a) *Control error profile for one day of propagation for the GCO formation of one MC run.*

(b) *Thrust error profile for one orbit of propagation for the GCO formation of one MC run.*

Figure 6.30: *Control error and thrust profile for the GCO maintenance, considering one sample of the MC runs.*

tial to understand the feasibility of the extension phase for the FFLAS case. Both the reconfiguration and the formation maintenance influence the possible extension period. Starting with the daily delta-v for formation maintenance, it is below $1\,\mathrm{cm\,s^{-1}}$. Including a 20% margin, a yearly consumption of $3.65\,\mathrm{m\,s^{-1}}$ is identified. For the reconfiguration manoeuvre, a delta-v of $7\,\mathrm{cm\,s^{-1}}$ is required only once at the beginning of the extension phase. The overall delta-v includes the yearly consumption for formation keeping and the initial manoeuvre effort. Furthermore, at the end of the nominal operations, the fuel remaining in the tanks can be considered around 1% to 3% of the one at the beginning of life. The overall delta-v at launch condition for FFLAS is about $2300\,\mathrm{m\,s^{-1}}$, corresponding to a remaining delta-v of $23\,\mathrm{m\,s^{-1}}$ to $115\,\mathrm{m\,s^{-1}}$ at the end-of-life. Table 6.13 shows the possible extension period depending on different levels of remaining fuel. Even with a small percentage (1% or 2%) of the remaining fuel in the tanks, the mission could continue in the GCO formation for a minimum of about 6 years, confirming the promising design of formation flying strategies based on GCO solutions.

Table 6.13: *FFLAS-FO extension period depending on the available delta-v at the end of the nominal phase.*

Parameter	**Value**		
Remaining fuel	1%	2%	3%
Available delta-v (m/s)	23	46	69
FFLAS-FO extension period (years)	$\sim$ 5.5	$\sim$ 11.3	$\sim$ 17

A final consideration is required on the stability and safety conditions of this approach. Differently from the analysis in Section 6.3.6, where a forced motion was required to keep the triangular formation, against the relative natural dynamics, in this case, the control is required to counteract the external perturbation to keep the close natural solution of the relative motion. A similar analysis as for the triangular configuration has been performed, propagating the initial conditions of the spacecraft for one day with no control effort. The results of the time evolution of the spacecraft separation are shown in Figure 6.31. In the case of FFLAS, the collision threshold was violated after less than half of an orbital period (see Section 6.3.6). In this case, the natural propagation does not violate the collision threshold up to 8 to 9 orbital period. This aspect has an important influence on the safety of the operations. First, in case a failure occurs to one engine, the formation has some time (up to 7 orbital periods) to move to a safe configuration. Moreover, even if it is advisable that an automatic routine is implemented on-board, it leaves some time for the ground control to adjust and modify the on-board operations.

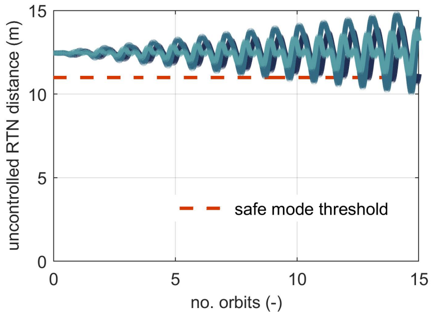

Figure 6.31: *Spacecraft separation under external perturbations of the LEO region with no control.*

Six-satellite formation The case of six satellites in the GCO configuration is analysed in this paragraph. The initial parameters of the simulation are reported in Table 6.10. Moreover, the simulation is initialised on 21/03/2025 at 12:00, and the formation is propagated over one day period, with a time step of $5\,\mathrm{s}$. The dynamical model considers the gravity field up to degree and order 6×6 and the drag effect is included. The simulation aims at analysing the feasibility of the formation maintenance over 1 day period in terms of:

- Delta-v budget and fuel consumption balancing among the spacecraft.
- On-board control accuracy on the relative state.

The first aspect analysed is the delta-v budget for formation maintenance. Continuous control is needed to counteract the external perturbations of the LEO environment. The delta-v is evaluated in the radial-transversal-normal frame for each platform of the formation over one day period. As before, it has been considered that the thrust is provided only in the transversal and normal direction, with no radial component, to reduce fuel consumption. The results are shown Figure 6.32a. An almost balanced delta-v budget among the six spacecraft in all directions is present, with a magnitude of the delta-v in every direction in the centimetre per second level. The most relevant term in the control must be provided in the transversal direction, with a daily delta-v of about $0.64\,\mathrm{cm\,s^{-1}}$. Moreover, the control required in the normal direction is less expensive, with a daily delta-v of about $0.08\,\mathrm{cm\,s^{-1}}$. The second aspect of primary importance is the evaluation of the control performance. The LQR controller is used to provide the commanded thrust to the model of the low-thrust engine, which introduces noises and delays in the command. These values are dependent on the engine selection. Moreover, a limitation on the thrust is imposed, and in this scenario, a maximum thrust of $1\,\mathrm{mN}$ was considered. The control accuracy on the relative state of the spacecraft was evaluated considering the error between the actual relative state and the reference trajectory, at each time instant. The results are reported in Figure 6.32b, describing the control accuracy in the radial-transversal-normal direction. The error in the control in the radial and normal directions is below $\pm 2\,\mathrm{cm}$ accuracy, while the transversal component is less accurate, with an error of about $\pm 5\,\mathrm{cm}$. Finally, note that similar considerations of FFLAS-FO applies to the safety conditions in case of on-board failure.

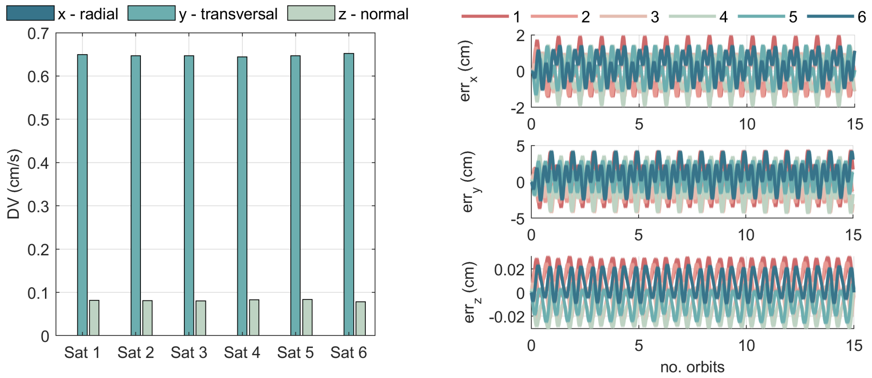

(a) *Delta-v budget for one day of formation maintenance.*

(b) *Control error profile for one orbit of propagation for the GCO formation for one day of propagation.*

Figure 6.32: *Control error and delta-v budget for the GCO maintenance, considering the six-satellite formation case.*

6.4.3 Conclusion

The promising results obtained for the science phase of distributed system in the GCO configuration, enhanced the study of a different mission concept, namely the TriHex preliminary study. The natural solution of the relative motion has the following benefits:

- The external perturbations cause a small oscillation and translation of the relative trajectories compared to the nominal natural motion.
- A small daily delta-v effort is required to counteract external perturbation and is balanced among the spacecraft.
- The natural behaviour in case of a failure requires the safe mode to be implemented in a maximum of one day period.

Moreover, the reduced delta-v budget required to keep the formation driven the solution for smaller and lighter platforms, going toward the first step toward the miniaturization of the distributed system for passive L-band observations. In the following section, the new TriHex concept is analysed, introducing promising aspects from both payload and operations points of view.

6.5 SP3: Three Hexagonal formation study

Starting from the outcome of the previous section, with the consortium of the FFLAS study (Manuel Martin-Neira - ESA-ESTC, Albert Zurita - Airbus D&S, and Berthyl Duesmann - ESA-ESTEC), a new mission concept to deal with the main limitations of the FFLAS study has been identified. One of the most important innovations is the design of an alias-free antenna, to deal with the non-planarity of the GCO configuration. The TriHex concept consists of three spacecraft flying on a GCO configuration with significantly reduced platform dimension compared to the FFLAS ones. The main features of the concept are the following [129]:

- The deployable feature of the structure of FFLAS is removed for the TriHex concept.
- The external diameter of the hexagonal platform is $3\,\mathrm{m}$, instead of the $8\,\mathrm{m}$ of FFLAS.
- The platforms are placed at $5\,\mathrm{m}$ separation centre-to-centre.
- Instead of having deployable solar panels, the sides of the hexagonal spacecraft are equipped with body-mounted solar panels on top and later sides of the spacecraft (see the light blue part in Figure 6.34).
- The antenna is designed to be alias-free, to deal with the non-planar nature of the Array Plane in the GCO configuration, differently from the antenna adopted for FFLAS. This innovative solution has been proposed and studied by Airbus D&S.
- A lower altitude of the reference absolute orbit has been selected w.r.t. FFLAS (i.e. $500\,\mathrm{km}$). This was driven by the need for the new interferometer antenna to guarantee high performances and, simultaneously, for the implementation of disposal policies at the end-of-life under natural decay.
- The estimated wet mass for each platform is $700\,\mathrm{kg}$ (dry mass of about $450\,\mathrm{kg}$), which is significantly lower than the $1600\,\mathrm{kg}$ wet mass of FFLAS.

The following section presents the operational and payload considerations for this new distributed concept.

6.5.1 Payload and operational considerations of TriHex

The graphical representation of the TriHex concept is shown in Figure 6.33. One can observe how the spacecraft are placed on the GCO with symmetric angular separation. Moreover, the relative motion causes the spacecraft to rotate around the central point (origin of the local RTN frame) and at the same time the formation moves along the reference orbit in $+y$ direction. Over one orbital revolution, the Sun describes a cone of ± 30 deg aperture around the "direction of the Sun" arrow. This aspect is quite important from both the payload and operations points of view.First, the GCO orbit is tilted by a constant angle (30 deg) around the direction of motion. Since the spacecraft point in a fixed direction, - i.e. the antenna points in $-h_I$ direction, with $-h_I$ the normal to the plane of the GCO relative trajectory -, the antennas never have the Sun in the field-of-view. At the same time, the opposite side of the platform is equipped with body-mounted spacecraft for power production purposes. This aspect is important for the payload performances, as the images acquired by the L-band interferometers are affected by the Sun interference [129], as also demonstrated for the SMOS mission.

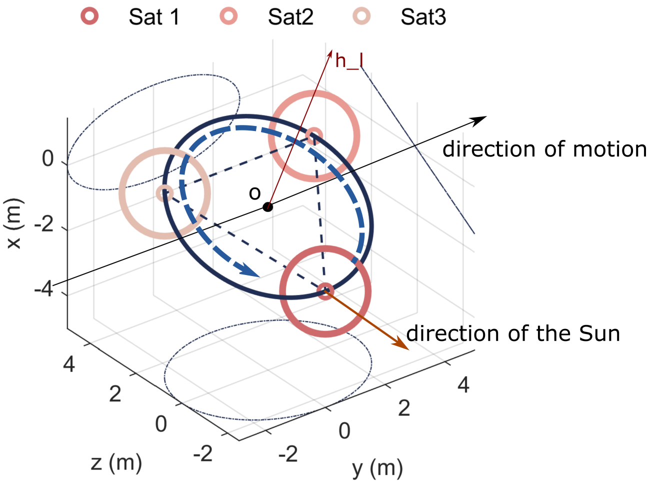

Figure 6.33: *Geometric representation of the TriHex concept.*

Moreover, as mentioned before, to remove any effect of the 30 deg tilt of the GCO on image acquisition, the payload is designed to be alias free, so that it can achieve the performances reported in Section 2.5. This configuration can provide up to 15 to 17 km of spatial resolution in boresight and nadir, which is a significant improvement compared to the SMOS mission. Note that FFLAS was capable of providing up to 10 km spatial resolution, but with a significantly larger and heavier platform. The platform configuration is reported in Figure 6.34, where different orientations are shown of the TriHex configuration. At this point, it is important to understand the control effort required to keep such formation and the implications on the low thrust engines.

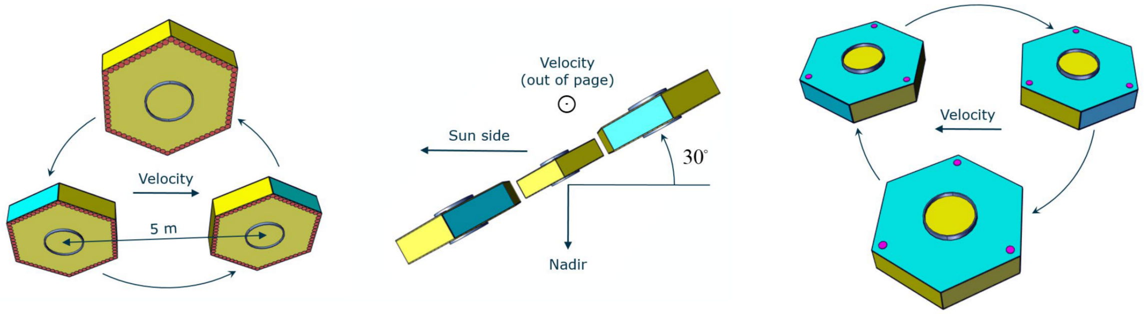

Figure 6.34: *Configuration of the TriHex concept with different orientations: bottom view (left), side view (centre), and top view (right). Credits: Manuel Martin-Neira - ESA-ESTEC.*

6.5.2 Formation keeping

The formation keeping analyses for the TriHex concept is based on the GNC framework developed in Chapter 5. The spacecraft dynamics include the gravitational perturbation up to order and degree 10×10, and the aerodynamic drag effect. Moreover, the nominal reference orbit has been selected as a 6 a.m. - 6 p.m. SSO at a mean altitude of $500\,\mathrm{km}$. The different selection of the mean altitude of the reference orbit compared to the SMOS mission and the FFLAS study was driven by the need to have more accurate payload performances [129]. In addition, it enhances a natural re-entry in less than 25 years. On the contrary FFLAS envisioned a disposal manoeuvre at the end of life to re-enter the atmosphere. Given the smaller mass and dimensions of the platform of TriHex, the possibility of a natural re-entry at the end of life is preferred.

The initial conditions for the set-up of the simulation are reported in Table 6.14. The mean Keplerian elements of the reference orbit, the GCO radius, the initial epoch, the step size and the simulation time are defined. The simulation is performed over 2 orbital periods and then extended to one day, to assess the daily delta-v budget.

Table 6.14: *Initial condition for the simulation and mean Keplerian parameters of the reference orbit.*

Parameter	**Value**
Mean Keplerian elements (m,-,deg)	$\{6878.1, \quad 0, \quad 98.51, \quad 270.83, \quad 0, \quad 0\}$
Initial epoch	21 March 2025 12:00
Step Size (sec)	10
Simulation Time	2 orbital period
GCO radius (m)	2.5
Phasing angle (deg)	30, 150, 270

During the simulation, we consider the navigation block based on the ground reconstruction knowledge of the spacecraft's absolute and relative state. In this case, accuracy in the navigation of $\pm\, 2\,\mathrm{mm}$ is considered for the three platforms. Moreover, the thrust has been limited to a maximum of $1\,\mathrm{mN}$ and the spacecraft can provide thrust in three directions. The idea is to equip each platform with six small thrusters aligned with the centre of mass, to control the relative motion of the formation. Similarly to the FFLAS case, a decentralised navigation approach is adopted for TriHex. Two cases have been analysed for formation maintenance:

1. The thrust is available in the three directions of the RTN frame.

2. The thrust is limited to the transversal and normal direction only, removing the radial component, for fuel saving.

Even if the first case, when the spacecraft thrust in the three directions, is less efficient from a fuel consumption point of view, the analysis has been carried out to assess a possible improvement in the control accuracy of the formation maintenance. The analysis has been carried out under a MC approach with 500 runs, considering a standard deviation of $20\,\mathrm{cm}$ for the GCO radius and of 5 deg for the phasing angles of Table 6.14.

The results of the analyses are described in Figure 6.35. The graphs on the top part represent the error on ROEs in terms of mean and standard deviation for case 1 (i.e. considering the thrust in the three directions of RTN). Figure 6.35a represents the error in the control comparing the actual and the nominal trajectory. A part from an initial moment of convergence, the error in the ROEs components is bounded below $\pm 2.5\,\mathrm{cm}$. Figure 6.35b shows the thrust profile during the formation maintenance. Similarly, Figures 6.35c and 6.35d describe the error in ROEs and the thrust profile for the case of no thrust component in the radial direction (i.e. case 2). The control accuracy is slightly worst than the three-axis case, specifically for the relative semi-major axis and the relative eccentricity vector components. For the thrust profile, initially, the effort is higher to make the control converge, and after a few instants, it stabilises in the nominal thrust profile to keep the formation geometry. One can observe that with the three-axis approach the convergence of the control is quicker for all the ROEs components. The corresponding delta-v is computed from the wet mass of each platform of about $700\,\mathrm{kg}$. Table 6.15 provides the delta-v budget for one day of formation maintenance in the radial, transversal and normal directions for cases 1 and 2. On average, for case 1, the most relevant component in the required delta-v is in the transversal direction, together with the radial one. It results in a total delta-v for each platform of about $4.5\,\mathrm{mm\,s^{-1}\,d^{-1}}$ for each day of formation maintenance. On the other hand, passing to case 2, one can observe that the solution is more efficient from the delta-v point of view. Specifically, the transversal component increases to compensate for no radial thrust: its magnitude is almost double than case 1. Nevertheless, the total delta-v is only slightly better than the three-axis thrust case, resulting in about $4.1\,\mathrm{mm\,s^{-1}\,d^{-1}}$ for each day of formation maintenance.

Table 6.15: *Daily delta-v budget for formation maintenance of the TriHex configuration.*

Spacecraft	**Radial**: Δv_x	**Transversal**: Δv_y	**Normal**: Δv_z
Case 1: thrust in the three directions of RTN			
Spacecraft 1 (cm/s)	0.17	0.14	0.12
Spacecraft 2 (cm/s)	0.15	0.19	0.08
Spacecraft 3 (cm/s)	0.18	0.22	0.05
Case 2: no thrust in the radial direction			
Spacecraft 1 (cm/s)	0	0.34	0.10
Spacecraft 2 (cm/s)	0	0.32	0.09
Spacecraft 3 (cm/s)	0	0.34	0.04

To conclude, some considerations have been identified. First, the thrust magnitude is significantly lower than the FFLAS case, where up to $25\,\mathrm{mN}$ are required over the nominal and non-nominal operations (see Chapter 7). For TriHex, sub-millilitre level thrust is required for formation maintenance for cases 1 and 2. Consequently, smaller low-thrust engines could be considered for this specific scenario. An important advantage of smaller electric engines relies on the lower power demand during operations, which could be a critical aspect in the design of the power subsystem. Another important aspect relates to the delta-v budget and the control error in the ROEs framework. Case 2, with no

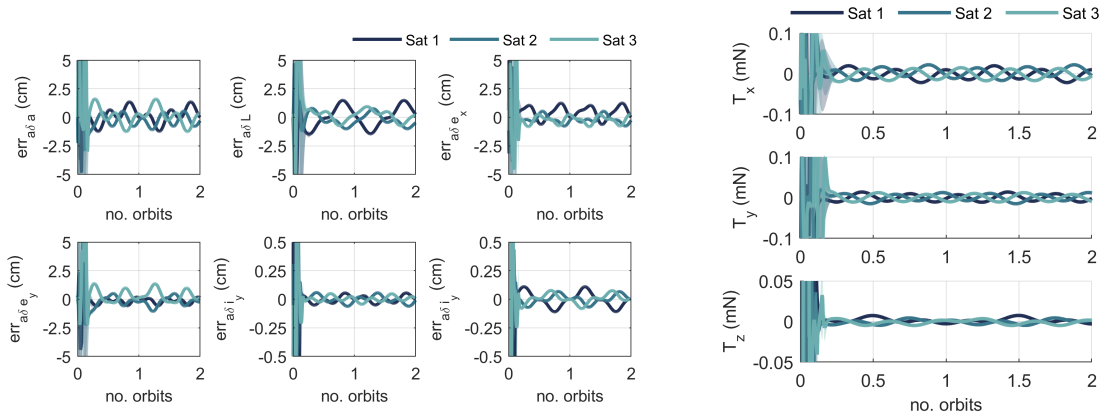

(a) *Control error with three axis control.*

(b) *Thrust profile with three axis control.*

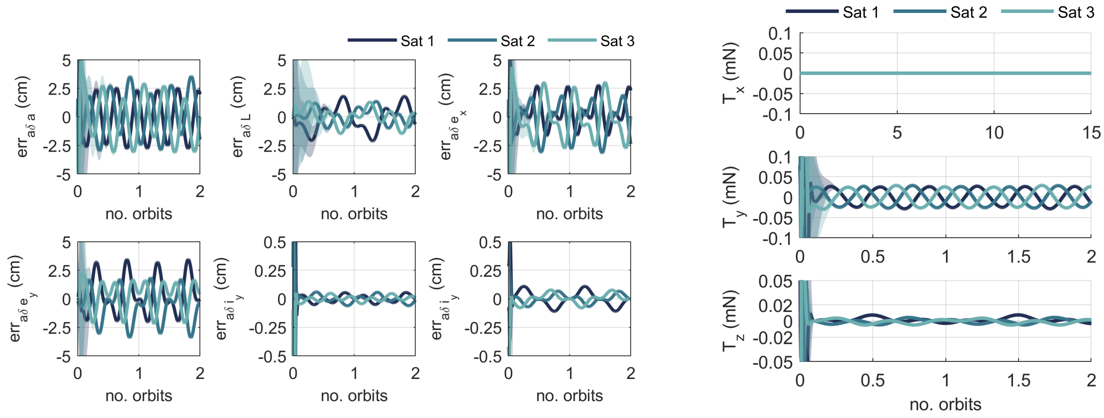

(c) *Control error with no radial control component.*

(d) *Thrust profile with no radial control component.*

Figure 6.35: *Formation maintenance for the TriHex configuration. Top: case 1. for three-axis control, bottom: case 2. with no radial component of the thrust.*

thrust in the radial component, is slightly more efficient than case 1 from a delta-v budget point of view, saving a few sub-millimetres per second per day. This could be relevant for setting up the mission's lifetime: even a slightly lower propellant consumption per day could significantly increase it. On the other hand, the accuracy in the formation maintenance is slightly better for case 1. This aspect is mainly relevant for the payload performances, as the interferometry response is more accurate as the error in the relative position is lower. Consequently, further analyses are needed to understand better the impact of the two strategies on payload performances. Furthermore, a detailed analysis of the required thrust profile over different mission phases, from launch to disposal, including formation establishment and orbital manoeuvre, is required. Specifically, in future work, the following analysis is envisioned:

- As for the FFLAS, the proper design of the manoeuvre for the transition to and back from the calibration mode should be designed.
- The formation acquisition and the transition to the safe mode are of primary importance to understand if a smaller engine with sub-millinewton level thrust could be employed for the

overall mission duration.

- Finally, it would be important to understand the feasibility of performing collision avoidance manoeuvre with the current debris population with such low-thrust engines.

The main idea for such analyses would be the application of either the MPC or the convex optimization algorithm for manoeuvre definition and, subsequently, the testing over the GNC framework, including the on-board navigation reconstruction.

6.6 Chapter conclusion

In conclusion, this chapter presented several approaches to realise both active and passive interferometry with distributed systems. The focus was on the formation geometry trade-off and selection and the control accuracy that continuous control can provide in different situations. Most analyses have been applied to passive interferometry, specifically the FFLAS study and the TriHex concept. These two scenarios are strictly connected to each other, as they provide two different approaches to propose innovative mission concepts. The TriHex has been developed as a follow-on study of the FFLAS, aiming to reduce the control effort and improve the formation's safety condition. Both of these tasks have been completed, and the TriHex has been identified as a promising baseline for future distributed systems in passive interferometry. On the other hand, other concepts have been proposed. For example, in the context of passive interferometry, a six-spacecraft scenario was also investigated, both as planar and non-planar formations. In this case, the main challenge was properly designing a fuel balance approach for the planar case, while the GCO solution could serve as an augmented baseline for the three-spacecraft geometry. One possibility could be to start the testing with a three-spacecraft mission (as TriHex or FFLAS) and then increase the baseline with three more spacecraft to realise a larger aperture plane and consequently improve the spatial resolution of scientific data (see Chapter 2). Finally, concerning the active SAR formation, two concepts currently under study in ESA-ESTEC have been analysed. The aim was to implement and test the GNC framework on different orbital situations, with much larger baselines (hundreds to thousands of kilometres of separation) compared to the passive case (in meter level). The flexibility and robustness of the GNC framework demonstrate the possibility of keeping the formation with similar technology implemented for the FFLAS scenario. These results could pave the way to the utilisation of low thrust. Specifically, the electric propulsion could also be applied to the active SAR missions, typically based on impulsive control techniques.

CHAPTER 7

Results Part II: FFLAS study

No great discovery was ever made without a bold guess.

— Isaac Newton

THIS chapter presents the analyses performed for the FFLAS study (SP1), the primary test case of this dissertation. The overview of the study has been outlined in Section 6.3 together with the main mission requirements. These led to the selection of the baseline triangular geometry based on several parameters, such as the Sun direction, possible thrust impingement and balance of the delta-v consumption among the platforms. This is essential to start the analysis and design of the complete life cycle of the study. To properly present the results of the simulation performed for FFLAS, the chapter is divided into two main parts. First, the definition of the operational mission scenarios is presented, together with the strategy and optimal manoeuvre design for different operation phases. The second part presents the numerical simulations performed with the GNC framework developed in Chapter 5. The performance in terms of navigation and control accuracies are described for different operational phases. Most of the analyses included in this chapter have been successfully presented in the final review of the ESA-funded FFLAS study, together with Airbus D&S Madrid, which was in charge of the design and development of the vehicle platform and payload technology.

7.1 Guidance and control of formation flight

This section presents the definition of the operational phases for the FFLAS study. The definition of the various phases is fundamental for assessing the control effort and the reconfigurations manoeuvres required during the operative life of the mission. As for the dissertation, first, the operational phases are described. Then, the design of the transition between the two specific nominal phases (i.e. science and payload calibration) is presented. Specifically, the detailed trade-off for defining the transition to the payload calibration is described, as it is a critical phase for the correct functioning of the interferometers. This section aims to present the basics for the complete simulations of the FFLAS study of Section 7.2.

7.1.1 Operational phases definition

For the FFLAS study, we identify five main operational phases as shown in Figure 7.1. First, the Launch and Early Orbit Phase (*LEOP*) and the *commissioning phase* consist of the study of the satellite separation from the launcher, the individual/formation commissioning and the assessment of the manoeuvrability and reconfiguration capability for the first establishment of the formation. Second, two *nominal phases* have been identified: the *science* and the *payload calibration* phases. The former consists of the nominal scenario for scientific observation of the Earth, where the vehicles fly in a rigid equilateral triangle formation. The latter is required for the correct functioning of the payload when pointing to the cold sky is enforced for calibration purposes. In addition, a set of non-nominal phases are envisioned to deal with unwanted behaviour or events during the operations. The *safe-mode* is devoted to Fault Detection, Isolation and Recovery (FDIR) activities. In the eventuality of failures that prevent the recovery of nominal operations, a *back-up formation* strategy is identified with fewer vehicles (two out of three). Finally, the last two phases are connected to the conclusion of the operational life of FFLAS. The *extension phase* addresses the possibility of performing science after the nominal operations. The last one, at the very end of life, the *disposal* is programmed to respect the end-of-life guidance for spacecraft in LEO region. Figure 7.1 schematically depicts the aforementioned operational phases, which are moreover subdivided into nominal and non-nominal categories, highlighting the possible transitions among them.

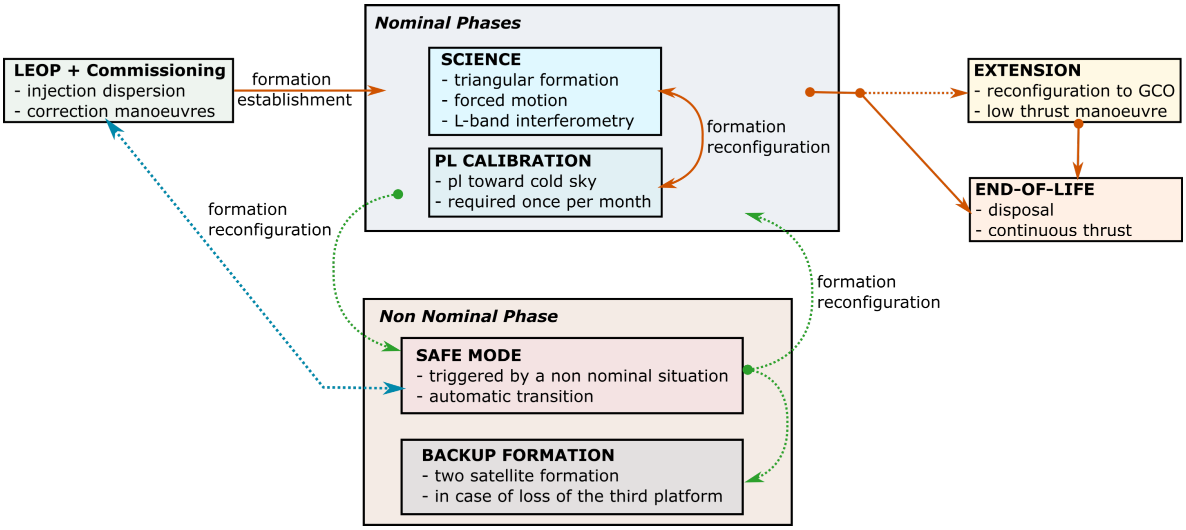

Figure 7.1: *Schematics of the simulation scenarios for FFLAS.*

7.1.2 Design of the transition between science and payload calibration

The calibration of the passive distributed antennas has to be performed twice a month and requires the formation to pass from Earth pointing (referred to as Earth Pointing Mode (EPM)) to cold sky pointing (referred to as Cold Sky Pointing Mode (CSPM)). We identify some requirements for the reconfiguration:

- The relative triangular formation shall be guaranteed at both the initial and final times of the manoeuvre.
- The attitude of the satellites shall be compliant with the Sun's direction during the whole phase transition to ensure enough power generation for the manoeuvre.
- The inter-satellite link shall be reactivated once the CSPM is established.

As a result, the whole triangular formation shall perform a manoeuvre to point the normal to the Aperture Plane to the zenith direction: both an attitude and an orbital manoeuvre are required. This dissertation focuses on the design of the orbital manoeuvre without modelling the attitude one. To start, the generic concept of the combined attitude and orbital manoeuvres is reported in Figure 7.2. In this final condition, in fact, the optical links and the solar panels are maintained in the correct attitude configuration to ensure power generation and data exchange among the platforms. One can note that a simple attitude rotation of each satellite to point the payload in the zenith direction does not guarantee the maintenance of the ISL among the platforms. The optical link has been depicted in Figure 6.19: each satellite is equipped with only two optical ISL antennas. A pitch rotation of 180 deg to point the normal of the interferometer to the zenith direction is not compatible with the reactivation of the ISL between spacecraft 2 and 3 (see Figure 6.19), violating the requirement RP-F1 in Table 6.5. Consequently, the only compliant solution, with respect to the requirements listed above, to achieve a combined attitude and orbital manoeuvre aiming at rigidly rotating the configuration in Figure 6.19. This operation results in a final triangular geometry, where spacecraft 2 and 3 are switched, compared to the EPM configuration. As a result, the attitude manoeuvre has to be combined with a reconfiguration of the satellites of the formation. During the design procedure, two approaches were

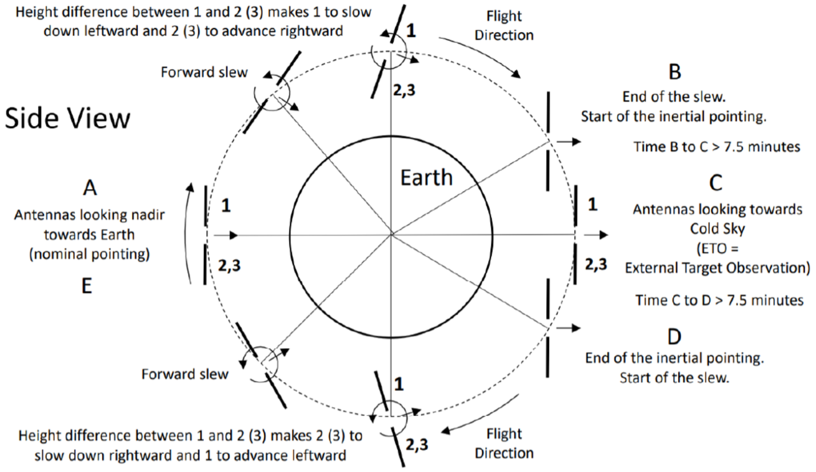

Figure 7.2: *Generic representation of the payload calibration manoeuvre for FFLAS.*

investigated to identify the most suitable strategy. The first option foresees employing an analytical trajectory to combine a circular orbital manoeuvre around the normal direction and a 180 deg pitch attitude rotation. The second strategy computes a delta-v optimal reconfiguration manoeuvre (based on Section 4.1) by solving the convex problem for the transition, decoupled by the 180 deg pitch rotation. The attitude rotation is performed only at the end of the orbital manoeuvre. In both cases, the inter-satellite minimum distance is set equal to $11\ \mathrm{m}$ to reduce the inter-satellite collision risk.

Analytical trajectory for the EPM to CSPM transition This first strategy combines the orbital manoeuvre counter-clockwise w.r.t. normal direction (z-axis) and the 180 deg pitch rotation to reach the configuration in Figure 7.2. This approach has been implemented in the initial part of the FFLAS study, and more strict constraints have been considered to design the manoeuvre:

- During the combined manoeuvre, the distance among the spacecraft must remain constant, i.e. the triangle shall remain rigid.
- The ISL shall be established during the whole duration of the reconfiguration, i.e. the relative attitude shall be kept fixed during the combined manoeuvre.
- The solar panels shall remain with their axis in the negative normal direction of the RTN, to keep the Sun pointing position.
- The reconfiguration shall last a maximum of 1 orbital period.

Those constraints have been driven mainly by the payload and the ISL configuration and by the deployable solar panels. With such strict constraints, most of the reconfiguration strategies analysed in literature (e.g. [75]) were incompatible. A shape-based methodology was proposed to keep the triangular formation rigid and, at the same time, swap the position of spacecraft 2 and 3. Under these considerations, a circular trajectory is imposed on the forced motion defined in Section 4.1 in a fixed

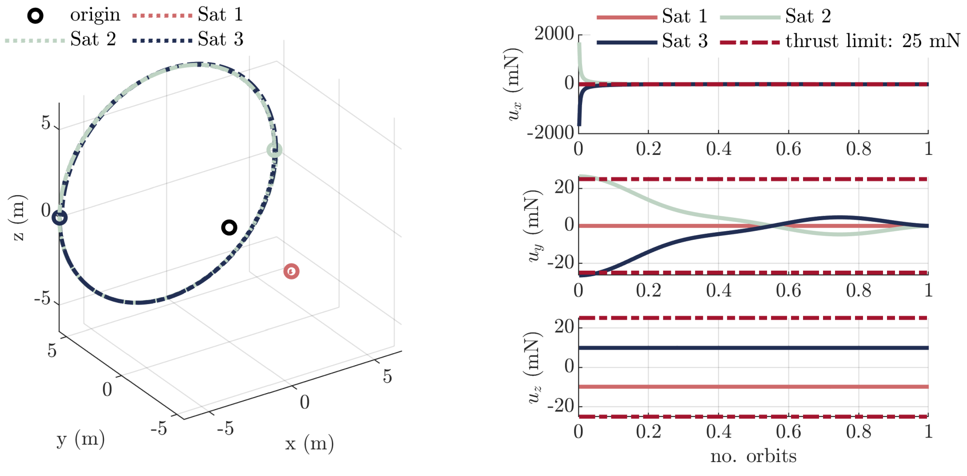

(a) *Circular trajectory of satellite 1 and 2 in the RTN frame.*

(b) *Thrust profile for the circular trajectory. The dotted line red represents the 25 mN limit of the thruster.*

Figure 7.3: *Analytical for the EPM to the CSPM transition of FFLAS.*

interval of time. Specifically, it is required that the overall transition lasts at most one orbital period. The circular trajectory is imposed on the satellites 2 and 3, while the satellite 1 has to perform the pitch attitude rotation only. The relative circular trajectory followed by spacecraft 2 and 3 is shown in Figure 7.3a. Imposing the circular motion in the $x-y$ plane corresponds to having a constant acceleration in the normal direction (z) to avoid natural oscillations. The thrust components for each satellite are shown in Figure 7.3b, where the dotted line red represents the technological limit of $25\,\mathrm{mN}$ given by the on-board thruster. The forced circular motion for satellite 2 and 3 requires a control effort in all three body axis directions (r, t, n). The thrust component required in the radial direction significantly exceeds the available thrust level given by the on-board engine because a relative trajectory shape-based strategy does not consider (and therefore advantageously exploit) the natural dynamics of the system. Thus, a different propulsive technology is needed to provide such a manoeuvre (e.g. chemical thrust). Note that the platform design solution of Section 6.3.3 foresees to embark nozzles in transversal and normal directions only. Therefore, this strategy has the additional drawback of requiring increased complexity in the spacecraft. As a consequence of this first analysis, the following requirements have been relaxed:

- The rigid triangle condition has been relaxed: only at the initial (i.e. the EPM starting point) and final instants (i.e. the CSPM arriving point) the triangular geometry must be kept.
- The ISL shall be re-established at the end of the reconfiguration, relying on the omnidirectional radio-frequency link during the orbital manoeuvre.

On the other hand, the limitation of the reconfiguration in a maximum of 1 orbital period and the constraints on solar panels have been kept. These new constraints have been considered in the design of the delta-v optimal orbital manoeuvre.

Optimal delta-v manoeuvre The second strategy implements a delta-v optimal orbital manoeuvre by solving the convex problem for the transition by means of the algorithms developed in Section 4.1. This strategy requires an additional 180 deg pitch attitude rotation at the end of the orbital manoeuvre to obtain the correct zenith pointing. Accordingly, there is no coupling between rotational and translational dynamics. The following hypotheses were considered during the manoeuvre design:

- A two-axis thruster configuration is considered in the transversal and normal axis of the body frame. This enables the use of solutions that are intrinsically candidates to become delta-v optimal manoeuvres, being burns in radial direction inefficient.
- The inter-satellite collision risk is managed by implementing a minimum separation among the satellites of $11\,\mathrm{m}$.
- The attitude of the satellite is considered fixed during the manoeuvre to ensure the correct thrusting in the normal and transversal directions.

The optimal problem was initialised considering the conditions in Table 7.1. The time for propagation is provided in terms of orbital periods, and the time step represents the discretization step along the orbit. The propagation time was selected to be three-quarters of the orbital period to deal with the constraint on the maximum available thrust, the minimum inter-satellite distance, and the time for the reconfiguration. After the implementation of the COCP in ROEs formulation, the delta-v optimal trajectory is obtained for the EPM to CSPM transition, as shown in Figure 7.4a. The trajectory is constrained to maintain an inter-satellite distance higher than $11\,\mathrm{m}$ and a thrust only in the transversal

Table 7.1: *Initial condition for the delta-v convex optimal problem for calibration phase design of FFLAS.*

Variable	Value
`UTC`	12:00 21/03/2022
Satellite wet mass	$1600\,\mathrm{kg}$
Maximum thrust	$25\,\mathrm{mN}$
Minimum separation	$11\,\mathrm{m}$
Propagation time	$3/4$ orbital periods
Time step	$20\,\mathrm{s}$
Initial ROEs	$\delta\boldsymbol{\alpha}(t_0)\left\{\begin{matrix} 0, & -0.0112, & 0, & 0, & 0, & +5.3997 \\ 0, & +6.2350, & 0, & 0, & 0, & -5.3997 \\ 0, & -6.2350, & 0, & 0, & 0, & -5.3997 \end{matrix}\right\}$ (m)
Final ROEs	$\delta\boldsymbol{\alpha}(t_f)\left\{\begin{matrix} 0, & -0.0112, & 0, & 0, & 0, & +5.3997 \\ 0, & -6.2350, & 0, & 0, & 0, & -5.3997 \\ 0, & +6.2350, & 0, & 0, & 0, & -5.3997 \end{matrix}\right\}$ (m)

and normal direction. The control law is shown in Figure 7.4b for satellites 2 and 3, while satellite 1 is kept at its original position, under forced motion. The control effort is bounded by the technological limitation of the on-board engine, with a maximum thrust of $25\,\mathrm{mN}$. The control effort is distributed in the transversal and normal direction, and the profile is almost symmetric for the two spacecraft. The total delta-v for the optimal manoeuvre is about $3.8\,\mathrm{cm\,s^{-1}}$. Figure 7.4c shows the time evolution of the spacecraft separation during the manoeuvre of the spacecraft separation. Note that the separation between vehicles 1-2 is below the one of spacecraft 1-3.The requirement of the minimum inter-satellite distance is met during the reconfiguration and influences the trajectory definition. The advantages of this strategy compared to the analytical trajectory design are:

- The optimal trajectory is achieved with the two-axis thrusters' configuration.
- The thrust level is in the range of the onboard engine of $25\,\mathrm{mN}$.
- The collision avoidance requirement is met, and the trajectory complies with the solar panels' configuration for power generation.

At the end of the manoeuvre, an attitude rotation of 180 deg of the three satellites is required to establish the correct ISL link and to calibrate the antennas.

Conclusion. To conclude, the baseline for the EPM to CSPM transition has been selected based on the delta-v optimal manoeuvre. The trade-off between the two strategies is reported in Table 7.2. The second strategy, corresponding to the delta-v optimal trajectory, respects all the requirements for the manoeuvre design, and therefore, it has been preferred over strategy 1. Finally, an additional consideration is required. A future study requires a parametric analysis on the initial argument of latitude u_0 to start the manoeuvre. In fact, depending on the position along the orbit, the optimisation could provide a trajectory with a slightly different delta-v budget, which could be exploited to reduce the manoeuvre's effort even more. Moreover, even if spacecraft 1 is not involved in the manoeuvre, this is not a problem for the fuel consumption balancing: this manoeuvre would be required once or twice per month maximum, with a small impact on the overall delta-v budget of the mission (i.e. about $3.8\,\mathrm{cm\,s^{-1}}$ compared to $2.7\,\mathrm{cm\,s^{-1}}$ of spacecraft 1).

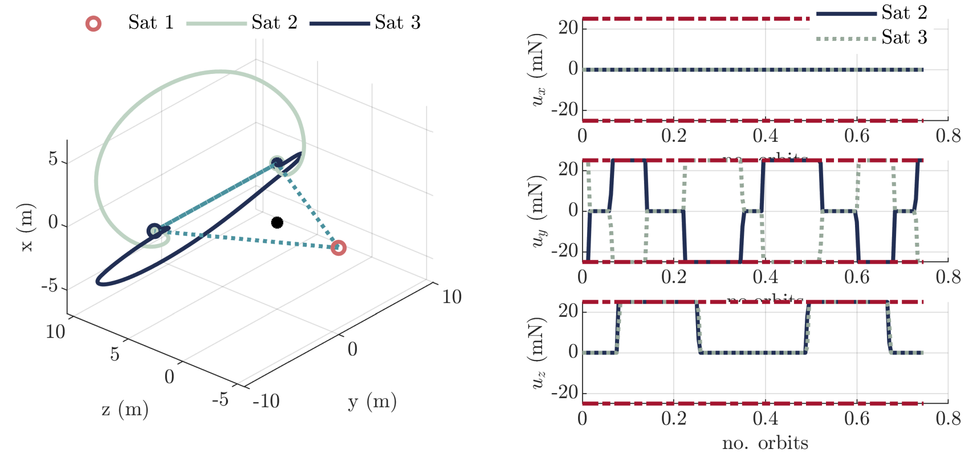

(a) *Delta-v optimal trajectory of satellite 1 and 2 in the RTN frame.*

(b) *Thrust profile for the delta-v optimal trajectory. The dotted line red represents the 25 mN limit of the thruster.*

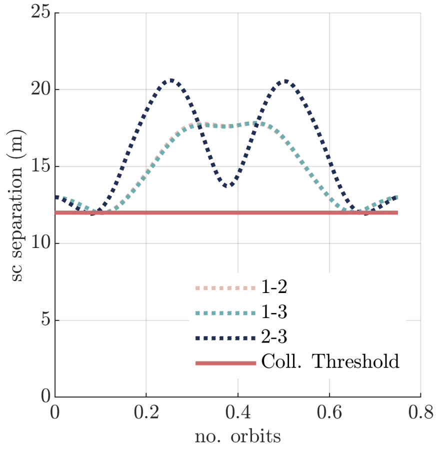

(c) *Time evolution of the spacecraft separation during the manoeuvre*

Figure 7.4: *Delta-v optimal trajectory for the EPM to the CSPM transition of FFLAS.*

7.2 GNC simulations for FFLAS

This section is devoted to the simulation results of various phases, as described in Figure 7.1. The first part describes the requirements identified during the FFLAS study for the simulation. Then, the simulations are presented for each phase, with their respective initial conditions.

7.2.1 Performance and simulation requirements

The evaluation of the performances with respect to the posed requirements for the FFLAS formation is essential for the assessment of a feasible geometry and safe operations. The relative navigation position knowledge and the relative position control requirements have been identified starting from the

Table 7.2: *Orbital elements of the FFLAS reference orbit.*

Variable	**Strategy 1**	**Strategy 2**
Thrust level < 25 mN	No	Yes
Delta-v budget (cm/s)	Sat 1 ~ 2.7	Sat 1 ~ 2.7
	Sat 2 and 3 ~ 7	Sat 2 and 3 ~ 3.8
Time for transition	0.5 orbital periods	0.75 orbital periods
Min separation > 11 m	Yes	Yes
Solar Panel compliance	Yes	Yes

results of TDX/TSX, GRACE and AVANTI missions [52]. Table 7.3 presents the main performance and simulation requirements identified for the FFLAS study and for the analysis in this chapter. Starting from the performance requirements, the first one, *B.1120*, defines the required control accuracy of the relative position vector. This is a quite challenging value for relative motion, and it was driven by two main aspects: the close distance among the spacecraft in the formation, around $12\,\mathrm{m}$, and the need to maintain a fixed and rigid geometry for combined interferometry purposes. The other two requirements, instead, are related to the navigation reconstruction accuracy. *B.1125* refers to the real-time relative position accuracy. It impacts the design e definition of the onboard relative navigation filter. Requirement *B.1130* refers to the navigation reconstruction accuracy post facto by means of precise orbit determination reprocessing of the raw measurement data downloaded from the telemetry. It defines the relative position knowledge required to generate scientific products. Following, the simulation requirements have been identified and reported in Table 7.3, to set up the GNC framework. The first requirement, *C.1000* presents the operational scenarios to be included in the simulation analysis. The initial phase shall include the release of the 3 satellites from the dedicated adapter and the establishment of the satellite formation for the first time. The Earth pointing consists of the nominal mode for Earth imaging. The Cold Sky pointing includes the cold sky calibration and the manoeuvres from and back into the Earth pointing mode. The safe-formation mode includes the scenario where the formation must be safely abandoned into the safe-formation configuration. And finally, the return to the nominal formation includes the necessary manoeuvres from the safe-formation mode and the re-establishment of the nominal operation. Then, requirements *C.1050* and *C.1070* define the required rate of change of the absolute and relative state vector during the simulation. This influences the selection of the output sampling of the simulations with the GNC framework. Finally, requirement *C.1100* defines the need to include reasonable noise terms for navigation sensors and uncertainties in the navigation filters, as the EKF. This is essential to design a model that includes the typical disturbances from the external orbit environment. Once the main requirements for the simulation of FFLAS have been identified, the coherent initialisation and parameter selection for the GNC framework is discussed. Before presenting the simulation results for the FFLAS study, it is important to define the set-up parameters and the initialisation procedure for the GNC framework.

Table 7.3: *FFLAS performance and simulation requirements.*

Performance requirements
B.1120 **Position Control of the Arrays within the Aperture** The relative position between the phase centres of any pair of antenna elements, belonging to the same array or different arrays, shall be controlled to be within ± $2\,\mathrm{cm}$ (1 sigma) from the nominal values (nominal hexagonal grid underlying the 3 arrays).
B.1125 **Navigation Position Knowledge of the Arrays within the aperture plane** The real-time relative position between the phase centres of any pair of antenna elements, belonging to the same array or different arrays, shall be known to ± $1\,\mathrm{cm}$ (1 sigma).
B.1130 **Position Knowledge reconstruction of the Arrays within the aperture plane** The ground reconstruction of the relative position between the phase centres of any pair of antenna elements, belonging to the same array or different arrays, shall be known within ± $1\,\mathrm{mm}$ (1 sigma).
Simulation requirements
C.1000 **Scope of Simulation** The simulation shall comprise five scenarios: 1. Initial phase: from launcher release to first formation establishing, 2. Earth pointing phase: a nominal scenario for scientific observation, 3. Cold Sky pointing phase: calibration phase scenario, 4. Safe-formation phase: off-nominal scenario after a fault detection, 5. Manoeuvring phase: from the off-nominal scenario return to the nominal formation.
C.1050 **Absolute Velocity Vectors** The absolute velocity vector shall be defined as the rate of change of the absolute position vector in 1 second.
C.1070 **Relative Velocity Vector** The relative velocity vector shall be defined as the rate of change of the relative position vector in 1 second.
C.1100 **Measurements Noise and Model Imperfections** The simulation shall include reasonable noise terms to all navigation sensors measurements, as well as reasonable imperfections to all models, with respect to the real world, used in the navigation filters.

7.2.2 GNC framework initialisation

This section presents the parameters for the correct initialisation of the GNC framework of Chapter 5 for the FFLAS study.

Earth's constants

First, the constants and parameters connected to the central body (Earth) are defined, together with the selection of external models for orbital perturbation modelling.

Table 7.4: *Parameters used for the simulation for FFLAS study.*

Parameter	Value
Constant	
Earth's radius	$6.3781363 \cdot 10^{6}$ m
Earth's gravitational constant	$3.9860 \cdot 10^{14}$ m^{3} s^{-2}
Earth's angular velocity	$7.2921 \cdot 10^{-5}$ rad s^{-1}
Time variation of Earth's RAAN	$1.9961 \cdot 10^{-7}$ rad s^{-1}
Perturbation models	
Earth's gravitational model	GRACE Earth Gravity model 02 (GGM02S)
Earth's Atmospheric Model	NRLMSISE-00 atmospheric model

Formation flight parameters

As described in Section 6.3.2, the reference orbit is defined as the nominal orbit of SMOS, i.e. a 6 am - 6 pm Sun-Synchronous Orbit (SSO) of 775 km altitude. The dusk-dawn orbit nature sets a requirement for the launch condition to meet the correct RAAN value. To obtain an ascending node of the reference orbit at dawn (6 a.m.), the satellites shall be launched southward at 6 p.m. Such orbit grants very favourable illumination conditions from the Sun. Specifically, the Sun's direction will always be in the negative normal direction, as shown in Figure 6.19, and the reference orbit undergoes eclipse conditions mainly around the winter solstice. Table 7.5 shows the initial UTC used for the simulations and the initial orbital elements of the reference orbit, both in Cartesian (EME2000) and Keplerian (osculating elements). The FFLAS formation flying is made of 3 hexagonal arrays of about 8.2 m in diameter (slightly smaller size than SMOS), flying with their centres at the vertices of an equilateral triangle of about 12.47 m side. Such formation would be equivalent to an aperture of $21\,\mathrm{m}$ diameter achieving $9.84\,\mathrm{m}$ nadir resolution with an effective sensitivity better than SMOS. The satellite's physical characteristics and the orbital elements are reported in Table 7.6, where the nominal relative RTN, the mean ROEs and physical characteristics of the spacecraft are reported.

Table 7.5: *Features of the FFLAS satellites and relative state of the nominal configuration.*

Variable	Value
`UTC`	12:00 21/03/2022
`X_EME`	$\left\{1.04848 \cdot 10^{5},\ -7.152367 \cdot 10^{6},\ 0,\ -1.10575 \cdot 10^{3},\ -16.209,\ 7.3824 \cdot 10^{3}\right\}$ (m, m/s)
α	$\left\{7.15313 \cdot 10^{6},\ 0,\ 97.479,\ 274.483,\ 0,\ 23.645\right\}$ (m,-,deg,deg,deg,deg)

Table 7.6: *Orbital elements of the FFLAS reference orbit.*

Variable	Symbol	**Value**
SC wet mass	`mass`	1736 kg
Drag coefficient	`CD`	2.0
Drag cross sectional area	`area`	$3.0\,\mathrm{m}^2$
Solar Radiation Pressure (SRP) coefficient	`CR`	1.1
SRP cross sectional area	`areaCR`	$8.1\,\mathrm{m}^2$
Relative Cartesian state	`xRTN`	$\left\{\begin{array}{cccccc} 0, & 0, & -5.3997, & 0, & 0, & 0 \\ 0, & 6.2350, & 5.3997, & 0, & 0, & 0 \\ 0, & -6.2350, & 5.3997, & 0, & 0, & 0 \end{array}\right\}$ (m,m/s)
ROEs state	`dalpha`	$\left\{\begin{array}{cccccc} 0, & -0.0112, & 0, & 0, & 0, & 5.3997 \\ 0, & 6.2350, & 0, & 0, & 0, & -5.3997 \\ 0, & -6.2350, & 0, & 0, & 0, & -5.3997 \end{array}\right\}$ (m)

GNSS navigation sensors

After the definition of the Cartesian and ROEs state of the formation, it is important to determine the parameters of sensors and actuators of the FFLAS spacecraft. As explained in Section 5.2.5, the navigation logic was selected according to the decentralised approach without the mediation from a specific satellite. Each spacecraft is supposed to have the same computational and data-handling capabilities and to elaborate its GNC algorithms autonomously. The continuous mutual exchange of GNSS navigation data enables the reconstruction of the absolute formation status at each time instant on-board every satellite. Moreover, each spacecraft could recover from the information on the absolute formation status and its relative state associated with a virtual spacecraft at the centre of the formation triangle. The elements of the virtual satellite are propagated in time thanks to the on-board dynamical propagator. The GNC algorithms are elaborated by each satellite of the formation in the RTN reference frame of the virtual platform. This architecture is shown in Figure 7.5, where the virtual platform is identified by dashed contours.

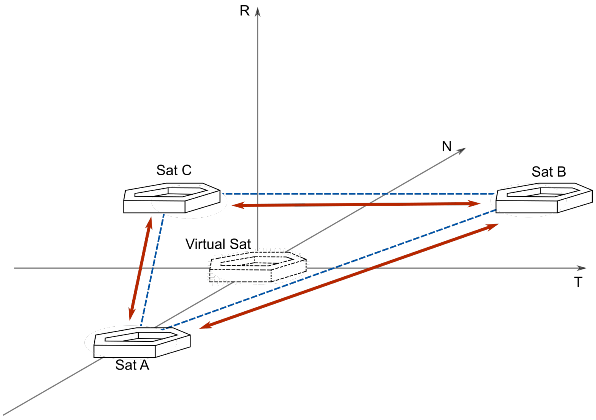

Figure 7.5: *Schematics of the navigation architecture for FFLAS.*

The selection of this architecture influences the selection of the on-board receivers. Specifically, the FFLAS platforms are equipped with two single frequency receivers used in cold redundancy during the nominal mode and two antennas. The baseline for the GNSS receivers is the *'RUAG Space LEORIX Single Frequency GNSS'* receiver[1]. The key features of the RUAG GNSS sensor are reported in Table 7.7. It can provide up to $1\,\mathrm{m}$ and $2\,\mathrm{mm\,s^{-1}}$ accuracy in the absolute on-board navigation solution.

Table 7.7: *LEORIX RUAG sensor performances.*

Variable	**Value**
On board navigation solution accuracy	
Position	$1.0\,\mathrm{m}$ 3D rms
Velocity	$2.0\,\mathrm{mm\,s^{-1}}$ 3D rms
Time off-set (1PPS)	$\leq 50\,\mathrm{ns}$
Data Outputs	
Carrier phase error	L1 < $1.2\,\mathrm{mm}$ rms
	E1 < $1.8\,\mathrm{mm}$ rms
Code measurement error	L1 < $0.7\,\mathrm{mm}$ rms
	E1 < $0.7\,\mathrm{mm}$ rms

Navigation filter

Tables 7.8 and 7.9 show the parameters used in the FFLAS simulations to provide the absolute and the relative state estimation in the close-loop of the GNC simulator. The term $\boldsymbol{L_n}$ represents a matrix where every entry equals one, with size $n \times n$. Likewise, the expression $a\boldsymbol{I}_n$ represents a matrix of size $n \times n$ whose elements in the diagonal are equal to a. These parameters are used as input for the EKF to estimate the actual state from the GNSS sensor measurements. In the Tables, the variance of the position and velocity is selected according to the estimated error in the measurements to make the filter converge to the ideal trajectory:

- For the absolute estimation, an error in the measurements in the order of 1 m and 0.002 m/s for the position and velocity, respectively, is considered in the variance evaluation.
- For the relative navigation estimation, an error in the measurements in the order of 1 mm and 0.001 mm/s is considered for the position and velocity, respectively.

For both absolute and relative state estimation, the initial state estimation covariance matrix P_0 is selected for the initial step and then, at each time, is updated in the algorithm considering the residual error from the previous step.

Control

For the FFLAS study, the closed-loop control is based on the Linear Quadratic Regulator (LQR) methodology, described in Section 4.2. It is used to perform trajectory tracking of the optimal open loop reconfiguration (see Section 4.1) or formation maintenance. In this analysis, we assumed that the onboard actuators guarantee the desired attitude, and the satellites provide the control only in the transversal and normal direction of the RTN frame (see Figure 6.19). The weights for the LQR gain matrices $\boldsymbol{Q}$ and $\boldsymbol{R}$ have been selected after a trade-off parametric analysis to improve the control accuracy outcome. Moreover, the FFLAS study is based on the ion-thruster engine technology. All the

---

[1] `https://www.satcatalog.com/component/leorix-gnss-receiver/`, last access 06/02/2023.

Table 7.8: *Parameters of the EKF for the absolute state estimation.*

Parameter	**Value**
Process noise standard deviation	$\text{PSD} = 3.2 \cdot 10^{-4}$
Process noise covariance matrix	$\boldsymbol{Q} = \text{PSD} \cdot \boldsymbol{L}_6 \cdot 10^6 \boldsymbol{I}_6$
Variance of the position	$\sigma_{pos} = \left(\frac{1}{\sqrt{3}}\right)^2$
Variance of the velocity	$\sigma_{vel} = \left(\frac{0.002}{\sqrt{3}}\right)^2$
Measurements noise covariance matrix	$\boldsymbol{R} = (\sigma_{pos}, \sigma_{vel})\boldsymbol{I}_6$
State estimation covariance matrix	$\boldsymbol{P}_0 = 9 \cdot 10^9 \cdot \boldsymbol{i}_6$

Table 7.9: *Parameters of the EKF for the relative state estimation.*

Parameter	**Value**
Initial process noise power spectral density	$\text{PSD} = 1.5 \cdot 10^{-6}$
Process noise covariance matrix	$\boldsymbol{Q} = \text{PSD} \cdot \boldsymbol{I}_6$
Variance of the position	$\sigma_{pos} = \left(\frac{1 \cdot 10^{-2}}{\sqrt{3}}\right)^2$
Variance of the velocity	$\sigma_{vel} = \left(\frac{3 \cdot 10^{-6}}{\sqrt{3}}\right)^2$
Initial measurements noise covariance matrix	$\boldsymbol{R}_0 = (\sigma_{pos}, \sigma_{vel})\boldsymbol{I}_6$
Initial state estimation covariance matrix	$\boldsymbol{P}_0 = 5 \cdot 10^3 \cdot \boldsymbol{I}_6$

vehicles are equipped with four thrusters (see Figure 6.19), which should provide continuous control to maintain the formation fixed and rigid. During the nominal operations of the FFLAS formation, the thrusters are kept oriented in the normal and transversal directions, respectively. At this stage, no thrust in the radial direction is provided to avoid an increase in the mass budget of the satellite. The baseline for the onboard actuator is the QinetiQ T5 low thrust engine[2], whose performances are reported in Table 7.10. Note that the attitude error has been included in the uncertainty in the thrust. In fact, the attitude simulation is not included in the GNC framework, and it is assumed satisfied for all mission phases. To introduce the accuracy level in the thrust direction due to misalignments of the attitude, an error on the three axis of the body frame is included. The value of 0.1 deg for attitude accuracy is recovered from the analysis performed during the FFLAS study by the attitude team in Airbus Defence and Space Madrid.

This section presents the results of the simulation with the GNC framework for the different operational phases described in Section 7.1.1. For each test case, first, a description of the operations and activities is provided, together with the initial state in the absolute/relative frame. Then, the results are discussed in terms of the accuracy of the on-board and of the control profile.

7.2.3 Simulation of LEOP and commissioning phase

The simulation of the initial phase consists of the analysis of the first formation establishment after the launcher release. The analysis is based on the optimal formation reconfiguration design with the delta-v convex optimal problem developed in Section 4.1. The deployment sequence from the launcher is enabled by the ejection springs in the separation mechanism, which allow the spacecraft to be injected

---

[2] `https://www.qinetiq.com/en/what-we-do/services-and-products/solar-electric-propulsion`, last access 06/02/2023

Table 7.10: *Parameters of the QinetiQ T5 engine.*

Parameter	**Value**
Thrust range	0 to $25\,\mathrm{mN}$
Thrust noise	$1.2\,\mathrm{mN}/\sqrt{\mathrm{Hz}}$ at $1\,\mathrm{MHz}$ $0.012\,\mathrm{mN}/\sqrt{\mathrm{Hz}}$ at $100\,\mathrm{MHz}$
Thrust vector stability	$< \pm$ 0.1 deg on the three axes
Thrust error	$\pm\, 5\,\%$ of thrust demand $\pm\, 1\,\%$ of thrust demand for thrust $>3\,\mathrm{mN}$
Attitude error	$< \pm$ 0.1 deg on the three axes
Delay in the thrust command	$0.125\,\mathrm{ms}$

into orbit in sequence. After the orbit injection, the following commissioning strategy was identified:

- *Comm. phase 1*: after the injection, the three spacecraft fly at a safe distance in the same orbit after the injection phase. This period could last some weeks and is required for the commissioning of the individual satellites.

- *Comm. phase 2*: the manoeuvrability of the three spacecraft is exercised to finally achieve the formation geometry (first nominal formation reconfiguration). This will be performed with a step-by-step reconfiguration to check whether the reconfiguration is working properly.

- *Comm. phase 3*: the commissioning phase of the constellation in formation is carried out. The performances of the formation and the L-band payloads are monitored and evaluated.

Commissioning phase 1: condition after the injection

The release of the FFLAS satellites from the space launcher can be conveniently studied in the ROEs framework, similar to the analysis in [67]. This strategy includes considerations on collision avoidance, the final delta-v cost to establish the formation, and operational constraints [155]. During the FFLAS study, a deployment and launch mechanism has been designed by the Airbus D&S team to inject the vehicles into orbit with a single launch. The ejection strategy is based on a deployment sequence of the spacecraft from the dispenser from the top to the bottom one. The deployment sequence is shown in Figure 7.6: each vehicle is ejected from the dispenser thanks to a spring mechanism [130] and then it is deployed in its final configuration.

During commissioning phase 1, the three spacecraft fly at a safe distance in the same orbit after the injection phase: The simulation period for this phase is selected to be 30 days, where no relative motion control is implemented, and the satellites evolve following the natural motion. Figure 7.7a shows the nominal initial conditions after the injection, considering a deployment with a 10 deg angle from the tangential direction and $10\,\mathrm{s}$ of waiting time among the satellites. The separation between the satellite and the rocket body after the deployment is shown in the plot. The simulation for this initial phase aims at testing the natural evolution of the satellites with the in-house high-fidelity propagator SKiLLeD. The trajectory followed by the spacecraft with initial conditions Figure 7.7b, where the evolution is represented in the RTN frame to provide a more meaningful representation of the situation. The relative trajectory of satellites 2 and 3 are described with respect to satellite 1 (considered in this phase as the chief satellite).

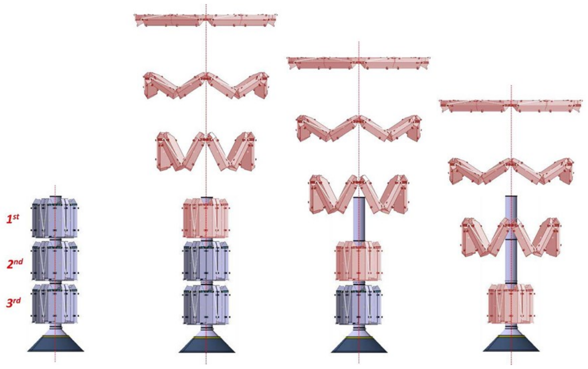

Figure 7.6: *Deployment sequence for the three satellites of FFLAS study (curtsey of Airbus D&S Madrid).*

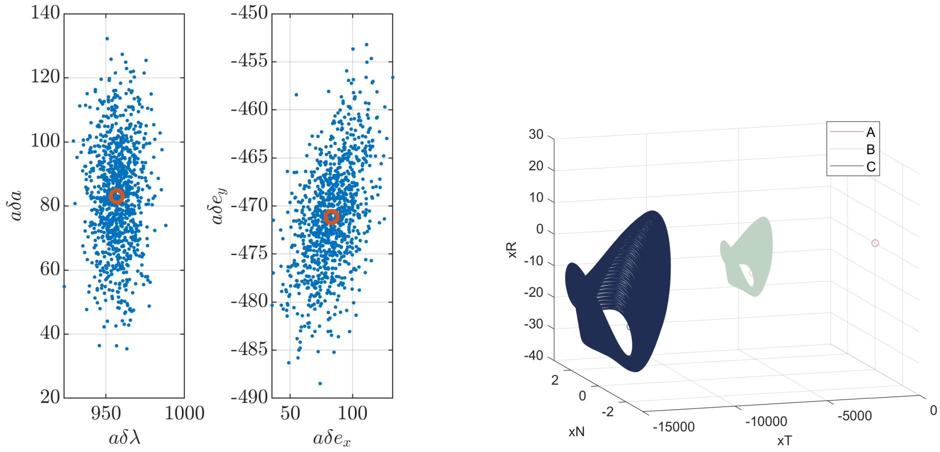

(a) *Distribution of ROEs after the launcher injection for one spacecraft.*

(b) *Dynamical propagation of one initial condition after the launcher injection.*

Figure 7.7: *Deployment phase of FFLAS.*

Commissioning phase 2: first nominal formation reconfiguration

The commissioning phase 2 has been simulated, to evaluate the possibility of autonomously performing the first formation acquisition and the need to include the ground reconstruction in the closed loop. The main parameters of this phase correspond to the final condition of the dynamical propagation of comm. phase 1.

The simulation aims at evaluating the feasibility of the first formation acquisition considering reconfiguration with the ground in the loop for navigation reconstruction.

A maximum thrust level of $25\,\mathrm{mN}$ has been considered to perform the formation reconfiguration. The manoeuvre could take up to 10 orbital period, to allow safe monitoring of the operations and activities during the geometry establishment. This is essential to monitor non-nominal or critical situations that could lead to a collision among the vehicles. The time step considered for the simulation is driven by the requirements in Table 7.3, and it is set equal to $\mathtt{dt}{=}1\,\mathrm{s}$. The inputs for the simulation in terms of initial t_0 and final t_{end} states in ROEs are described as:

$$a\delta\boldsymbol{\alpha}_{dep}(t_0) = \left\{ \begin{array}{c} a\delta\boldsymbol{\alpha}_1(t_0) \\ a\delta\boldsymbol{\alpha}_2(t_0) \\ a\delta\boldsymbol{\alpha}_3(t_0) \end{array} \right\} = \left\{ \begin{array}{cccccc} -0.11 & -30.04 & 0 & 0 & -0.004 & 0.007 \\ -26.68 & -6.8213 \cdot 10^3 & -17.74 & -21.06 & -0.18 & -1.54 \\ -53.27 & -1.35 \cdot 10^4 & -35.44 & -41.98 & -0.36 & -3.085 \end{array} \right\} \tag{7.1}$$

$$a\delta\boldsymbol{\alpha}_{dep}(t_{end}) = \left\{ \begin{array}{c} a\delta\boldsymbol{\alpha}_1(t_{end}) \\ a\delta\boldsymbol{\alpha}_2(t_{end}) \\ a\delta\boldsymbol{\alpha}_3(t_{end}) \end{array} \right\} = \left\{ \begin{array}{cccccc} 0, & -0.0112, & 0, & 0, & 0, & 5.3997 \\ 0, & 6.2350, & 0, & 0, & 0, & -5.3997 \\ 0, & -6.2350, & 0, & 0, & 0, & -5.3997 \end{array} \right\} \tag{7.2}$$

The initial conditions $a\delta\boldsymbol{\alpha}_{dep}(t_0)$ corresponds to the final condition after the commissioning phase 1. The final state corresponds to the nominal formation configuration during the science phase when the vehicles are in the Earth's pointing mode. The logic adopted for the simulation of the first formation reconfiguration is the following:

1. After the natural propagation of the dynamics after the launcher injection, the spacecraft are well separated in terms of $\delta\lambda$, with an inter-satellite distance in the order of thousands of kilometres (see Figure 7.10a).
2. The reconfiguration is based on the optimal manoeuvre developed with the open-loop delta-v convex optimisation of Section 4.1.
3. During the reconfiguration, each vehicle continuously monitors the separation from the others, and the ground station is maintained in the navigation loop to improve the accuracy of the state reconstruction and monitor the manoeuvre itself.
4. The final configuration consists of the nominal triangular formation geometry, selected in section 6.3.3 for the science phase. The orbit maintenance in the triangular formation is simulated over 3 orbital periods to assess the stability of the control after the first reconfiguration.

Simulation results Figure 7.8 shows the reconfiguration trajectory in the RTN frame for the assessment of the nominal science configuration, and Figure 7.9 the corresponding time variation of the ROEs parameters. During the reconfiguration, the onboard absolute and relative GNSS navigation is considered with the ground station in the loop, and the relative position among the satellites is monitored to check for possible collision risk areas. The real-time inter-satellite distance is shown in Figure 7.10a: the satellites gradually approach each other and reduce the inter-satellite distance toward the nominal $12.47\,\mathrm{m}$ separation of the science phase. Due to the criticality of the first reconfiguration, during operational planning of the mission, proximity tests for the relative navigation should be performed before the first complete reconfiguration. This is important to assess the performance of on-board navigation and control system. The error in the control during the reconfiguration over the guidance trajectory is reported in Table 7.11 in terms of mean and standard deviation, considering the whole formation reconfiguration manoeuvre. The error is higher in the initial part, where the inter-satellite distance is at the kilometre level, while it reduces below $10\,\mathrm{cm}$ in the final part of the reconfiguration. The control law required for the reconfiguration is shown in the body and EME2000 frame in Figure 7.10b. Up to two over four engines are required to thrust simultaneously during the reconfiguration. Moreover, during the manoeuvre, the thrust is mainly required in the z_b body axis while maintaining the science configuration (i.e. the fixed equilateral triangle) mainly the thrust in the x_b. The attitude of the spacecraft is assumed to be maintained so that x_b and z_b correspond to the normal and transversal direction of the RTN frame:

$$\left\{ \; x_b \quad y_b \quad z_b \; \right\}_{\text{comm phase 2}} = \left\{ \; z \quad x \quad y \; \right\}_{\text{RTN}} \tag{7.3}$$

This results in a thrust mainly in the transversal direction during the reconfiguration and in the normal direction for formation maintenance. The radial component of the thrust is not present, reducing the delta-v and fuel consumption. The corresponding delta-v budget for the overall phase is reported in Table 7.11. Centimetre level of delta-v budget is required for a reconfiguration in about 10 orbital periods.

Table 7.11: *Control accuracy and delta-v budget for the science phase of FFLAS.*

Spacecraft	**Delta-V budget** (cm/s)	**Control accuracy (RTN components)** x, mean ± std (cm)	y, mean ± std (cm)	z, mean ± std (cm)
Satellite 1	12.61	1.23 ± 4.60	25.59 ± 29.14	1.01 ± 1.92
Satellite 2	30.46	0.93 ± 4.74	26.41 ± 31.74	0.17 ± 0.31
Satellite 3	50.11	1.14 ± 4.25	21.79 ± 32.72	1.02 ± 0.83

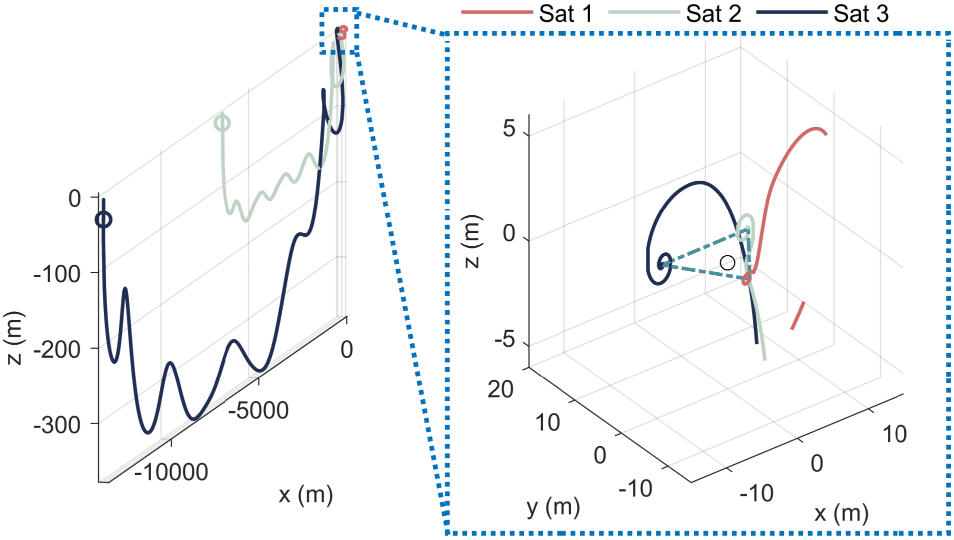

Figure 7.8: *Trajectory representation of the reconfiguration manoeuvre during the commissioning phase. On the right, it is reported the zoom of the final part of the reconfiguration.*

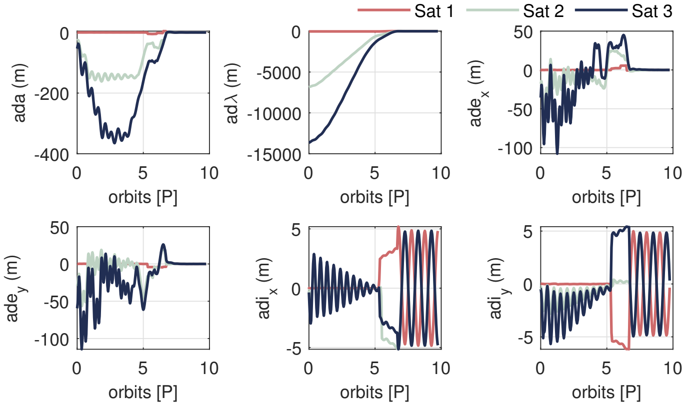

Figure 7.9: *Time evolution of the ROEs during the commissioning phase.*

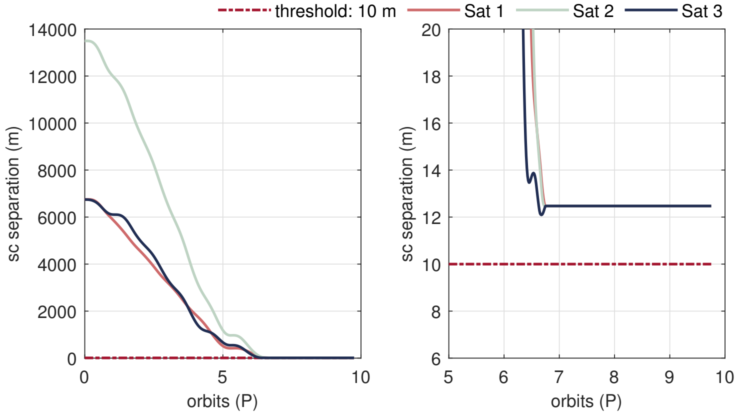

(a) *Time evolution of the spacecraft separation during the reconfiguration.*

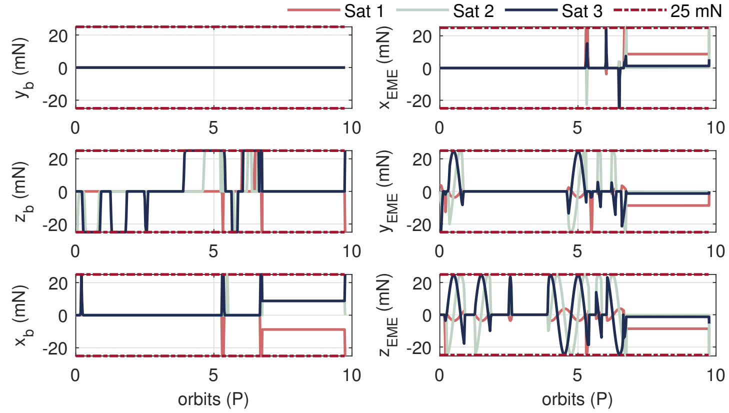

(b) *Actuator control law during the reconfiguration.*

Figure 7.10: *Spacecraft reconfiguration and control law for FFLAS during the commissioning phase.*

7.2.4 Simulation of Science Phase

The simulation of the Science Phase consists of the analysis of the nominal scenario for scientific observation when the satellites fly in the triangular formation with the aperture plane of the payloads pointing toward the Earth. At the end of the commissioning phase, the formation begins the nominal remote sensing phase. This section provides the GNC simulation of the formation maintenance of the triangular configuration for 2 orbital period.

The simulation aims at evaluating the feasibility of the formation maintenance during the interferometry activities.

A maximum level of $25\,\mathrm{mN}$ is imposed for the thrust profile, and the navigation reconstruction is considered based on the on-board filter only, without the post-processed data from the ground. The time step considered is equal to $1\,\mathrm{s}$ and the simulator is initialised at the spring equinox (21/03/2022). The nominal condition for the reference orbit is described in the ROEs framework with respect to the central point of the triangle, as:

$$a\delta\boldsymbol{\alpha}_{dep} = \left\{ \begin{array}{c} a\delta\boldsymbol{\alpha}_1 \\ a\delta\boldsymbol{\alpha}_2 \\ a\delta\boldsymbol{\alpha}_3 \end{array} \right\} = \left\{ \begin{array}{cccccc} 0, & -0.0112, & 0, & 0, & 0, & 5.3997 \\ 0, & 6.2350, & 0, & 0, & 0, & -5.3997 \\ 0, & -6.2350, & 0, & 0, & 0, & -5.3997 \end{array} \right\} \tag{7.4}$$

This condition should be maintained during the science phase, and the following steps are considered:

- The closed-loop control algorithm relies on on-boards GNSS navigation for reconstructing the state of the formation.
- The onboard actuators provide the thrust only in the x-z body axis, corresponding to the transversal and normal direction of the RTN frame.

Simulation results The maintenance of the nominal triangular formation is assessed, and the satellites can maintain their nominal position at the vertex of the equilateral triangle. Figure 7.11a represents the trajectory of the triangular formation in the RTN frame. The satellites' positions are identified with three different colours, while the central point represents the virtual reference trajectory. Figure 7.11b shows the time evolution of the relative state in ROEs framework. The $\delta\lambda$ parameter is kept constant to maintain the triangular geometry, similar to the relative eccentricity vector and the relative semi-major axis. On the contrary, the evolution of the relative inclination vectors undergoes a sinusoidal variation to keep the formation, to counteract the relative natural dynamics for obtaining a fixed displacement in the normal direction. During the maintenance, the controller monitor continuously the spacecraft separation. The inter-satellite distance must never be below the collision threshold, for the safety of the operations. The time evolution of the spacecraft separation is reported in Figure 7.12a. Finally, it is important to compute the control thrust profile of the onboard engines. The control profile is shown in Figure 7.12b. The evolution is described in the body frame, where only the component in the normal direction (x_b) is present. As for the commissioning phase, the attitude of the spacecraft is assumed to be maintained so that x_b and z_b correspond to the normal and transversal direction of the RTN frame:

$$\left\{ \begin{array}{ccc} x_b & y_b & z_b \end{array} \right\}_{\mathrm{comm\,phase\,2}} = \left\{ \begin{array}{ccc} z & x & y \end{array} \right\}_{\mathrm{RTN}} \tag{7.5}$$

A constant thrust of about $10\,\mathrm{mN}$ is required apart from the initial set-up of the controller to reach the convergence. The corresponding delta-v budget and control error for the science phase is reported

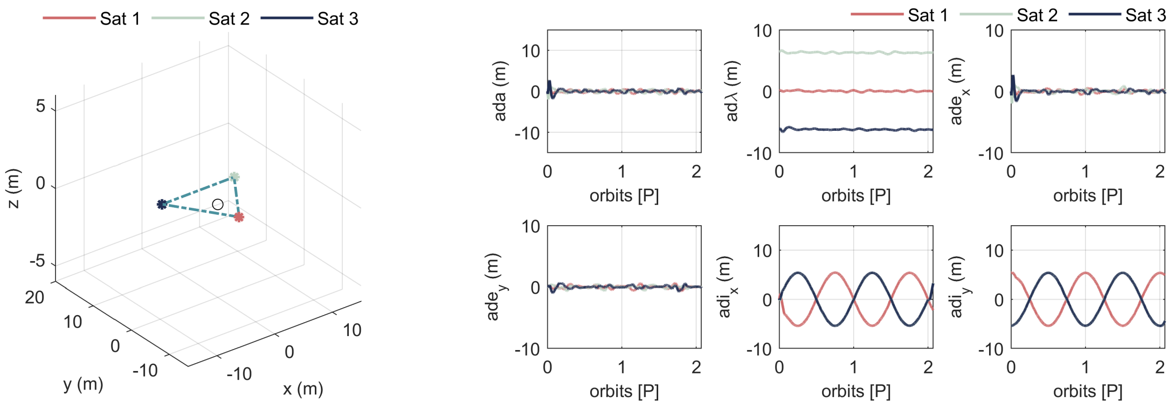

(a) *Formation maintenance during science phase.*

(b) *Time evolution of the ROEs during science phase.*

Figure 7.11: *Formation maintenance for the science phase of FFLAS.*

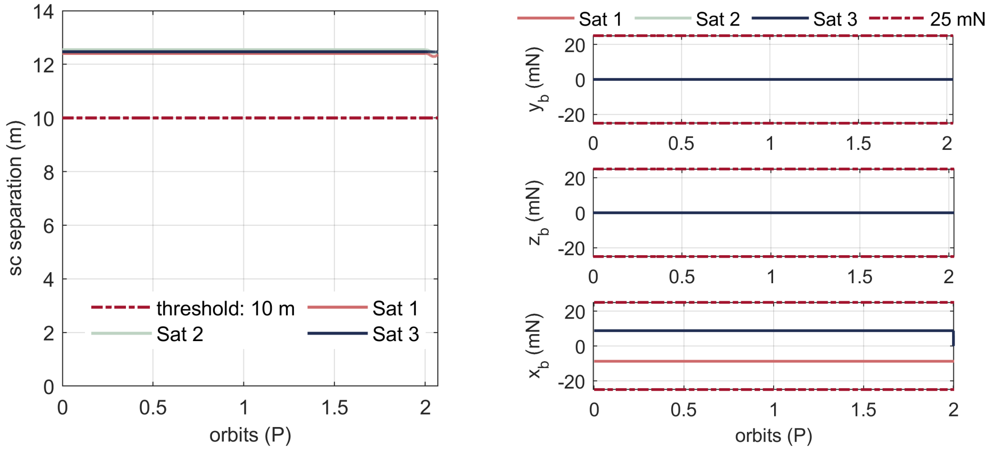

(a) *Time evolution of the spacecraft separation during the Earth pointing mode.*

(b) *Actuator control law during the Earth pointing mode.*

Figure 7.12: *Spacecraft reconfiguration and control law for FFLAS during the Earth pointing mode.*

in Table 7.12. Centimetre level of delta-v budget is required for a reconfiguration in about 10 orbital periods. The mean of the control error is in a few centimetre range, with a deviation up to $6\,\mathrm{cm}$. Specifically, after the initial instants where the controller needs to converge, the error in the formation maintenance is limited below $10\,\mathrm{cm}$ level.

An important parameter to consider in the performance evaluation of the simulation is navigation accuracy. The simulation is performed considering GNSS-based navigation implemented on-board the satellites, while the possible optical/vision-based sensor could be included to improve the reliability of the results in the future development of the study. The solution from the onboard navigation state reconstruction is essential to guarantee autonomous formation maintenance during the nominal scientific phase of the mission. The estimation of the state is used as an input to the control block to define the commanded thrust to the actuator. Thanks to the implementation of the EKF on-board

Table 7.12: *Control accuracy and delta-v budget for the science phase of FFLAS.*

Spacecraft	**Delta-V budget** (cm/s)	**Control accuracy (RTN components)**		
		x, mean ± std (cm)	y, mean ± std (cm)	z, mean ± std (cm)
Satellite 1	7.54	2.13 ± 1.60	5.59 ± 2.41	1.21 ± 1.95
Satellite 2	7.52	2.40 ± 1.89	5.14 ± 2.29	1.22 ± 0.82
Satellite 3	7.52	2.14 ± 1.52	5.69 ± 2.60	1.22 ± 0.83

the satellite, the real-time onboard navigation accuracy is $0.94\,\mathrm{cm} \pm 0.90\,\mathrm{cm}$, in terms of mean and standard deviation, for the three satellites.

Paylaod considerations The performance of the payload is evaluated over one orbital period of formation maintenance by assessing the mean error of the full impulse response, compared to the nominal one (see Figure 2.12e). First, the discrepancy in terms of ξ and η cut is evaluated. Figure 7.13a shows the error between the nominal and the mean impulse response over one orbital period. The discrepancy is almost negligible for the main and the first side lobes, while it reaches up to $4\,\mathrm{dB}$ error in the secondary lobes. A good representation of the mean error over one orbital period is also described in terms of impulse response contour, as shown in Figure 7.13b. This analysis demonstrates that the error level during the formation maintenance is suitable to keep the payload performances close to the nominal one during the science phase. In fact, if a larger error was present on the relative state (e.g. considering a mean error of $30\,\mathrm{cm}$), the loss in performances is more evident starting from the first side lobe. Considering a $30\,\mathrm{cm}$ control error, the payload performances are shown in Figure 7.14. An error on the impulse response cut of about $10\,\mathrm{dB}$ to $15\,\mathrm{dB}$ is present, and this reflects in the response error contour, with a degradation of combined interferometry.

Final considerations The analysis of the science phase demonstrates the feasibility of the maintenance of a rigid and tight formation to perform combined interferometry. The main challenge of this phase is the accurate on-board navigation solution, which must be kept at a few centimetre levels. This is essential to guarantee a small control error of the formation geometry. Specifically, from the analysis, a continuous thrust in the normal direction is essential to keep the formation and maintain the control error below $10\,\mathrm{cm}$ level. However, the delta-v to keep such formation is in the order of $7.5\,\mathrm{cm\,s^{-1}}$ over two orbital periods. This results in a daily delta-v budget of about $50\,\mathrm{cm\,s^{-1}}$. This level of control effort influences the design of the propulsive system, and cannot be provided by small platformers (such as CubeSats of small satellites). Instead, for the FFLAS study, the platforms have been designed accordingly, with a wet mass in the order of $1600\,\mathrm{kg}$, to provide a $10\,\mathrm{year}$ mission lifetime.

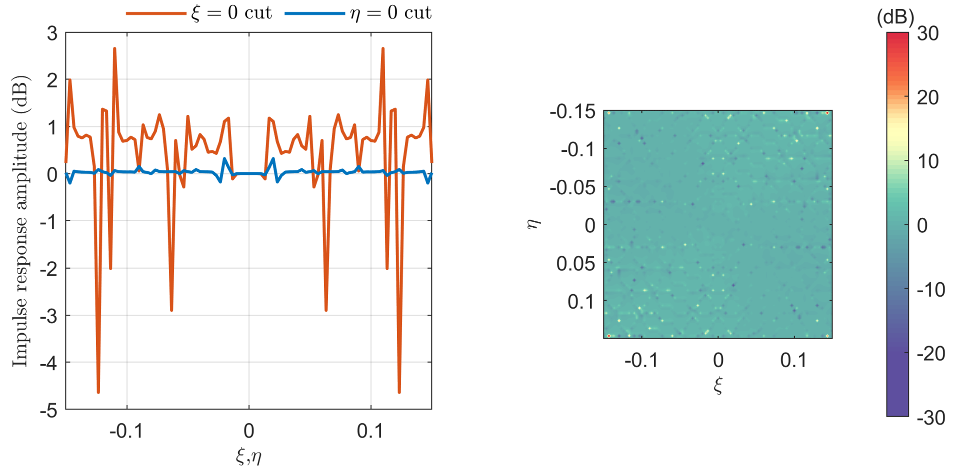

(a) *Mean error on the impulse response amplitude.* **(b)** *Mean error on the impulse response contour.*

Figure 7.13: *L-band interferometer performances during the science phase over 1 orbital period.*

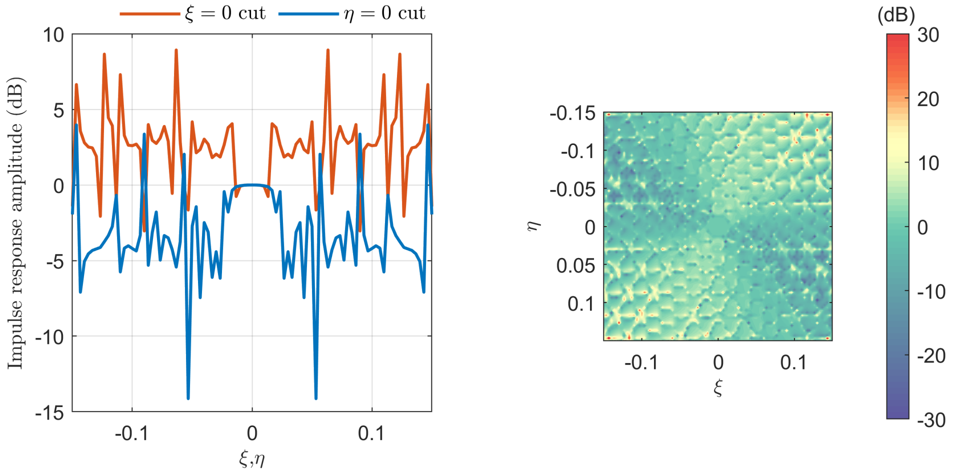

(a) *Mean error on the impulse response amplitude.* **(b)** *Mean error on the impulse response contour.*

Figure 7.14: *Error on the L-band interferometer performances with a mean error on the relative position of* $30\,\mathrm{cm}$.

7.2.5 Simulation of Payload Calibration Phase

The simulation of the payload calibration phase consists of the analysis of the scenario for the calibration of the scientific payload when the satellites should be able to change their attitude of the aperture plane from nadir to inertial pointing. The analyses are based on the outcomes of Section 7.1.2.

The simulation aims at evaluating the feasibility of the science to payload calibration reconfiguration with autonomous on-board navigation reconstruction.

The calibration phase is required at least once per month to calibrate the instruments. The simulation considers the following steps:

- A first orbital manoeuvre to change from nadir to inertial pointing, as described in Section 7.1.2.
- A second period of at least 15 minutes, when the Aperture plane points to the zenith direction.
- A final orbital manoeuvre to change back from inertial to nadir pointing.

The idea is to evaluate the compliance of the simulator with the required accuracy level of both the navigation and the controller. In addition, the necessity to include post-processing navigation accuracy is also discussed. The initial conditions of the science phase and the one for the payload calibration configuration are the same as the one reported in Table 7.1. As before, the maximum thrust is set equal to $25\,\mathrm{mN}$, and the time step is $1\,\mathrm{s}$ for the simulation.

Simulation results The trajectory followed during the transition to and back the calibration configuration is shown in Figure 7.15a. It can be seen that satellites 2 and 3 follow a specular trajectory for the transition, as in Section 7.1.2, while satellite 1 remains stable in its original position. The satellites' positions are identified with three different colours, while the central point represents the reference virtual trajectory. Figure 7.15b represents the time evolution of the relative state in ROEs frame. The simulations steps are the following:

1. One orbital period in Earth pointing configuration is simulated for formation maintenance.
2. The manoeuvre to cold sky pointing is implemented, where satellites 2 and 3 switch their position.
3. Then, an attitude manoeuvre is performed to point the satellites' payload to the cold sky, and the inertial pointing is maintained for at least 15 minutes (in the simulation, 30 minutes are considered to margin possible delay in the control), implementing formation maintenance.
4. At the end of the calibration phase, another attitude manoeuvre is performed to point the Aperture Plane of the payload toward the Earth and the manoeuvre to switch the position of spacecraft 2 and 3 is performed again.
5. Finally, the maintenance of Earth pointing formation for one orbital period is performed.

Similarly to the science phase, the inter-satellite distance is continuously monitored during the phase, to ensure a safe flight. The time evolution of the spacecraft separation is reported in Figure 7.16a. The minimum spacecraft separation of $10\,\mathrm{m}$ is respected even in presence of external perturbations. The control thrust profile required for this phase is reported in Figure 7.16b, where the control in the RTN frame is on the left, while the one in the EME2000 frame is on the right. It can be seen that the control required for satellite 1 consists of the pure formation maintenance control, with a constant thrust in the normal direction of about $10\,\mathrm{mN}$. On the other hand, satellites 2 and 3 start with the formation maintenance control before entering the manoeuvre control profile. The thrust to switch their position is only in the normal and transversal direction. Around the second orbital period, there is a 30-minute slot where the satellites return in the formation maintenance control profile, to maintain the zenith pointing for the payload calibration. The maximum thrust is limited by the technological performances of the QinetiQ T5 engine of $25\,\mathrm{mN}$ maximum.

The corresponding delta-v budget and the control error for the overall phase are reported in Table 7.13. A centimetre level of delta-v budget is required for the overall phase. The error in the control for the calibration transition phase is reported in terms of mean and standard deviation over the phase. After the initial instants where the controller needs to converge, the error in the control in the radial

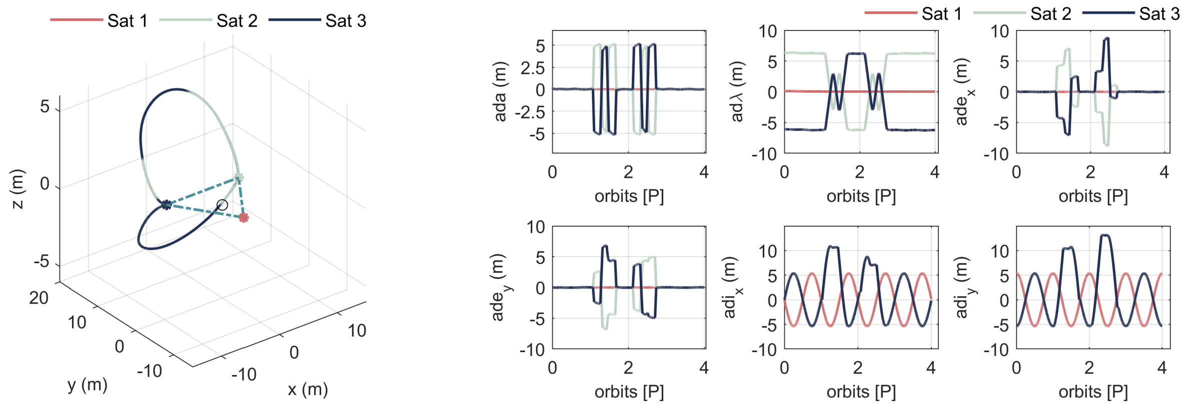

(a) *Formation maintenance during calibration phase.*

(b) *Time evolution of the ROEs during calibration phase.*

Figure 7.15: *Formation reconfiguration for the calibration phase of FFLAS.*

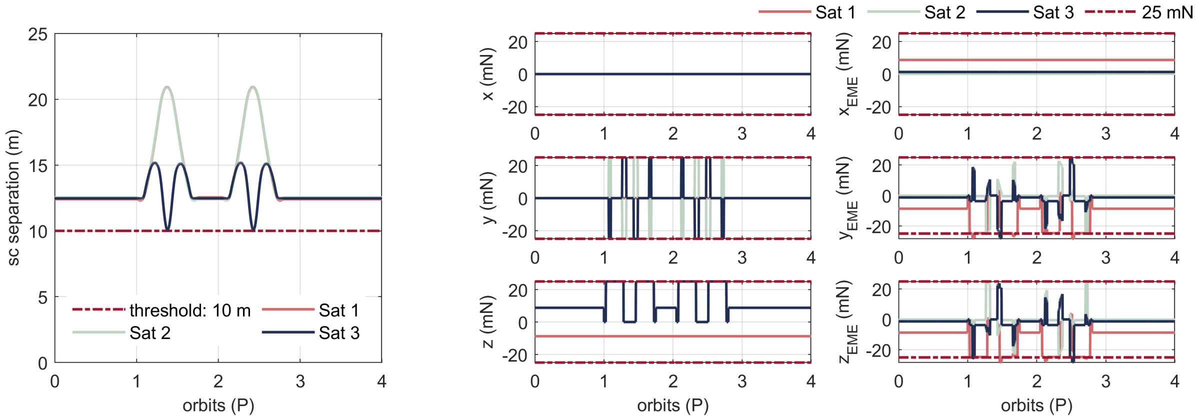

(a) *Time evolution of the spacecraft separation during the Earth pointing mode.*

(b) *Actuator control law during the Earth pointing mode.*

Figure 7.16: *Spacecraft reconfiguration and control law for FFLAS during the calibration phase.*

Table 7.13: *Control accuracy and delta-v budget for the calibration phase of FFLAS.*

Spacecraft	**Delta-V budget** (cm/s)	**Control accuracy (RTN components)** x, mean ± std (cm)	y, mean ± std (cm)	z, mean ± std (cm)
Satellite 1	14.13	2.36 ± 1.92	10.47 ± 5.06	1.18 ± 1.86
Satellite 2	21.14	2.21 ± 1.77	6.00 ± 5.54	1.59 ± 1.84
Satellite 3	21.14	2.04 ± 1.71	5.01 ± 4.75	1.48 ± 1.50

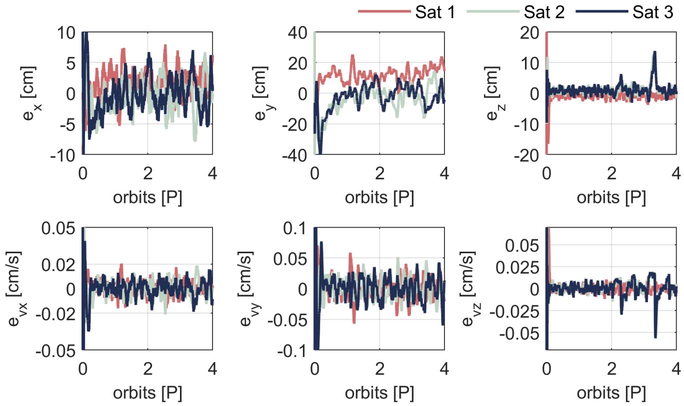

Figure 7.17: *Control accuracy solution for the calibration phase of FFLAS.*

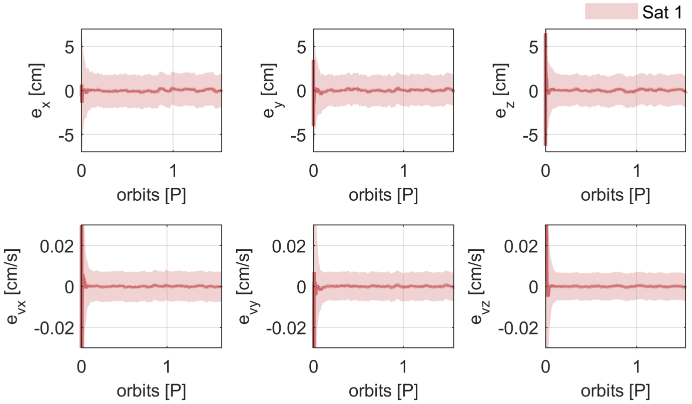

Figure 7.18: *On-Board navigation solution for Satellite 1*

and normal direction is of a few centimetres with a standard deviation below $2\,\mathrm{cm}$. This is similar to the results for the science phase. On the contrary, the control in the transversal direction is less accurate (up to $10.47\,\mathrm{cm} \pm 5.06\,\mathrm{cm}$). This was an expected result, as the transversal component of the relative motion is the most difficult to accurately estimate. The corresponding temporal behaviour of the control error is reported in Figure 7.17, where the time evolution for the three satellite in the formation is reported in terms of control error in the relative Cartesian frame. Particularly, the control accuracy is reduced mainly during the initial steps of the transition between the science phase and the start of the manoeuvre to switch position between satellites 2 and 3 (corresponding to some of the peaks in the graph). This is due to the need for the controller to converge again for a different situation than the one of the formation maintenance. Therefore, in a successive phase of the study, an optimisation of the controller is envisioned, to improve the controller's performance and accuracy. The solution from the onboard navigation state reconstruction is essential to guarantee the autonomous GNC setting for FFLAS during the payload calibration phase of the mission. The estimation of the state is used as an input to the control block to define the commanded thrust to the actuator. The real-time onboard navigation accuracy is about $1.01\,\mathrm{cm} \pm 0.91\,\mathrm{cm}$, in terms of mean and standard deviation, for the three satellites. The navigation solution for satellite 1 in the formation is shown in Figure 7.18, where the shadowed part is the confidence interval of the navigation.

7.2.6 Simulation of Safe Mode Phase

The simulation of the off-nominal scenario of the mission study is of primary importance to set a baseline in case of non-nominal behaviour of the formation, such as fault detection. This phase is triggered by any off-nominal scenarios: whenever a subsystem failure occurs or the spacecraft separation is below the threshold, the distributed system automatically implements the manoeuvre to move in the safe mode configuration. The transition to the Safe-Mode configuration during the Failure Detection, Isolation and Recovery operations is simulated.

The idea is to evaluate the feasibility of autonomous transition to a safe mode configuration with on-board navigation reconstruction.

The design of the safe mode was based on the following mission constraints:

- Ideally the ISL must be granted during the safe mode, i.e. the relative attitude based on the triangular geometry shall be kept in the new configuration.
- The spacecraft should belong to the same plane, nominally the transversal-normal one.
- The solar panels shall be kept aligned with the negative normal direction, to provide power for the platform.

As a consequence, the initial strategy for the safe mode has been to move the platform on an augmented equilateral triangle formation lying on the transversal-normal plane. This first strategy does not provide passive safety but is consistent with the previous requirements. Specifically, a larger separation among the spacecraft (about $26\,\mathrm{m}$) has been imposed starting on the maximum available thrust to keep the formation. This solution results in a proper ISL among the platform and solar panels orientation for power generation. This configuration has been called the "planar safe mode solution".

Simulation results for planar safe mode solution The simulation is performed, considering the followings:

- The closed-loop control algorithm relies on on-boards GNSS navigation for reconstructing the state of the formation.
- The control algorithm provides a command thrust to the onboard actuators, which are limited to $25\,\mathrm{mN}$ maximum.
- The onboard actuators provide the thrust only in the y-z axis, corresponding to the transversal and normal direction of the RTN frame.

Figure 7.19a represents the three-dimensional trajectory followed by the three spacecraft to enter the Safe Mode configuration. The case reported in this work considers the following condition to increase the formation baseline:

- The new triangular formation lies on the transversal-normal plane with an equilateral triangle of $26\,\mathrm{m}$ sides.
- The new geometry has been selected to ensure the possibility to control the oscillation in the normal component with a maximum thrust of $25\,\mathrm{mN}$.

Figure 7.19b reports the time evolution of the components of the trajectories in the ROEs frameworks. it can be seen that the separation in $\delta\lambda$ increases, but the condition on the relative eccentricity/inclination vector remains similar to the initial situation. This results in a non-passive safety condition of the strategy, and, hence, the behaviour of the spacecraft separation should be analysed. Figure 7.20a represents the variation in the inter-satellite distance among the satellites for two cases. First, the case of transition to safe mode is analysed when no thruster failure is present. Figure 7.20a (left) shows that the spacecraft separation passes from about $12\,\mathrm{m}$, to more than $25\,\mathrm{m}$. The corresponding control profile to keep such formation is shown in Figure 7.20b. One can observe that this solution requires the spacecraft to continuously control in the normal direction (out-of-plane) to keep this formation geometry. The control required by the satellites 1, 2, and 3 during the initial science and the final safe mode configurations corresponds to a constant thrust of about $10\,\mathrm{mN}$ and $24\,\mathrm{mN}$, respectively, in the normal direction. On the other hand, during the transition to safe mode, the satellites provide thrust in both normal and transversal directions. The maximum thrust is limited by the technological performances of the QinetiQ T5 engine of $25\,\mathrm{mN}$ maximum, as represented by the red line in the body-fixed frame control in Figure 7.20b. The second case is depicted in Figure 7.20a (left), where the case when one spacecraft undergoes a thruster failure is analysed: the separation remains larger than $15\,\mathrm{m}$. Specifically, the situation when all four thrusters of satellite 1 fail have been considered. In this situation, the relative motion of spacecraft 1 is no more controlled and undergoes relative natural dynamics. As soon as this condition is triggered, spacecraft 2 and 3 immediately move to their safe mode condition. The figure shows that the threshold of $10\,\mathrm{m}$ is respected during the reconfiguration. A similar analysis can be performed in the case of failure on the other satellites.

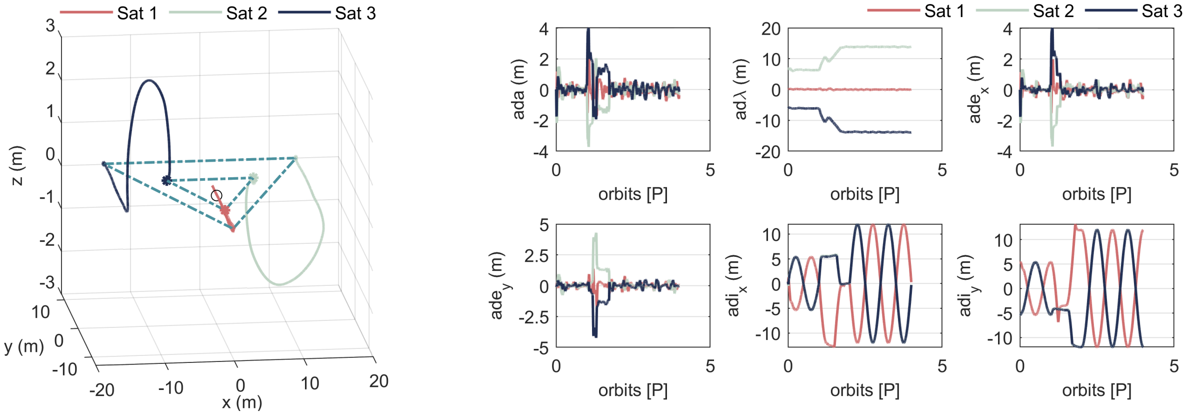

(a) *Formation reconfiguration to safe mode.*

(b) *Time evolution of the ROEs during safe mode.*

Figure 7.19: *Formation reconfiguration to the safe mode for FFLAS.*

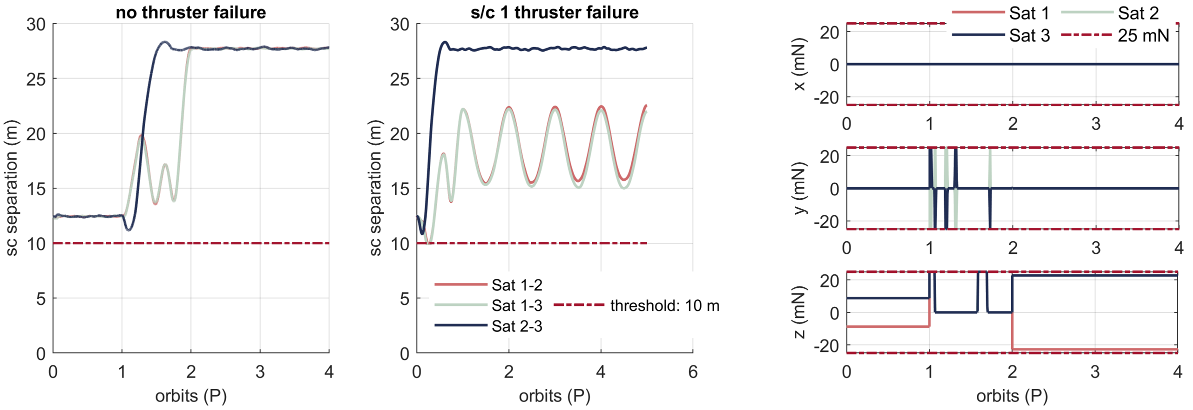

(a) *Time evolution of the spacecraft separation during the Earth pointing mode.*

(b) *Actuator control law during the Earth pointing mode.*

Figure 7.20: *Spacecraft separation and control law during the transition to safe mode.*

The delta-v budget for the transition between science and safe mode is reported in Table 7.14. A level of a few tens of centimetres is required to increase the baseline geometry. Concerning the accuracy of the control, it has been described in terms of mean and standard deviation. A quite accurate control is obtained, with a deviation from the nominal trajectory below $10\,\mathrm{cm}$. As for the case of the calibration phase, the less accurate control is in the transversal direction, reaching a level of $4.74\,\mathrm{cm} \pm 4.82\,\mathrm{cm}$. These results are possible only by considering an on-board navigation solution of a state reconstruction with a few centimetre accuracies, as in Figure 7.18. Specifically, the on-board navigation solution is around $0.98\,\mathrm{cm} \pm 0.85\,\mathrm{cm}$. Therefore, for this study, robust and accurate autonomous navigation is required.

Table 7.14: *Control accuracy and delta-v budget for the safe mode phase of FFLAS.*

Spacecraft	Delta-V budget (cm/s)	Control accuracy (RTN components) x, mean ± std (cm)	y, mean ± std (cm)	z, mean ± std (cm)
Satellite 1	28.10	2.06 ± 1.49	4.61 ± 3.81	1.35 ± 1.15
Satellite 2	24.21	2.36 ± 1.93	4.74 ± 4.82	1.22 ± 1.17
Satellite 3	24.16	1.79 ± 1.78	4.80 ± 3.95	1.19 ± 1.19

Alternative solutions for safe mode configuration The non-passive safety nature of the planar safe mode solution arises the need for a preliminary investigation of different approaches. First, one important configuration widely studied in literature to provide passive safety is the relative helix motion, implementing the (anti-) parallel relative eccentricity/inclination vectors separation [74]. The relative dynamics for this solution have been described in Section 3.3. The reconfiguration of the triangular geometry into a helix trajectory could be implemented based on the delta-v optimal COCP of Section 4.1.2, based on ROEs. An example of the possible reconfiguration is depicted in Figure 7.21. The parameters of the helix trajectory are $a\delta\boldsymbol{\alpha} = \{0,\,0,\,0,\,24.5,\,0,\,24.5\}$, and the three spacecraft are placed on it with a phasing angle of 120 deg. During the reconfiguration, the minimum distance of $12\,\mathrm{m}$ is imposed during a reconfiguration time of $3/4$ of the orbital period. The orbital manoeuvre requires a delta-v of about $5.6\,\mathrm{cm\,s^{-1}}$ and the thrust is limited to $25\,\mathrm{mN}$, with only transversal and normal components. Once the spacecraft is in helix formation, the passive safety is established, and similar considerations to the analyses in Section 6.1 can be done. Nevertheless, the following limitations of this approach have been identified for the FFLAS case:

- During the safe mode in helix configuration, the relative attitude based on the triangular geometry is not respected: i.e. the ISL could not be used to share telemetry data among the platform, and only the radio frequency link is available.
- The orbit requires a specific attitude profile to keep the solar panels in Sun pointing (aligned with the negative normal direction): the combination of on-board thrusters and attitude profile could not be feasible and required additional analysis.

Such a solution has not been analysed further in this thesis, because it did not satisfy the specific constraint for FFLAS study (i.e. ISL, transversal-normal plane of the relative orbit, and solar panels issues). A modification of the current spacecraft configuration and the requirements for the safe mode must be analysed in a future development of the FFLAS concept.

A final configuration that only deals with the need of establishing the ISL could be found in the GCO relative trajectory. In this second case, the separation among the spacecraft remains constant and guarantees the relative triangular configuration among the spacecraft. The reconfiguration to the

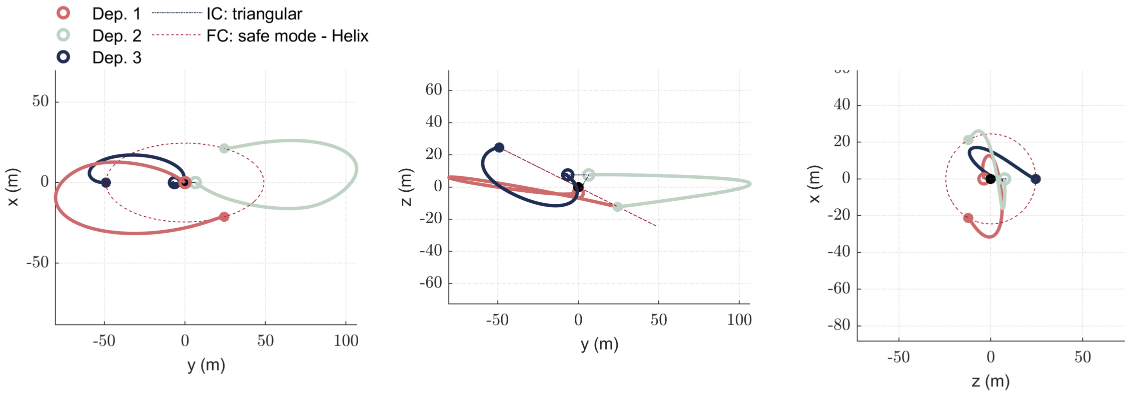

Figure 7.21: *Alternative safe mode solution: helix formation.*

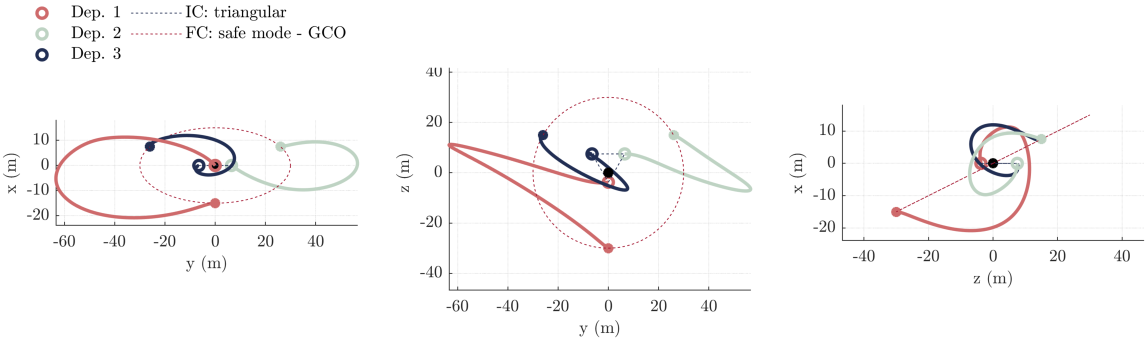

Figure 7.22: *Alternative safe mode solution: GCO formation.*

GCO trajectory has been performed based on the delta-v optimal COCP of Section 4.1.2 in the ROEs framework. The parameters for the initialisation of the GCO are the relative orbit radius set equal to $15\,\mathrm{m}$ and the phase angle among the vehicles is 120 deg. As for the helix solution, the manoeuvre has been initialised considering a minimum distance among the spacecraft of $12\,\mathrm{m}$ and a maximum thrust $25\,\mathrm{mN}$, with only transversal and normal components. The reconfiguration in $3/4$ of the orbital period is represented in Figure 7.22. Thanks to the circular nature of the GCO, the ISL could theoretically be established if the spacecraft keep a proper relative attitude on the relative orbit plane. Further analyses are required to understand the compatibility of such a solution with the Sun pointing requirements of the solar panels and the thrust components for formation maintenance. Even if this solution does not guarantee passive safety in the presence of orbital perturbation, it is a more stable solution than the planar case, as it relies on the analytical solution of the relative motion. This solution has not been analysed further but could be considered in a future study based on the FFLAS concept.

7.3 Chapter conclusion

To conclude, this chapter describes the simulations and the results obtained for the FFLAS study, introducing the main operational phases of a space mission. Specifically, the following modes have been tested to assess the feasibility of the control based on on-board navigation techniques:

- Formation maintenance in the nominal science phase for Earth observation.
- Transition and back to the calibration phase for the payload calibration once per month.
- Transition to safe mode and formation maintenance in Safe Mode configuration.

On the other hand, the launch to commissioning phase with the first formation acquisition is based on the ground reconstruction control. In fact, for this phase, it is critical to monitor the correct behaviour of thrusters to safely acquire the triangular geometry. During the simulations, it was crucial to obtain an onboard navigation reconstruction with an accuracy below $5\,\mathrm{cm}$, also considering the confidence interval. This is in line with the navigation performance requirements, where accuracy in the order of a few centimetres $(2\,\mathrm{cm})$ was required. These outcomes are essential to assess feasible solutions in terms of control effort. The controller based on the Linear Quadratic Regulator can provide accuracy in the order of a few centimetres for all the case scenarios simulated, in particular the accuracy level is below $10\,\mathrm{cm}$, with some exceptions during the reconfiguration between science and calibration. In future developments of the FFLAS study, the controller and the on-board navigation should be optimised and tested against robustness for the main operative phase of the mission. Specifically, given the criticality from the safety point of view and the delta-v budget to keep the formation, a more promising future development of the FFLAS study has been identified in the TriHex concept, described in Section 6.5. Moreover, it provides some advantages compared to the FFLAS study:

- The daily delta-v for maintenance is about $0.45\,\mathrm{cm\,s^{-1}}$, compared to the $50\,\mathrm{cm\,s^{-1}}$ of FFLAS.
- The trajectory selected to ensure safe operations even in the absence of control for about one day of propagation.
- The three platforms have a significantly lower mass compared to FFLAS, reducing the cost and removing the complex deployable mechanism.
- The 30 deg inclination of the relative obit ensures that the payload field-of-view is away from the Sun, improving performance.

CHAPTER 8

Conclusions

No great discovery was ever made without a bold guess.

— Isaac Newton

REMOTE sensing poses several challenges to current and future space missions for Earth observation. Improving the spatial resolution, specifically for passive microwave antennas, enables significant contributions to monitoring natural events on planet Earth, not observable otherwise. The SMOS and SMAP single satellite missions demonstrated the potential of microwave observations for L-band interferometry. Currently, these missions are in their extended operative phase, and the scientific community requires new concepts to either provide continuity in the L-band observation or improve the current level of spatial resolution (i.e. $40\,\mathrm{km}$). To potentially improve the spatial resolution, the past trend has been focusing on the design of larger and deployable antennas to increase the Antenna Aperture. A different approach comes from the active SAR missions, where distributed systems in space have been introduced to combine the data acquired from other platforms to improve the current resolution in microwave observations. An important example in this sense is the TanDEM-X-TerraSAR-X mission, comprising a two-spacecraft formation in LEO. This study opens up a new path for active SAR based on formation and swarm of satellites. Furthermore, the concept of distributed systems for passive interferometry can also be applied to increase virtually the Antenna Aperture without deploying large and heavy antennas. However, current studies mainly focused on active SAR and failed to propose a suitable architecture for distributed systems for passive interferometry. Furthermore, given the different nature of passive and active interferometry, specific and accurate procedures are needed to understand the geometry and formation design under mission-related requirements. This thesis proposes new techniques and methodologies to design formation flying mission concepts carrying passive interferometers. The synthetic aperture is realised by combining distributed antenna arrays as part of a unique virtual instrument to improve spatial resolution. The lack of study in this field is mainly caused by the need to maintain a rigid and fixed geometry among the platforms with a few tens of metres of separation. This thesis tackles the challenges posed to the relative Guidance, Navigation, and Control (GNC) design and development and proposes two innovative concepts for future mission realisation for passive interferometry. At the same time, two studies for distributed SAR missions are investigated by applying some of the developed control methodologies considering the synergies between passive and active applications and in view of future studies in the LEO region. An extensive summary and a description of the main contribution of this work are given in Section 8.1. In addition, the limitations of the proposed methodologies together with considerations on future improvement and applicability are provided in Section 8.2.

8.1 Summary and contributions

As discussed in Chapter 1, the main objective of this research is the

> *"definition of a preliminary design strategy for future distributed multi-satellites missions for high-resolution interferometry, including main operational and payload constraints".*

This goal has been explored through three research questions. First, the understanding of the current EO missions and the identification of the requirements for future innovative microwave missions have been evaluated. Simultaneously, the need of proposing novel approaches has been investigated to accurately and precisely model optimal reconfiguration manoeuvres under continuous control techniques. In addition, design of robust and autonomous algorithms for distributed systems is evaluated within a GNC framework, flexible for different formation flying scenarios. The following sections detail how these objectives have been obtained.

8.1.1 Methodology

To start, state-of-the-art methods and techniques are studied, and the operational constraints of active SAR and passive interferometers are discussed. Then, the algorithms to model the visibility function and the impulse response of distributed antennas are identified from suitable candidates in the literature (i.e. windowing functions, array factor, and visibility samples). This approach can support the prediction of the preliminary performances of distributed systems with a scalable number of spacecraft. Hence, the method is presented to propose multiple-satellite interferometer geometries and five different configurations are analysed. The formulation results in two promising compositions based on a three-satellite concept, i.e. FFLAS and TriHex. In this context, the procedure enables the identification of the advantages and limitations of distributed systems for passive interferometry. On one side, the improvement in the spatial resolution and payload performances is connected to the combination of different numbers of spacecraft. However, increasing the number of vehicles flying in formation poses severe challenges to the spacecraft's manoeuvrability and operations from ground, resulting in a preference for an initial design with 3 to 4 platforms. At the same time, the idea of distributed systems is highly flexible. For example, a formation initialised with 3 spacecraft could be augmented up to six vehicles to increase the Antenna Aperture even after months or years of operations. Similarly, the geometry is highly reconfigurable, providing a robust condition against single failures.

Next to advancements in payload performances, an extension of classical models for absolute and relative dynamics is presented, mainly based on ROEs description of the relative motion. The models, based on the inclusion of the most relevant perturbing effect for LEO environment (i.e. Earth oblateness and atmospheric drag), provide an analytical formulation of the relative motion that serves as starting point for the development of control methodologies. The control techniques consider the challenges of distributed systems carrying passive interferometry. The need to keep spacecraft at short separation (i.e. 10 to $20\,\mathrm{m}$) is an important limitation to the operations of the formation and to the possibility of monitoring the dynamics from ground, due to the fast behaviour of the relative motion. At the same time, for the FFLAS study, the completely forced motion of the formation poses an important threat to safety in case of non-nominal behaviour or a failure of the thrusters. To tackle these problems, control methodologies to introduce onboard autonomy are investigated, both in the open- and closed-loop. Additionally, a new open-loop control is implemented, extending the design of delta-v optimal manoeuvres in classical relative states to the ROEs framework. The new model includes boundaries in terms of thrust level and inter-satellite collision avoidance and expresses the problem in a convex formulation to get a unique solution of the optimal relative trajectory. This model serves to quickly evaluate the delta-v optimal reconfiguration of multiple spacecraft flying in formation under J_2 and differential drag effects. At the same time, two closed-loop control strategies are proposed for a robust inclusion of uncertainties over the initial condition of the relative states. First, a more classical LQR technique is implemented for the trajectory tracking problem, taking as reference the results of the open-loop convex algorithm. Subsequently, for a real-time optimal trajectory implementation, a MPC is built up over the open-loop convex algorithm to provide formation reconfiguration with real-time feedback on inaccuracies of the trajectory. The performance of the first method (i.e. open-loop convex algorithm) is tested against an increasing number of spacecraft to understand the applicability to a large swarm. This verification proves the efficient and fast solution of the delta-v optimal trajectory for a limited number of spacecraft (e.g. up to six to ten vehicles). Subsequently, the performances decrease exponentially with the number of spacecraft, thus, the methodology could not be suitable for a swarm of tens of vehicles. On the other hand, the closed-loop methodologies do not scale poorly with the number of spacecraft, given a more flexible environment for formation design when tens to thousands of vehicles are considered. Nevertheless, the verification method proves adequate for the context analysed in this thesis. For active SAR, distributed systems of two- to three-spacecraft have been considered. The efficiency of the developed methodologies could constitute a starting point for on-board algorithm implementation for autonomous control.

The developed techniques for guidance and control are implemented in a new suite for the propagation, guidance, navigation, and control of multiple satellite formations. The resulting GNC framework is highly modular in terms of the number of spacecraft and orbital perturbations. It implements GNSS-based navigation for on-board absolute and relative state reconstruction based on a decentralised architecture approach. Furthermore, it implements closed-loop control with a model of the actuators (i.e. low-thrust engines), capable of dealing with the needs and requirements of different mission phases. The GNC framework is based on a straightforward initialisation procedure in MATLAB®, which defines the main interfaces and input files for the framework in the SIMULINK® environment. The implementation removes the need for a manual framework set-up, providing a highly flexible environment for fast evaluation of navigation and control performances. Simultaneously, it also provides a preliminary assessment of the payload performances, in terms of the impulse response of the antenna, based on the actual relative state of the formation (i.e. including the control error). The GNC framework provides a fundamental tool for the design of distributed missions. It has been applied to the design of multiple mission concepts in the context of this thesis.

8.1.2 Applications

The methodologies proposed in Section 8.1.1 are implemented for novel formation flying concepts for active and passive interferometers. Hence, the GNC framework based on low thrust control is used for performance characterisation and comparison with the impulsive control architecture, typically implemented for active SAR. Given the two studies, ROSE-L and HARMONY, considered in this thesis, the framework proved to be capable of simulating the formation maintenance in a fast and effective way in different situations. Furthermore, the analysis demonstrated the capability of the low thrust control, limited to a maximum of 2 to $15\,\mathrm{mN}$, to keep the helix formation and maintain the relative eccentricity and inclination vectors in anti-parallel configuration - see Section 6.1. Thus, the methodology could be a valid alternative to the impulsive approach.

Next to active SAR, the GNC framework has been used to perform simulations for the two most relevant scenarios identified from the passive interferometer analysis on payload performances. First, for the FFLAS case, a trade-off analysis for the nominal geometry and the operational constraints demonstrates the need to include a fuel balance strategy. Having the same propellant mass and physical properties for all the platforms minimises the effect of the differential drag on the relative dynamics, resulting in a lower control effort to keep the formation. Then, an entire chapter - Chapter 7 - is dedicated to the simulation of the main operational phases of FFLAS. This serves as a validation of the methodology and as a feasibility study for the FFLAS concept from the operational point of view. Specifically, the manoeuvre transition during the payload calibration phase and the transition to safe mode have been simulated considering autonomous navigation and control, based on on-board absolute and relative state reconstruction from the GNSS sensors. The main limitation of the FFLAS mission concept relies on the requirement of a continuous forced motion to keep the triangular formation against the relative dynamics. Not only this requires a higher fuel consumption for formation keeping, but it also results in critical situations to be handled on-board in case of failure to avoid any possible collision among the vehicles. To deal with these limitations, the innovative possibility to exploit natural solutions for passive remote sensing was proposed, e.g. for the TriHex concept. Differently from the typical trajectory used for active SAR, passive distributed L-band sensors require a natural relative trajectory that keeps a constant separation among the spacecraft. Consequently, the GCO solution (i.e. a circular relative trajectory) of the relative motion has been adopted for this original application. As demonstrated for both three- and six-satellite formations in a GCO, the fuel consumption is significantly reduced for formation maintenance. E.g. the daily delta-v budget for formation keeping passes to $0.45\,\mathrm{cm\,s^{-1}}$ of TriHex from the $40\,\mathrm{cm\,s^{-1}}$ of FFLAS. Furthermore, the selection of the GCO solution brings other operational advantages: the nature of the motion is more stable, resulting in a more safe and robust configuration against failures and non-nominal situations; the titled angle of the relative orbit can be set so that the Sun is always away from the field of view of the payload, improving performances (e.g. lower thermal stress and noise). To conclude, this work demonstrates the feasibility of a new formation concept specifically designed to provide a continuation for L-band passive observation. The FFLAS and TriHex concepts serve as a starting point for future mission development, already providing important consideration in terms of the operational constraints, control and navigation accuracies, and payload performances.

8.2 Limitations and remarks

Despite the achievements in this thesis for future remote sensing mission design, there are some limitations to be addressed in possible future works. From the methodology point of view, the main limitation of the GNC framework relies on the need to adapt the code for on-board implementation (e.g. tests with hardware in the loop). Specifically, part of the framework is already based on C++ mexed codes for SIMULINK®, i.e. the absolute dynamical propagator, while the remaining part of the code requires a rewriting to be tested with hardware in the loop. The need to test for autonomy and on-board implementation is essential for the mission concept presented in this work, as they will require a high autonomy level when in orbit. At the same time, more realistic modelling of the GNSS sensors and navigation tasks should be implemented and tested with different methodologies available in the literature to assess the accuracy required by the onboard navigation reconstruction. In case the current GNSS-based technologies would not be enough to guarantee such a level of accuracy, the system could be enhanced by including other sensors for relative navigation. Given the short distance among the platforms, an optical link could be used to provide observations on the range and the angle of the other platforms, to improve both the navigation solution and the monitoring of the spacecraft separation for safety reasons. However, to properly include optical sensors, fiducial markers should be considered in the design of the platform. This aspect could pose an additional constraint, increasing the complexity the platforms' design. Furthermore, to reduce the relative positioning and velocity accuracy below centimetre level is a challenging task, even implementing cooperative visual based techniques. Regarding the control methods, the accuracy could be improved by performing an adaptive and automatic gain selection of the LQR algorithm. In the current implementation of GNC framework, the trajectory optimisation is performed a priori, with the open-loop convex optimisation algorithm. Consequently, the developed MPC should be included in the closed-loop GNC framework to assess the improvement in the guidance and control when uncertainties in the navigation are present. For future development, simulations with hardware in the loop are envisioned to test the robustness and compatibility with spacecraft components (e.g. on-board memory).

At the same time, the improvement of the payload model should be tackled. The connection between the payload performances and the control accuracy should be further extended. Promising results in this sense were demonstrated in the analysis in Section 7.2 for the science phase of FFLAS and in the preliminary study in [112]. As continuation of this work, including the error on the synthetic aperture reconstruction in the feedback control could significantly improve the overall performances of the combined interferometry. With this in mind, a possible solution relies first on understanding the real-time availability of the synthetic aperture solution. Then, the error with respect to the nominal solution could be included in the feedback control once or twice per orbit, and a sensitivity analysis should be performed to assess the performance improvement. Furthermore, starting from the analysis in [129], it is fundamental to extend the payload model by including considerations on the field-of-view, radiometric and effective sensitivity, and physical temperature of the antenna. An additional interesting feature could be the inclusion of impulsive control techniques for a more flexible GNC framework, adaptable to several mission concepts, not only in the remote-sensing field. At the same time, the model development for active SAR performance assessment could be included in the simulator. These aspects might lead to a new tool for the fast and accurate design of multiple-satellite formations and swarms, including the performances of the interferometer payload. Furthermore, a future development of the GNC framework entirely based on a C++ environment could profit from becoming more flexible with hardware-in-the-loop testing.

To conclude, currently, the framework is designed to be flexible in terms of formation baseline and spacecraft number. Therefore, it can be applied to several scenarios for mission design and GNC performance assessment. Based on the outcomes of this work, a wrap-up of the possibilities for future developments is outlined here:

- A follow-on study that includes models of both active and passive microwave antennas in the GNC framework, aiming not only at providing interferometer performances as outputs but also including the error with respect to the nominal situation in the feedback loop. This study should assess whether the control accuracy and robustness could benefit from such an addition.

- A follow-on study focused on developing accurate navigation algorithms, exploring not only GNSS-based navigation but also different techniques (e.g. vision-based and laser-based). This research should focus on the development of appropriate strategies for close-range formations (as for passive distributed radiometers) when the spacecraft separation is within a few tens of metres. The outcomes of this work are essential to improve the autonomy and the feasibility of distributed system studies.
- A follow-on research to extend the current GNC framework for hardware-in-the-loop simulation. At the same time, different control techniques should be implemented in the closed-loop framework, including the proposed MPC methodology. This analysis is essential to test the feasibility of including the framework on-board a spacecraft and test the performances with real sensors and actuators.

Bibliography

[1] Herbert J Kramer et al. *Observation of the Earth and its Environment: Survey of Missions and Sensors*, volume 1982. Springer Berlin, Heidelberg, 2002.

[2] NASA. First photo of earth from a weather satellite, tiros-1. `https://www.nasa.gov/topics/earth/earthday/gall_tiros.html`. Last Accessed: 2022-10-31.

[3] UN. Office for Outer Space Affairs and European Global Navigation Satellite Systems Agency. *European Global Navigation Satellite System and Copernicus: supporting the Sustainable Development Goals - building blocks towards the 2030 Agenda*. United Nations, 2018.

[4] Katherine Anderson, Barbara Ryan, William Sonntag, Argyro Kavvada, and Lawrence Friedl. Earth observation in service of the 2030 agenda for sustainable development. *Geo-spatial Information Science*, 20(4):77–96, Jun 2017. doi: 10.1080/10095020.2017.1333230.

[5] Nicholas H Crisp, Peter CE Roberts, Sabrina Livadiotti, Vitor Toshiyuki Abrao Oiko, Steve Edmondson, SJ Haigh, Claire Huyton, LA Sinpetru, KL Smith, SD Worrall, et al. The benefits of very low earth orbit for earth observation missions. *Progress in Aerospace Sciences*, 117:100619, 2020.

[6] Vitor CF Gomes, Gilberto R Queiroz, and Karine R Ferreira. An overview of platforms for big earth observation data management and analysis. *Remote Sensing*, 12(8), 2020.

[7] UCS. Ucs satellite database. `https://www.ucsusa.org/resources/satellite-database`. Last Accessed: 2022-10-31.

[8] CP Escoubet, M Fehringer, and M Goldstein. Introduction the cluster mission. In *Annales Geophysicae*, volume 19, pages 1197–1200. Copernicus GmbH, 2001.

[9] Eigil Friis-Christensen, Hermann Lühr, D Knudsen, and R Haagmans. Swarm–an earth observation mission investigating geospace. *Advances in Space Research*, 41(1):210–216, 2008.

[10] D Steitz, A Kenitzer, G Diller, K Henry, D Ainsworth, and M Neiman. Terra: Flagship of the earth observing system. *NASA press kit, release*, (99-120):26, 1999.

[11] Claire L Parkinson. Aqua: An earth-observing satellite mission to examine water and other climate variables. *IEEE Transactions on Geoscience and Remote Sensing*, 41(2):173–183, 2003.

[12] Mark R Schoeberl, Anne R Douglass, Ernest Hilsenrath, Pawan K Bhartia, Reinhard Beer, Joe William Waters, Michael R Gunson, Lucien Froidevaux, John C Gille, John J Barnett, et al. Overview of the eos aura mission. *IEEE Transactions on Geoscience and Remote Sensing*, 44(5):1066–1074, 2006.

[13] Graeme L Stephens, Deborah G Vane, Ronald J Boain, Gerald G Mace, Kenneth Sassen, Zhien Wang, Anthony J Illingworth, Ewan J O'connor, William B Rossow, Stephen L Durden, et al. The cloudsat mission and the a-train: A new dimension of space-based observations of clouds and precipitation. *Bulletin of the American Meteorological Society*, 83(12):1771–1790, 2002.

[14] PG Edwards and D Pawlak. Metop: The space segment for eumetsat's polar system. *ESA bulletin*, pages 7–18, 2000.

[15] Yann H Kerr, Philippe Waldteufel, J-P Wigneron, JAMJ Martinuzzi, Jordi Font, and Michael Berger. Soil moisture retrieval from space: The soil moisture and ocean salinity (smos) mission. *IEEE transactions on Geoscience and remote sensing*, 39(8):1729–1735, 2001.

[16] Manfred Zink, Hauke Fiedler, Irena Hajnsek, Gerhard Krieger, Alberto Moreira, and Marian Werner. The tandem-x mission concept. In *2006 IEEE International Symposium on Geoscience and Remote Sensing*, pages 1938–1941. IEEE, 2006.

[17] Dara Entekhabi, Eni G Njoku, Peggy E O'Neill, Kent H Kellogg, Wade T Crow, Wendy N Edelstein, Jared K Entin, Shawn D Goodman, Thomas J Jackson, Joel Johnson, et al. The soil moisture active passive (smap) mission. *Proceedings of the IEEE*, 98(5):704–716, 2010.

[18] Waleed Abdalati, H Jay Zwally, Robert Bindschadler, Bea Csatho, Sinead Louise Farrell, Helen Amanda Fricker, David Harding, Ronald Kwok, Michael Lefsky, Thorsten Markus, et al. The icesat-2 laser altimetry mission. *Proceedings of the IEEE*, 98(5):735–751, May 2010. doi: 10.1109/JPROC.2009.2034765.

[19] Oliver Reitebuch, Christian Lemmerz, Engelbert Nagel, Ulrike Paffrath, Yannig Durand, Martin Endemann, Frederic Fabre, and Marc Chaloupy. The airborne demonstrator for the direct-detection doppler wind lidar aladin on adm-aeolus. part i: Instrument design and comparison to satellite instrument. *Journal of Atmospheric and Oceanic Technology*, 26(12):2501–2515, 2009.

[20] Frank Flechtner, Phil Morton, Mike Watkins, and Frank Webb. Status of the grace follow-on mission. In *Gravity, geoid and height systems*, pages 117–121. Springer, 2014.

[21] Rosa Loizzo, M Daraio, Rocchina Guarini, Francesco Longo, Rino Lorusso, Luigi Dini, and Ettore Lopinto. Prisma mission status and perspective. In *IGARSS 2019-2019 IEEE International Geoscience and Remote Sensing Symposium*, pages 4503–4506. IEEE, 2019.

[22] Alfredo Renga, Maria Daniela Graziano, Marco Grasso, and Antonio Moccia. Evaluation of design parameters for formation flying sar. In *EUSAR 2021; 13th European Conference on Synthetic Aperture Radar*, pages 1–4. VDE, 2021.

[23] M Grasso, A Renga, G Fasano, MD Graziano, M Grassi, and A Moccia. Design of an end-to-end demonstration mission of a formation-flying synthetic aperture radar (ff-sar) based on microsatellites. *Advances in Space Research*, 67(11):3909–3923, 2021.

[24] Gerhard Krieger, Irena Hajnsek, Konstantinos Panagiotis Papathanassiou, Marwan Younis, and Alberto Moreira. Interferometric synthetic aperture radar (sar) missions employing formation flying. *Proceedings of the IEEE*, 98(5):816–843, 2010.

[25] Eberhard Gill and Hartmut Runge. Tight formation flying for an along-track sar interferometer. *Acta Astronautica*, 55(3-9):473–485, 2004.

[26] Nemesio J Rodríguez-Fernández, Eric Anterrieu, François Cabot, Jacqueline Boutin, Ghislain Picard, Thierry Pellarin, Olivier Merlin, Jerome Vialard, Frederic Vivier, Josiane Costeraste, et al. A new l-band passive radiometer for earth observation: Smos-high resolution (smos-hr). In *IGARSS 2020-2020 IEEE International Geoscience and Remote Sensing Symposium*, pages 5978–5981. IEEE, 2020.

[27] Manuel Martín-Neira, Martin Suess, Nikos Karafolas, Petri Piironen, François Deborgies, Albert Catalán, Roger Vilaseca, José Montero, Montserrat Puertolas, Diego Outumuro, et al. Technology developments for an advanced l-band radiometer mission. In *IGARSS 2020-2020 IEEE International Geoscience and Remote Sensing Symposium*, pages 6507–6510. IEEE, 2020.

[28] Manuel Martín-Neira. Smos follow-on - h. In *L-Band Continuation Workshop, CESBIO (Toulouse, France)*, pages 1–15. CESBIO, From personal communication, 2017.

[29] Eugene A Sharkov. *Passive microwave remote sensing of the Earth: physical foundations*. Springer Science & Business Media, 2003.

[30] Nicholas J Willis. *Bistatic radar*, volume 2. SciTech Publishing, 2005.

[31] Carl A Wiley. Synthetic aperture radars. *IEEE Transactions on Aerospace and Electronic Systems*, (3):440–443, 1985.

[32] Antonio Moccia and Alfredo Renga. Bistatic synthetic aperture radar. In *Distributed Space Missions for Earth System Monitoring*, pages 3–59. Springer, 2013.

[33] Marco D&'Errico. *Distributed space missions for earth system monitoring*, volume 31. Springer Science & Business Media, 2012.

[34] Antonio Moccia and Giancarlo Rufino. Spaceborne along-track sar interferometry: Performance analysis and mission scenarios. *IEEE Transactions on Aerospace and Electronic systems*, 37(1):199–213, 2001.

[35] Richard M Goldstein and HA Zebker. Interferometric radar measurement of ocean surface currents. *Nature*, 328(6132):707–709, 1987.

[36] Roland Romeiser and Hartmut Runge. Theoretical evaluation of several possible along-track insar modes of terrasar-x for ocean current measurements. *IEEE Transactions on Geoscience and Remote Sensing*, 45(1):21–35, 2006.

[37] Gerhard Krieger, Alberto Moreira, Hauke Fiedler, Irena Hajnsek, Marian Werner, Marwan Younis, and Manfred Zink. Tandem-x: A satellite formation for high-resolution sar interferometry. *IEEE Transactions on Geoscience and Remote Sensing*, 45(11):3317–3341, 2007.

[38] Fuk K Li and Richard M Goldstein. Studies of multibaseline spaceborne interferometric synthetic aperture radars. *IEEE Transactions on Geoscience and Remote Sensing*, 28(1):88–97, 1990.

[39] Didier Massonnet. The interferometric cartwheel: a constellation of passive satellites to produce radar images to be coherently combined. *International Journal of Remote Sensing*, 22(12):2413–2430, 2001.

[40] Ali Khenchaf. Bistatic scattering and depolarization by randomly rough surfaces: application to the natural rough surfaces in x-band. *Waves in random media*, 11(2):61, 2001.

[41] Fawwaz T Ulaby. Microwave remote sensing active and passive. *Rader remote sensing and surface scattering and emission theory*, pages 848–902, 1982.

[42] AW Straiton, CW Tolbert, and CO Britt. Apparent temperatures of some terrestrial materials and the sun at 4.3-millimeter wavelengths. *Journal of Applied Physics*, 29(5):776–782, 1958.

[43] Td Schmugge. Remote sensing of surface soil moisture. *Journal of Applied Meteorology (1962-1982)*, pages 1549–1557, 1978.

[44] David M Le Vine, Th T Wilheit, Robert E Murphy, and Calvin T Swift. A multifrequency microwave radiometer of the future. *IEEE transactions on geoscience and remote sensing*, 27(2):193–199, 1989.

[45] David M Le Vine. Synthetic aperture radiometer systems. *IEEE Transactions on Microwave Theory and Techniques*, 47(12):2228–2236, 1999.

[46] J-P Wigneron, TJ Jackson, P O'neill, Gabrielle De Lannoy, Patricia de Rosnay, JP Walker, P Ferrazzoli, V Mironov, Simone Bircher, JP Grant, et al. Modelling the passive microwave signature from land surfaces: A review of recent results and application to the l-band smos & smap soil moisture retrieval algorithms. *Remote Sensing of Environment*, 192:238–262, 2017.

[47] Ahmed Kiyoshi Sugihara El Maghraby, Angelo Grubišić, Camilla Colombo, and Adrian Tatnall. A novel interferometric microwave radiometer concept using satellite formation flight for geostationary atmospheric sounding. *IEEE Transactions on Geoscience and Remote Sensing*, 56(6):3487–3498, 2018.

[48] Li Feng, Qingxia Li, and Yufang Li. Imaging with 3-d aperture synthesis radiometers. *IEEE Transactions on Geoscience and Remote Sensing*, 57(4):2395–2406, 2018.

[49] Michael Kirschner, Oliver Montenbruck, and Srinivas Bettadpur. Flight dynamics aspects of the grace formation flying. In *2nd International Workshop on Satellite Constellations and Formation Flying*, pages 19–20. Citeseer, 2001.

[50] Simone D'Amico, Oliver Montenbruck, Christian Arbinger, and Hauke Fiedler. Formation flying concept for close remote sensing satellites. In *15th AAS/AIAA Space Flight Mechanics Conference, Copper Mountain, Colorado, January 23-27*, volume AAS.

[51] Alexander Härting, C RAJASINGH, M ECKSTEIN, A LEIBOLD, and K SRINIVASAMURTHY. On the collision hazard of colocated geostationary satellites. In *Astrodynamics Conference*, page 4239, 1988.

[52] Jean-Sébastien Ardaens, Gabriella Gaias, and Ralph Kahle. From grace to avanti: 15 years of formation-flying experience at dlr. In *Proc. of 69th International Astronautical Congress (IAC 2018)*, pages 1–8, Bremen, Germany, 2018. International Astronautical Federation, IAF. url: https://hdl.handle.net/11311/1139269.

[53] Giancarmine Fasano and Marco D'Errico. Modeling orbital relative motion to enable formation design from application requirements. *Celestial Mechanics and Dynamical Astronomy*, 105(1):113–139, 2009.

[54] Antonio Moccia and Giancarmine Fasano. Analysis of spaceborne tandem configurations for complementing cosmo with sar interferometry. *EURASIP Journal on Advances in Signal Processing*, 2005(20):1–12, 2005.

[55] Nicola Baresi and Daniel J Scheeres. Design of bounded relative trajectories in the earth zonal problem. *Journal of Guidance, Control, and Dynamics*, 40(12):3075–3087, Aug 2017. doi: 10.2514/1.G002603.

[56] Roberto Opromolla, Giancarmine Fasano, Giancarlo Rufino, and Michele Grassi. Design of relative trajectories for in orbit proximity operations. *Acta Astronautica*, 145:342–356, 2018.

[57] S Sarno, M D'Errico, J Guo, and E Gill. Path planning and guidance algorithms for sar formation reconfiguration: Comparison between centralized and decentralized approaches. *Acta Astronautica*, 167:404–417, 2020.

[58] Richard Bamler and Philipp Hartl. Synthetic aperture radar interferometry. *Inverse problems*, 14(4):R1–R54, Feb 1998. doi: 10.1088/0266-5611/14/4/001.

[59] Daniel P Scharf, Fred Y Hadaegh, and Scott R Ploen. A survey of spacecraft formation flying guidance and control (part ii): Control. In *Proceedings of the 2004 American control conference*, volume 4, pages 2976–2985. Ieee, 2004.

[60] Kyle T Alfriend and Hui Yan. Evaluation and comparison of relative motion theories. *Journal of Guidance, Control, and Dynamics*, 28(2):254–261, May 2005. doi: 10.2514/1.6691.

[61] Ryan P Russell. Survey of spacecraft trajectory design in strongly perturbed environments. *Journal of Guidance, Control, and Dynamics*, 35(3):705–720, 2012.

[62] Marco B Quadrelli, Lincoln J Wood, Joseph E Riedel, Michael C McHenry, MiMi Aung, Laureano A Cangahuala, Richard A Volpe, Patricia M Beauchamp, and James A Cutts. Guidance, navigation, and control technology assessment for future planetary science missions. *Journal of Guidance, Control, and Dynamics*, 38(7):1165–1186, 2015.

[63] Joshua Sullivan, Sebastian Grimberg, and Simone D'Amico. Comprehensive survey and assessment of spacecraft relative motion dynamics models. *Journal of Guidance, Control, and Dynamics*, 40(8):1837–1859, 2017.

[64] Giuseppe Di Mauro, Margaret Lawn, and Riccardo Bevilacqua. Survey on guidance navigation and control requirements for spacecraft formation-flying missions. *Journal of Guidance, Control, and Dynamics*, 41(3):581–602, 2018.

[65] George William Hill. Researches in the lunar theory. *American journal of Mathematics*, 1(1):5–26, 1878.

[66] WH Clohessy and RS Wiltshire. Terminal guidance system for satellite rendezvous. *Journal of the Aerospace Sciences*, 27(9):653–658, 1960.

[67] Oliver Montenbruck, Michael Kirschner, Simone D'Amico, and Srinivas Bettadpur. E/i-vector separation for safe switching of the grace formation. *Aerospace Science and Technology*, 10(7):628–635, 2006.

[68] Kyle T Alfriend, Srinivas R Vadali, Pini Gurfil, Jonathan P How, and Louis Breger. *Spacecraft formation flying: Dynamics, control and navigation*, volume 2. Elsevier, 2009. ISBN: 978-0-75-068533-7.

[69] D Izzo, M Sabatini, and C Valente. A new linear model describing formation flying dynamics under j2 effects. In *Proceedings of the 17th AIDAA National Congress*, volume 1, pages 15–19, 2003.

[70] Samuel A Schweighart and Raymond J Sedwick. High-fidelity linearized j model for satellite formation flight. *Journal of Guidance, Control, and Dynamics*, 25(6):1073–1080, 2002.

[71] Marco Sabatini and Giovanni B Palmerini. Linearized formation-flying dynamics in a perturbed orbital environment. In *2008 IEEE aerospace conference*, pages 1–13. IEEE, 2008.

[72] Hanspeter Schaub and Kyle T Alfriend. J2 invariant relative orbits for spacecraft formations. *Celestial Mechanics and Dynamical Astronomy*, 79(2):77–95, 2001.

[73] Dong-Woo Gim and Kyle T Alfriend. State transition matrix of relative motion for the perturbed noncircular reference orbit. *Journal of Guidance, Control, and Dynamics*, 26(6):956–971, 2003.

[74] Simone D'Amico and Oliver Montenbruck. Proximity operations of formation-flying spacecraft using an eccentricity/inclination vector separation. *Journal of Guidance, Control, and Dynamics*, 29(3):554–563, 2006.

[75] Gabriella Gaias, Jean-Sébastien Ardaens, and Oliver Montenbruck. Model of j2 perturbed satellite relative motion with time-varying differential drag. *Celestial Mechanics and Dynamical Astronomy*, 123(4):411–433, 2015.

[76] Adam W Koenig, Tommaso Guffanti, and Simone D'Amico. New state transition matrices for spacecraft relative motion in perturbed orbits. *Journal of Guidance, Control, and Dynamics*, 40(7):1749–1768, 2017.

[77] GVM Gaias and C Colombo. Semi-analytical framework for precise relative motion in low earth orbits. In *7th International Conference on Astrodynamics Tools and Techniques (ICATT)*, pages 1–10, 2018.

[78] Gabriella Gaias, Camilla Colombo, and Martin Lara. Analytical framework for precise relative motion in low earth orbits. *Journal of Guidance, Control, and Dynamics*, 43(5):915–927, 2020.

[79] Jean-Sébastien Ardaens and Denis Fischer. Tandem-x autonomous formation flying system: Flight results. *IFAC Proceedings Volumes*, 44(1):709–714, Jan 2011. doi: 10.3182/20110828-6-IT-1002.02374.

[80] S Vadali, Hanspeter Schaub, and K Alfriend. Initial conditions and fuel-optimal control for formation flying of satellites. In *Guidance, Navigation, and Control Conference and Exhibit*, page 4265, 1999.

[81] SR Vadali, SS Vaddi, and Kyle T Alfriend. An intelligent control concept for formation flying satellites. *International Journal of Robust and Nonlinear Control: IFAC-Affiliated Journal*, 12(2-3):97–115, 2002.

[82] SS Vaddi, Kyle T Alfriend, SR Vadali, and P Sengupta. Formation establishment and reconfiguration using impulsive control. *Journal of Guidance, Control, and Dynamics*, 28(2):262–268, 2005.

[83] Srinivas R Vadali, Prasenjit Sengupta, Hui Yan, and Kyle T Alfriend. Fundamental frequencies of satellite relative motion and control of formations. *Journal of Guidance, Control, and Dynamics*, 31(5):1239–1248, 2008.

[84] Callum S. Arnot, Colin R McInnes, Rob J. McKay, Malcolm Macdonald, and James Biggs. Orbit period modulation for relative motion using continuous low thrust in the two-body and restricted three-body problems. *Celestial Mechanics and Dynamical Astronomy*, 130(2):1–23, Jan 2018. doi: 10.1007/s10569-017-9807-3.

[85] Marco Sabatini, Dario Izzo, and Riccardo Bevilacqua. Special inclinations allowing minimal drift orbits for formation flying satellites. *Journal of Guidance, Control, and Dynamics*, 31(1):94–100, 2008.

[86] Corinne Lippe and Simone D'Amico. Minimization of delta-v for satellite swarm maintenance using a virtual chief. *IEEE Journal on Miniaturization for Air and Space Systems*, 1(3):197–218, 2020.

[87] Michael Tillerson, Gokhan Inalhan, and Jonathan P How. Co-ordination and control of distributed spacecraft systems using convex optimization techniques. *International Journal of Robust and Nonlinear Control: IFAC-Affiliated Journal*, 12(2-3):207–242, 2002.

[88] Behcet Acikmese, Daniel Scharf, Fred Hadaegh, and Emmanuell Murray. A convex guidance algorithm for formation reconfiguration. In *Proc. of AIAA Guidance, Navigation, and Control Conference and Exhibit*, pages 1–17, Keystone, Colorado, Aug 2006. doi: 10.2514/6.2006-6070.

[89] S Sarno, J Guo, M D'Errico, and E Gill. A guidance approach to satellite formation reconfiguration based on convex optimization and genetic algorithms. *Advances in Space Research*, 65(8):2003–2017, 2020.

[90] Gabriella Gaias and Jean-Sébastien Ardaens. Flight demonstration of autonomous noncooperative rendezvous in low earth orbit. *Journal of Guidance, Control, and Dynamics*, 41(6):1337–1354, 2018.

[91] Daniel Morgan, Soon-Jo Chung, and Fred Y Hadaegh. Model predictive control of swarms of spacecraft using sequential convex programming. *Journal of Guidance, Control, and Dynamics*, 37(6):1725–1740, 2014.

[92] Julian Scharnagl, Panayiotis Kremmydas, and Klaus Schilling. Model predictive control for continuous low thrust satellite formation flying. *IFAC-PapersOnLine*, 51(12):12–17, 2018.

[93] Robin Larsson, Sten Berge, Per Bodin, and Ulf T Jönsson. Fuel efficient relative orbit control strategies for formation flying and rendezvous within prisma. In *Guidance and Control 2006, 4-8 February 2006, Breckenridge, CO, USA*, pages 25–40. Univelt Inc., USA, 2006.

[94] Yuri Ulybyshev. Long-term formation keeping of satellite constellation using linear-quadratic controller. *Journal of Guidance, Control, and Dynamics*, 21(1):109–115, 1998.

[95] Fred Y Hadaegh, Ali R Ghavimi, Gurkirpal Singh, and Marco Quadrelli. A centralized optimal controller for formation flying spacecraft. In *International Conference on Intelligent Technologies. Bangkok, Thailand*, pages 1–6, 2000.

[96] David Folta, J Russell Carpenter, and Christoph Wagner. Formation flying with decentralized control in libration point orbits. In *Space Flight Dynamics*, 2000.

[97] Leonel Palacios, Matteo Ceriotti, and Gianmarco Radice. Close proximity formation flying via linear quadratic tracking controller and artificial potential function. *Advances in Space Research*, 56(10):2167–2176, 2015.

[98] Trevor Bennett and Hanspeter Schaub. Continuous-time modeling and control using nonsingular linearized relative-orbit elements. *Journal of Guidance, Control, and Dynamics*, 39(12):2605–2614, Oct 2016. doi: `doi.org/10.2514/1.G000366`.

[99] Mai Bando and Akira Ichikawa. Periodic orbits of nonlinear relative dynamics and satellite formation. *Journal of guidance, control, and dynamics*, 32(4):1200–1208, May 2009. doi: 10.2514/1.41438.

[100] Gregory R Frey, Christopher D Petersen, Frederick A Leve, Ilya V Kolmanovsky, and Anouck R Girard. Constrained spacecraft relative motion planning exploiting periodic natural motion trajectories and invariance. *Journal of Guidance, Control, and Dynamics*, 40(12):3100–3115, 2017.

[101] Jason Speyer. Computation and transmission requirements for a decentralized linear-quadratic-gaussian control problem. *IEEE Transactions on Automatic Control*, 24(2):266–269, 1979.

[102] Adam W Koenig and Simone D'Amico. Safe spacecraft swarm deployment and acquisition in perturbed near-circular orbits subject to operational constraints. *Acta Astronautica*, 153:297–310, 2018.

[103] Adam W Koenig and Simone D'Amico. Fast algorithm for fuel-optimal impulsive control of linear systems with time-varying cost. *IEEE Transactions on Automatic Control*, 66(9):4029–4042, 2020.

[104] Danil Ivanov, Uliana Monakhova, and Mikhail Ovchinnikov. Nanosatellites swarm deployment using decentralized differential drag-based control with communicational constraints. *Acta Astronautica*, 159:646–657, 2019.

[105] Simone D'Amico, Eberhard Gill, Miquel Fernandez Garcia, and Oliver Montenbruck. Gps-based real-time navigation for the prisma formation flying mission. In *3rd ESA workshop on satellite navigation user equipment technologies, NAVITEC*, 2006.

[106] Joseph Guinn and Ronald Boain. Spacecraft autonomous navigation for formation flying earth orbiters using gps. In *Astrodynamics Conference*, page 3655, 1996.

[107] Sunny Leung and Oliver Montenbruck. Real-time navigation of formation-flying spacecraft using global-positioning-system measurements. *Journal of Guidance, Control, and Dynamics*, 28(2):226–235, 2005.

[108] Remco Kroes, Oliver Montenbruck, William Bertiger, and Pieter Visser. Precise grace baseline determination using gps. *Gps Solutions*, 9(1):21–31, 2005.

[109] Jean-Sébastien Ardaens, Simone D'Amico, and Josef Sommer. Gps navigation system for challenging close-proximity formation-flight. In *24th International Symposium on Space Flight Dynamics*, pages 1–15, Laurel, Maryland, USA, May 2014.

[110] Oliver Montenbruck, Martin Wermuth, and Ralph Kahle. Gps based relative navigation for the tandem-x mission-first flight results. *Navigation*, 58(4):293–304, 2011.

[111] Francesca Scala, Gabriella Gaias, Camilla Colombo, and Manuel Martìn-Neira. Formation flying l-band aperture synthesis: Design challenges and innovative formation architecture concept. In *Proc. of 71st International Astronautical Congress (IAC 2020)*, pages 1–10, Virtual conference, Oct 2020. url: `https://hdl.handle.net/11311/1153224`.

[112] Cristina Erbeia, Francesca Scala, and Camilla Colombo. Robustness analysis and station-keeping control of an interferometer formation flying mission in low earth orbit. *Submitted for review to Advances in Space Research*, 2023.

[113] Francesca Scala, Gabriella Gaias, Camilla Colombo, and Manuel Martín-Neira. Design of optimal low-thrust manoeuvres for remote sensing multi-satellite formation flying in low earth orbit. *Advances in Space Research*, 68(11):4359–4378, Dec 2021. doi: 10.1016/j.asr.2021.09.030.

[114] Francesca Scala, GVM Gaias, Camilla Colombo, Manuel Martìn Neira, et al. Three satellites formation flying: Deployment and formation acquisition using relative orbital elements. *Advances in the Astronautical Sciences*, 175:3981–3997, Jan 2021. url: `https://hdl.handle.net/11311/1146013`.

[115] Alejandro Montero Miñan, Francesca Scala, and Camilla Colombo. Manoeuvre planning algorithm for satellite formations using mean relative orbital elements. *Advances in Space Research*, 71(1):585–603, Jan 2022. doi: 10.1016/j.asr.2022.09.043.

[116] Francesca Scala, Camilla Colombo, Gabriella Gaias, and Manuel Martìn-Neira. Gnss-based navigation for a remote sensing three-satellite formation flying. In *Proc. of SpaceOps 2021 Virtual Edition*, pages 1–18, Virtual conference, May 2021. url: `https://hdl.handle.net/11311/1172794`.

[117] Francesca Scala, Camilla Colombo, and Manuel Martìn-Neira. A decentralised approach for formation flying reconfiguration and maintenance using gnss-based navigation. In *Proc. of AIAA Scitech 2022 Forum*, page 2463, San Diego, CA, USA, Jan 2022. doi: 10.2514/6.2022-2463.

[118] Francesca Scala, Camilla Colombo, and Manuel Martìn-Neira. Design of natural collision-free trajectories for the mission extension phase of a remote sensing formation flying mission. In *Proc. of 72nd International Astronautical Congress (IAC 2021)*, pages 1–11, Dubai, United Arab Emirates, Oct 2021. url: `hdl.handle.net/11311/1189478`.

[119] Francesca Scala, Camilla Colombo, Miguel Piera, Albert Zurita, Berthyl Duesmann, and M Martín Neira. Performance assessment of the formation flying l-band aperture synthesis mission concept. In *ESA Living Planet Symposium 2022*, Bonn, Germany, May 2022. url: `https://hdl.handle.net/11311/1217925`.

[120] Alberto M Zurita, Ignasi Corbella, Manuel Martin-Neira, Miguel A Plaza, Francesc Torres, and F Javier Benito. Towards a smos operational mission: Smosops-hexagonal. *IEEE Journal of Selected Topics in Applied Earth Observations and Remote Sensing*, 6(3):1769–1780, 2013.

[121] Ignasi Corbella, Manuel Martin-Neira, Roger Oliva, Francesc Torres, and Nuria Duffo. Reduction of secondary lobes in aperture synthesis radiometry. *IEEE Geoscience and Remote Sensing Letters*, 9(5):977–979, 2012.

[122] Masami Onoda and Oran R Young. *Satellite earth observations and their impact on society and policy*. Springer Nature, 2017.

[123] Josef Aschbacher. Esa's earth observation strategy and copernicus. *Satellite earth observations and their impact on society and policy*, pages 81–86, 2017.

[124] Markus Bachmann, Manfred Zink, Dirk Geudtner, Allan Bojarski, Michele Martone, Ralph Kahle, Gerhard Krieger, Matteo Pardini, Jens Reimann, Maximilian Schandri, et al. Rose-l tandem–bistatic extension for single-pass interferometry. In *EUSAR 2022; 14th European Conference on Synthetic Aperture Radar*, pages 1–4. VDE, 2022.

[125] Martin Suess, Erik De Witte, and Bjoern Rommen. Earth explorer 10 candidate mission harmony. In *EUSAR 2022; 14th European Conference on Synthetic Aperture Radar*, pages 1–4. VDE, 2022.

[126] Adriano Camps, Javier Bará, Ignasi Corbella Sanahuja, and Francesc Torres. The processing of hexagonally sampled signals with standard rectangular techniques: Application to 2-d large aperture synthesis interferometric radiometers. *IEEE Transactions on Geoscience and Remote Sensing*, 35(1):183–190, 1997.

[127] Harry Nyquist. Certain topics in telegraph transmission theory. *Transactions of the American Institute of Electrical Engineers*, 47(2):617–644, 1928.

[128] Claude E Shannon. Communication in the presence of noise. *Proceedings of the IRE*, 37(1):10–21, 1949.

[129] Manuel Martín-Neira, Francesca Scala, Albert Zurita, Martin Suess, Miguel Angel Piera, Berthyl Duesmann, Camilla Colombo, Don De Wilde, Josep Closa, Erio Gandini, Raul Diez-Garcia, Roger Oliva, and Ignasi Corbella. Trihex: combining formation flying, general circular orbits and alias-free imaging, for high resolution l-band aperture synthesis. In *Unpublished manuscript. Submitted for review to IEEE Transactions on GeoScience and Remote Sensing Journal*, pages 1–14. IEEE, 2023.

[130] Miguel Piera Martinez, Francesca Scala, Camilla Colombo, Albert Zurita, Berthyl Duesmann, and Manuel Martín-Neira. Formation flying l-band aperture synthesis mission concept. In *Unpublished manuscript. Submitted for review to IEEE Transactions on GeoScience and Remote Sensing Journal*, pages 1–14. IEEE, 2023.

[131] David A Vallado. *Fundamentals of astrodynamics and applications*, volume 4th edition. Microcosm Press (Space Technology Library), 2013.

[132] Oliver Montenbruck, Eberhard Gill, and Fh Lutze. Satellite orbits: models, methods, and applications. *Appl. Mech. Rev.*, 55(2):B27–B28, 2002.

[133] Simone D'Amico. *Autonomous formation flying in low earth orbit*. PhD thesis, TU Delft, 2010.

[134] Byron Tapley, J Ries, S Bettadpur, D Chambers, M Cheng, F Condi, B Gunter, Z Kang, P Nagel, R Pastor, et al. Ggm02–an improved earth gravity field model from grace. *Journal of Geodesy*, 79:467–478, 2005.

[135] Nikolaos K Pavlis, Simon A Holmes, Steve C Kenyon, and John K Factor. The development and evaluation of the earth gravitational model 2008 (egm2008). *Journal of geophysical research: solid earth*, 117(B4), 2012.

[136] Charles E Roberts. An analytic model for upper atmosphere densities based upon jacchia's 1970 models. *Celestial Mechanics*, 4(3):368–377, 1971.

[137] JM Picone, AE Hedin, D Pj Drob, and AC Aikin. Nrlmsise-00 empirical model of the atmosphere: Statistical comparisons and scientific issues. *Journal of Geophysical Research: Space Physics*, 107(A12):SIA–15, 2002.

[138] Gabriella Gaias and Marco Lovera. Trajectory design for proximity operations: The relative orbital elements' perspective. *Journal of Guidance, Control, and Dynamics*, 44(12):2294–2302, 2021.

[139] Giancarmine Fasano, Alfredo Renga, and Marco D'Errico. Formation geometries for multistatic sar tomography. *Acta Astronautica*, 96:11–22, 2014.

[140] G Di Mauro, R Bevilacqua, D Spiller, J Sullivan, and S D'Amico. Continuous maneuvers for spacecraft formation flying reconfiguration using relative orbit elements. *Acta Astronautica*, 153:311–326, 2018.

[141] Stephen Boyd, Stephen P Boyd, and Lieven Vandenberghe. *Convex optimization*. Cambridge university press, New York, USA, 2004. doi: 10.1017/CBO9780511804441.

[142] Derek Rowell. State-space representation of lti systems. *URL: http://web. mit. edu/2.14/www/Handouts/StateSpace. pdf*, pages 1–18, 2002.

[143] Michael Grant, Stephen Boyd, and Yinyu Ye. Disciplined convex programming. *Global optimization: From theory to implementation*, pages 155–210, 2006.

[144] Jos F Sturm. Using sedumi 1.02, a matlab toolbox for optimization over symmetric cones. *Optimization methods and software*, 11(1-4):625–653, 1999.

[145] Kim-Chuan Toh, Michael J Todd, and Reha H Tütüncü. Sdpt3a matlab software package for semidefinite programming, version 1.3. *Optimization methods and software*, 11(1-4):545–581, 1999.

[146] Gurobi Optimization, LLC. Gurobi Optimizer Reference Manual, 2021.

[147] Michael C Grant and Stephen P Boyd. Graph implementations for nonsmooth convex programs. In *Recent advances in learning and control*, pages 95–110. Springer, 2008.

[148] Michael Grant, Stephen Boyd, and Y Ye. Cvx: Matlab software for disciplined convex programming, version 2.0 beta. `http://cvxr.com/cvx`, 2013.

[149] Mohamed Shouman, Mai Bando, and Shinji Hokamoto. Output regulation control for satellite formation flying using differential drag. *Journal of guidance, control, and dynamics*, 42(10):2220–2232, 2019.

[150] Karl Johan Åström and Richard M. Murray. *Feedback systems: an introduction for scientists and engineers, second edition*. Princeton university press, 6 Oxford Street, Woodstock, Oxfordshire OX20 1TW, 2021. ISBN-13: 978-0-691-13576-2.

[151] Behçet Açıkmeşe, John M Carson III, and David S Bayard. A robust model predictive control algorithm for incrementally conic uncertain/nonlinear systems. *International Journal of Robust and Nonlinear Control*, 21(5):563–590, Feb 2011. doi: 10.1002/rnc.1613.

[152] Rebecca Foust, Soon-Jo Chung, and Fred Y Hadaegh. Optimal guidance and control with nonlinear dynamics using sequential convex programming. *Journal of Guidance, Control, and Dynamics*, 43(4):633–644, 2020.

[153] Arthur Richards and Jonathan P How. Robust variable horizon model predictive control for vehicle maneuvering. *International Journal of Robust and Nonlinear Control: IFAC-Affiliated Journal*, 16(7):333–351, 2006.

[154] Alberto Bemporad and Manfred Morari. Robust model predictive control: A survey. In *Robustness in identification and control*, pages 207–226. Springer, 2007.

[155] Jae-Ik Park, Han-Earl Park, Sang-Young Park, and Kyu-Hong Choi. Hardware-in-the-loop simulations of gps-based navigation and control for satellite formation flying. *Advances in Space Research*, 46(11):1451–1465, 2010.

[156] Dan Simon. *Optimal state estimation: Kalman, Hinf, and nonlinear approaches.*, volume 10. 2006.

[157] Peter N Randall, RA Lewis, SD Clark, and KW Hall. T5 performance, industrialisation and future applications. In *Proceedings of the 36th International Electric Propulsion Conference, vol. University of Vienna, Austria. QinetiQ Space UK*, 2019.